University of Bath

PHD

Modelling the Skin and Systemic Dispositions of Amino Acids to Assess the Potential for Transdermal, Non-Invasive Monitoring: Phenylalanine as a Case Study

Woodford, Andrew

Award date:
2017

Awarding institution:
University of Bath

Link to publication

Alternative formats
If you require this document in an alternative format, please contact:
openaccess@bath.ac.uk

Copyright of this thesis rests with the author. Access is subject to the above licence, if given. If no licence is specified above, original content in this thesis is licensed under the terms of the Creative Commons Attribution-NonCommercial 4.0 International (CC BY-NC-ND 4.0) Licence (https://creativecommons.org/licenses/by-nc-nd/4.0/). Any third-party copyright material present remains the property of its respective owner(s) and is licensed under its existing terms.

Take down policy
If you consider content within Bath's Research Portal to be in breach of UK law, please contact: openaccess@bath.ac.uk with the details. Your claim will be investigated and, where appropriate, the item will be removed from public view as soon as possible.

Download date: 05. May. 2023

Modelling the Skin and Systemic Dispositions of Amino Acids to Assess the Potential for Transdermal, Non-Invasive Monitoring: Phenylalanine as a Case Study

submitted by

Andrew S. Woodford

for the degree of Doctor of Philosophy

of the

University of Bath

Department of Mathematical Sciences

September 2016

COPYRIGHT

Attention is drawn to the fact that copyright of this thesis rests with the author. A copy of this thesis has been supplied on condition that anyone who consults it is understood to recognise that its copyright rests with the author and that they must not copy it or use material from it except as permitted by law or with the consent of the author.

This thesis may be made available for consultation within the University Library and may be photocopied or lent to other libraries for the purposes of consultation with effect from ..

.....

Signed on behalf of the Faculty of Science .....

Acknowledgements

Firstly I would like to thank my supervisors Dr Jane White, Dr Begoña Delgado-Charro and Professor Richard Guy for their continued support, patience and advice throughout the PhD. I would also like to thank them for introducing me to such an interesting field and helping to broaden my knowledge of where mathematics can be applied in the real world.

I would also like to thank Dr Frank Hilker for encouraging me to embark on the PhD and the BBSRC for funding it. I would also like to thank Sarah Cordery for her technical expertise in the pharmacy lab.

A big thank you to my parents who kept me fed and supplied with copious amounts of tea during the write up phase. I would like to also thank them for their support throughout my entire academic career, I could not have got this far without them.

Finally I would also like to thank my friends, especially William Povey, Thomas Folland and Matthew Hull for making my time in Bath far more enjoyable.

Summary

This thesis investigates the potential for monitoring current and historic blood serum concentrations of amino acids via transdermal extraction using phenylalanine as a case study. This work furthers the field of non-invasive monitoring of amino acid disorders which have several advantages over invasive methods such as blood tests. In this thesis we derive models to simulate blood serum concentrations, the formation of the skin reservoir and, finally, transdermal extraction of amino acids under an applied electric field.

Chapter 1 concerns itself with the biological background and sets up motivation of the thesis by discussing amino acids, associated amino acid disorders, the overarching clinical problem, skin structure and transdermal extraction methods. Chapter 2 then considers mathematical techniques utilised throughout the thesis.

Chapter 3 formulates a model for the distribution of phenylalanine in blood serum. One compartment and two compartment approaches are considered in both a fasting state and a non-fasting state. We consider if these have a noticeable effect on the blood serum concentration of phenylalanine.

Having obtained a model for the distribution of phenylalanine in blood serum, chapter 4 models the formation of reservoirs of amino acids in the skin. Prior work has identified the existence of such a reservoir, but its formation has not been addressed. The models developed consider the effect of the removal of outer layers of skin, the stratum disjunctum, and production of amino acids in the skin. Unknown parameters are estimated by comparing the model to *in vivo* and *in vitro* data.

Chapter 5 and 6 are concerned with transdermal extraction under an applied electric field. Chapter 5 formulates the velocity induced by applying an electric field across a charged interface. Chapter 6 utilises these results for modelling extraction of compounds through the skin under an applied electric field.

Contents

Chapter 1

Background

The aim of this chapter is to introduce the key biological concepts behind the thesis. We begin by introducing amino acids and associated amino acids disorders, focusing on the amino acid phenylalanine and the associated amino acid disorder, phenylketonuria. Having considered amino acid disorders, we then discuss the current clinical problems associated with monitoring these disorders. The main clinical problem revolves around having to use invasive methods, such as blood tests, to monitor such conditions. Due to problems associated with invasive sampling methods, prior work has proposed that an alternative to invasive sampling is non-invasive sampling through the skin, called transdermal extraction [1, 2]. Mathematically modelling transdermal extraction is the primary goal of this thesis, hence, once the clinical problem has been discussed, the skin and the transdermal extraction methods, such as passive diffusion and reverse iontophoresis, are considered.

The chapter is concluded with an overview of the structure of the thesis.

1.1 Amino Acids

The primary function of amino acids in the body is to form proteins. Proteins are polymer chains comprised of over 50 amino acids linked by peptide chains [3]. Proteins are incredibly important in the human body and perform a variety of tasks essential to life, such as being the building blocks of body tissue, forming antibodies that help prevent disease and infection as well as being a major source of energy [4]. Due to the multitude of roles proteins play in the body, the human body is approximately 20% protein by weight [4].

Forming proteins is not the only biologically important role amino acids play in the body. Amino acids also perform other roles such as acting as chemical messengers, either as neurotransmitters or hormones, and playing an essential role in metabolism [3].

1.1.1 Phenylalanine

Phenylalanine is an example of an amino acid [5]. From the structure of phenylalanine shown in Figure 1-1 it is clear that phenylalanine has an aromatic ring, which allows it to absorb UV radiation. Due to this, phenylalanine is useful in skin protection and an important part of the natural moisturising factor (NMF) that controls skin hydration [5]. Additionally, phenylalanine's primary metabolite is tyrosine which is important in melanin synthesis [6]; melanin is important in protecting the body from UV radiation.

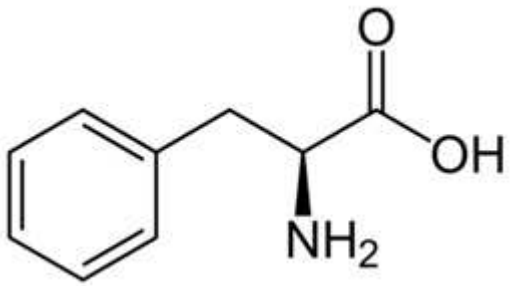

Figure 1-1: Structure of Phenylalanine. The chemical formula for this compound is $C_9H_{11}NO_2$ with an aromatic ring on the far left of the structure. Taken from [7].

Phenylalanine is taken into the body either by food intake, as it is present in meat, fish, dairy products, nuts and aspartame, an artificial sweetener, or by the decomposition of proteins in both the skin and general body muscle [8]. As an amino acid, phenylalanine is hydrophilic and hence it is distributed evenly throughout total body water [9].

There are several ways that phenylalanine is eliminated from the body which can be broadly split into metabolism and excretion. The metabolic pathways for phenylalanine are shown in Figure 1-2. Route 1 represents hydroxylation of phenylalanine into tyrosine, a reaction that is catalysed by the enzyme phenylalanine hydroxylase (PAH). This step is the rate limiting part of the conversion of phenylalanine into carbon dioxide and water and is responsible for approximately 75% of phenylalanine clearance [6] in the body.

The second route identified for metabolism is transamination into phenylpyruvate, which is then metabolised into other compounds. Other metabolic routes exist, but these are considered to be negligible in comparison to hydroxylation and transamination [10].

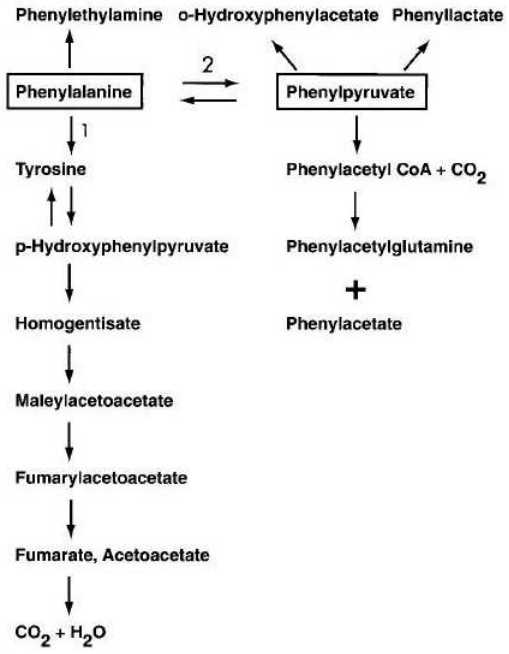

Figure 1-2: Metabolic pathways of phenylalanine. Route 1 represents hydroxylation of phenylalanine into tyrosine and responsible for approximately 75% of phenylalanine clearance in the body. Route 2 represents transamination into phenylpyruvate which is another important metabolic process, especially in patients with phenylketonuria. Taken from [10].

Removal of phenylalanine from the body also occurs via the formation of muscle. Correspondingly, muscle degradation can also generate phenylalanine. Typically serum phenylalanine concentration in a healthy patient in a fasting state is between 0.057-0.060mM [10], and is expected to be higher than this if food intake is considered [11].

1.2 Amino Acid Disorders

Amino acids, such as phenylalanine, are very important in biological processes [3]. Metabolism is a key process in biological systems either involved in building up new compounds, anabolism, or breaking down organic matter, catabolism. Enzymes are proteins that catalyse metabolic reactions with almost all metabolic processes in the body requiring enzymes to achieve rates fast enough to sustain life [12].

Modern biochemical genetics has shown how proteins with specific structural and metabolic properties are synthesised from genetic information [13]. Genetic information is stored in chromosomes in cell nuclei encoded in DNA. Mutations in DNA can alter the structure of a protein which can have several effects on the protein formed. The exact effect can vary

from affecting the function of the protein to the rate of synthesis depending upon the part of the protein effected [13]. In enzymes, this can lead to reduced metabolism of an amino acid which, depending on severity, can cause a variety of medical complications [13].

We consider the most frequent of amino acid disorders, phenylketonuria, which inhibits the metabolism of phenylalanine.

1.2.1 Phenylketonuria (PKU)

Phenylketonuria (PKU) is the most frequent of inherited amino acid disorders and affects 1 in 10,000 people [14]. This particular disorder affects the PAH enzyme, limiting its ability to metabolise phenylalanine and, depending on the severity of the condition, can lead to a significant increase in blood serum concentration of phenylalanine. This is a problem as phenylalanine is transported from the blood into the brain along with other large, neutral amino acids (LNAAs) via LNAA type 1 transporter [15]. Phenylalanine has the highest binding affinity to this transporter, thus will be selected for transport preferentially over other compounds [15]. Hence, higher levels of phenylalanine increasingly limits the transport of other LNAAs transported into the brain via LNAA type 1 transporter. Limiting the transport of these compounds causes a decrease in cerebral protein synthesis (CPS) which has been shown to be very important in cognitive development [15].

In short, phenylketonuria can cause mental health problems ranging from severe retardation to minor IQ loss [15], hence it is important to begin treatment of this condition as soon as possible. Due to this, in combination with its prevalence, phenylketonuria is tested for about a week after birth via a blood test with the sample taken from the heel of the foot [16]. Phenylalanine levels and the ratio of phenylalanine/tyrosine are tested using this sample and PKU is diagnosed if systemic levels of phenylalanine are above 0.12-0.13mM with a phenylalanine:tyrosine ratio of 2 or greater [16].

One of the considerations while doing this test is that 2% of positive PKU tests are a result of a BH_4 metabolism disorder, which needs to be treated very differently from PKU. For this reason, PKU confirmation tests are done after the initial blood sample [16].

Once PKU has been identified, phenylalanine levels are then monitored at intervals throughout the patient's life. Phenylalanine levels are also monitored closely in pregnant women as elevated phenylalanine levels in the mother can damage the unborn child [8].

The severity of the condition can be identified via a tolerance test, which is repeated through-

out childhood to get progressive measurements. This classification provides guidelines to the amount of phenylalanine that should be in the patients diet. These different classifications are detailed below and are relative to the bodyweight of the patient [16].

Classical PKU Phenylalanine tolerance less than 20mg/kg/day.

Moderate PKU Phenylalanine tolerance of 20-25mg/kg/day.

Mild PKU Phenylalanine tolerance of 25-50mg/kg/day.

Mild hyperphenylanemia (HPA) Phenylalanine tolerance of greater than 50mg/kg/day. In this case a special diet is not required.

There has also been work into classifying PKU based on the results of genetic tests. Currently over 500 different PAH mutations have been identified [16] and several databases exist which predict the type of PKU a patient has based on their genotype combination. In this, different allele mutations are given a mutation score of 1, 2, 4 or 8, with 1 being a severely inhibiting mutation and 8 being a mildly inhibiting mutation [16]. The scores for the two relevant alleles are then added together to give the assigned phenotypic effect of mutant PAH alleles score (AV score) which can then be used to predict the severity of PKU [16].

There are some discrepancies in the genetic method, making tolerance tests still important [17]. Additionally, recent papers have suggested that tolerance for adult patients is affected by BMI and gender. A higher BMI results in a lower phenylalanine tolerance and women typically have a lower tolerance than men [17]. This difference is likely due to BMI affecting the volume of distribution for phenylalanine. Phenylalanine is hydrophilic [9] and hence distributes itself throughout total body water. Total body water is normally considered to be about 57% in a man at ideal body weight, but can decrease significantly, as low as 45%, with higher BMIs. However, the reduction in tolerance has only been tested on a very small scale [17], so follow up needs to be investigated before the effect of this result on phenylalanine tolerance can be confirmed.

1.3 The Clinical Problem

Patients with amino acid disorders often have serum concentrations monitored via blood samples which is an invasive procedure [10]. Invasive procedures have several drawbacks such as risk of infection, patient discomfort and the requirement for trained personnel to administer

[18]. Finding a non-invasive method, such as transdermal extraction, would eliminate all of these problems and allow tests to be administered more conveniently.

Due to the prevalence of amino acid disorders, especially PKU, there has been research into finding blood serum concentrations of amino acids, like phenylalanine, via transdermal extraction [1, 2]. *In vivo* research has indicated that there is a significant reservoir of phenylalanine in the epidermis which takes over 4 hours to completely clear before systemic levels can be measured [1]. This is due to phenylalanine being formed in the skin as part of the natural moisturising factor (NMF) which is discussed in more detail in section 1.4.2. Mathematically modelling how this skin reservoir is formed and extracted based on historic systemic levels would potentially allow PKU severity to be assessed using a short sampling time on the skin.

The goal of this thesis is to attempt to form mathematical models for the formation and extraction of skin reservoirs of amino acids using phenylalanine as a case study. In later chapters we will extend the model to also consider other amino acids, such as tyrosine.

1.4 The Skin

Clearly, a critical element in transdermal extraction is the skin itself. In this section, we detail the main properties of the skin, starting by considering the overall structure before focusing on the epidermis as this layer is the main barrier to transport through the skin.

1.4.1 Overall structure

Although skin samples vary between patients and areas of the body - scalp skin has a greater density of hair follicles than skin from the palm etc - the main features of the skin remain the same. Figure 1-3 shows a cross section of human skin sub-divided into 3 distinct layers, the epidermis, the dermis and subcutaneous tissue.

Subcutaneous tissue is a layer of fat and muscle that varies significantly between patients and is primarily used for insulation from heat and shock [20].

The dermis is comprised of connective tissue between the subcutaneous tissue and the epidermis. The dermis is primarily concerned with regulating body temperature, supplying oxygen and nutrients to the epidermis and removing toxins from the epidermis [18]. It is also helpful in shielding the body from stress and strain [18].

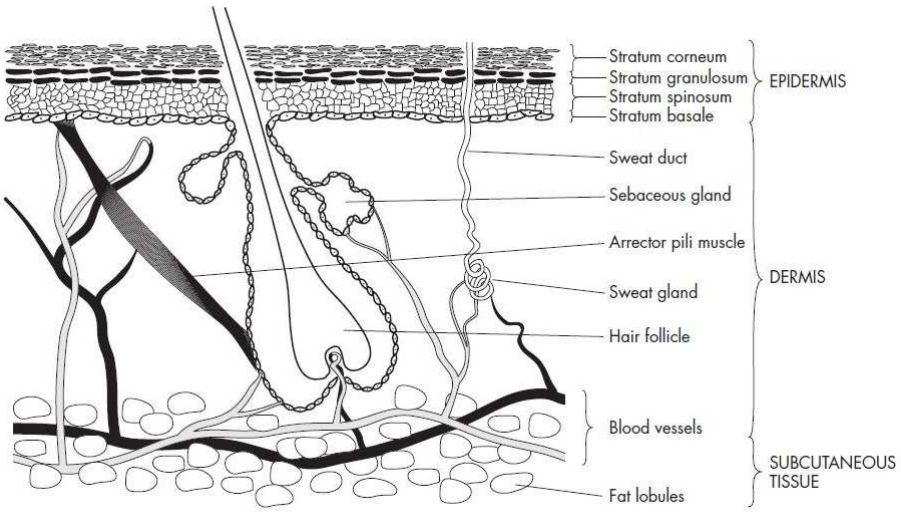

Figure 1-3: Cross section of human skin. Taken from [19].

The outermost layer is the epidermis which is comprised of several layers of keratinocytes whose primary function is to provide a barrier between the body and invading pathogens [18]. The outermost layer of the epidermis is called the stratum corneum and can range from 10-40μm thick in a brick and mortar type arrangement with keratinocytes in the final stage of terminal differentiation, called cornoecytes, forming the bricks and a mixture of lipids forming the mortar [18].

It has been previously shown that, due to this special architecture, for all but small, highly lipophilic molecules, the stratum corneum is the rate-limiting layer for the transport of compounds through the skin [21].

1.4.2 Epidermis

When examining chemical reservoirs in the stratum corneum, it is prudent to consider the whole epidermis and the processes involved in forming the stratum corneum. This then allows an understanding to be developed as to where these compounds come from. It is also worth noting that there is no blood flow through the epidermis.

The structure of the epidermis is shown in Figure 1-4 [22]. The deepest layer is called the stratum basale or basal layer and from here cells, known as keratinocytes, migrate upwards through the layers undergoing a process called cornification [22] until they are eventually shed from the surface of the skin by a process called desquamation [22]. The stratum basale is a base layer of skin stem cells that generate other cells by asymmetric division [22]. The

new cells cease to divide and start moving towards the surface of the skin.

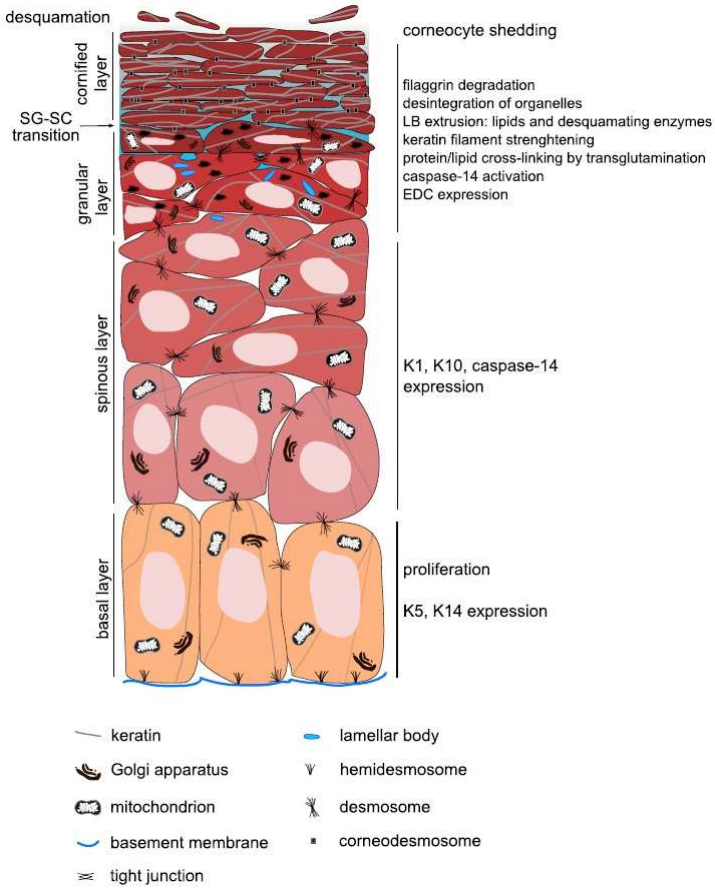

Figure 1-4: Cross section of human epidermis. Taken from [22].

From the stratum basale, cells enter the stratum spinosum or spinous layer. In this layer, the keratinocytes become connected by desmosomes [22]. Desmosomes are cell structures specialised for cell to cell adhesion [23] and connect the cells in the stratum spinosum together, giving rise to the name spinuous layer as the cells appear to be spiky and connected via small tendrils.

Above the stratum spinosum lies the stratum granulosum or granular layer in which keratinocytes begin to lose their nuclei and intracellular lipids are released into the extracellular space to start forming the lipid matrix between cells [22]. This lipid matrix makes the stratum corneum quite impermeable and could potentially trap materials, limiting the transport of compounds both into out and out of the body.

In this layer, cells also start to become more rigid with intermediate keratinocyte rods reinforcing the cell structure [24]. This process culminates in the stratum corneum with cells becoming very rigid and developing a cornified envelope, making transport between cells and

the intercellular space difficult. In this, cells remain tightly linked by corneodesmosomes which are desmosomes integrated into the cornified layer around cells [22]. Water content in this layer is also reduced significantly [24] which could lead to an increase in concentration of other compounds.

In the stratum corneum, or cornified layer, not only do cells become more rigid with a very impermeable lipid matrix, but the natural moisturising factor (NMF) is also formed. This is due to decomposition of a protein called filaggrin and corneodesmosomes between cells into smaller amino acids which form the NMF [2, 22]. These amino acids keep the skin hydrated despite exposure to external conditions by drawing in moisture from the surrounding environment.

One of the amino acids formed in the NMF is phenylalanine, which is part of the reason that skin reservoirs of phenylalanine are larger than would normally be expected [2].

The upper layer of the stratum corneum is sometimes split into a separate layer called the stratum disjunctum [25]. This is a partially detached layer of the stratum corneum about to be removed via desquamation.

1.5 Physiologically Based Pharmacokinetic Modelling

Pharmacokinetics is a branch of pharmacy that studies the movement of compounds in the body. Physiologically based pharmacokinetic modelling (PBPK) is a sub-branch of pharmacokinetics that utilises mathematical modelling techniques such as enzyme kinetics [26]. This is commonly used to describe the exact progression of drugs, toxins, nutrients and hormones between different body areas. The body areas are usually split into different compartments with movement of compounds between these compartments based on factors such as lipholicity, molecule size and charge. For example, a highly lipophilic molecule will be found in higher concentrations in fatty tissues than non-fatty tissues.

A prime example of a use of PBPK modelling comes when considering digoxin, a drug used to treat heart failure [27]. Digoxin has been used for over 200 years, yet digitalis poisoning, which is caused by toxic build up of digoxin, remains one of the most common causes of drug-related hospitalisation [27]. This problem is an example of one that can severely reduced by the application of PBPK modelling, which can identify if a dose, or series of doses, will cause a toxic build up in the body.

When considering amino acid reservoirs in the skin, it will be necessary to consider movement of amino acids from the blood to the inner layers of the skin, the epidermis, and then into the stratum corneum. This will require consideration of PBPK techniques, especially when dealing with metabolism of amino acids in the body.

1.6 Dermal Extraction Routes

Movement of compounds through the skin can occur via several routes as demonstrated in Figure 1-5. These routes can be broadly split into [28]:

Intercellular route - Transport through torturous pathways through the lipid matrix surrounding corneocytes.

Intracellular route - Transport via penetration alternating through corneocytes and lipid matrix.

Transappendageal route - Transport via appendages such as hair follicles.

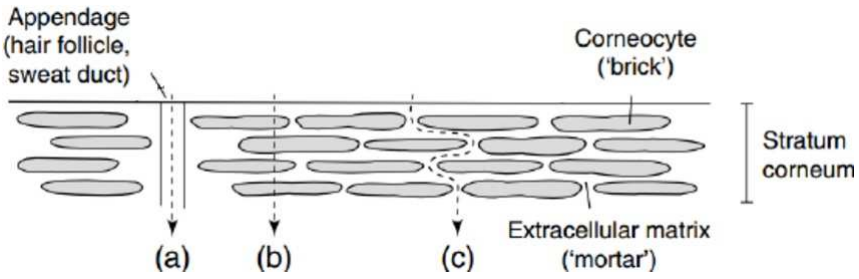

Figure 1-5: Diagram of extraction routes through the stratum corneum. (a) represents the appendageal route, (b) the intracellular route and (c) the intercellular route. Modified from [29].

It is generally accepted that, due to the cornified envelope around cells in the stratum corneum, the main route of transport for all but small, hydrophilic molecules, like water, is the intercellular pathway [30]. Due to appendages covering approximately 0.1% of the total skin surface area, this route is generally considered to be insignificant in transdermal penetration [31]. However, recent work using scanning electrochemical microscopy and laser scanning confocal microscopy has suggested that the appendageal pathway dominates transport through the skin [32].

Prior work into flow through the skin has identified an empirically derived 'reflection factor' which decreases the flux of larger molecules through the skin [33]. An alternative approach

is to use the Potts and Guy equation [34]

$$\log_{10}(k_p \text{cms}^{-1}) = -6.36(\pm 0.18) - 6.0(\pm 0.6)\text{x}10^{-3} MW + 0.74(\pm 0.07)\log_{10} k_{OW},$$

which expresses the permeability coefficient, k_p, of a compound in terms of its molecular weight, MW, and its octanol-water partition coefficient, k_{OW}. Higher permeability coefficients correspond to more transport through the stratum corneum and, from the expression, larger molecules therefore have less transport through the stratum corneum. The Potts and Guy equation also links transport rates to the hydrophilic nature of the compound considered with more hydrophilic compounds, corresponding to a lower k_{OW}, also having slower transport through the stratum corneum.

Work into hindered transport through capillaries in membranes also suggests that the larger a molecule is in comparison to the tube, the more restricted its flow through that capillary is [35]. This concept is investigated in more detail in chapter 6, but again suggests that the flow of large compounds will be restricted through small tubes.

1.7 Extraction Methods

This section briefly discusses passive diffusion and reverse iontophoresis through the skin. These concepts are more fully explored in later chapters.

1.7.1 Passive Diffusion

The simplest skin transport mechanism is passive diffusion, the movement of substance from an area of high concentration to one of lower concentration down a concentration gradient. This allows compounds to be either extracted or inserted into the skin.

To extract compounds transdermally via passive diffusion, areas of skin are cleaned before being put into contact with a buffer solution either by dipping the skin in, in the case of a finger, or attaching a chamber to the skin. The concentration gradient of amino acids and other compounds between the skin and the buffer causes movement of these compounds from within the skin to the buffer, for extraction, or vice-versa, for delivery.

When considering passive diffusion path length is an important factor, especially as the skin

has a very complex organisation, and has been previously considered in transdermal drug delivery [23]. As mentioned in section 1.6, there are also several different routes through the skin each with different diffusion rates and path lengths.

Although passive diffusion is cheap and easy to use, it does have some drawbacks such as speed with prior research into the extraction of amino acids suggesting it takes several hours for a steady state to be reached [1, 2]. These issues make methods to enhance the amount transported a current area of interest in drug delivery and non-invasive skin sampling [21].

1.7.2 Reverse iontophoresis

Iontophoresis is a method of transdermal drug delivery that works via application of a small electric current to the skin [21]. This method has been used since the early 20th century [36] in order to treat certain disorders of the eye [37] and skin [38]. Iontophoresis is now used for treatment of Parkinsons disease and migraine pain [39] as well as having applications in paediatric medicine [18] as problems with invasive methods, highlighted in section 1.3, are often magnified in young children.

More recently, iontophoresis has been applied in reverse in order to extract compounds through the skin; this technique is called reverse iontophoresis. Reverse iontophoresis is the subject of current research [21] due to its potential to monitor compounds in the body non-invasively. The GlucoWatch used reverse iontophoresis to continuously monitor blood glucose levels in patients with diabetes and was trialled in the USA in 2002 [40]. Unfortunately, this product did not make it to widespread distribution due to costs.

Although iontophoresis and reverse iontophoresis are effectively the same process applied in opposite directions, prior research has shown that the flow rate for compounds into the skin can be different to that of compounds out of the skin under an applied current [33]. This is due to the skin being electrically asymmetric.

Reverse iontophoresis works by applying two oppositely charged electrodes to the skin and putting a constant DC current between them. This enhances the transport of compounds through the skin by two means. Firstly, ions move towards the oppositely charged electrode, called electro-migration, and, secondly, bulk solvent flow through the skin carries both ions and uncharged compounds through the skin, electro-osmosis. Under physiological conditions, electro-osmosis occurs towards the cathode. Both mechanisms are well documented transport phenomena [21, 33, 32, 41] and are displayed in Figure 1-6 [21].

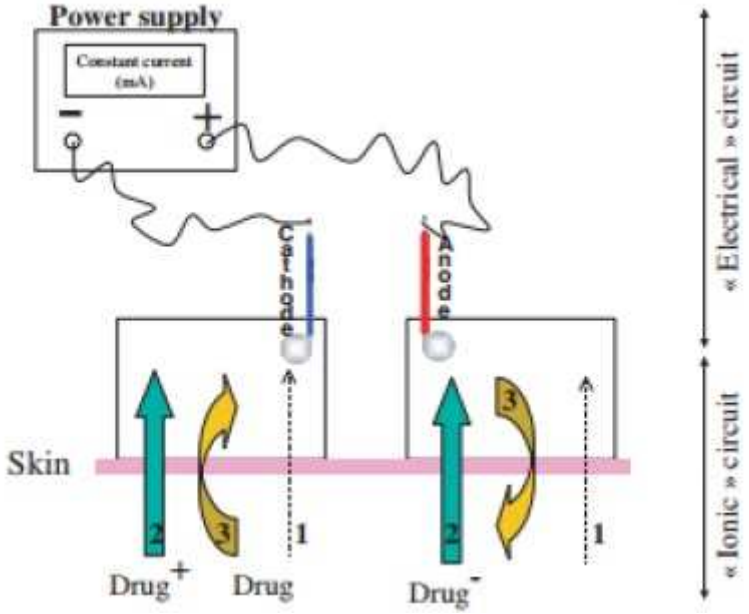

Figure 1-6: Reverse iontophoresis in diagrammatic form. Route (1) represents passive diffusion which occurs in equal amounts to each compartment. Route (2) represents electro-migration with positively charge compounds going towards the cathode and negatively charged compounds towards the anode. Route (3) shows electro-migration into the cathode compartment. Taken from [21].

In the case of phenylalanine, which is an uncharged molecule, we primarily focus on electro-osmotic flow. Experimental work has also shown that phenylalanine is mostly collected in the cathode compartment as would be expected from electro-osmotic flow [2].The role of electro-osmostic flow in transdermal iontophoresis has been previously investigated [33].

1.8 Thesis Structure

The aim of this thesis is to model the skin and systemic disposition of amino acids and investigate the potential for these compounds to be monitored via transdermal extraction methods using phenylalanine as a case study. The thesis starts by introducing the core mathematical techniques used through the thesis before moving on to model phenylalanine distribution through the body.

Chapter 2 details the key mathematical techniques used throughout the thesis including methods to solve and analyse ordinary and partial differential equations. This section also details propagation of error, parameter estimation and Bessel functions.

Chapters 3 to 6 each follow a similar structure. Firstly, the objective of the chapter is introduced and a breakdown of key parameters is given as a reference for the rest of the chapter. Having done this, key background concepts for the chapter will be introduced before moving on to form appropriate models for that section and analyse them. Each of these chapters is then completed with a summary.

Chapter 3 considers phenylalanine concentrations in the blood. Firstly prior serum models for phenylalanine are assessed before presenting several new approaches for the systemic profile of phenylalanine. A final model for use throughout the report is then chosen from these. This chapter also considers the effect of food intake on serum concentrations of phenylalanine.

Chapter 4 moves on to consider time-dependent profiles of phenylalanine through the stratum corneum based on the profiles found in chapter 3 in order to get an idea of the effect of blood concentrations on the skin reservoir. Parameter estimations are obtained using *in vivo* data [2].

Electro-osmotic flow is a complex topic which is critical to understanding the extraction of uncharged compounds from the skin. Hence, chapter 5 gives detailed theory into electro-osmotic flow dynamics using the Navier-Stokes equations, surface chemistry and micro-capillary theories. This chapter aims to find the electro-osmotic flow velocity during reverse iontophoresis in terms of known properties of the system.

Chapter 6 builds on the work presented in chapter 5 and forms a time-dependent system for extraction of uncharged compounds from the skin using both passive diffusion and reverse iontophoresis. Extraction is considered to occur through hair follicles and the intercellular space separately. Results from *in vitro* extraction of mannitol [42, 43] are used to estimate parameters such as the surface of the skin covered by pores. These results are then analysed and the model changed accordingly to incorporate hindrance effects. Other potential changes, including changes in skin resistance under an applied electric field, are also considered.

The final chapter then summarises the results presented in the thesis and suggests further experimental work to validate the model structures presented and giving possible methods to further improve the model based on the results of these experiments.

Chapter 2

Mathematical Techniques

In order to model the formation and extraction of chemical reservoirs from the skin, a variety of mathematical techniques are used to analyse ordinary and partial differential equations, estimate parameters and calculate error in calculated parameters. The objective of this chapter is to detail these methods for use in later chapters and introduce the concept of Bessel functions.

2.1 Steady State Analysis

2.1.1 Stability

For the n-dimensional system

$$\frac{\mathrm{d}\mathbf{x}}{\mathrm{d}t} = \mathbf{f}(\mathbf{x}) \qquad \mathbf{x} \in \mathbb{R}^n, \quad \mathbf{f} \in \mathbb{R}^n, \quad t \in \mathbb{R}, \quad n \in \mathbb{N},$$

the steady state, $\mathbf{x}^*$ such that $\mathbf{f}(\mathbf{x}^*) = 0$, is said to be asymptotically stable if there exists some $\epsilon > 0$ such that if $||\mathbf{x}(0) - \mathbf{x}^*|| < \epsilon$ then $\mathbf{x}(t) \to \mathbf{x}^*$ as $t \to \infty$. This occurs if all eigenvalues, λ, of the Jacobian matrix

$$J_{ij}(\mathbf{x}^*) = \left(\frac{\partial f_i}{\partial x_j}\right)\Bigg|_{\mathbf{x}=\mathbf{x}^*} \qquad i, j = 1, ..., n,$$

where eigenvalues are roots of the characteristic polynomial

$$\det|J - \lambda I| = 0,$$

have negative real parts.

2.1.2 Resilience

Resilience measures the asymptotic rate of return to a stable steady state, or the asymptotic rate of departure from an unstable steady state, after a small perturbation [44]. There are several different methods for measuring resilience with the most frequently used being based on the eigenvalues of the system near the steady state considered. In line with the problems encountered in this thesis, we consider the case where eigenvalues are real and distinct. For this case, consider the linear system/the linearisation of a non-linear system near the steady state where $J \in \mathbb{R}^{nxn}$, $\mathbf{x} \in \mathbb{R}^n$, $n \in \mathbb{N}$ and $t \in \mathbb{R}$:

$$\frac{\mathrm{d}\mathbf{x}}{\mathrm{d}t} = J\mathbf{x} \qquad \mathbf{x}(0) = \mathbf{x}_0. \tag{2.1}$$

This system has an exact solution given by

$$\mathbf{x} = \mathbf{x}_0 e^{Jt},$$

or

$$\mathbf{x} = c_1 e^{\lambda_1 t}\mathbf{v}_1 + c_2 e^{\lambda_2 t}\mathbf{v}_2 + c_3 e^{\lambda_2 t}\mathbf{v}_3 + ..., \tag{2.2}$$

where $\lambda_{1,...,n}$ are real and distinct eigenvalues of J with corresponding eigenvectors $\mathbf{v}_{1,...,n}$.

Assuming, without loss of generality, that λ_1 has the largest real part of all eigenvalues, then the return time to $\mathbf{x}^*$ after a perturbation is dominated by this component. This can be shown by rearranging equation (2.2):

$$e^{-\lambda_1 t}\mathbf{x} = c_1\mathbf{v}_1 + c_2 e^{(\lambda_2-\lambda_1)t}\mathbf{v}_2 + c_3 e^{(\lambda_3-\lambda_1)t}\mathbf{v}_3 + ... \tag{2.3}$$

λ_1 has the largest real part of all the eigenvalues of A, hence $\forall k \leq n$, $k \in \mathbb{N}$, $k \neq 1$, $\lambda_k - \lambda_1 < 0$. Considering the limit as $t \to \infty$ of equation (2.3), it is clear that

$$\lim_{t\to\infty} e^{-\lambda_1 t}\mathbf{x} \propto \mathbf{v}_1,$$

hence for large time, the system's decay rate will be approximately equal to λ_1 and $\mathbf{x}$ will be proportional to $\mathbf{v}_1$[44].

Considering the decay rate at large t, the time taken for $\mathbf{x}$ to reduce by a factor of $^1/_e$ is $^{-1}/_{Re(\lambda_1)}$ and is known as the return time. The resilience of the system is defined as the reciprocal of the return time:

$$\text{Resilience} = -Re(\lambda_1).$$

For the system to be stable, the real part of all eigenvalues must be less than zero, hence if resilience is less than zero then the system is unstable [44]. The larger the resilience, the faster the system returns to the steady state after a perturbation. For complex or repeated eigenvalues, there are alternative methods for calculating resilience discussed in [45, 46].

Resilience is used to measure the long term effect of a perturbation on the system, but ignores short term transient behaviour.

2.1.3 Reactivity

Reactivity is a measure of instability and used to investigate the behaviour of the system immediately after a perturbation [44].

If a system is reactive, then some small perturbations from the equilibrium will initially grow in magnitude. If the system is not reactive then no small perturbations from the steady state will initially grow in magnitude. This is demonstrated graphically in Figure 2-1.

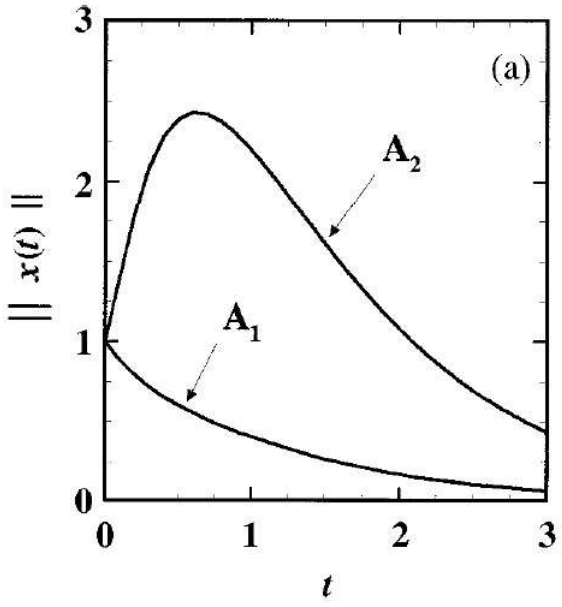

Figure 2-1: Demonstration of the difference between a reactive and an unreactive function. The system described by A_1 is unreactive and tends immediately to the steady state, whereas the system described by A_2 is reactive and increases in magnitude before tending back to the steady state. Both systems start after a perturbation from a stable equilibrium. Modified from [44].

Reactivity is a transient behaviour in the system; it is possible for a system to be both reactive and stable.

Reactivity is defined as the maximum amplification rate, over all initial perturbations, immediately following the perturbation [44]. Like resilience, considering the linear system or linearisation of a non linear system

$$\frac{\mathrm{d}\mathbf{x}}{\mathrm{d}t} = J\mathbf{x} \qquad \mathbf{x}(0) = \mathbf{x}_0,$$

means that

$$\text{Reactivity} = \max_{||\mathbf{x}||\neq 0} \left[\left(\frac{1}{||\mathbf{x}||} \frac{\mathrm{d}||\mathbf{x}||}{\mathrm{d}t} \right) \Big|_{t=0} \right], \tag{2.4}$$

which is the maximum proportional increase in the system state.

Expanding the differential term on the right hand side of the above equation results in:

$$\begin{aligned}\frac{\mathrm{d}||\mathbf{x}||}{\mathrm{d}t} &= \frac{\mathbf{x}^{\mathrm{T}}\left({}^{\mathrm{d}\mathbf{x}}/_{\mathrm{d}t}\right) + \left({}^{\mathrm{d}\mathbf{x}}/_{\mathrm{d}t}\right)^{\mathrm{T}}\mathbf{x}}{2||\mathbf{x}||}, \\ &= \frac{\mathbf{x}^{\mathrm{T}}\left(J + J^{\mathrm{T}}\right)\mathbf{x}}{2||\mathbf{x}||}.\end{aligned} \tag{2.5}$$

Given that $\left(J + J^{\mathrm{T}}\right)$ is the Hermitian part of J, $H(J)$, and combining equations (2.4) and (2.5) results in:

$$\left(\frac{1}{||\mathbf{x}||}\frac{\mathrm{d}||\mathbf{x}||}{\mathrm{d}t}\right)\Bigg|_{t=0} = \frac{\mathbf{x}_0^{\mathrm{T}} H\left(J\right)\mathbf{x}_0}{\mathbf{x}_0^{\mathrm{T}}\mathbf{x}_0}. \tag{2.6}$$

The expression on the right hand side of equation (2.6) is known as the Rayleigh quotient and the maximum value of this term over all possible initial conditions, $\mathbf{x}_0$, will give the reactivity of the system [44]. By Rayleigh's principle [47] this expression is maximised when $\mathbf{x}_0$ is equal to the eigenvector, $\mathbf{v}_1$, corresponding to the largest eigenvalue of $H(J)$, $\lambda_1(H(J))$. Using this in equation (2.6) and recognising that $H(J)\mathbf{v}_1 = \lambda_1(H(J))\mathbf{v}_1$ results in:

$$\begin{aligned}\text{Reactivity} &= \frac{\mathbf{v}_1^{\mathrm{T}} H\left(J\right)\mathbf{v}_1}{\mathbf{v}_1^{\mathrm{T}}\mathbf{v}_1}, \\ &= \frac{\lambda_1(H(J))\mathbf{v}_1^{\mathrm{T}}\mathbf{v}_1}{\mathbf{v}_1^{\mathrm{T}}\mathbf{v}_1} = \frac{\lambda_1(H(J))||\mathbf{v}_1||}{||\mathbf{v}_1||}, \\ &= \lambda_1(H(J)).\end{aligned}$$

Hence, reactivity is determined by the largest eigenvalue of the Hermitian matrix of A. As the Hermitian matrix is real and symmetric by definition, the eigenvalues of $H(A)$ will be real with orthogonal eigenvectors.

If reactivity is greater than zero, then the system will be reactive and some perturbations will initially increase in magnitude with higher reactivities causing a more pronounced effect [44]. If the reactivity is less than zero, the system is unreactive and an inital perturbation from the steady state will not increase in magnitude.

2.1.4 Amplification envelope

Reactivity quantifies the initial response of the system to a perturbation from the steady state and resilience the long-term asymptotic response. In a resilient and reactive system, neither property quantifies the behaviour of the system between the initial perturbation and behaviour as $t \to \infty$. This is normally quantified by considering the amplification envelope [44] and from this the maximal possible amplification of the perturbation and how long this takes to occur.

The amplification envelope, $\rho(t)$, is defined as the maximum possible amplification at time $t \geq 0$ after a perturbation, $\mathbf{x}(0) = \mathbf{x}_0$, to the asymptotically stable equilibrium at $\mathbf{x} = 0$ to the linear, or linearisation of the non-linear, system given in equation (2.1) [44]. Hence:

$$\rho(t) = \max_{||\mathbf{x}_0|| \neq 0} \frac{||\mathbf{x}(t)||}{||\mathbf{x}_0||}.$$

Considering that $\mathbf{x}(t) = \mathbf{x}_0 e^{Jt}$ is the solution for $\mathbf{x}(t)$ in the linearised system, $\rho(t)$ can be rewritten as

$$\rho(t) = \max_{||\mathbf{x}_0|| \neq 0} \frac{||\mathbf{x}_0 e^{Jt}||}{||\mathbf{x}_0||},$$

which is the definition of the Euclidean norm of the exponential matrix, e^{Jt}.

From this definition of the amplification envelope, it is possible to find the largest possible amplification of a perturbation, ρ_{max}, and the time at which maximum amplification is achieved, t_{max}. This is done by considering

$$\rho_{max} = \max_{t \geq 0} \rho(t), \tag{2.7}$$

and t_{max} being the time, t, at which this maximum is achieved.

We used the MATLAB function 'expm()' to find the exponential matrix via the Padé approximation and 'norm()' to find the largest singular value of the resulting matrix and hence the matrix norm following [44].

2.2 Parameter estimation - Gauss-Newton Algorithm

In mathematical modelling, it is not uncommon for some parameters to be completely unknown. Regression analysis is a branch of statistics that can estimate the value of unknown parameters. As most of the parameter estimation problems in this thesis involve non-linear regression, it is necessary to consider an iterative approximation method to find the best parameter estimate. In this case, we consider the Gauss-Newton method [48] in order to find parameters that minimise the sum of squares between the predicted results and the experimentally obtained data.

In general, the Gauss-Newton algorithm [48] takes m functions, often called residuals, $\mathbf{r} = (r_1, \quad r_2, ..., \quad r_m)$ and n variables $\boldsymbol{\beta} = (\beta_1, \beta_2, ...\beta_n)$ with $n \leq m$ and iteratively selects $\boldsymbol{\beta}$ to minimise the sum of squares:

$$\mathbf{S}(\boldsymbol{\beta}) = \sum_{i=1}^{m} r_i^2(\boldsymbol{\beta}). \tag{2.8}$$

Given an initial estimate, $\boldsymbol{\beta} = \boldsymbol{\beta}^0$, and the Jacobian matrix, J

$$J_{ij} = \left(\frac{\partial r_i}{\partial \beta_j}\right), \quad i \in [1, m], \quad j \in [1, n]$$

the method proceeds to estimate $\boldsymbol{\beta}$ iteratively using

$$\boldsymbol{\beta}^{s+1} = \boldsymbol{\beta}^s - (J^T J)^{-1} J^T \mathbf{r}(\boldsymbol{\beta}^s), \tag{2.9}$$

where s is the iteration number.

In this thesis, the Gauss-Newton algorithm is used to find parameters for input into a model function $y = f(x, \boldsymbol{\beta})$ that minimises the sum of squares to data points (x_i, y_i). To do this, the residuals are selected to be [48]:

$$r_i = y_i - f(x_i, \beta).$$

Considering that

$$J_{ij} = \left(\frac{\partial r_i}{\partial \beta_j}\right) = -\left(\frac{\partial f(x_i, \beta)}{\partial \beta_j}\right), \quad i \in [1, m], \quad j \in [1, n],$$

the iterative formula in equation (2.9) can be rewritten in terms of the Jacobian of f with respect to $\boldsymbol{\beta}$, J_f:

$$\boldsymbol{\beta}^{s+1} = \boldsymbol{\beta}^s + (J_f^T J_f)^{-1} J_f^T \mathbf{r}(\boldsymbol{\beta}^s).$$

Over iterations, $\boldsymbol{\beta}^s$ should tend to some limit, β_∞, resulting in an approximation of the unknown parameter set that minimises the sum of squares given in equation (2.8).

2.2.1 Goodness of Fit

Having obtained parameter estimates using the Gauss-Newton algorithm, it is then prudent to consider the goodness of fit of the predicted data to real data. In linear regression, it is common to use a coefficient of determination, R^2, test to see how well the model fits experimental data. Prior work has shown that this approach is not appropriate when considering non-linear regression [49]. As this thesis mainly deals with non-linear regression problems, alternative methods were considered.

As an alternative, we consider the standard error of the estimate, σ, which is defined as

$$\sigma^2 = \frac{\sum_{i=1}^{N}(y_i - f_i)^2}{N}, \tag{2.10}$$

where y_i is the predicted measurement and f_i is the corresponding expected measurement at data point i. N is the number of measurements considered [50]. The standard error represents the average distance at that observed values are from the predicted line. Hence, the lower the standard error the better the model fits the predicted results.

2.3 Propagation of Error

In biological systems, there is usually a significant amount of variation between individuals. Hence parameters for biological systems are usually expressed as a value $\pm$ the standard deviation based on the spread of results. If we have some parameter, y, which is linked to other parameters, x_i, $i \in [1, n]$ by

$$y = f(\mathbf{x}), \quad \mathbf{x} = (x_1, x_2, ..., x_n),$$

where each x_i has corresponding standard deviation σ_i and $f(x)$ is a linear or non-linear function. In order to find the standard deviation in the calculated parameter y, σ_y, we combine the standard deviations of x_i [51]:

$$\sigma_y^2 = \sum_{i=1}^{n} \sigma_i^2 \left(\frac{\partial f}{\partial x_i} \right)^2.$$

2.4 Continuity Equations

A continuity equation describes the movement of some quantity, for example energy, mass or charge, through a system. These equations can deal with both quantities that are conserved and quantities that are not conserved in a system. These equations are very useful in mathematical modelling and see frequent application in fluid dynamics, population dynamics and biological systems. The general form of a conservation equation is

$$\frac{\partial C(x, y, z, t)}{\partial t} + \nabla . \mathbf{J}(x, y, z, t) = f(x, y, z, t) \tag{2.11}$$

for the operator

$$\nabla \equiv \left(\frac{\partial}{\partial x}, \frac{\partial}{\partial y}, \frac{\partial}{\partial z} \right)^T,$$

where $C(x, y, z, t)$ is the concentration of interest based on position, (x, y, z), and time, t. $f(x, y, z, t)$ represents the rate of formation and decay of the quantity of interest in the

system and $\mathbf{J}(x, y, z, t)$ represents the flux. If the quantity considered is conserved in the system, then $f(x, y, z, t)$ is equal to zero.

Selection of the flux changes the behaviour of the system. In the next two sections we consider the selection of flux to represent a diffusion and advection-diffusion based system.

2.5 Diffusion Partial Differential Equation

Mathematically, diffusion can be derived from the continuity equation, given in section 2.4, combined with Fick's first law, which states that materials move from a high concentration to a lower concentration with a magnitude proportional to the concentration gradient [52].

Considering Fick's first law, the flux in a diffusion only system is given by

$$\mathbf{J}(x, y, z, t) = -\mathbf{D}(x, y, z, t)\nabla C(x, y, z, t), \tag{2.12}$$

where $\mathbf{D}(x, y, z, t)$ is the diffusion coefficient. Hence, using equation (2.11), diffusion is modelled via:

$$\frac{\partial C(x, y, z, t)}{\partial t} - \nabla.(\mathbf{D}(x, y, z, t)\nabla C(x, y, z, t)) = f(x, y, z, t).$$

Considering the quantity of interest to be conserved in the system, $f(x, y, z, t) = 0$, with constant diffusion coefficients, $\mathbf{D}(x, y, z, t) = (D_x, D_y, D_z)^T$, in one spatial dimension, x, as has been done previously for skin models [52], results in:

$$\frac{\partial C(x, t)}{\partial t} = D_x \frac{\partial^2 C(x, t)}{\partial x^2}.$$

2.6 Advection-Diffusion Partial Differential Equation

Advection-diffusion equations are commonly found partial differential equations that describe the distribution of physical quantities, such as particles or energy, in a system where diffu-

sion and advection are occurring. Flux due to advection and diffusion is usually considered to be additive with advection flux being directly proportional to the velocity of advection, $\mathbf{v}(x, y, z, t)$. Considering the continuity equation in equation (2.11), the flux in a diffusion system given in equation (2.12) and the flux due to advection results in:

$$\mathbf{J}(x, y, z, t) = -\mathbf{D}(x, y, z, t)\nabla C(x, y, z, t) + \mathbf{v}(x, y, z, t)C(x, y, z, t). \tag{2.13}$$

Combining equations (2.11) and (2.13) hence results in the advection-diffusion equation:

$$\frac{\partial C(x, y, z, t)}{\partial t} - \nabla.(\mathbf{D}(x, y, z, t)\nabla C(x, y, z, t) - \mathbf{v}(x, y, z, t)C(x, y, z, t)) = f(x, y, z, t).$$

Considering $\mathbf{v}(x, y, z, t)$ and $\mathbf{D}(x, y, z, t)$ to be constant in x, y and z directions

$$\mathbf{v} = (v_x, v_y, v_z)^T, \tag{2.14}$$

$$\mathbf{D} = (D_x, D_y, D_z)^T, \tag{2.15}$$

the advection-diffusion equation in 3 spatial dimensions can be written as

$$\frac{\partial C(x, y, z, t)}{\partial t} + \mathbf{v}.\nabla C(x, y, z, t) = \nabla.(\mathbf{D}\nabla C(x, y, z, t)) + f(x, y, z, t), \tag{2.16}$$

with the 1 spatial dimension, x, form being:

$$\frac{\partial C(x, t)}{\partial t} + v_x\frac{\partial C(x, t)}{\partial x} = D_x\frac{\partial^2 C(x, t)}{\partial x^2} + f(x, t). \tag{2.17}$$

2.6.1 Generalised Integral Transform Technique

The Generalised Integral Transform Technique (GITT) is a method of exactly solving advection diffusion equations [53] of the form given in equation (2.16) with non-homogeneous boundary conditions and initial condition:

$$C(x, y, z, 0) = C_0(x, y, z). \tag{2.18}$$

The method presented in [53] solves these equations via a series of steps:

1. Homogenise the boundary conditions.

2. Reduce the advection-diffusion equation to a diffusion equation via substitution.

3. Implement the GITT to solve the resulting diffusion equation.

4. Transform back to find the analytical solution for the original equation.

Homogenising Boundary Conditions

In order to homogenise the boundary conditions, we consider the substitution for $C(x, y, z, t)$

$$C(x, y, z, t) = M(x, y, z, t) + F(x, y, z, t), \tag{2.19}$$

where $F(x, y, z, t)$ is any function that satisfies the original boundary conditions of $C(x, y, z, t)$ and $M(x, y, z, t)$ is the new variable of interest. Using this substitution, equation (2.16) becomes

$$\frac{\partial M(x, y, z, t)}{\partial t} + \mathbf{v}.\nabla M(x, y, z, t) = \nabla.(\mathbf{D}\nabla M(x, y, z, t)) + G(x, y, z, t), \tag{2.20}$$

where $G(x, y, z, t)$ combines $f(x, y, z, t)$ and all terms containing $F(x, y, z, t)$. For simplicity when considering time-independent boundary conditions, $F(x, y, z, t)$ is normally taken as the steady state solution to equation (2.16) and hence $G(x, y, z, t)$ contains no terms related

to $F(x, y, z, t)$. The new initial condition for $M(x, y, z, t)$ is given by:

$$M(x, y, z, 0) = C_0(x, y, z) - F(x, y, z, 0).$$

The boundary conditions for equation (2.20) are homogeneous as $F(x, y, z, t)$ satisfies the boundary conditions on equation (2.16).

Reducing to Diffusion Equation

We now have a diffusion advection equation with homogeneous boundary conditions. The next stage in finding an exact solution for $C(x, y, z, t)$ is to reduce the problem to a diffusion equation which can then be solved using GITT.

Consider the substitution

$$M(x, y, z, t) = \theta(x, y, z, t) \exp(p_1 x + p_2 y + p_3 z + t(q_1 + q_2 + q_3)), \tag{2.21}$$

where p_i, q_i, $i \in [1, 3]$ are currently undefined constants. Using (2.20) this substitution results in:

$$\begin{aligned}
\frac{\partial \theta(x, y, z, t)}{\partial t} &+ \theta(x, y, z) \left[(q_1 + q_2 + q_3) \right. \\
&\left. + p_1(-D_x p_1 + v_x) + p_2(-D_y p_2 + v_y) + p_3(-D_z p_3 + v_z) \right] \\
&+ (-2D_x p_1 + v_x) \frac{\partial \theta(x, y, z, t)}{\partial x} - D_x \frac{\partial^2 \theta(x, y, z, t)}{\partial x^2} \\
&+ (-2D_y p_2 + v_y) \frac{\partial \theta(x, y, z, t)}{\partial y} - D_y \frac{\partial^2 \theta(x, y, z, t)}{\partial y^2} \\
&+ (-2D_z p_3 + v_z) \frac{\partial \theta(x, y, z, t)}{\partial z} - D_z \frac{\partial^2 \theta(x, y, z, t)}{\partial z^2} \\
&= \frac{G(x, y, z, t)}{\exp(p_1 x + p_2 y + p_3 z + t(q_1 + q_2 + q_3))}.
\end{aligned} \tag{2.22}$$

The advection terms from equation (2.22) can be eliminated by selecting the constants

$$p_1 = \frac{v_x}{2D_x}; \quad p_2 = \frac{v_y}{2D_y}; \quad p_3 = \frac{v_z}{2D_z}; \quad q_1 = -\frac{v_x^2}{4D_x}; \quad q_2 = -\frac{v_y^2}{4D_y}; \quad -\frac{v_z^2}{4D_z},$$

which reduces equation (2.22) to

$$\frac{\partial\theta(x,y,z,t)}{\partial t} = \nabla.(\mathbf{D}\nabla\theta(x,y,z,t)) + \frac{G(x,y,z,t)}{\exp(p_1x + p_2y + p_3z + t(q_1+q_2+q_3))}, \tag{2.23}$$

with initial condition on $\theta(x,y,z,t)$

$$\theta(x,y,z,0) = \frac{C_0(x,y,z) - F(x,y,z,0)}{\exp(p_1x + p_2y + p_3z)}, \tag{2.24}$$

and homogeneous boundary conditions.

GITT

The original partial differential equation for $C(x,y,z,t)$ has now been reduced to the diffusion equation presented in equation (2.23) with homogeneous boundary conditions and initial condition given in equation (2.24). In order to find an exact solution for $C(x,y,z,t)$, we solve the diffusion equation given in equation (2.23) using GITT to find an exact solution for $\theta(x,y,z,t)$.

To implement the GITT method, we select an eigenvalue problem

$$\nabla_D^2\psi(x,y,z)) + \mu^2\psi(x,y,z) = 0,$$

with the operator

$$\nabla_D^2 = D_x\frac{\partial^2}{\partial x^2} + D_y\frac{\partial^2}{\partial y^2} + D_z\frac{\partial^2}{\partial z^2}, \tag{2.25}$$

and the same type of boundary conditions as those found for $\theta(x,y,z,t)$. Solving this eigenvalue problem yields non-trivial solutions for certain values, eigenvalues, of $\mu = \mu_i$, $i \in [1,\infty)$

with corresponding normalised, linearly independent eigenvectors $\psi_i(x, y, z)$.

Using the orthogonality property of eigenvectors, the integral-transform pair for GITT over the space the system is considered in, V, can be derived as:

$$\bar{\theta}_i(t) = \int_V \psi_i(x, y, z)\theta(x, y, z, t)\mathrm{d}V, \quad \text{(Transform)}$$

$$\theta(x, y, z, t) = \sum_{i=1}^{\infty} \psi_i(x, y, z)\bar{\theta}_i(t). \quad \text{(Inverse)}$$

Applying this transformation to equation (2.23) reduces the partial differential equation to an infinite series of decoupled ordinary differential equations of the form:

$$\frac{\mathrm{d}\bar{\theta}_i}{\mathrm{d}t} + \mu_i^2\bar{\theta}_i(t) = \bar{G}_i(t), \quad i \in [1, \infty),$$

where

$$\bar{G}_i(t) = \int_V \psi(x, y, z)\frac{G(x, y, z)}{\exp(p_1x + p_2y + p_3z + t(q_1 + q_2 + q_3))}\mathrm{d}V,$$

with initial conditions:

$$\bar{\theta}_i(0) = \bar{f}_i = \int_V \psi_i(x, y, z)\frac{C_0(x, y, z) - F(x, y, z, 0)}{\exp(p_1x + p_2y + p_3z)}\mathrm{d}V.$$

Hence the solution for $\bar{\theta}_i(t)$

$$\bar{\theta}_i(t) = \exp(-\mu_i^2t)\left(\bar{f}_i + \int_0^t \bar{G}_i(t)\exp(\mu_it)\mathrm{d}t\right),$$

and use the inverse transform to obtain:

$$\theta(x, y, z, t) = \sum_{i=1}^{\infty} \psi_i(x, y, z)\exp(\mu_i^2t)\left(\bar{f}_i + \int_0^t \bar{G}_i(t)\exp(\mu_it)\mathrm{d}t\right).$$

Using equations (2.19) and (2.21), we know that

$$\begin{aligned} C(x,y,z,t) &= \theta(x,y,z,t)\exp(p_1x+p_2y+p_3z+t(q_1+q_2+q_3))+F(x,y,z,t), \\ &= \theta(x,y,z,t)\exp\left(\frac{v_xx}{2D_x}+\frac{v_yy}{2D_y}+\frac{v_zz}{2D_z}-t\left(\frac{v_x^2}{4D_x}+\frac{v_y^2}{4D_y}+\frac{v_z^2}{4D_z}\right)\right)+F(x,y,z,t), \end{aligned} \tag{2.26}$$

hence we have obtained the solution to the diffusion advection equation presented in equation (2.16) with a spatially dependent initial condition and non-homogeneous boundary conditions.

Solution in 1D

Most advection-diffusion equations through the skin are considered to only vary in one spatial dimension, x, in domain Ω. The GITT can be applied to a one-dimensional advection diffusion equation with constant diffusion coefficient and velocity of advection

$$\frac{\partial C(x,t)}{\partial t}-D_x\frac{\partial^2C(x,t)}{\partial x^2}+v_x\frac{\partial C(x,t)}{\partial x}=f(x,t). \tag{2.27}$$

under non-homogeneous boundary conditions and initial condition:

$$C(x,0)=C_0(x).$$

Using GITT, the resulting solution is

$$C(x,t)=\theta(x,t)\exp\left(\frac{v_xx}{2D_x}-t\frac{v_x^2}{4D_x}\right)+F(x,t), \tag{2.28}$$

where

$$\theta(x,t)=\sum_{i=1}^{\infty}\psi_i(x)\exp(\mu_i^2t)\left(\bar{f}_i+\int_0^t\bar{G}_i(t)\exp(\mu_it)\mathrm{d}t\right),$$

$$\bar{f}_i = \int_\Omega \psi_i(x) \frac{C_0(x) - F(x,0)}{\exp(px)} \mathrm{d}x,$$

$$\bar{G}_i(t) = \int_\Omega \psi(x) \frac{G(x)}{\exp(px+qt)} \mathrm{d}V,$$

$$G(x) = \left(-\frac{\partial F(x,t)}{\partial t} - v_x \nabla F(x;t) + D_x \nabla^2 F(x,t) \right) + f(x,t),$$

$$p = \frac{v_x}{2D_x}, \quad q = -\frac{v_x^2}{4D_x},$$

and $F(x,t)$ is any function that solves the boundary conditions of equation (2.27). Finally, μ_i and $\psi_i(x)$ are determined by the eigenvalue problem formed during the GITT.

2.6.2 Numerical Solutions

In some cases, obtaining an exact solution to an advection diffusion equation, or indeed most systems represented by partial differential equations, is very complex. Examples of situations where this occurs can include a spatial or time dependent velocity or a non-constant diffusion coefficient. When this occurs numerical solutions are often used to view non-steady state behaviour. This section briefly runs through the method of lines for solving systems represented by partial differential equations with one spatial dimension, x, and one time dimension, t, numerically.

The main aim of the method of lines is to replace the spatial derivatives in the partial differential equation with algebraic approximations [54]. Doing this will reduce the partial differential equation to a series of time-dependent ordinary differential equations which can then be solved using numerical methods such as the Runge-Kutta method [54].

To apply the method of lines, the 1D space the problem is considered over, $[a,b]$ $a < b$, is split into a grid with n points and spacing between points $h = {}^{(b-a)}/_{n}$. We then define $u_i(t) = C(a+ih,t)$, $i \in [1,...,N]$ to be the value of the variable of interest at each grid point. Hence, using the finite difference method [54]

$$\left.\frac{\partial C}{\partial x}\right|_{x=a+ih} \approx \frac{u_{i+1} - u_{i-1}}{2h}, \tag{2.29}$$

and:

$$\left.\frac{\partial^2 C}{\partial x^2}\right|_{x=a+ih} \approx \frac{\left.\frac{\partial C}{\partial x}\right|_{x=a+i\frac{h}{2}} - \left.\frac{\partial C}{\partial x}\right|_{x=a-i\frac{h}{2}}}{h} \approx \frac{u_{i+1} - 2u_i + u_{i-1}}{h^2}. \tag{2.30}$$

Higher order terms can be found in the same manner. Applying the approximations given in equations (2.29) and (2.30) to a partial differential equation system will reduce the partial differential equation to a system of ordinary differential equations. By construction, u_0 and u_{n+1} will be outside the defined range $[a, b]$. This problem is solved by considering the boundary conditions present at $x = a$, corresponding to u_0, and $x = b$, corresponding to u_{n+1}. This method generally allows u_0 and u_{n+1} to be expressed in terms of known grid points and constants.

2.7 Laplace Transform

If $f(t)$ is fully defined and locally integrable over $t \in [0, \infty)$, then the Laplace transform of $f(t)$, $\mathcal{L}\{f(t)\}(s) = \hat{f}(s)$, is defined as [55]:

$$\hat{f}(s) = \int_0^\infty \exp(-st) f(t) \mathrm{d}t. \tag{2.31}$$

One of the key reasons for considering the Laplace transform is that it transforms linear integral and ordinary differential equations into polynomial equations [55]. Polynomial equations are usually easier to solve and the resulting solution to the original system can be found by applying the inverse transform. The inverse Laplace transform is complex to apply hence, in practice, it is more convenient to decompose the function being inverse transformed into functions with known inverse transforms. The inverse transform is then found by inspection [55].

In the case of partial differential equations in one spatial dimension and time, applying the Laplace transform can reduce the system to an ordinary differential equation, which is generally easier to solve. The solution to the partial differential equation can then be obtained

by inverse transforming the solution to the ordinary differential equation.

2.8 Bessel Functions

Bessel functions, $J_n(x)$, are standard solutions to the differential equation [56]

$$x^2\frac{\mathrm{d}^2y}{\mathrm{d}x^2}(x) + x\frac{\mathrm{d}y}{\mathrm{d}x}(x) + (x^2 - n^2)y(x) = 0, \tag{2.32}$$

for arbitrary complex number n, also called the order of the function. Depending on the properties of the initial condition, $y(x = 0)$, and n, Bessel functions can have radically different behaviour.

In this thesis, the Bessel functions encountered are modified Bessel functions of the first kind, $I_n(x)$, which correspond to Bessel differential equations of the form

$$x^2\frac{\mathrm{d}^2y}{\mathrm{d}x^2}(x) + x\frac{\mathrm{d}y}{\mathrm{d}x}(x) - (x^2 + n^2)y(x) = 0, \tag{2.33}$$

with no singularity at the origin, $x = 0$ [56]. Modified Bessel functions of the first kind are defined by the contour integral

$$I_n(x) = \frac{1}{2\pi i}\oint \exp\left(\frac{x(t+1)}{2t}\right) t^{-n-1}\mathrm{d}t, \tag{2.34}$$

where the contour integral encloses the origin and moves in an anticlockwise direction [56].

A sketch of the behaviour of these functions for the integers $n = [0, 4]$ given in Figure 2-2 with $I_n(x) \to \infty$ as $x \to \infty$. Figure 2-3 considers $I_n(x)\exp(-x)$ over the same range of n. From this, it is clear that ${}^{I_n(x)}/_{I_m(x)} \to 1$ as $x \to \infty$ for $m, n \in \mathbb{N}_0$.

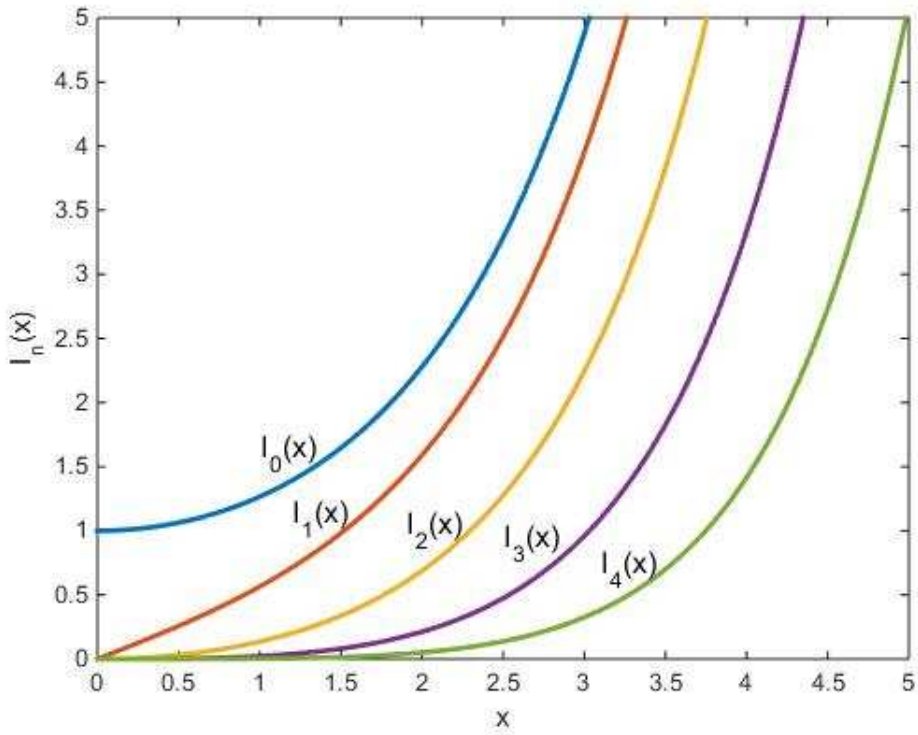

Figure 2-2: Behaviour of modified Bessel functions for $x \in [0, 4]$.

2.9 Chapter Summary

This chapter has detailed several useful mathematical methods including steady state and stability analysis, parameter estimation using the Gauss-Newton algorithm, propagation of error, methods of evaluating advection diffusion equations and has defined Bessel functions.

These techniques will be used throughout the thesis. The next chapter moves on to consider models of amino acids in the blood serum.

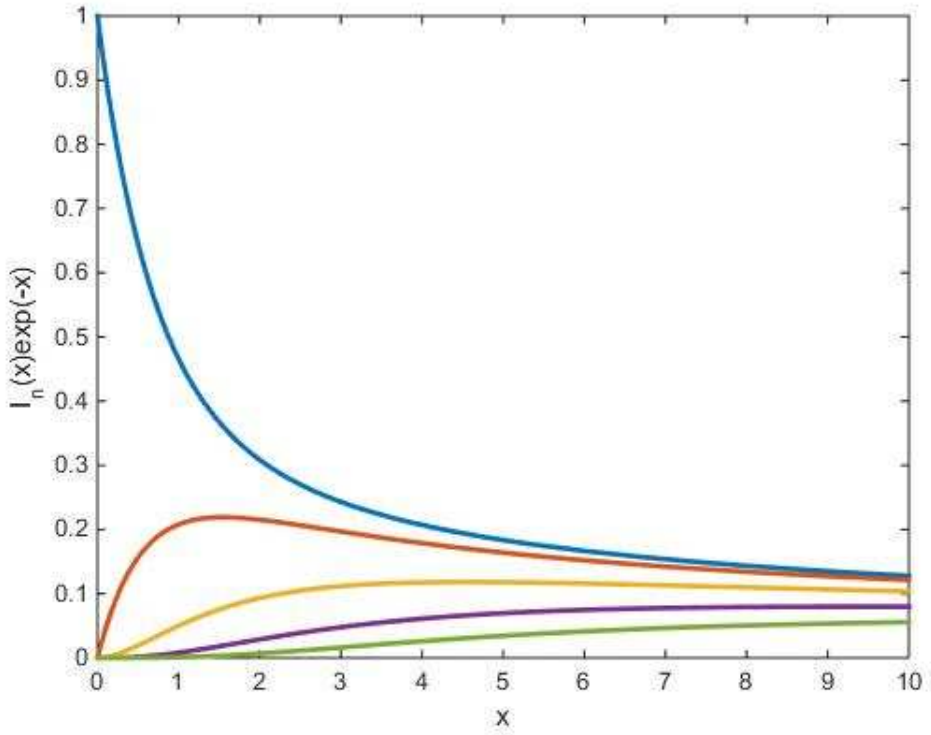

Figure 2-3: Using the same line colours as Figure 2-2, this figure shows that modified Bessel functions of the first kind are very different close to $x = 0$, but come closer together as $x \to \infty$.

Chapter 3

Systemic Profile of Phenylalanine

3.1 Chapter Objective

The objective of this chapter is to mathematically model the systemic distribution of phenylalanine with food intake. To do this, we first consider the biological background for metabolism and input of amino acids into the body before moving on to consider a fasting state model of phenylalanine. Fasting state blood serum phenylalanine has been previously modelled as a single compartment model [10] and does not consider that the metabolism of this compound primarily occurs in the liver [57]. We consider both a single-compartment model and a two-compartment model that includes the effect of liver only metabolism and compare the models before incorporating food intake.

As art of the comparison between the single-compartment and two-compartment approach, we consider resilience and reactivity, detailed in sections 2.1.2 and 2.1.3, in order to measure the response of both systems to a perturbation. Differences in this behaviour may indicate differences in system dynamics once food intake is introduced.

3.2 Parameter Summary

Table 3.1 summarises all the parameters and variables used in this chapter with their definitions and, where appropriate, values and standard deviations for reference through this chapter. Due to the incredibly diverse nature of humans around the world, we consider a man of average height at ideal body weight with a balanced diet to calculate phenylalanine dose

into the body. Human diversity is considered later in this chapter. This table is designed to be used for reference.

Table 3.1: Table summarising parameters in systemic phenylalanine model [10].

Parameter/Variable	**Definition**	**Value/Units**	**Source**
t	Time	h	-
v	Rate of reaction	mMh^{-1}	-
v_{PAH}	Rate of hydroxylation	mMh^{-1}	-
v_{TRANS}	Rate of transamination	mMh^{-1}	-
v_{NPD}	Rate of natural protein degradation	$0.012mMh^{-1}$	[10]
k_1	Rate of formation of the enzyme-substrate complex	mMh^{-1}	-
k_{-1}	Rate of breakdown of the enzyme-substrate complex	mMh^{-1}	-
k_2	Rate of product formation	mMh^{-1}	-
V_m	Maximum rate of metabolism	mMh^{-1}	-
K_s	Dissociation constant	mM	-
$[E]$	Enzyme concentration	mM	-
$[S]$	Substrate concentration	mM	-
$[Pr]$	Product concentration	mM	-
K_a	Activation constant	0.54mM	[10]
a	Dose into the body	45.7 mg/kg of bodyweight	[58]
k_3	Rate of uptake	$1h^{-1}$	[11]
$C(t)$	Concentration of compound of interest	mM	-
V	Volume of distribution	40L	[59]
C_0	Initial concentration in stomach	mM	-
$N(t)$	Number of doses into the body	-	-
τ	Dosing interval	8 h	-
K_m	Dissociation constant of hydroxylation	0.51mM	[10]

K_T	Dissociation constant of transamination	1.37mM	[10]
V_m^P	Maximum rate of hydroxylation	0.90mMh^{-1}	[10]
V_m^T	Maximum rate of transamination	0.063mMh^{-1}	[10]
$P(t)$	Blood serum phenylalanine concentration - one compartment case	mM	-
R	Resilience	-	-
$P_s(t)$	Blood serum phenylalanine concentration - two compartment case	mM	-
V_s	Systemic volume of distribution - two compartment case	2337±66ml	[59]
$A_s(t)$	Amount of phenylalanine in blood serum - two compartment case	mol	-
$P_l(t)$	Liver phenylalanine concentration - two compartment case	mMh^{-1}	-
V_l	Liver volume of distribution - two compartment case	334±10ml	[59, 60]
$A_l(t)$	Amount of phenylalanine in the liver - two compartment case	mol	-
$V_{m_l}^P$	Maximum rate of hydroxylation in the liver	7.2 mMh^{-1}	[10, 59, 60]
$V_{m_l}^T$	Maximum rate of transamination in the liver	0.504±0.018mMh^{-1}	[10, 59, 60]
K_{m_l}	Dissociation constant of hydroxylation in the liver	0.51mM	[10]
K_{a_l}	Activation constant in the liver	0.54mM	[10]
K_{T_l}	Dissociation constant of transamination in the liver	1.37mM	[10]
$A(t)$	Total amount of phenylalanine in the body	mol	-
b	Body weight	70.5kg	[61, 62]
c	Total body water percentage	57%	[62, 61, 61]
k_{IN}	Rate of movement from systemic to the liver compartment	42.4±4.0 h^{-1}	[63]
k_{OUT}	Rate of movement from liver to systemic compartment	297±28 h^{-1}	[63]
k_4	First order transamination rate	mMh^{-1}	-
k_5	Rate of protein synthesis	mMh^{-1}	-
P_0	Initial concentration of phenylalanine	1mM	[10]
a_c	Constant input rate from the stomach	mMh^{-1}	-

α^{-1}	Volume ratio between systemic and liver compartment	7.00	-
β	Fraction of blood serum that is water	90%	[59]

3.3 Background Biology

When considering systemic disposition of amino acids, it is important to consider several biological concepts. Firstly, one of the primary methods of removal of amino acids in the body is via metabolism. Modelling metabolic processes, or enzyme kinetics, mathematically has been researched extensively and we begin by considering this.

Many amino acids, like phenylalanine, are taken into the body via food intake, so the Bateman function is then considered as a method of mathematically modelling the input of amino acids into the body via food intake and how this then distributes through the body.

3.3.1 Enzyme Kinetics

Enzymes are large biological molecules whose sole purpose is to catalyse reactions [64]. Enzyme kinetics deals with the rates of enzyme-catalysed reactions [64] and is important to consider when trying to model phenylalanine concentrations in the body as metabolism of phenylalanine into its metabolites is governed by enzymes.

The first general rate equation for reactions involving enzymes was developed by Henri in 1903 [64]. This method accounted for the rate of a reaction, v, being directly proportional to the concentration of the reactant, referred to as substrate, but increasing in a non-linear manner tending to a maximum rate as the concentration of substrate was increased.

The derivation of the Henri equation has several assumptions [64], namely that:

1. The enzyme is a catalyst, which means it remains unchanged after the reaction has occurred.

2. The enzyme and substrate react rapidly to form an enzyme substrate complex.

3. Only a single substrate and single enzyme-substrate complex are involved and these break down directly into one product and one enzyme.

4. The reaction from enzyme + substrate into enzyme-substrate complex is at equilibrium, this is called the quasi-equilibrium assumption.

5. The substrate concentration is much greater than that of the enzyme, hence formation

of the enzyme-substrate complex does not affect the substrate concentration.

6. The rate limiting part of the reaction is the breakdown of the enzyme-substrate complex into enzyme and product.

7. The reverse reaction is considered to be insignificant.

These assumptions result in the chemical equation given in equation (3.1). In this, the enzyme, E, and substrate, S, combine at rate k_1 to form an enzyme substrate complex, ES, which then either dissociates at rate k_{-1} back into enzyme and substrate, or reacts at rate k_2 to form the product, Pr, and the original enzyme.

$$E + S \underset{\mathrm{k}_{-1}}{\overset{\mathrm{k}_1}{\rightleftarrows}} ES \xrightarrow{k_2} E + Pr \tag{3.1}$$

By consideration of the law of mass action and using the quasi-steady state assumption, it is then possible to derive the Michaelis-Menten equation [64]:

$$v = \frac{V_m[S]}{K_s + [S]}.$$

In the Michaelis-Menten equation, the rate of reaction, v, is given in terms of the maximum rate of reaction, V_m, the concentration of the substrate, $[S]$, and the dissociation constant of the enzyme-substrate complex, K_S, which is related to the rate of reactions given in the chemical equation in equation (3.1) by:

$$K_S = \frac{k_{-1}}{k_1} = \frac{[E][S]}{[ES]}.$$

This approach was used to consider the transamination pathway for phenylalanine metabolism in the body. The metabolic pathways of phenylalanine are shown in section 1.1.1.

The Michaelis-Menten equation is a fundamental part of enzyme kinetics and the method of formulating this equation can also be used to consider more complex problems.

Previous research has modelled the metabolism of phenylalanine into tyrosine via hydroxylation using a two-site ordered binding model [10, 64]. The base reaction for a two-site ordered

binding model is shown in equation (3.2).

$$E + S \overset{\mathrm{K_a}}{\rightleftarrows} SE + S \overset{\mathrm{K_m}}{\rightleftarrows} SES \xrightarrow{k_p} E + Pr \tag{3.2}$$

In this equation the dissociation constant of activation is given as K_a and the dissociation constant of the substrate-catalytic site complex, SES, is given by K_m. The two stage process in equation (3.2) represents activation of the enzyme by the substrate by having one molecule of the substrate bind to the enzyme first, which then produces a complex that acts as a catalyst for the substrate to product reaction.

Using the same method as before [64], it can then be shown that

$$v = \frac{V_m}{1 + \frac{K_m}{[S]} + \frac{K_m K_a}{[S]^2}},$$

which is used to show the rate of reaction in a two-site ordered binding model.

3.3.2 Bateman Model for Food Intake

The Bateman function has been previously used to model food absorption from the stomach to systemic circulation [11]. It represents food intake, neglecting any clearance or metabolic effects in the body. Considering a dose of amount a into the stomach, we assume that

1. Rate of uptake to the systemic circulation, k_3, is constant over time, t.

2. The only removal of the compound from the stomach is into the systemic circulation.

3. The compound instantaneously distributes evenly throughout the volume of distribution, V, which in the case of phenylalanine is total body water.

Using these assumptions, the systemic concentration at time t, $C(t)$, is governed by

$$\frac{\mathrm{d}C}{\mathrm{d}t}(t) = \frac{a}{V} k_3 e^{-k_3 t},$$

which has solution

$$C(t) = C_0 + \frac{a}{V}\left(1 - e^{-k_3 t}\right),$$

based on an initial concentration in systemic circulation, C_0, which is shown in Figure 3-1.

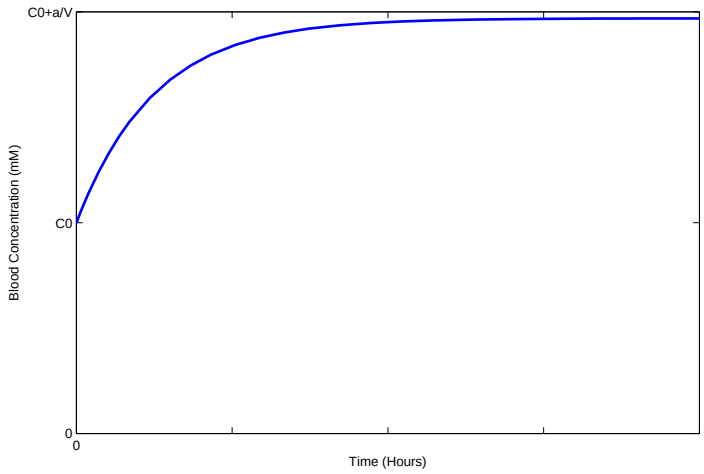

Figure 3-1: Behaviour of a Bateman function modelling the absorption of a single dose from the stomach to the blood with the dose given at time zero.

For a repeated dose with a fixed dosing interval, τ, this model can be expanded to

$$\frac{\mathrm{d}C}{\mathrm{d}t}(t) = \frac{1}{V}k_3 \sum_{n=1}^{N} a_n e^{-k_3(t-n\tau)} H(t-n\tau) = \frac{1}{V}k_3 e^{-k_3 t} \sum_{n=1}^{N} a_n e^{k_3 n\tau} H(t-n\tau),$$

where N is the number of doses and $H(t)$ is the Heaviside step function. The first dose is considered to be at $t = 0$. Figure 3-2 shows the time dependent solution to the multiple dose case for a fixed dose applied at three evenly spaced intervals.

Total body water

The Bateman function highlights the importance of volume of distribution in understanding drug concentrations in the body. As discussed in section 1.1.1, phenylalanine is hydrophilic and hence distributes itself throughout total body water (TBW) [11]. TBW percentage varies between individuals and over time for a given individual. An average man of ideal bodyweight

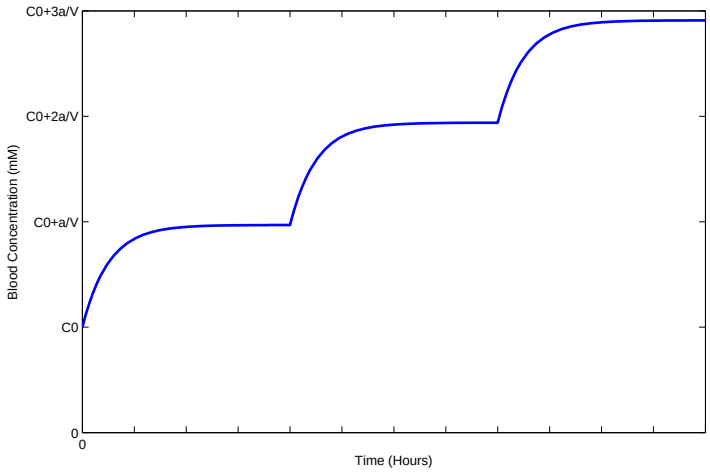

Figure 3-2: Expected behaviour of a sum of Bateman functions modelling the absorption of three doses of equal amount and spacing from the stomach to the blood with the first dose given at time zero.

has an estimated TBW percentage of 57% [59].

Obesity can reduce TBW percentage to as low as 45% [17]. Tolerance to phenylalanine is measured in mg/kg of total body weight. As a consequence a large increase in weight from a patient suffering from PKU would increase their bodyweight, but decrease their tolerance relative to their bodyweight as their volume of distribution does not increase proportionately to total weight [17]. Due to this, significant changes in a patient's physiology can change the treatment needed to manage a chronic illness. This suggests that phenylalanine tolerance should be regularly assessed and should not rely on childhood data.

Blood composition

Blood circulates oxygen and other nutrients through the body as well as removing waste compounds such as carbon dioxide. Blood is comprised of a yellowish liquid called plasma, 55% by volume, in which billions of cells are suspended [59]. Plasma is approximately 92% water with the other 8% comprising a variety of substances vital to the body including the clotting protein fibrinogen [59]. Blood serum is the blood plasma without fibrinogen and is approximately 90% water by volume [59].

In a fasting state, blood serum concentration of phenylalanine is between 0.055-0.060mM in a normal person, increasing in excess of 1.2mM in a patient with classical PKU [10].

3.3.3 The Human Body

The human body and dietary intake of phenylalanine is important to consider when calculating the increase in concentration of phenylalanine in blood serum.

Considering a range of prior studies amalgamated in [65] it is clear that body weight, height and body mass index vary significantly between countries, ethnic backgrounds, gender and age. Considering a trial person as a man at average height for the UK, 177.8cm [61], at ideal body weight, calculated using the Miller Formula to be 70.5kg [62], resulting in a total body water volume of 40L. Considering a balanced diet results in a daily phenylalanine intake of approximately 137mg of phenylalanine per kg of body weight [58].

Variations in body weight and phenylalanine intake only contribute to serum concentration in a non-fasting state. When considering the non-fasting state, we begin by considering this trial person and then expand the results to consider a range.

3.3.4 Phenylalanine in Skeletal Muscle

In the human body, a major store of phenylalanine is in skeletal muscle [10, 66]. Hence formation of this muscle removes phenylalanine from systemic circulation and its breakdown releases phenylalanine back into systemic circulation [10].

In a fasting state, muscular breakdown in the body exceeds formation. This leads to the release of phenylalanine into systemic circulation which has been previously considered to be at a constant rate calculated from phenylalanine present in skeletal muscle [10].

3.4 Fasting State Model for Phenylalanine

A loading test in a pharmaceutical sense involves giving a patient a large dose of a compound and observing the rate of decay of this compound over a period of time. PKU has been previously identified and classified via loading tests of patients in a fasting state [16]. A fasting state is used as phenylalanine is present in lots of foods, hence eating during the loading test would introduce more phenylalanine into the system making it harder to classify PKU. It has been previously suggested that the only significant factors that replenish the plasma pool of phenylalanine are food intake and the breakdown of proteins in the body [10]. In a fasting state, delivery of phenylalanine via food intake can be ignored hence the only

method of intake is via natural protein degradation.

In this section, we consider modelling phenylalanine concentration in a fasting state. First, a single compartment model from previous literature [10] is considered before splitting this model into two compartments to more realistically model the metabolism of phenylalanine in the body as metabolism of this compound primarily occurs in the liver [67]. These two models are then compared.

3.4.1 Single compartment model

Several mathematical models have been developed to explore underlying processes that impact on systemic phenylalanine levels [10, 11]. The model presented in [10] considers systemic phenylalanine levels of a patient in a fasting state via a single compartment model with rate of change of phenylalanine concentration, $P(t)$, in the blood given as a sum of the rate of hydroxylation, v_{PAH}, transamination, v_{TRANS}, and natural protein degradation, v_{NPD}:

$$\frac{\mathrm{d}P}{\mathrm{d}t} = -v_{PAH} - v_{TRANS} + v_{NPD}.$$

Hydroxylation is assumed to follow a two-site ordered binding process [10], transamination a single site binding process and natural protein degradation is assumed to be at a constant rate. This results in

$$\frac{\mathrm{d}P}{\mathrm{d}t} = -\frac{V_m^P P^2}{P^2 + K_m P + K_m K_a} - \frac{V_m^T P}{P + K_T} + v_{NPD} = f(P), \tag{3.3}$$

where constants are defined in table 3.2 and include parameter estimates based on experimental work published for non-PKU suffering patients [10]. Based on the constants in table 3.2, P is in mM and t is in hours.

The concentrations predicted from this model, including steady state and half life, were found to be comparable to experimental data [10]. PKU suffering patients were investigated by changing V_m^P, effectively limiting the maximum rate of phenylalanine metabolism in the body. The result of this over a ten hour period is shown in Figure 3-3.

Consideration of the B route in Figure 3-3 also showed that transamination has a very small effect compared to hydroxylation. However, as shown by case D and previous research [9], the

Table 3.2: Table of constants in systemic phenylalanine model obtained from [10]. Standard deviation is given for K_T but was not available for other parameters.

Constant	Symbol	Value
Maximum rate of hydroxylation	V_m^P	0.90mMh^{-1}
Maximum rate of transamination	V_m^T	0.063mM^{-1}h^{-1}
Natural protein degradation	v_{NPD}	0.012mM^{-1}h^{-1}
Kinetic constant for PAH activation	K_a	0.54mM
Dissociation constant for PAH	K_m	0.51mM
Dissociation constant for transamination	K_T	1.37±0.14mM

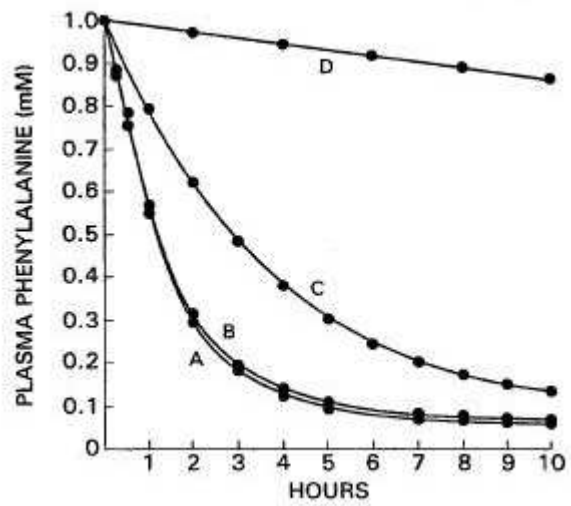

Figure 3-3: Model for blood phenylalanine levels over a 10 hour period. A represents a healthy patient, B represents the effect of removing the transamination pathway, C represents a 50% effective PAH enzyme and D represents a 0% effective PAH enzyme. Taken from [10].

transamination pathway is important in patients with classic PKU and needs to be considered in tests that measure phenylalanine levels in response to treatments such as BH_4 response tests [9]. Beyond confirming the steady states were consistent with experimentally obtained results, previous published work did not analyse the model in detail [10].

3.4.2 Analysis of the single compartment model

Figure 3-4 reproduces data from [10], shown in Figure 3-3, but additionally considers the impact of activation of phenylalanine hydroxylase on phenylalanine concentrations. Without activation, $K_a = 0$, the hydroxylation term in equation (3.3) reduces from a two-site ordered binding equation to a single site binding process resulting in:

$$\frac{\mathrm{d}P}{\mathrm{d}t} = -\frac{V_m^P P}{P + K_m} - \frac{V_m^T P}{P + K_T} + v_{NPD}. \tag{3.4}$$

Figure 3-4 shows that the effect of this is that stable levels of phenylalanine are significantly lowered, which suggests that activation is an important component in phenylalanine dynamics; in some previous studies it has been omitted [11].

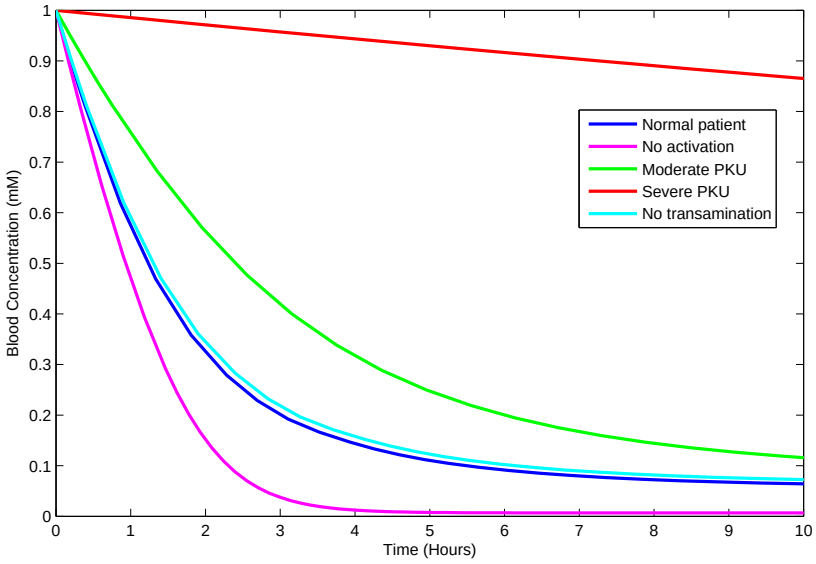

Figure 3-4: Plot of blood phenylalanine levels over time in a fasting state. Initial phenylalanine concentrations are set at 1mM to simulate a loading test and be in line with the previous model [10]. The red line represents classical PKU, the green line moderate PKU, the blue line a normal person, the black line a normal person with no transamination pathway and purple the effect of the activation term in the activity of PAH.

Steady state analysis of equation (3.3)

Under physiological conditions, all parameters and variables given in equation (3.3) must be greater than 0. Hence under physiological conditions:

$$f'(P) = -\frac{V_m^P P K_m \left(P + 2K_a\right)^2}{\left(P^2 + K_m P + K_a K_m\right)^2} - \frac{V_m^T K_T}{\left(P + K_T\right)^2} < 0. \tag{3.5}$$

As $f'(P) < 0$, this means that $f(P)$ is a decreasing function on $[0, \infty)$ with $f(0) = v_{NPD} > 0$ and $f(P) \to v_{NPD} - V_m^T - V_m^P$ as $P \to \infty$.

Hence equation (3.3) has a globally asymptotically stable positive steady state P^* if $V_m^T + V_m^P > v_{NPD}$, which is biologically realistic regardless of severity of PKU, while $f(P) > 0$ and $P(t) \to \infty$ as $t \to \infty$ if $V_m^T + V_m^P < v_{NPD}$, which is not.

In order to find the globally asymptotic steady state, we consider

$$0 = f(P^*) = -\frac{V_m^P P^{*2}}{P^{*2} + K_m P^* + K_m K_a} - \frac{V_m^T P^*}{P^* + K_T} + v_{NPD}.$$

which can be re-arranged to create the cubic

$$\alpha_1 P^{*3} + \beta_1 P^{*2} + \gamma_1 P^* + \delta_1 = 0, \tag{3.6}$$

with coefficients:

$$\begin{aligned}
\alpha_1 &= v_{NPD} - V_m^P - V_m^T, \\
\beta_1 &= [K_m + K_T]v_{NPD} - K_T V_m^P - K_m V_m^T, \\
\gamma_1 &= [K_m K_T + K_m K_a]v_{NPD} - K_m K_a V_m^T, \\
\delta_1 &= K_m K_a K_T v_{NPD} > 0.
\end{aligned}$$

Solving equation (3.6) we obtain 3 roots P_k^*, $k = 1, 2, 3$ where

$$P_k^* = \frac{-1}{3\alpha}\left(\beta + u_k + \frac{\Delta_0}{u_k \Omega}\right), \quad k \in \{1, 2, 3\},$$

$$\Omega = \sqrt[3]{\frac{\Delta_1 + \sqrt{\Delta_1^2 - 4\Delta_0^3}}{2}},$$

$$\Delta_0 = \beta_1^2 - 3\alpha_1\gamma_1,$$

$$\Delta_1 = 2\beta_1^3 - 9\alpha_1\beta_1\gamma_1 + 27\alpha_1^2\delta,$$

and

$$u_1 = 1, \quad u_2 = \frac{-1 + i\sqrt{3}}{2}, \quad u_3 = \frac{-1 - i\sqrt{3}}{2}.$$

Using the parameters given in table 3.2 for a patient without PKU results in

$$\mathbf{P}^* = \begin{pmatrix} P_1^* \\ P_2^* \\ P_3^* \end{pmatrix} = \begin{pmatrix} 0.057 \pm 0.006 \\ -1.30 \pm 0.15 \\ -0.064 \pm 0.07 \end{pmatrix} \text{mM},$$

with one positive steady state, P_1^*, as expected. Figure 3-5 demonstrates that decreasing V_m^P, corresponding to increasing severity of PKU, causes P_1^* to increase, as expected.

In Figure 3-6 we show the dependence of P_1^* on V_m^P and v_{NPD} with other parameters fixed from table 3.2.

Beyond considering the existence and stability of the steady states in the model, it is also interesting to examine the rate at which the steady state is approached and the nature of that approach. To do this we employ the following measures: resilience which measures the rate of return to the steady state following a small perturbation; and reactivity which measures if the initial perturbation grows in magnitude. The methods for calculating these measures are discussed in sections 2.1.2 and 2.1.3 respectively.

Resilience The single compartment model linearises using

$$P(t) = P_1^* + p(t),$$

to:

$$\frac{\mathrm{d}p}{\mathrm{d}t} = f'(P_1^*)p.$$

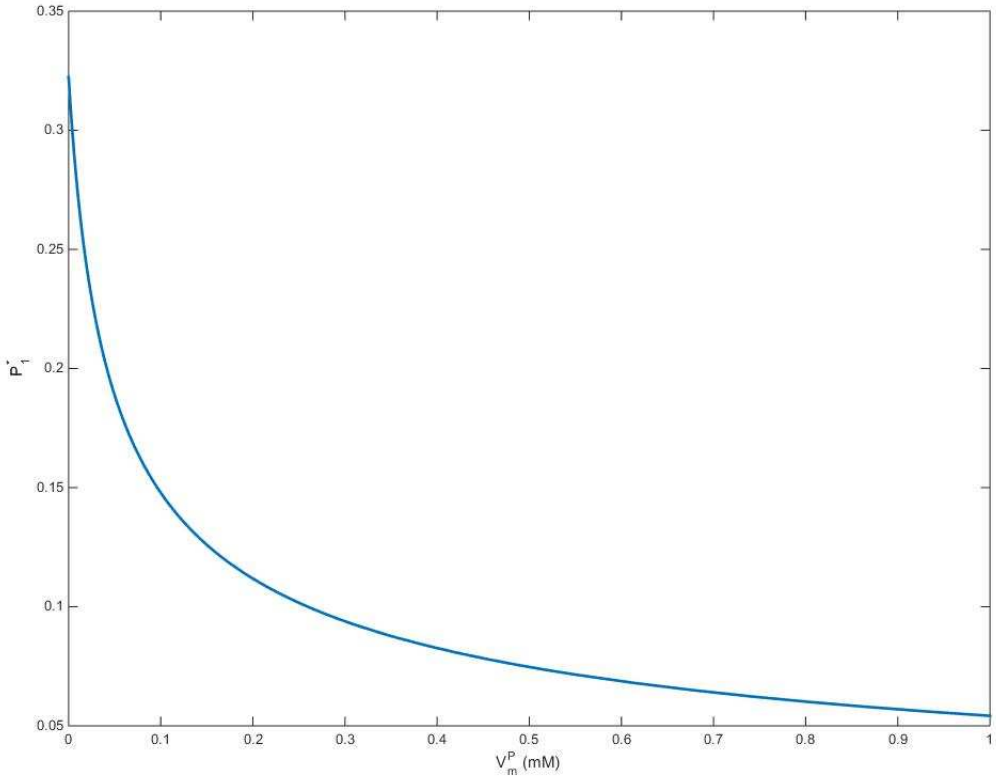

Figure 3-5: Using the parameters for all but V_m^P given in table 3.2, the effect of PKU on the steady state P_1^* is shown. Severity of PKU is represented by changing V_m^P with more severe cases being reflected by this parameter decreasing.

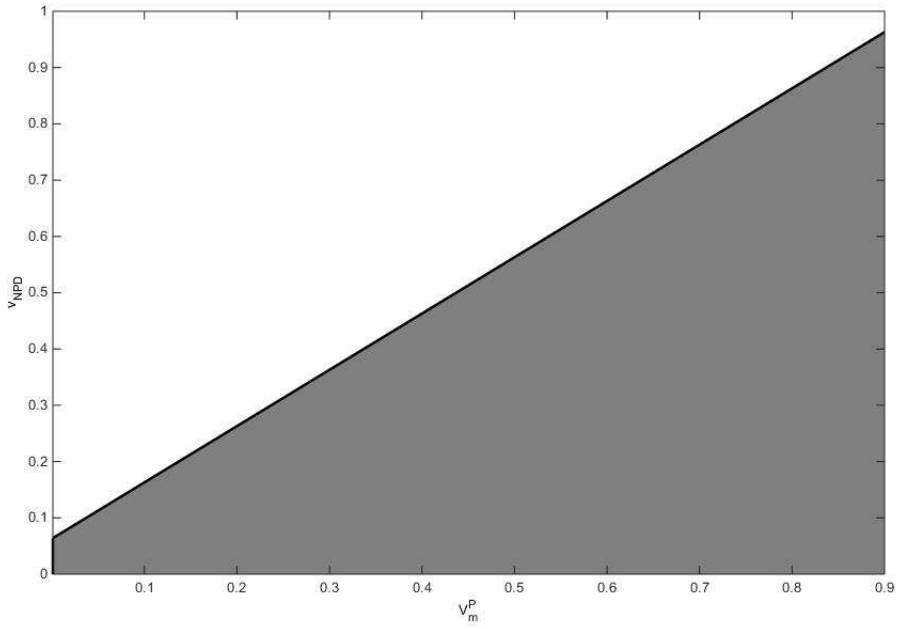

Figure 3-6: The shaded area on the plot shows the conditions under which a positive, stable steady state exists. For the parameters considered in table 3.2, all patients are in the shaded area.

Hence, for the single compartment model:

$$\begin{aligned} \text{Resilience} &= -f'(P_1^*), \\ &= \frac{V_m^P(K_m P_1^* + 2K_m K_a)}{(P_1^{*2} + K_m P_1^* + K_m K_a)^2} + \frac{V_m^T K_T}{(P_1^* + K_T)^2}, \\ &> 0 \quad \forall P_1^* \geq 0. \end{aligned} \tag{3.7}$$

In Figure 3-7 we show how resilience depends upon V_m^P. For low values of V_m^P, which correspond to a severe PKU scenario, resilience increases non-linearly with V_m^P as demonstrated by Figure 3-8. The initial non-linearity is likely due to metabolism via transamination, represented by the transamination term in equation (3.7), dominating overall metabolism and hence the return to the steady state at low values of V_m^P. In the real world, this means that, as patients with PKU have a lower V_m^P compared to the rest of the population, patients with PKU will take longer to return to a steady state concentration of phenylalanine after a perturbation than a normal patient. This is especially concerning when considering food intake and raises the question as to whether it is better to have a large dose of phenylalanine once

a day or a continuous infusion and whether this preference changes with severity of PKU.

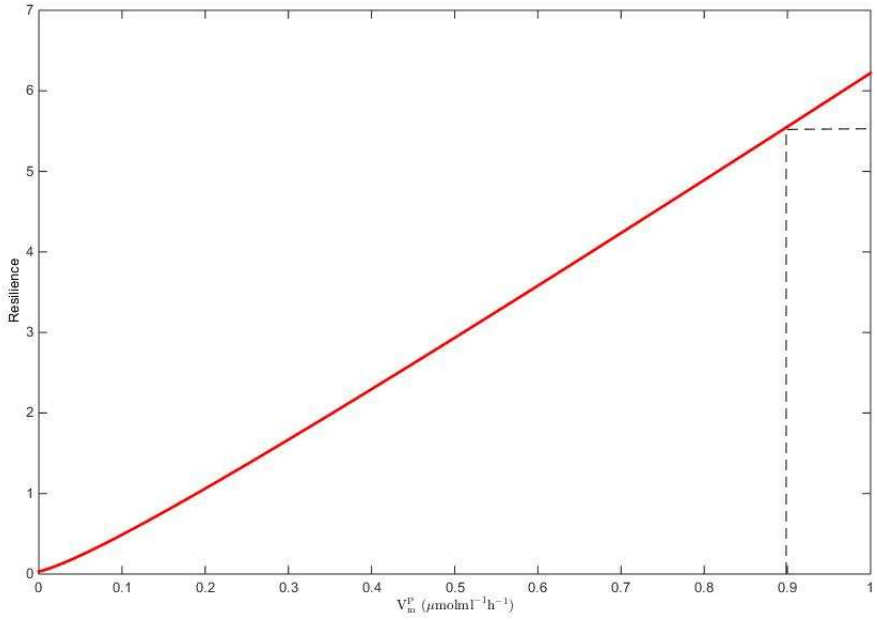

Figure 3-7: Graph showing the effect of V_m^P on the resilience of the fasting state model. The dotted line represents V_m^P in a non-PKU suffering patient.

Figure 3-9 considers the rate of change of resilience with respect to V_m^P, ${}^{\partial R}/_{\partial V_m^P}$. As expected, this function started with a non-linear increase with V_m^P and tended to a constant as $V_m^P \to \infty$. This would result in the non-linear to linear behaviour demonstrated by resilience in Figures 3-7 and 3-8.

Figure 3-9 also suggests that a small increase in V_m^P close to 0 can have a large effect on resilience. Hence strategies to improve V_m^P by a small amount in PKU suffering patients would be very effective.

Reactivity For a single compartment model,

$$\text{Reactivity} = -\text{Resilience} < 0,$$

and we will not observe a reactive system. This means that any small perturbation from the steady state will return to that steady state monotonically.

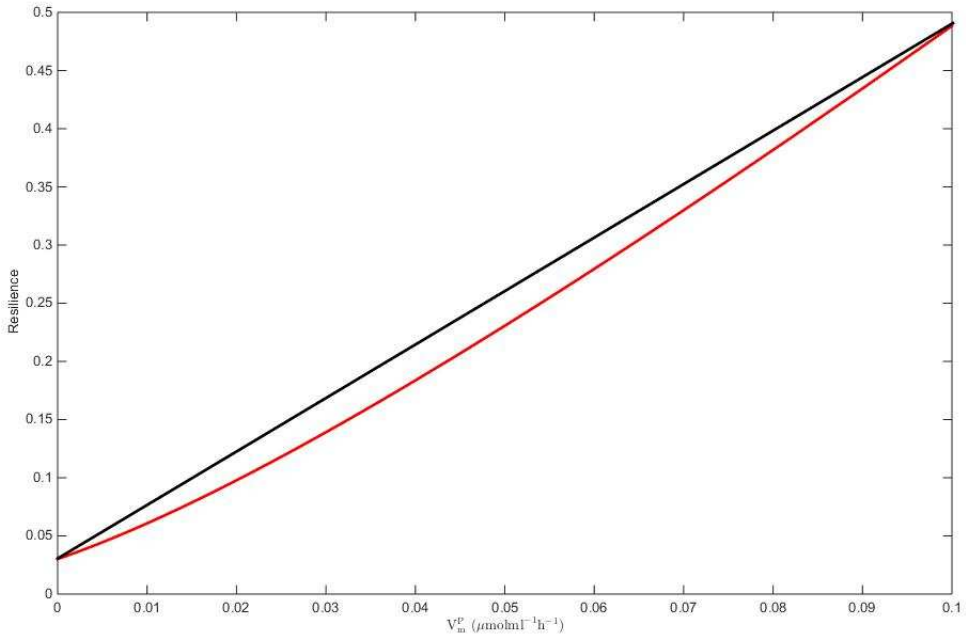

Figure 3-8: Zoomed in version of figure 3-7 to demonstrate the initial non-linearity. The black line on the plot is linear for comparison.

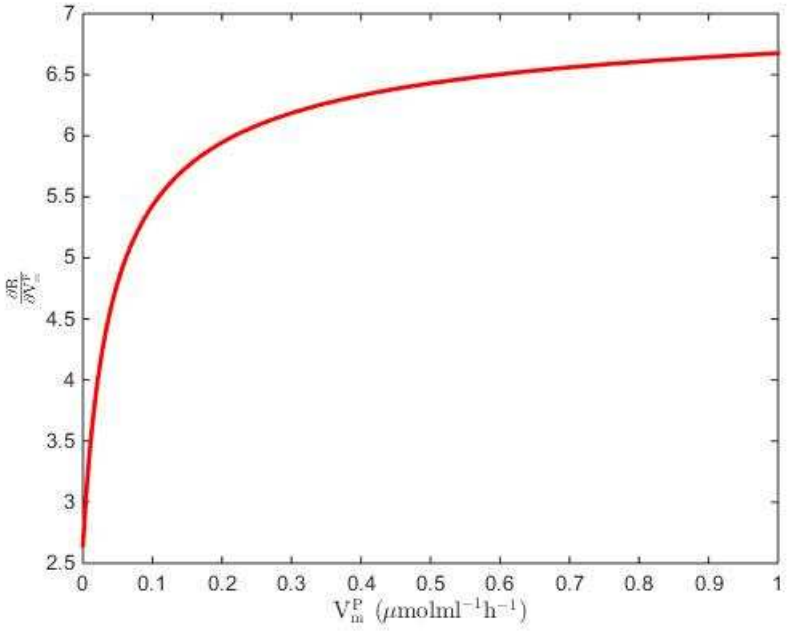

Figure 3-9: Graph showing the effect of V_m^P on rate of change of resilience with respect to V_m^P.

3.4.3 Two-compartment model

In the single-compartment model, metabolism is considered to happen throughout the whole blood serum compartment [10, 11]. In reality it has been shown that metabolism of phenylalanine in humans occurs primarily in the liver [67] and so we extend the model to a two compartment structure.

We split the single compartment model into systemic, where no metabolism occurs, and liver compartments, where metabolism occurs, and compare the behaviour of this to the single compartment model.

Model formation

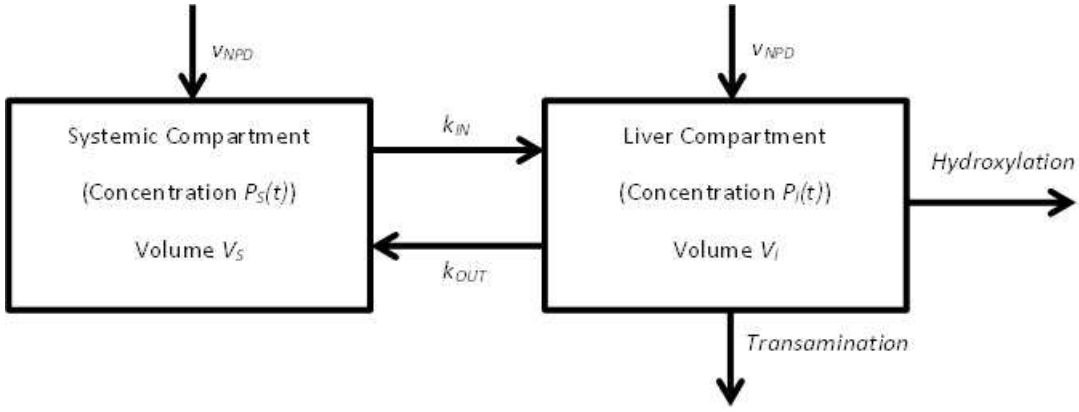

Figure 3-10: Two compartment model diagram.

We split the body into two compartments, the systemic and liver compartment, as shown in Figure 3-10. The systemic compartment has concentration of phenylalanine, $P_S(t)$, over a fixed volume, V_S, with intake via natural protein degradation at rate v_{NPD}, influx from the liver compartment at rate k_{OUT} and outflow into the liver compartment at rate k_{IN}.

The liver compartment has a concentration of phenylalanine, $P_l(t)$, over a fixed volume, V_l, with intake via natural protein degradation at rate v_{NPD}, influx from the systemic compartment at rate k_{IN} and outflow into the systemic compartment at rate k_{OUT}. Metabolism of phenylalanine occurs in the liver via hydroxylation and transamination. The mechanisms for transamination and hydroxylation are the same in both the one compartment and two compartment models using adjusted model parameters described below.

Using the conservation principle, the rate of change of amount of phenylalanine in the systemic, $A_S(t)$, and liver compartment, $A_l(t)$, with respect to time under constant volume

assumption for both compartments is given by

$$\frac{\mathrm{d}A_s}{\mathrm{d}t} = -k_{IN}A_S + k_{OUT}A_l + v_{NPD}V_S,$$
$$\frac{\mathrm{d}A_l}{\mathrm{d}t} = k_{IN}A_S - k_{OUT}A_l - \frac{V_{m_l}^P P_l^2}{P_l^2 + K_{m_l}P_l + K_{m_l}K_{a_l}}V_l - \frac{V_{m_l}^T P_l}{P_l + K_{T_l}}V_l + v_{NPD}V_l.$$

As the volumes of both compartments are assumed to be constant, this results in the following system of differential equations for concentration of phenylalanine

$$\frac{\mathrm{d}P_s}{\mathrm{d}t} = -k_{IN}P_S + \alpha k_{OUT}P_l + v_{NPD}, \tag{3.8}$$
$$\frac{\mathrm{d}P_l}{\mathrm{d}t} = \frac{1}{\alpha}k_{IN}P_S - k_{OUT}P_l - \frac{V_{m_l}^P P_l^2}{P_l^2 + K_{m_l}P_l + K_{m_l}K_{a_l}} - \frac{V_{m_l}^T P_l}{P_l + K_{T_l}} + v_{NPD}, \tag{3.9}$$

where:

$$\alpha = \frac{V_l}{V_S}.$$

Parameters

Most of the parameters for this model were found exactly from previous literature or adapted from the one compartment systemic model.

Firstly, the dissociation constants of hydroxylation and transamination metabolism are properties of the enzyme and the same for both the one compartment and two compartment model[10], hence:

$$K_{m_l} = K_m = 0.51\text{mM}, \quad K_{a_l} = K_a = 0.54\text{mM}, \quad K_{T_l} = K_T = 1.37 \pm 0.14\text{mM}.$$

It is known that the average adult has 4.85±0.15L of blood in the body [59] of which 55% is serum [59], hence there is 2.67±0.08L of serum in the body. As phenylalanine is measured in blood serum this means that:

$$V_S + V_l = 2670 \pm 80\text{ml}.$$

It is also known that, on average, the liver contains 12.5% [60] of the blood in the body, hence $V_S = 2336.25 \pm 66$ml, $V_l = 333.75 \pm 10$ml and $\alpha^{-1} = 7$.

Blood flow into the liver is equal to blood flow out of the liver and is known to be $9.9 \pm 0.9\text{x}10^4\text{mlh}^{-1}$ [63]. Rate of influx and outflow of phenylalanine concentration in the liver was calculated from this. Compensating for the volume change between the two compartments gives:

$$k_{IN} = \frac{9.9\text{x}10^4}{V_S} = 42.4 \pm 4.0\text{h}^{-1},$$
$$k_{OUT} = \frac{9.9\text{x}10^4}{V_l} = 297 \pm 28\text{h}^{-1}.$$

As natural protein degradation occurs in both compartments, v_{NPD} remains unchanged from the one compartment model at 0.012mMh^{-1}. Published values for V_m^P and V_m^T are obtained by considering the initial rate of metabolism after a loading test based on metabolism occurring throughout systemic circulation. When considering metabolism to occur in the liver, we adjust the maximum rates of hydroxylation and transamination based on the volume change to obtain:

$$V_m^P = \frac{V_l}{V_l + V_S} V_{m_l}^P, \quad V_m^T = \frac{V_l}{V_l + V_S} V_{m_l}^T.$$

Using the volumes obtained earlier in the section, the maximum rate of metabolism for hydroxylation and transamination in the liver compartment are 8 times higher than in the single compartment model

$$V_{m_l}^T = 0.504 \pm 0.018\text{mMh}^{-1} \quad \text{and} \quad V_{m_l}^P \in [0, 7.2]\,\text{mMh}^{-1},$$

where $V_{m_l}^P$ depends on the severity of PKU.

Using these parameters, the model behaviour for non-PKU, moderate PKU and classic PKU patients is shown in Figure 3-11 for the two compartment model. This shows that both the

systemic and liver concentrations decrease over time towards a steady state. The rate of decrease is lower in patients with severe PKU compared to those without PKU. The systemic and the liver compartment have very similar concentrations in each case with the systemic concentration being slightly higher than the liver throughout.

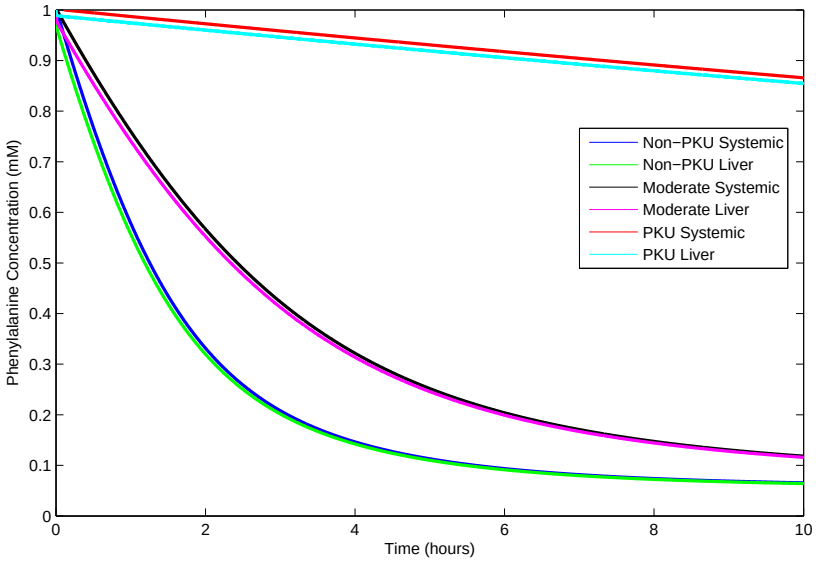

Figure 3-11: Two compartment model for blood serum phenylalanine concentration using parameters obtained from the literature or adapted from the one compartment model.

Steady state analysis

At steady state, equations (3.8) and (3.9) become:

$$\begin{aligned} 0 &= -k_{IN}P_S + \alpha k_{OUT}P_l + v_{NPD} \\ &= -k_{IN}P_S + k_{IN}P_l + v_{NPD}, \end{aligned} \tag{3.10}$$

$$\begin{aligned} 0 &= \frac{1}{\alpha}k_{IN}P_S - k_{OUT}P_l - \frac{V_{m_l}^P P_l^2}{P_l^2 + K_{m_l}P_l + K_{m_l}K_{a_l}} - \frac{V_{m_l}^T P_l}{P_l + K_{T_l}} + v_{NPD} \\ &= k_{OUT}P_S - k_{OUT}P_l - \frac{V_{m_l}^P P_l^2}{P_l^2 + K_{m_l}P_l + K_{m_l}K_{a_l}} - \frac{V_{m_l}^T P_l}{P_l + K_{T_l}} + v_{NPD}. \end{aligned} \tag{3.11}$$

Substituting for P_S into equation (3.11), we determine that:

$$h(P_l) = -\frac{V_{m_l}^P P_l^2}{P_l^2 + K_{m_l} P_l + K_{m_l} K_{a_l}} - \frac{V_{m_l}^T P_l}{P_l + K_{T_l}} + \frac{\alpha + 1}{\alpha} v_{NPD} = 0.$$

The steady state for P_l is determined by the cubic equation

$$\alpha_2 P_l^3 + \beta_2 P_l^2 + \gamma_2 P_l + \delta_2 = 0,$$

where:

$$\begin{aligned}
\alpha_2 &= \frac{(\alpha+1)}{\alpha} v_{NPD} - V_{m_l}^P - V_{max_l}^T, \\
\beta_2 &= (K_{m_l} + K_{T_l}) \frac{(\alpha+1)}{\alpha} v_{NPD} - K_{T_l} V_{m_l}^P - K_{m_l} V_{m_l}^T, \\
\gamma_2 &= (K_{m_l} K_{T_l} + K_{m_l} K_{a_l}) \frac{(\alpha+1)}{\alpha} v_{NPD} - K_{m_l} K_{a_l} V_{m_l}^T, \\
\delta_2 &= \frac{(\alpha+1)}{\alpha} K_{m_l} K_{a_l} K_{T_l} v_{NPD}.
\end{aligned}$$

As with the single compartment model, since $\delta_2 > 0$ and provided $\alpha_2 < 0$, at least one positive non-trivial steady state exists for P_l with:

$$P_S = P_l + \frac{v_{NPD}}{k_{IN}} > 0.$$

Moreover, $h(P_l)$ is monotonically decreasing for $P_l \geq 0$ since:

$$\begin{aligned}
h'(P_l) &= -\frac{V_{m_l}^P P_l K_{m_l} (P_l + 2K_{a_l})}{(P_l^2 + K_{m_l} P_l + K_m K_a)^2} - \frac{V_{m_l}^T K_T}{(P + K_T)^2}, \\
&< 0.
\end{aligned}$$

Since $h(0) > 0$ and given that $h(P_l)$ is monotonically decreasing for $P_l \geq 0$, as all parameters

in $h'(P_l)$ are positive. This means that $h'(P_l) < 0 \ \forall P_l \geq 0$. Considering that $h(P_l)$ is monotonically decreasing combined with

$$\begin{aligned}\lim_{P_l \to \infty} h(P_l) = \frac{\mathrm{d}P_l}{\mathrm{d}t} &\to \frac{\alpha+1}{\alpha} v_{NPD} - \left(V_{m_l}^P + V_{m_l}^T\right), \\ &= \frac{\alpha+1}{\alpha}\left(v_{NPD} - V_{m_l}^{P_l} - V_{m_l}^T\right).\end{aligned}$$

Then provided, as in the single compartment case, $v_{NPD} < V_m^P + V_m^T$ the single non-trivial steady state exists. Figure 3-12 demonstrates this behaviour using the parameters obtained in section 3.4.3 for a normal patient.

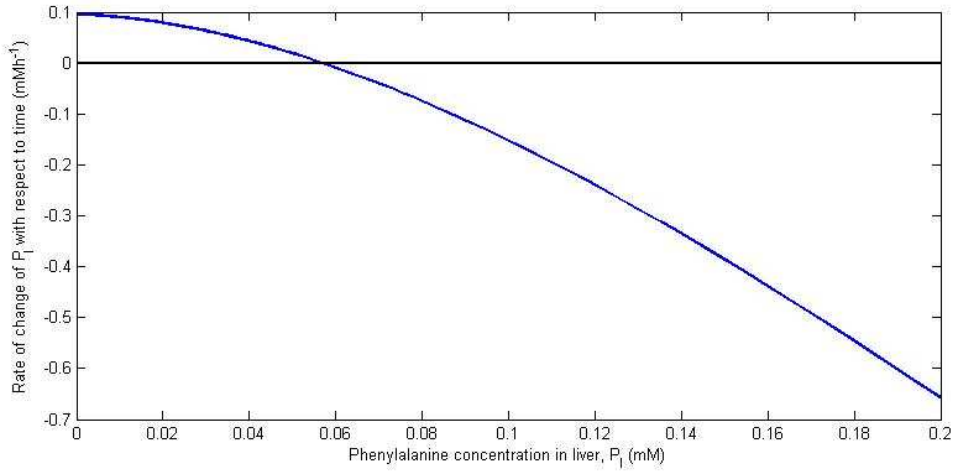

Figure 3-12: Rate of change of P_l against P_l. One crossing point exists showing the location of the steady state.

Using the parameters given in section 3.4.3 for a normal patient only one physiologically realistic - real and non-negative - steady state, $\mathbf{P}^*$, exists at

$$\mathbf{P}^* = \begin{pmatrix} P_S^* \\ P_l^* \end{pmatrix} = \begin{pmatrix} 0.0569 \\ 0.0566 \end{pmatrix} \pm \begin{pmatrix} 0.0070 \\ 0.0070 \end{pmatrix} \text{mM},$$

with the liver concentration being slightly lower than the systemic concentration. The systemic concentration is comparable to that obtained experimentally [10]. For a patient with classic PKU, $V_{m_l}^P = 0$, only one physiologically realistic steady state exists at $P_s^* \approx P_l^* = 0.32\text{mM}$, which is also comparable to experimentally obtained results [10].

Stability of the steady state As the system is two-dimensional, we use the Routh-Hurwitz criterion to evaluate the stability of steady states of the system. The Jacobian matrix is:

$$J(\mathbf{P}^*) = \begin{pmatrix} -k_{IN} & k_{OUT}\frac{V_l}{V_S} \\ k_{IN}\frac{V_S}{V_l} & -k_{OUT} - \frac{V_{m_l}^T K_{T_l}}{\left(P_l^* + K_{T_l}\right)^2} - \frac{V_{m_l}^P \left(K_{m_l} P_l^* + 2K_{m_l} K_{a_l}\right) P_l^*}{\left(P_l^{*2} + K_{m_l} P_l^* + K_{m_l} K_{a_l}\right)^2} \end{pmatrix}.$$

Now

$$\mathrm{tr}(J) = -k_{IN} - k_{OUT} - \frac{V_{m_l}^T K_{T_l}}{\left(P_l^* + K_{T_l}\right)^2} - \frac{V_{m_l}^P \left(K_{m_l} P_l^* + 2K_{m_l} K_{a_l}\right) P_l^*}{\left(P_l^{*2} + K_{m_l} P_l^* + K_{m_l} K_{a_l}\right)^2} < 0 \quad \text{for} \quad P_l \geq 0,$$

and

$$\begin{aligned} \det(J) &= k_{IN} k_{OUT} + k_{IN} \frac{V_{m_l}^T K_{T_l}}{\left(P_l^* + K_{T_l}\right)^2} + k_{IN} \frac{V_{m_l}^P \left(k_{m_l} P_l^* + 2K_{m_l} K_{a_l}\right) P_l^*}{\left(P_l^{*2} + K_{m_l} P_l^* + K_{m_l} K_{a_l}\right)^2} - k_{IN} k_{OUT}, \\ &= \frac{k_{IN} V_{m_l}^T K_{T_l}}{\left(P_l^* + K_{T_l}\right)^2} + \frac{k_{IN} V_{m_l}^P \left(K_{m_l} P_l^* + 2K_{m_l} K_{a_l}\right) P_l^*}{\left(P_l^{*2} + K_{m_l} P_l^* + K_{m_l} K_{a_l}\right)^2} > 0 \quad \text{for} \quad P_l \geq 0. \end{aligned}$$

Hence the steady state is locally stable.

Resilience Resilience in the two compartment model is determined using the characteristic equation

$$\begin{aligned} 0 &= \det(J - \lambda I), \\ &= \lambda^2 + \beta_3 \lambda + \gamma_3, \end{aligned}$$

where J is the Jacobian matrix, λ is an eigenvalue with constants:

$$\beta_3 = -\mathrm{tr}J > 0,$$
$$\gamma_3 = \det J > 0.$$

Resilience is defined by considering the eigenvalue of J with the largest real part, $\lambda_1(J)$. In Figure 3-13 shows the resilience over the normally found range of $V^P_{m_l}$.

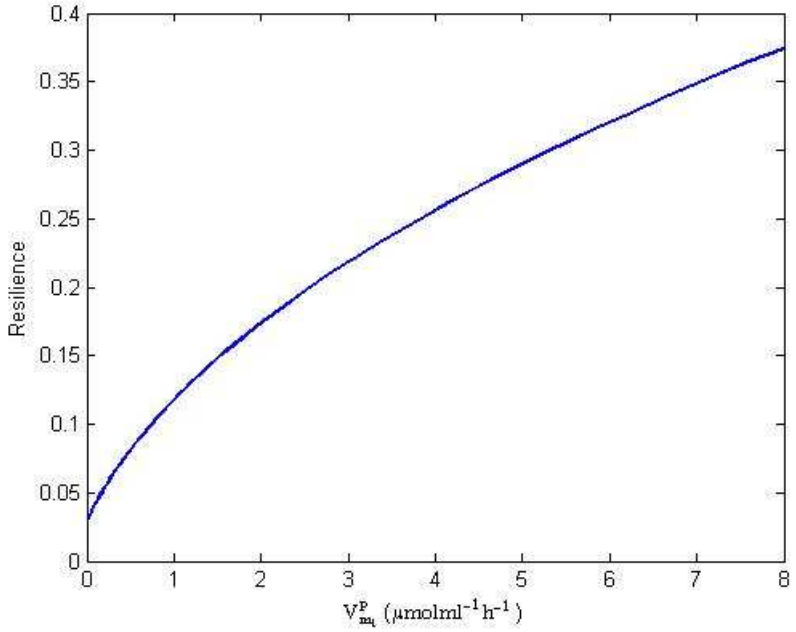

Figure 3-13: Resilience as a function of $V^P_{m_l}$ over a physiologically expected range. $V^P_{m_l}$ in a patient without PKU is 7.2μmolml^{-1}h^{-1}.

The behaviour of resilience suggests that patients with classic PKU, corresponding to very low $V^P_{m_l}$, take longer to reach the steady state after a perturbation than normal patients. This behaviour is the same as the single compartment model.

Reactivity The Hermitian matrix for the two compartment model is:

$$H(J) = \frac{A + A^T}{2} = \begin{pmatrix} -k_{IN} & \frac{k_{OUT}\frac{V_l}{V_S} + k_{IN}\frac{V_S}{V_l}}{2} \\ \frac{k_{OUT}\frac{V_l}{V_S} + k_{IN}\frac{V_S}{V_l}}{2} & -k_{OUT} - \frac{V^T_{m_l}K_{T_l}}{\left(P^*_l + K_{T_l}\right)^2} - \frac{V^P_{m_l}\left(K_{m_l}P^*_l + 2K_{m_l}K_{a_l}\right)P^*_l}{\left(P^{*2}_l + K_{m_l}P^*_l + K_{m_l}K_{a_l}\right)^2} \end{pmatrix}.$$

with eigenvalues given by the characteristic equation

$$\lambda^2 + \beta_4 \lambda + \gamma_4 = 0,$$

where

$$\begin{aligned}
\beta_4 &= k_{IN} + k_{OUT} + \frac{V_{m_l}^T K_{T_l}}{\left(P_l^* + K_{T_l}\right)^2} + \frac{V_{m_l}^P \left(K_{m_l} P_l^* + 2K_{m_l} K_{a_l}\right) P_l^*}{\left(P_l^{*2} + K_{m_l} P_l^* + K_{m_l} K_{a_l}\right)^2}, \\
\gamma_4 &= \frac{-1}{4}\left(k_{OUT}^2 \frac{V_l^2}{V_S^2} - 2k_{OUT} k_{IN} + k_{IN} \frac{V_S^2}{V_l^2}\right) \\
&\quad + k_{IN}\left(\frac{V_{m_l}^T K_{T_l}}{\left(P_l^* + K_{T_l}\right)^2} + \frac{V_{m_l}^P \left(K_{m_l} P_l^* + 2K_{m_l} K_{a_l}\right) P_l^*}{\left(P_l^{*2} + K_{m_l} P_l^* + K_{m_l} K_{a_l}\right)^2}\right).
\end{aligned}$$

Figure 3-14 shows how these eigenvalues vary with $V_{m_l}^P$ and indicate that the two compartment model is not reactive as the largest eigenvalue of the Hermitian matrix is negative.

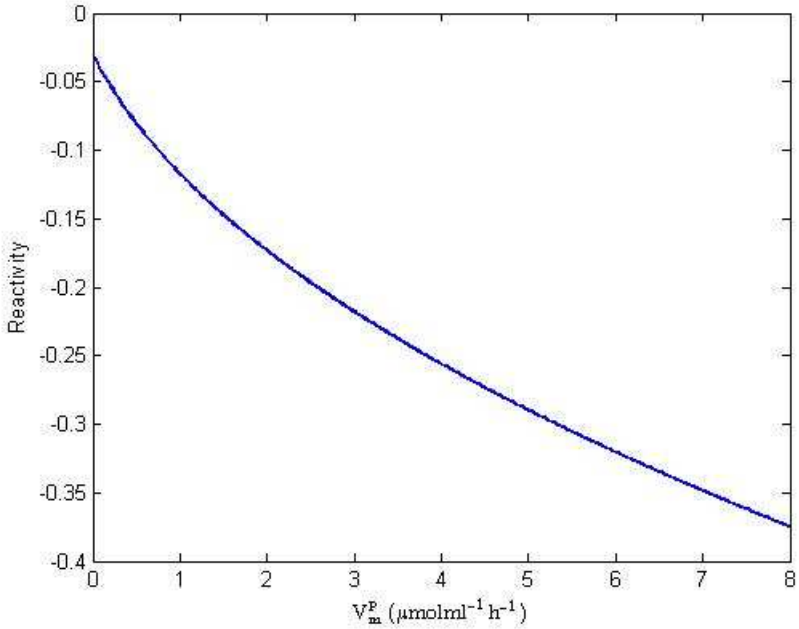

Figure 3-14: Reactivity, calculated by considering the largest eigenvalue of the Hermitian matrix of J.

3.4.4 Comparison of the one and two compartment systemic model

The derivation of the relationship between V_m^P and $V_{m_l}^P$ ensures that both the single compartment and two compartment approach attain equivalent steady states as show in Figures 3-15 and 3-16. Figure 3-15 also shows that the behaviour of both models under loading tests produce similar decay patterns. This is likely due to the transport between the stomach and the systemic system in the two compartment model being rapid and hence well mirrored by the single compartment system.

Both models also have the same conditions for a steady state to exist, namely:

$$V_m^P + V_m^T > v_{NPD}.$$

However, there are some noticeable differences between these two models. In the single compartment model, resilience is linearly related to V_m^P at large times whereas the two compartment model tends asymptotically to a limit. This effect is only noticeable at large values of V_m^P and is similar for both models over physiologically realistic ranges, so is unlikely to have a clinical effect. Over the range of V_m^P found in humans with and without PKU, the single compartment model has much higher resilience. This means that the single compartment model will return to the steady state faster after a small perturbation. From a clinical standpoint, this means that considering metabolism throughout the body, rather than in the just the liver, may lead to the model predicting faster declines of systemic phenylalanine concentration than are actually observed.

Reactivity is not observed in either the one or two-compartment models. Hence, neither model predicts that any perturbation will initially increase in magnitude before returning the steady state.

3.5 Intake of food into the systemic model

The models presented up until this point have only considered patients in a fasting state to allow comparisons to loading tests. Since we are interested in build up and maintenance of phenylalanine levels over time, we extend the work to consider regular food intake.

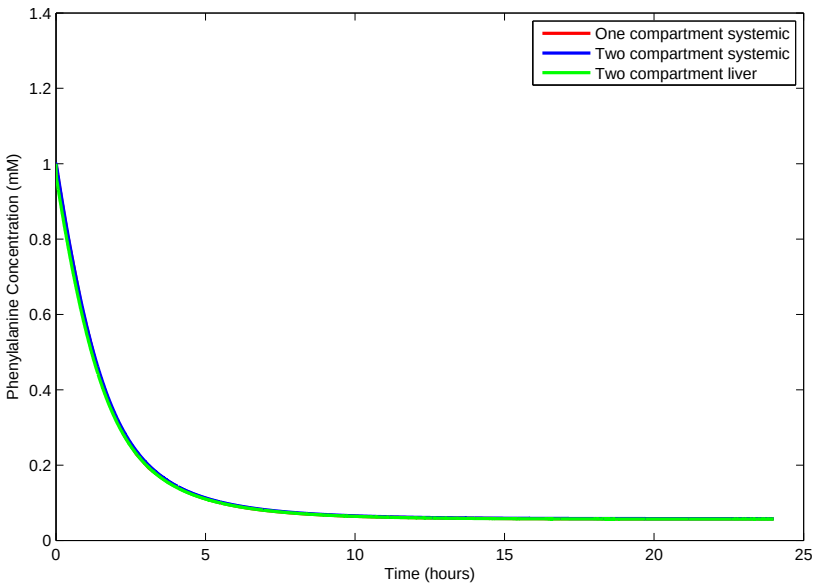

Figure 3-15: Comparison between the one and two compartment models.

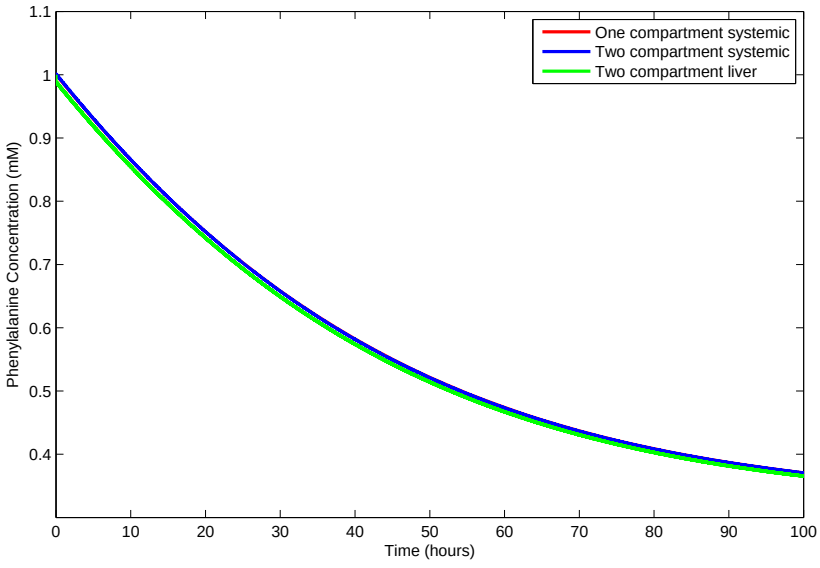

Figure 3-16: Comparison between the one and two compartment models.

3.5.1 Previous food intake model using the Bateman function for food intake

Previous work [11] considered blood serum phenylalanine levels in patients not in a fasting state using the Bateman function for food intake from the stomach. The structure of this model is shown in Figure 3-17.

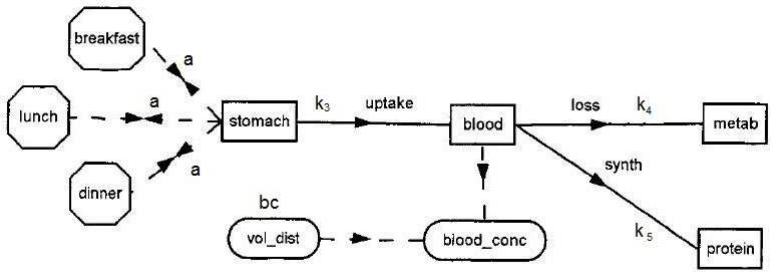

Figure 3-17: Structure of a systemic phenylalanine model that includes food intake of 3 meals per day. Adapted from [11] by removing the model label and changing the parameter labels to be consistent with this work.

The resulting differential equation governing concentration of phenylalanine in the blood, $P(t)$, with a single dose of amount a is given by

$$\frac{\mathrm{d}P}{\mathrm{d}t}(t) = \frac{a}{bc}k_3 e^{-k_3 t} - k_4 P(t) - \frac{k_5}{c},$$

where the dose is considered to be evenly distributed throughout total body water calculated using body weight, b, multiplied by percentage water, c. First order rate constants were used to model rate of resorption from the stomach, k_3, and rate of phenylalanine conversion into tyrosine, k_4, with rate of protein synthesis, k_5, considered as a zero-order term. This has exact solution [11]:

$$P(t) = P_0 e^{-k_4 t} + \frac{ak_3}{bc\,(k_3 - k_4)}\left(e^{-k_4 t} - e^{-k_3 t}\right) + \frac{k_5}{ck_4}\left(e^{-k_4 t} - 1\right).$$

A constant input rate from the stomach, a_c, was also considered for multiple doses resulting in the model equation:

$$\frac{\mathrm{d}P}{\mathrm{d}t}(t) = \frac{a_c}{bc} - k_4 P(t) - \frac{k_5}{c}.$$

The solution in both cases exhibits non-oscillatory behaviour increasing monotonically to the steady state, and an increase in the steady state blood concentration compared to a fasting state model.

The model presented in [11] was able to mimic data from a selection of classic PKU sufferers and presented a good method for dealing with food intake throughout the day. Moreover, it raised the need to consider protein synthesis in a non-fasting state model as well as confirming that the volume of distribution for phenylalanine was over total body water.

However, the model did not include the transamination and hydroxylation pathway seperately, and considered both as a single stage process, ignoring the activation behaviour of the hydroxylation pathway.

3.5.2 Food intake systemic model - Single compartment

To model phenylalanine concentration in blood serum in a non-fasting state, the single compartment fasting state model in section 3.4.2 was extended to include food intake via a Bateman function. This is displayed diagrammatically in Figure 3-18. The volume of distribution for phenylalanine, V, was considered to be total body water volume. This resulted in the modified model equation:

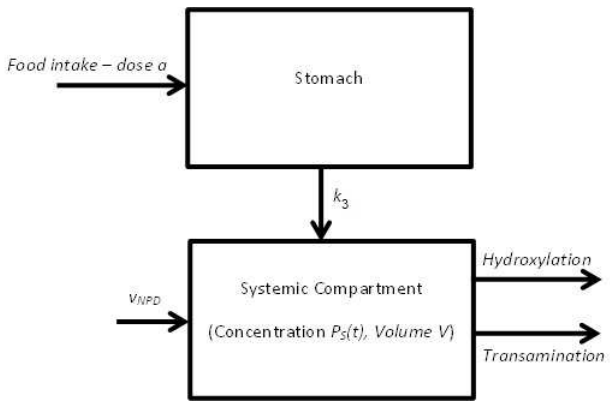

Figure 3-18: Structure of single compartment systemic phenylalanine model that includes food intake. The stomach compartment is listed but the concentration not modelled. This is similar to the model given in Figure 3-17 [11], but additionally includes the activation behaviour of the hydroxylation pathway.

$$\frac{\mathrm{d}P}{\mathrm{d}t} = -\frac{V_m^P}{1+\frac{K_m}{P}+\frac{K_m K_a}{P^2}} - \frac{V_m^T}{1+\frac{K_T}{P}} + v_{NPD} + \frac{1}{V}k_3 e^{-k_3 t}\sum_{n=1}^{N(t)} a_n e^{k_3 n\tau} H(t-n\tau). \qquad (3.12)$$

To demonstrate the model behaviour we assume that 3 meals are consumed equally spaced over 24 hours. The first order absorption rate from the stomach was $k_3 = 1\mathrm{h}^{-1}$ [11].

As discussed in section 3.3.3, we consider a European man at average height and ideal body weight [58, 61, 62] initially and then extend this to a range later in this chapter. For an individual of 70.5kg we take TBW=40L, and assume that 137mg of phenylalanine per kg of bodyweight is consumed at each meal, corresponding to a total 9612mg/day.

Figure 3-19 shows the model behaviour under these conditions using all other model parameters from table 3.2.

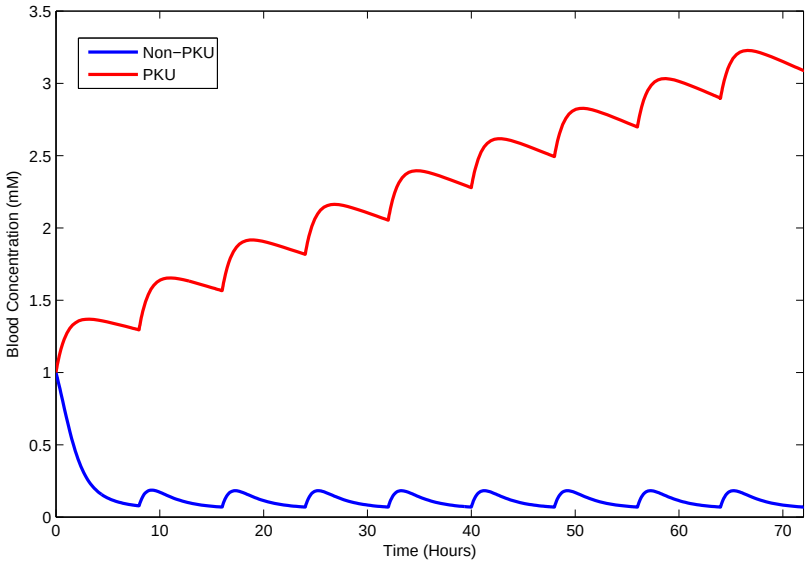

Figure 3-19: Numerical solution of the single compartment systemic model with food intake for patients with classic and no PKU.

Whilst a patient without PKU maintains stable phenylalanine concentrations within a small window, $[0.069, 0.182]$mM, the PKU suffering patient has an unbounded increase in phenylalanine concentration under these conditions.

This behaviour is supported by considering food intake at an average rate over time, $0.0558\mathrm{mMh}^{-1}$ under the current diet, and evaluating equation (3.12) with the food intake term replaced

with constant infusion rate a_c

$$\frac{\mathrm{d}P}{\mathrm{d}t} = -\frac{V_m^P}{1+\frac{K_m}{P}+\frac{K_m K_a}{P^2}} - \frac{V_m^T}{1+\frac{K_T}{P}} + v_{NPD} + a_c, \tag{3.13}$$

as $P(t) \to \infty$ when $V_m^P = 0$, corresponding to severe PKU. This results in

$$\begin{aligned}\lim_{P\to\infty} \frac{\mathrm{d}P}{\mathrm{d}t} &= -V_m^P - V_m^T + v_{NPD} + a_c, \\ &= -0 - 0.063 + 0.012 + 0.0558 > 0,\end{aligned}$$

indicating unbound growth. Unbound growth is unlikely to be observed in a realistic scenario and this level of overdosing would lead to serious medical complications such as nerve damage and seizures [68].

Recommendations propose that classic PKU sufferers should maintain intake below 20mgkg^{-1}day^{-1}, equivalent to 8.12μMh^{-1}. This intake gives rise to a positive steady state of 0.6428mM, and is still far higher than that for fasting state patient behaviour. The difference between the reduced diet behaviour and the normal diet behaviour in a PKU suffering patient is shown in Figure 3-20.

3.5.3 Food intake model - Two compartment

Incorporating food intake into the two compartment model gives rise to the system:

$$\begin{aligned}\frac{\mathrm{d}P_s}{\mathrm{d}t} &= -k_{IN}P_S + k_{OUT}P_l\frac{V_l}{V_S} + v_{NPD} + \frac{\beta}{V_S}ke^{-kt}\sum_{n=1}^{N} a_n e^{kn\tau}H(t-n\tau), \\ \frac{\mathrm{d}P_l}{\mathrm{d}t} &= k_{IN}P_S\frac{V_S}{V_l} - k_{OUT}P_l - \frac{V_{m_l}^P P_l^2}{P_l^2 + K_{m_l}P_l + K_{m_l}K_{a_l}} - \frac{V_{m_l}^T P_l}{P_l + K_{T_l}} + v_{NPD}.\end{aligned}$$

The two-compartment system is also represented diagrammatically in Figure 3-21. V_S represents the volume of distribution in serum, ie total body water volume, V, minus the volume of blood in the liver, V_l. Figure 3-22 shows the time profile for phenylalanine concentration

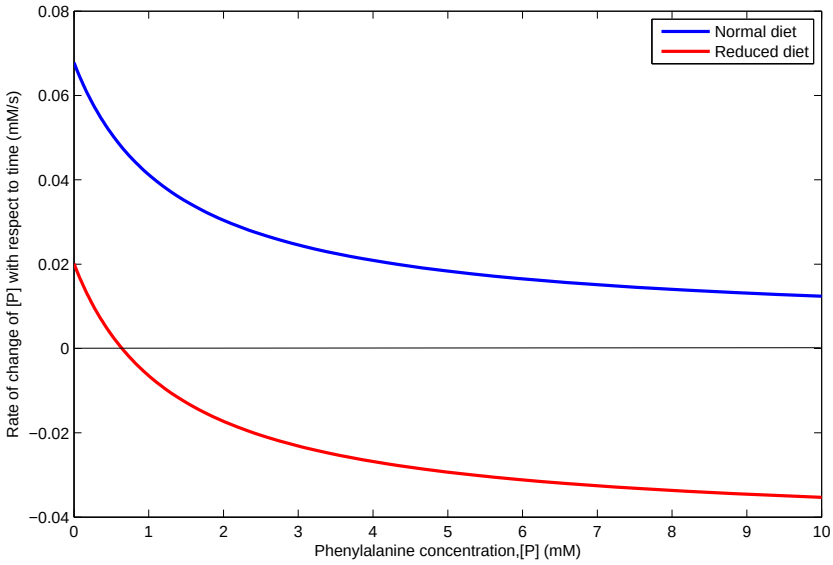

Figure 3-20: Effect of phenylalanine concentration on a rate of change of phenylalanine concentration in a patient with PKU with normal and reduced phenylalanine intake. This model uses equation (3.13).

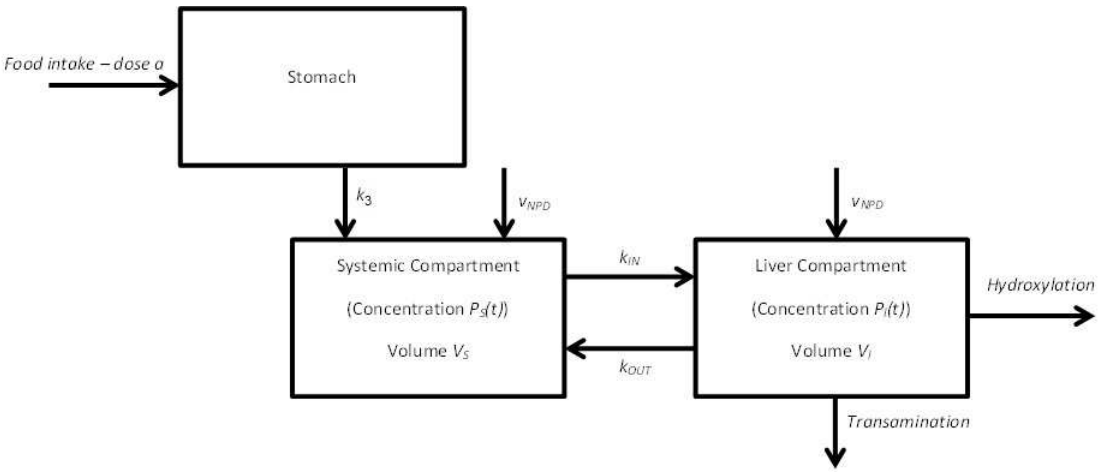

Figure 3-21: Diagrammatic model of food intake in a two compartment model.

using parameters given in table 3.1

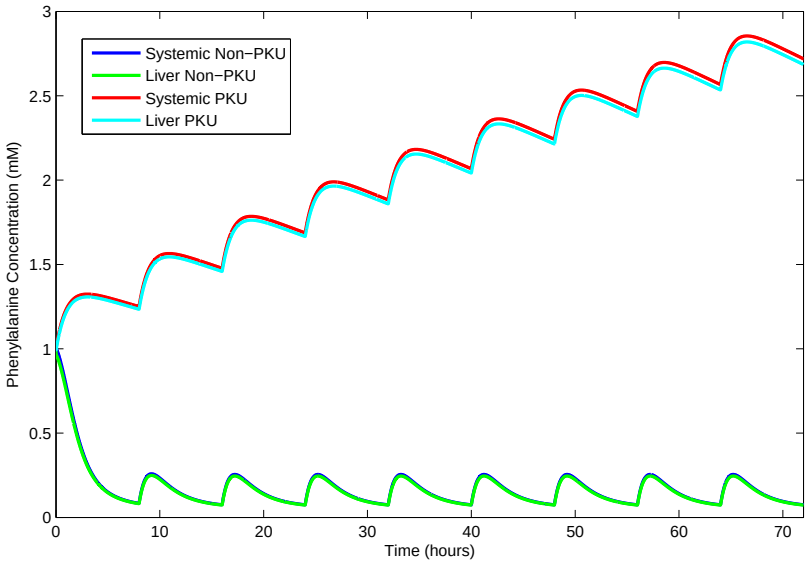

Figure 3-22: Numerical solution of the two compartment systemic model with food intake for patients with classic and no PKU.

Using the two compartment model for food intake results in non-PKU suffering patients having an phenylalanine concentration in the blood in the range [0.075mM, 0.255mM] with liver concentration being just below this. Patients suffering from classic PKU have phenylalanine concentration in both the blood and liver increasing unbounded, much like the single compartment model for food intake in section 3.5.2. Using the recommended dosage for a PKU patient, the steady state for PKU suffering patients was found to be 0.598mM for the blood and slightly lower for the liver.

The minima and maxima for the two compartment model for non-PKU patients is higher than for the single compartment model and the steady state lower for patients suffering from PKU under recommended food intake, although both show similar behaviour.

3.5.4 Varying food intake

Up until this point, food intake was considered based on a trial man at average height and ideal bodyweight with a balanced diet resulting in a total body water volume of 40L and a daily intake of 9658mg/day. This corresponds to an intake of 241 mg/L of total body water.

Figure 3-23 considers a range of intakes per L of total body water, namely 50, 150, 250 and

350 mg/L, using the single compartment food intake model. This demonstrates that a greater intake of phenylalanine per litre of total body water causes larger oscillations, as would be expected. Figure 3-23 also demonstrates that lower phenylalanine intakes in patients with PKU leads to a steady state being reached but this takes a very long time. Additionally, it is worth noting that 50mg/L of bodyweight corresponds to 28mg/kg of bodyweight which is just above the recommended maximum intake of 20mg/kg for a severe PKU suffering patient.

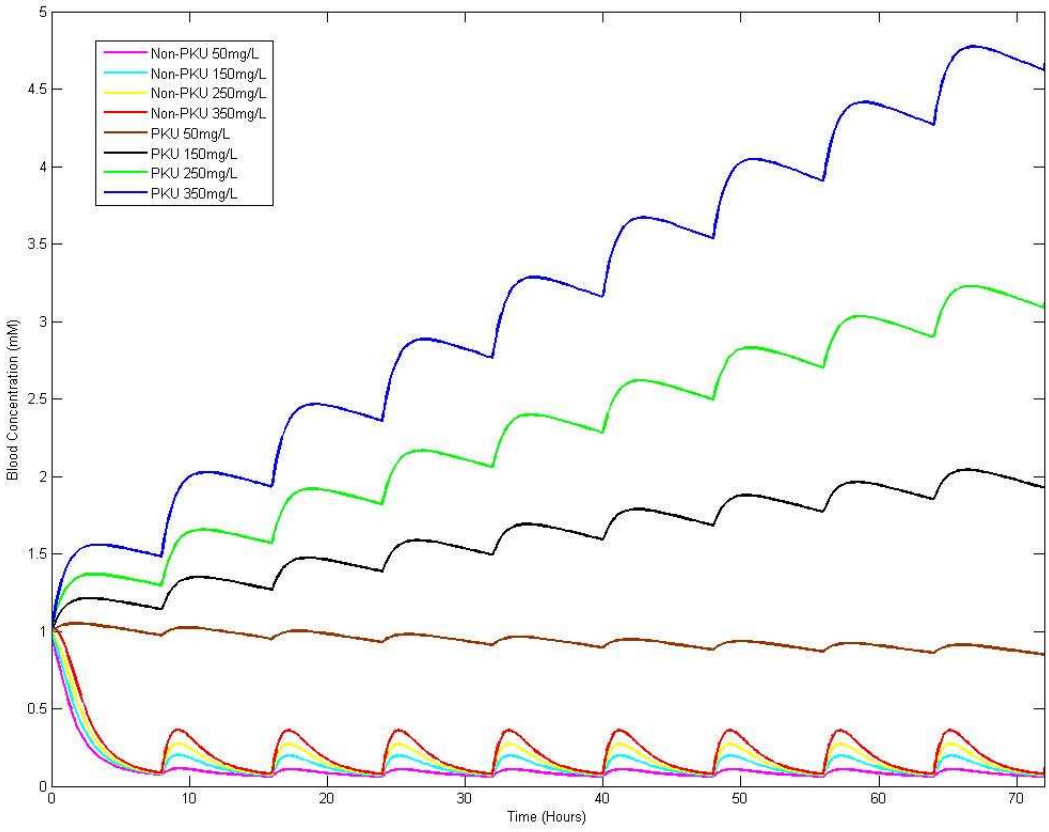

Figure 3-23: Numerical solution of the single compartment model for both PKU suffering and non-PKU suffering patients under a variety of food intakes.

3.6 Chapter Summary

The objective of this chapter was to model the systemic distribution of phenylalanine in the body for later input into a model for distribution of phenylalanine in the skin. Fasting state and food intake models for both PKU suffering and non-PKU suffering patients were considered as well as single compartment and multiple compartment approaches to the body.

For the fasting state model, in line with prior work [10], phenylalanine was considered to be generated via natural protein degradation at a constant rate and metabolised via two pathways, transamination and hydroxylation. Hydroxylation is catalysed by phenylalanine hydroxylase, the enzyme altered by PKU, and transamination is catalysed by phenylalanine transaminase, which is unaffected by PKU. Prior work [10] considered the hydroxylation pathway to operate via a two site ordered binding model in order to model the activation of phenylalanine hydroxylase. We considered the effect of the activation term on the model and found that it was significant when considering the dynamics of phenylalanine. Having done this, we also considered the effect of the transamination route and showed that it was not significant for normal patients, but became more significant with increasing severity of PKU.

Having investigated the terms in the fasting state model, the existence and behaviour of steady states were considered. For a physiologically realistic stable steady state to exist the creation of phenylalanine must be less than its removal, $v_{NPD} < V_m^P + V_m^T$, which, considering realistic parameters, is true for all normal and PKU suffering patients and again demonstrates the importance of the transamination term for severe PKU patients where $V_m^P \to 0$.

As we intended to add food intake into the model, resilience and reactivity of the fasting state model was considered. This showed that a perturbation to the system at steady state did not initially increase in magnitude, but returned monotonically to the steady state. The rate of return was approximately linearly dependent on V_m^P with higher V_m^P causing a faster rate of return.

The final consideration for the fasting state model was to consider the effect of liver-only metabolism on the system as phenylalanine hydroxylase is only active in the liver [67]. This was modelled using a time dependent two-compartment approach. Both the one and two compartment approach had almost identical behaviour in the fasting state under a loading test and identical steady state conditions. Neither model demonstrated reactive behaviour.

Both the one and two compartment approach were considered when adding food intake. Food intake was considered by adding a Bateman function to the systemic compartment in order to compensate for movement of phenylalanine from the stomach to the blood [11]. For test purposes, phenylalanine intake was initially based upon a UK male at average height and bodyweight with a balanced diet [58, 61, 62] having 3 evenly spaced meals with equal doses of phenylalanine. In this case, Figures 3-19 and 3-22 both show an unbounded increase in serum phenylalanine concentration for PKU patients with food intake of 137mg/kg of body weight per meal and oscillatory behaviour for non-PKU suffering patients.

Figure 3-23 considers a range of food intakes and, critically, shows that a controlled diet in

patients with PKU does not cause an unbounded increase in serum phenylalanine concentrations.

There is currently no experimental work measuring systemic phenylalanine concentration in non-fasting patients to compare the results of either model to, hence it is difficult to say which is most appropriate for use. The only visible difference between the one and two compartment approach for the trial patient is the magnitude of oscillation under food intake. The magnitude change is small, changing from 0.133mM to 0.188mM in the case of a normal patient, hence we decide to use the one compartment model to model blood phenylalanine concentration in later chapters as adding the additional complexity of the two compartment does not make it much more accurate.

The model could be improved by investigating the effect of food intake on protein degradation and synthesis, as this could change the value of v_{NPD}. Previous work on modelling phenylalanine in a non-fasting state [11] suggested that protein synthesis outweighed degradation and caused an overall drop in systemic phenylalanine levels, rather than an increase in the fasting state [10]. However, the non-fasting model selected parameters to fit a very specific set of data, so in order to get a better parameter prediction, consideration of background theory into protein formation and catabolism is required.

Chapter 4

Stratum Corneum Profile of Phenylalanine

4.1 Chapter Objective

Based on the work into systemic concentration of amino acids, specifically phenylalanine, we now consider the distribution of phenylalanine in the skin. The objective of this section will be to produce a time and spatially dependent profile of phenylalanine in the skin based on systemic concentration in a non-fasting state. We consider the effect that different systemic levels have on phenylalanine concentration in the skin and if variation from food intake has a noticeable effect on the skin reservoir.

In this chapter, we also investigate the effect of considering the stratum corneum to be split into the stratum corneum and stratum disjunctum. The stratum disjunctum represents layers of the stratum corneum that have started to separate from the lipid matrix. We test the validity of the model by comparing the predictions to *in vivo* and *in vitro* data. We also use the model to consider another, similar amino acid, tyrosine.

4.2 Parameter Summary

Table 4.1 summarises all the parameters and variables used in this chapter with their definitions and, where appropriate, values and ranges found in the literature. Where possible,

standard deviations are used however this is not given for many parameters. Parameters listed with source 'R' are found using regression analysis. This table is designed for reference.

Table 4.1: Table of trial parameters. Parameters listed with source 'R' are found using least squares regression analysis later in the paper.

Parameter	**Definition**	**Range**	**Value used**	**Sources**
L	Depth of the outer skin layers	[10,40]μm	20μm	[18]
d	Depth of the stratum disjunctum	[3.2,7.0]μm	6.67 μm	[1, 2]
v	Velocity of stratum corneum corneocytes towards the surface of the skin	[0.83,3.31]x10^{-11}ms^{-1}	1.65x10^{-11}ms^{-1}	[69]
k_1	Absorbtion rate of amino acids from the stomach	-	2.78x10^{-4}s^{-1}	[11]
k_2	Production rate in cells	0	0	R
k_3	Production rate in the intercellular space	[0.08,0.25]mmolm^{-3}s^{-1}	0.14mmolm^{-3}s^{-1}	R
v_{NPD}	Production rate of amino acid in the body	-	0.0033mmolm^{-3}s^{-1}	[10]
V_{m1}	Maximum rate of metabolism via hydroxylation	-	0.25mmolm^{-3}s^{-1}	[10]
V_{m2}	Maximum rate of metabolism via transamination	-	0.0175mmolm^{-3}s^{-1}	[10]
K_m	Dissocation constant for hydroxylation	-	0.51mM	[10]
K_a	Activation constant	-	0.54mM	[10]
K_T	Dissocation constant for transamination	[1.23,1.51]mM	1.37mM	[10]
B	Fraction of blood serum that is water	-	90%	[10]
a	Dose into the body	-	1.93x10^3mmol	[58]
τ	Dosing interval	-	8h	-
D	Diffusion coefficient	-	m^{2}s^{-1}	-
D_1	Diffusion coefficient of phenylalanine in the intercellular space	[4.46,17.82]x10^{-15}m^{2}s^{-1}	8.91x10^{-15}m^{2}s^{-1}	[34, 70]
D_2	Diffusion coefficient of tyrosine in the intercellular space	[4.46,17.82]x10^{-15}m^{2}s^{-1}	8.91x10^{-15}m^{2}s^{-1}	[34, 70]
λ	Removal rate of cells from the stratum disjunctum	-	2.76x10^{-6}s^{-1}	[18, 69, 71]
σ	Removal rate in the stratum disjunctum	[0.58,3.25]m^{-1}s^{-1}	1.54m^{-1}s^{-1}	R
p_e	Packing fraction in the viable epidermis	-	80.6%	[72]

p	Packing fraction in the stratum corneum	91.6±23%	91.6%	[71]
l_x	Length of stratum corneum corneocyte	40±0.4μm	40μm	[71]
l_y	Width of stratum corneum corneocyte	40±0.4μm	40μm	[71]
l_z	Depth of stratum corneum corneocyte	0.8±0.08μm	0.8μm	[71]
l_{ps}	Depth of stratum corneum lipid layer	-	0.07μm	[71]
l_s	Side length of viable epidermis corneocyte	-	12.4μm	[72]
l_h	Height of viable epidermis corneocyte	-	23.0μm	[72]
l_p	Depth of viable epidermis lipids	-	1.0μm	[72]
A_{SC}	Cross sectional area of the stratum corneum unit cell	1605.6±226.7μm^2	1605.6μm^2	[71]
A_{VE}	Cross sectional area of the viable epidermis unit cell	-	495.8x10^{-12}m^2	[72]
h_{SC}	Height of stratum corneum unit cell	0.87±0.8x10^{-6}m	0.87x10^{-6}m	[71]
h_{VE}	Height of viable epidermis unit cell	-	24x10^{-6}m	[72]
V_{SC}	Volume of the stratum corneum unit cell	1396.9±235.3x10^{-18}m^3	1396.9x10^{-18}m^3	[71]
C_1	Systemic concentration of phenylalanine	-	mmolm^{-3}	-
C_2	Viable epidermis concentration of phenylalanine	-	mmolm^{-3}	-
C_3	Stratum corneum corneocytes concentration of phenylalanine	-	mmolm^{-3}	-
C_4	Stratum corneum intercellular space concentration of phenylalanine	-	mmolm^{-3}	-
C_5	Stratum disjunctum corneocytes concentration of phenylalanine	-	mmolm^{-3}	-
C_6	Stratum disjunctum intercellular space concentration of phenylalanine	-	mmolm^{-3}	-
V_1	Plasma volume	2.67±0.08x10^{-3}m^3	2.67x10^{-3}m^3	[59]
V_2	Volume of viable epidermis unit cell	-	1.19x10^{-14}m^3	[72]
V_3	Volume of a stratum corneum corneocyte	1.28±0.22x10^{-15}m^3	1.28^{-15}m^3	[71]
V_4	Volume of lipid around a stratum corneum corneocyte	1.17±4.57x10^{-16}m^3	1.17x10^{-16}m^3	[71]
V_5	Volume of a stratum disjunctum corneocyte	1.28±0.22x10^{-15}m^3	1.28^{-15}m^3	[71]
V_6	Volume of lipid around a stratum disjunctum corneocyte	1.17±4.57x10^{-16}m^3	1.17x10^{-16}m^3	[71]

$\mathbf{\Omega}$	Unknown parameter set - used in regression analysis	-	-	-
$T(x, \mathbf{\Omega})$	Total amount of amino acid per unit area	-	-	-
S	Standard error of the estimate	-	-	-

4.3 Background Biology

Prior work has shown that the rate limiting step for movement of all but small, highly lipophilic compounds through the skin is the stratum corneum [1, 2, 52]. Amino acids are not small, highly lipophilic compounds hence the stratum corneum is the rate limiting barrier to transport. In this section, we split the epidermis, described in section 1.4.2, into the viable epidermis, stratum corneum and stratum disjunctum and investigate the structure of each compartment including its unit cell, the packing fraction - the volume fraction occupied by corneocytes - and the velocity of cell movement. As discussed in section 1.4.2, there is no blood flow through the epidermis.

We also consider prior *in vivo* work into amino acid profiles through the stratum corneum.

4.3.1 Stratum Corneum

The stratum corneum is the outermost layer of the skin and is 10-40μm thick [18]. Figure 4-1 shows the stratum corneum in a brick and mortar type arrangement of corneocytes, forming the bricks, and an extended lipid bilayer structure, or lipid matrix, forming the mortar [18, 73].

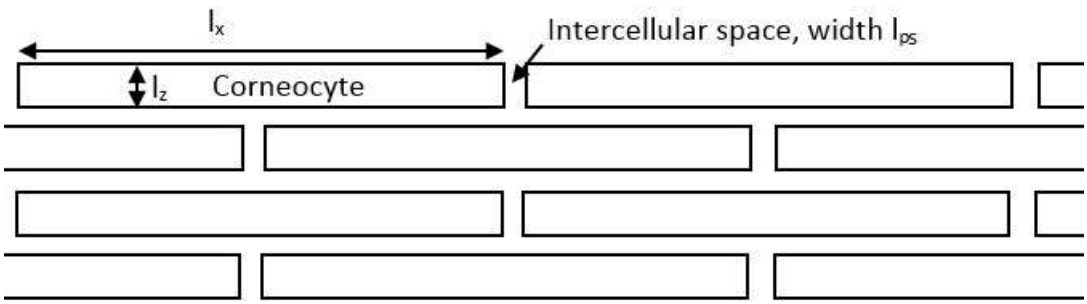

Figure 4-1: Brick and mortar arrangement of the stratum corneum. The measurements shown are: corneocyte length, l_x, corneocyte depth, l_z and intercellular space channel size, l_{ps}. We consider corneocytes to have equal length and width, $l_x = l_y$.

Corneocytes are keratinocyte cells in their final stage of cell differentiation. In the corneocyte stage, the cell has no nucleus or cytoplasmic organelles and are considered to be biologically 'dead' [22]. Corneocytes have a rigid outer layer and are interlocked via protein chains called corneodesmosomes. The permeability of corneocytes within intact stratum corneum is unknown with opinions varying between completely impermeable to highly permeable [73].

The lipid matrix between corneocytes is composed primarily of fatty acids, cholesterol and

sphingolipids [73]. These lipids form the skin natural moisturising factor which is important in maintaining the barrier properties of the skin and is key in the skin healing process [2].

The Unit Cell

Packing fraction in the stratum corneum was calculated by considering the dimensions of corneocytes and intercellular channels in a unit cell of the stratum corneum, shown in Figure 4-1, found in the literature [71]:

$$\begin{aligned} < l_x > = < l_y > &= 40\mu\text{m}, \sigma_{lx,ly} = 10\% \\ < l_z > &= 0.8\mu\text{m}, \sigma_{lz} = 10\% \\ l_{ps} &= 0.07\mu\text{m}. \end{aligned}$$

Using these values, stratum corneum corneocyte volume, V_3, is 1280±221.7μm^3 and the corresponding intercellular space volume around that corneocyte, V_4, is 117±457x10μm^3. Using Figure 4-1, we obtained the packing fraction of cells in the intercellular space by dividing the volume of a single corneocyte by the volume of a unit cell in this structure given by $(l_x + l_{ps})(l_y + l_{ps})(l_z + l_{ps})$. The packing fraction of cells is hence 0.92±0.23.

Cell Velocity

The stratum corneum is known to fully replenish every two weeks [69] with cells being pushed towards the surface of the skin by the formation of new cells. Using this replenishment rate and knowing stratum corneum depth is between 10-40μm, the velocity of the movement of skin towards the surface through the stratum corneum, v, can be calculated to be in the range 0.83-8.27x10^{-11}ms^{-1}.

4.3.2 Stratum Disjunctum

Cells are removed from the surface of the skin via a process called desquamation [74]. This process is still poorly understood [74] and can be affected by pathogens in the skin. This process occurs in the top few layers of the stratum corneum, known as the stratum disjunctum [75].

The stratum disjunctum has a similar structure to the stratum corneum. The main difference is that corneodesmosomes break down in this layer, resulting in whole cells being removed from this layer non-uniformly.

4.3.3 Viable Epidermis

The viable epidermis consists of the stratum basale, stratum spinosum and stratum granulosum. Although this is not the rate limiting band for transport through the viable epidermis for amino acids - the concentration in this compartment is still important to consider as it governs flow of compounds into the stratum corneum. These layers are described in more detail in section 1.4.2.

The Unit Cell

The structure of the viable epidermis varies through the skin. As the majority of the viable epidermis is the stratum spinosum, with the exact fraction depending on the area of the body considered, we consider this layer as a basis for the viable epidermis unit cell. In the stratum spinosum, keratinocytes are idealised as hexagonal prisms arranged in a hexagonal lattice with columns aligned vertically [72], as shown in Figure 4-2, with dimensions found in the literature [72]:

$$\begin{aligned} l_{\text{side}} &= 12.4\mu\text{m}, \\ l_{\text{height}} &= 23\mu\text{m}, \\ l_p &= 1.0\mu\text{m}. \end{aligned}$$

Using these dimensions, it is clear that the volume of the unit cell, V_2, is $1.19\text{x}10^{-14}\text{m}^3$. As each viable epidermis cell transitions into a single stratum corneum cell, the change from hexagonal structure to a brick and mortar type array is not considered to have any additional effects.

Velocity of Cells

As the volume of the stratum corneum is considered to be constant, the number of cells leaving the stratum corneum must be equal to the number of cells entering. It is known that

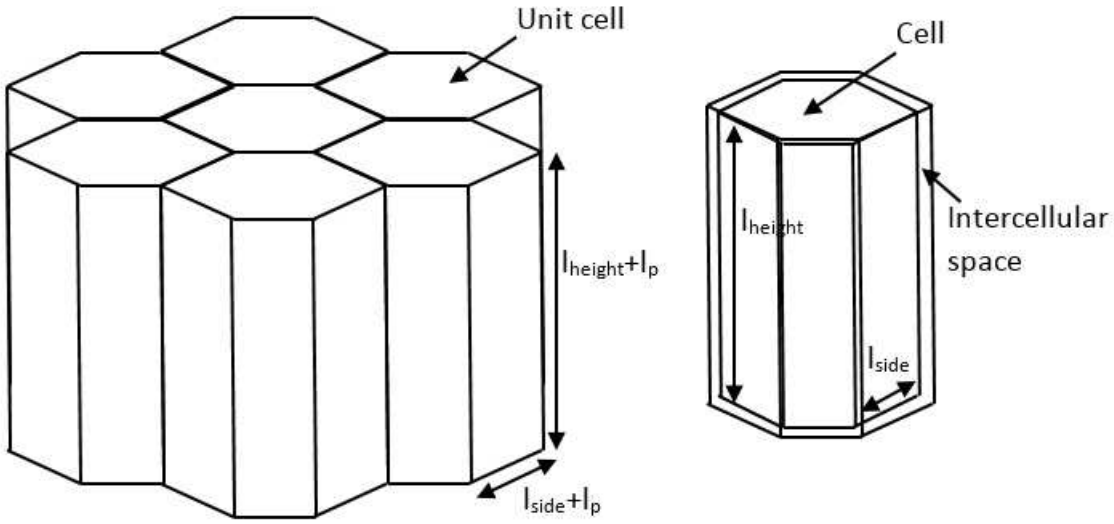

Figure 4-2: Viable epidermis unit cells organised in a lattice of hexagonal prisms, left, and a single unit cell consisting of one cell surrounded by intercellular space, right. The intercellular space is of thickness $^{l_p}/_2$ on all sides.

the number of cells pushed into the stratum disjunctum from the stratum corneum over a 1cm^2, or 10^{-4}m^2, surface area per second is

$$\text{Loss/second} = \frac{10^{-4}}{A_{SC}}.\frac{v}{h_{SC}},$$

where A_{SC} and h_{SC} are, respectively, the cross sectional area and height of the stratum corneum unit cell in m^2. Influx of cells behaves in much the same way

$$\text{Gain/second} = \frac{10^{-4}}{A_{VE}}.\frac{v_e}{h_{VE}},$$

where A_{VE} and h_{VE} are, respectively, the cross sectional area and height of the viable epidermis unit cell. Equating gain and loss and rearranging, we obtain the velocity of cells in the viable epidermis based on the velocity of corneocytes in the stratum corneum:

$$v_e = \frac{A_{VE}h_{VE}}{A_{SC}h_{SC}}v = \frac{V_2}{V_3 + V_4}v.$$

4.3.4 Potts and Guy Model

The Potts and Guy correlation presents a method of determining the diffusion coefficient, D, of compounds through the stratum corneum [34]

$$\log_{10}(k_p \text{cms}^{-1}) = -6.36(\pm 0.18) - 6.0(\pm 0.6)\text{x}10^{-3} MW + 0.74(\pm 0.07)\log_{10} k_{OW}, \qquad (4.1)$$

where MW is the molecular weight of the compound considered, k_{OW} is the octanol/water partition coefficient of the compound. k_p is the permeability coefficient based on the path length through the skin, δ, and the stratum corneum/water partition coefficient k_m:

$$k_p = \frac{k_m D}{\delta}.$$

The path length through the stratum corneum intercellular space, δ, is known to be in the range [500,880]μm [76] and the the stratum corneum/water partition coefficient, k_m, was approximated using the octanol/water partition coefficient.

Phenylalanine The molecular weight of phenylalanine is 165.18 [70] and $\log_{10} k_{OW} = -1.43$ [77]. Using the Potts and Guy correlation, the diffusion coefficient of phenylalanine in the stratum corneum intercellular space, D_1, is in the range [1.29,14.5]x10^{-15}m^{2}s^{-1}.

Tyrosine The molecular weight of tyrosine is 181.19 [70] and $\log_{10} k_{OW} = -2.26$ [77]. Using the Potts and Guy correlation, the diffusion coefficient of tyrosine in the stratum corneum intercellular space, D_2, is in the range [3.55,23.6]x10^{-13}m^{2}s^{-1}.

4.3.5 *In Vivo* Results

Previous work *in vivo* into transdermal extraction of amino acids using reverse iontophoresis and passive diffusion [2] has shown that there is a large reservoir of amino acids in the stratum corneum. This reservoir can take over 4 hours to clear and it is suggested that there is limited transport of amino acids from the viable epidermis to the stratum corneum over this time

period [1]. This makes it impractical to directly assess systemic concentrations of amino acids via transdermal extraction.

In vitro [1] and *in vivo* [2] experiments used tape stripping to assess reservoirs of amino acids in the skin. Tape stripping involves applying a length of tape to a fixed area of skin to remove exterior layers of the stratum corneum. The depth of the stratum corneum removed is calculated by weighing the amount extracted, using the area considered and the density of skin, 1gcm^{-3} [2]. The content of the sample is then assessed via a variety of methods. The results of tape stripping through the stratum corneum *in vivo* [2], shown in Figure 4-3, also suggested that amino acid levels through the stratum corneum have a non-constant spatial distribution. There appear to be concentration peaks within the stratum corneum rather than on its boundaries.

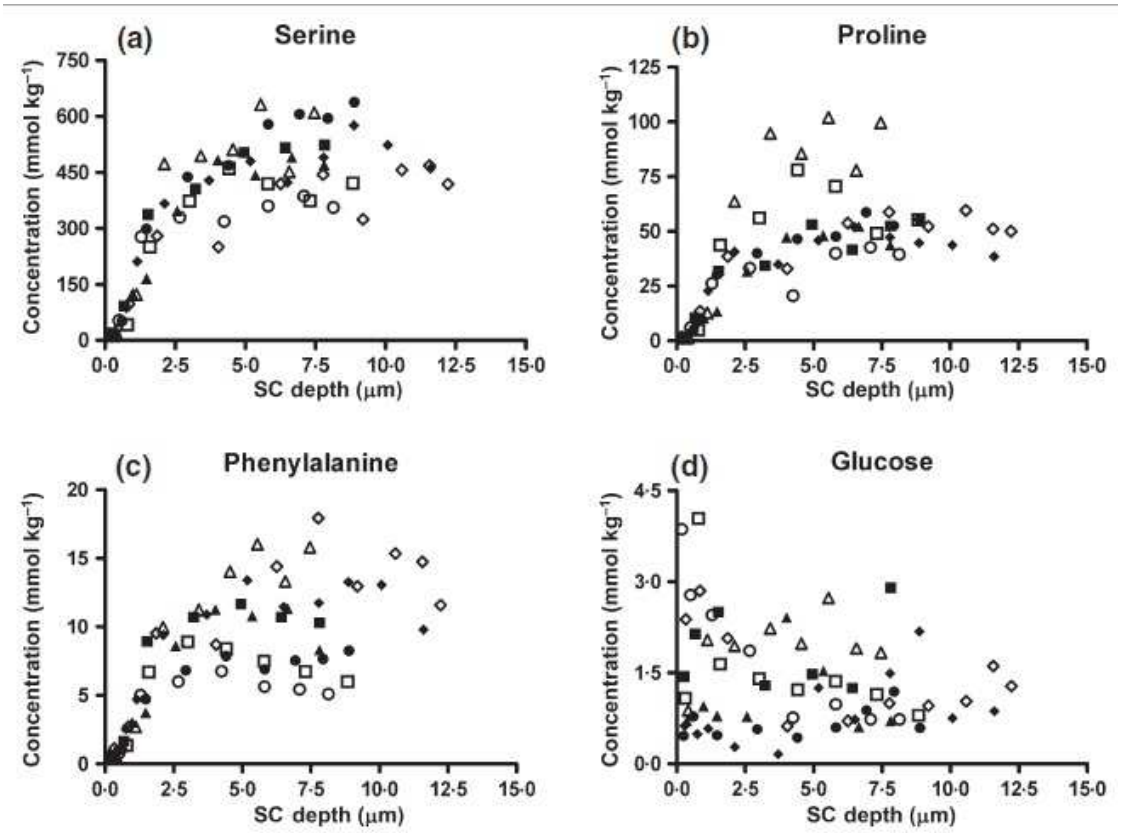

Figure 4-3: Experimental results for the spatial distribution of amino acids through human stratum corneum *in vivo* [2]. These results consider the top 75% of the stratum corneum which determined by measuring transepidermal water loss (TEWL) starting at the surface of the skin corresponding to SC depth = 0. Each different symbol represents a different patient. Taken from [2].

Reservoirs of amino acids obtained in [2] were larger than anticipated due to the production of amino acids, such as phenylalanine, in the skin [2]. This production is due to the irreversible

breakdown of proteins, such as filaggrin, to form the natural moisturising factor (NMF) in the skin [2]. NMF is important for maintaining the barrier properties of the skin and is key in the skin's healing process [78]. Due to the importance of NMF and future transdermal extraction methods, mathematically modelling amino acid distribution through the stratum corneum would be very useful.

Prior mathematical modelling work into amino acids is largely focussed on systemic distributions considering dosing via vectors such as food intake [15] and IV bolus [10]. Metabolism is considered using a variety of enzyme kinetic techniques [64] such as Michaelis-Menten and two site ordered binding models [10] depending on the enzyme considered. There are also mathematical models of amino acids in other organs in the body such as the brain [15]. This particular example uses a three compartment approach with one compartment modelling sytemic levels and the other two focussed on bound and unbound amino acid in the brain. However, prior mathematical modelling work into concentrations of amino acids through the skin is limited. Chapter 3 addresses previous approaches to modelling phenylalanine concentrations in blood serum as well as new approaches to modelling blood serum phenylalanine concentrations with food intake.

Mathematical modelling of compounds within the stratum corneum is primarily concerned with transdermal delivery of various drugs [52, 73, 33] rather than establishing the formation of the chemical reservoir. Changes in the architecture of the skin are generally considered negligible over the time period considered for extraction experiments. Passive delivery and extraction through the stratum corneum has hence been considered using diffusion models based on Fick's first and second laws [52].

Fick's first law states that the diffusive flux, $\mathbf{J}(\mathbf{x}, t)$, of concentration, $C(\mathbf{x}, t)$, is proportional to the concentration gradient in the spatial domain, $\mathbf{x}$, going from areas of high concentration to areas of low concentration [52]:

$$\mathbf{J}(\mathbf{x}, t) = -\mathbf{D}\nabla C(x, t).$$

Fick's second law applies Fick's first law to the mass conservation equation to obtain:

$$\frac{\partial C(\mathbf{x}, t)}{\partial x} - \nabla.(\mathbf{D}\nabla C(x, t)) = 0. \tag{4.2}$$

Fick's law has been utilised directly by considering a uniform membrane in one spatial di-

mension in order to model diffusion of drugs through the stratum corneum [79, 80].

Movement of compounds in the stratum corneum has also been modelled using discrete methods [81]. In this, the stratum corneum lipid matrix is modelled via nodes. Transport between nodes was modelled to be either linearly dependent on the concentration difference between adjacent nodes or to have diffusivity increased in areas of high concentration to represent membrane damage [81]. Both mechanisms showed Fick-like diffusion and came up with various drug delivery theories which are not discussed here.

More complex mathematical models consider the architecture of the brick and mortar structure demonstrated in Figure 4-1. [73] considers a uniform brick and mortar structure with the compound of interest allowed to move between corneocytes and the intercellular space with the aim of assessing how permeable corneocytes are in relation to the lipid matrix. This work suggested that corneocytes are 1000 times less permeable than the lipid matrix and hence most transport occurs along the intercellular route. Other work into the effect of the brick and mortar structure has also suggested that the change in path length and tortousity of the lipid route has a significant effect on the diffusion coefficient through the stratum corneum [52].

In contrast, recent work by Wang *et al.* has considered movement of compounds through the skin with varying levels of permeability of stratum corneum cells, ranging from impermeable to transparent [82]. The approach presented compares a diffusion based model in two spatial dimensions at steady state to measured extraction fluxes through human skin for water, ethanol, nicotinamide and testosterone. Based on these results, it is suggested that there is significant transport through the intracellular route straight through the stratum corneum and that corneocytes are highly permeable to these compounds [82]. However, experimental work into extraction flux using mercuric chloride through porcine skin has suggested that stratum corneum cells are highly impermeable [83]. This discrepancy could potentially be due to the theoretical work by Wang *et al.* neglecting appendageal pathways through the stratum corneum [82] which have been shown to be very important during extraction experiments [32] and could explain the straight through pathway theorised by Wang *et al.* Permeability and extraction of compounds through the stratum corneum is discussed further in chapters 5 and 6.

The effect of movement and desquamation of corneocytes and production of compounds in the stratum corneum layer on skin reservoirs have, to date, not been considered. Additionally, peaks in concentration within the skin reservoir have not been predicted in prior models. The Potts and Guy model, discussed in section 4.3.4 also suggests that the the effective diffusion coefficient of large molecules through the stratum corneum is less than that for

small molecules. Hence, for large compounds, such as amino acids, movement through the stratum corneum will be slow and movement processes in the skin may have a significant impact on the stratum corneum distribution.

4.4 Model Formation

In order to model skin reservoirs of amino acids, we begin by setting up a linked model structure for systemic and skin concentrations of amino acids and parameters for our case study compound, phenylalanine. We first address assumptions that hold throughout the model then address specific assumptions for corneocytes and the intercellular space. In order to form the linked model, it is assumed that:

1. Amino acids in the blood are instantaneously evenly distributed through the whole compartment, hence systemic concentration only varies in time. This follows the model presented in chapter 3.

2. Phenylalanine gets into the skin both from the blood and production in the skin. Production of amino acids in the stratum corneum has been suggested in prior experimental work [1, 2].

3. As there is limited experimental work into amino acids the viable epidermis and this layer is not the rate limiting barrier to transport through the skin, we consider the viable epidermis to be spatially uniform and in dynamic equilibrium with the systemic compartment. This assumption also means that the viable epidermis cells and intercellular cells are considered to have equal concentrations of phenylalanine.

4. The skin is considered to be replenished at the same rate as it is removed, hence the volume of each compartment is constant.

5. The stratum corneum is considered to vary with time and one spatial dimension, depth through the skin x.

6. The stratum corneum is considered to be at a constant depth L and split into the stratum corneum (SC), $x \in (d, L]$, and stratum disjunctum (SD) $x \in [0, d]$. $x = 0$ represents the surface of the skin.

7. Corneocytes in the stratum corneum and stratum disjunctum are completely imperme-

able to amino acids because amino acids are large and mostly hydrophilic and has been suggested in prior work [73].

8. Corneocytes moving through the stratum corneum are in the final stages in terminal differentiation. Hence breakdown of filaggrin and other proteins to form amino acids will occur in the deeper layers of the stratum corneum and be at a far reduced rate at the surface of the skin as filaggrin becomes depleted. In order to simplify the model, we initially assume that this production rate of amino acids is constant in the stratum corneum and zero in the stratum disjunction.

9. Removal of cells and compounds from the skin only occurs in the stratum disjunctum, being the layers closest to the skin surface. Although it is possible that removal occurs in deeper layers of the stratum corneum, this is considered to be negligible. The stratum disjunctum occupies the top few cell layers of the stratum corneum [75], distance d, based on where amino acid concentrations in skin begin to decrease in prior experimental work [1, 2].

10. The outer layer of the skin is considered to be completely replenished every 2 weeks [69].

11. Cell packing fraction is considered to be constant in the stratum corneum and viable epidermis. As whole cells are lost from the SD, the volume fraction occupied by cells is considered to be non-constant in this layer, altering the packing fraction.

Given this, concentration of amino acid in each compartment is denoted:

Systemic $C_1(t)$, $\forall t \geq 0$.

Viable epidermis $C_2(t) = C_1(t)$, $\forall t \geq 0$.

Stratum corneum corneocytes $C_3(x,t)$, $x \in (d, L]$ $\forall t \geq 0$.

Stratum corneum intercellular space $C_4(x,t)$, $x \in (d, L]$ $\forall t \geq 0$.

Stratum disjunctum intercellular space $C_5(x,t)$, $x \in [0, d]$ $\forall t \geq 0$.

Stratum disjunctum corneocytes $C_6(t)$, $\forall t \geq 0$.

Each compartment has corresponding volume V_i, $i \in [1, 6]$ which is considered to be constant. Using these assumptions and definitions results in the schematic diagram given in Figure 4-4.

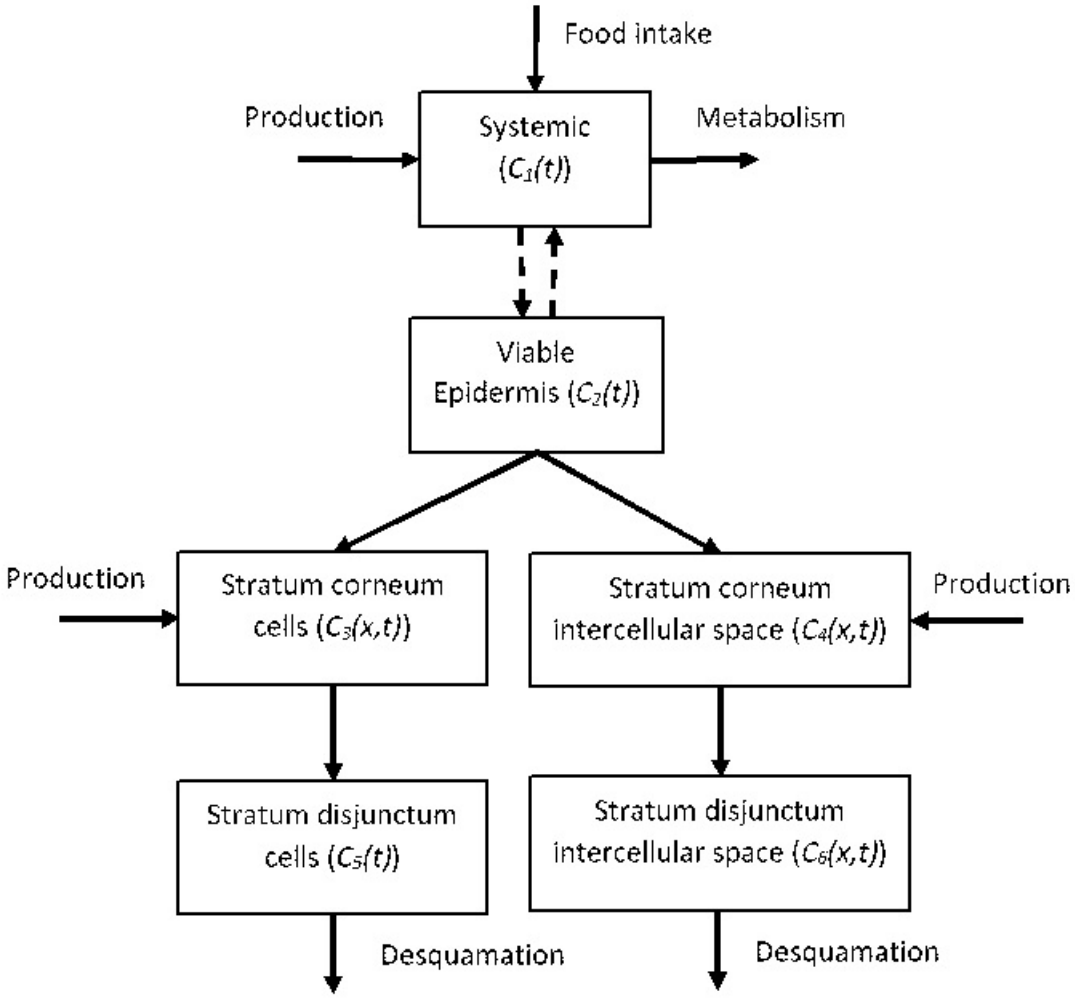

Figure 4-4: Schematic diagram of the overall model. The viable epidermis and systemic compartments are considered to be in dynamic equilibrium. x is a spatial variable where $x = 0$ represents the surface of the skin and t is time.

Parameters in the system, using phenylalanine as a trial compound, are given in table 4.1. These parameters are derived from published sources where possible and discussed in more detail in section 4.3. Unknown parameters were calculated using least square regression analysis on *in vivo* data. The Gauss-Newton method for numerically solving least squares regression problems is detailed in section 2.2.

Having established a linked model, governing equations are now formed for concentration in the blood serum and stratum corneum. The viable epidermis is considered to be in dynamic equilibrium with the blood serum at all times.

4.4.1 Phenylalanine in the Blood

For phenylalanine in the blood, we use the single compartment model presented in chapter 3 in a non-fasting state. Food intake is considered via a Bateman function. It is assumed that the viable epidermis rapidly reaches a dynamic equilibrium with the systemic compartment and that the volume of the viable epidermis in comparison to the blood is small. Hence we do not consider there to be a significant drop in blood serum concentration due to movement into the viable epidermis.

As cells and intercellular space are considered separately in the outer layers of the skin, it is important to mention that, as the viable epidermis is considered to be spatially invariant at constant unit cell volume, V_2, the volume occupied by cells is equal to $p_e V_2$, where p_e is the packing fraction in the viable epidermis, and intercellular space volume in the viable epidermis is $(1 - p_e)V_2$.

4.4.2 Corneocyte Model

Figure 4-5 gives a graphical representation of the corneocyte model. As whole cells are removed from the stratum disjunctum, we consider the concentration in corneocytes in this compartment to be spatially invariant. For cells, we additionally assume that:

1. As corneocytes are considered to be impermeable to amino acids and fixed in the lipid matrix, movement of amino acids in corneocytes is only due to movement of the cells towards the surface of the skin at velocity $v > 0$.

2. Corneocytes are removed from the stratum disjunctum at a constant rate λ.

Using the assumptions given, the governing equation for $C_3(x,t)$ is

$$\frac{\partial C_3}{\partial t}(x,t) - v\frac{\partial C_3}{\partial x}(x,t) = k_2, \quad x \in (d, L], \quad \forall t \geq 0, \tag{4.3}$$

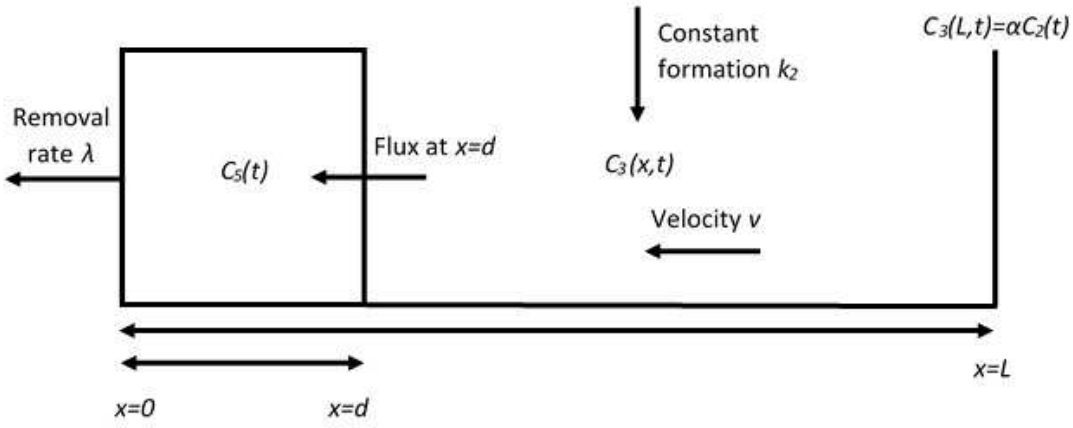

Figure 4-5: Graphical representation of the model for amino acid concentration in corneocytes in the skin. In this the SC compartment is considered as a spatially dependent model and the SD as a compartment with flux in based on flux out of the SC.

and for $C_5(t)$ is:

$$\frac{\mathrm{d}C_5}{\mathrm{d}t}(t) = -\lambda C_5(t) + \frac{vC_3(d,t)}{d}, \quad x \in [0,d], \quad \forall t \geq 0. \tag{4.4}$$

As the volume of the SD is constant, the influx of cells into this compartment per unit time, $^{v}/_{d}$, must equal the outflow of corneocytes per unit time, λ, hence:

$$\frac{\mathrm{d}C_5}{\mathrm{d}t}(t) = \frac{v}{d}(C_3(d,t) - C_5(t)), \quad x \in [0,d] \quad , \forall t \geq 0. \tag{4.5}$$

Flux out of the viable epidermis must be equal to the flux into the SC on the boundary between these two layers, $x = L$. As movement across this boundary on both sides is solely due to advection, this results in the boundary condition:

$$vC_3(L,t) = v_e C_2(t). \quad \forall t \geq 0. \tag{4.6}$$

As we consider there to be a constant number of cells in the stratum cornem, we can relate the velocity of cell movement in the stratum corneum to the velocity in the viable epidermis via

$$v_e = \frac{V_2}{V_3 + V_4} v = \alpha v, \tag{4.7}$$

with the derivation shown in detail in section 4.3.3. Equation (4.6) and (4.7) hence yield the boundary condition:

$$C_3(L, t) = \alpha C_2(t).$$

The problem is fully specified by introducing arbitrary constant initial conditions:

$$\begin{aligned} C_3(x, 0) &= C_{3s}, \quad x \in (d, L], \\ C_5(0) &= C_{5s}. \end{aligned}$$

4.4.3 Intercellular Space Model

Figure 4-6 gives a graphical representation of the proposed intercellular space model. For intercellular space, we additionally assume that:

1. As amino acids are not fixed in corneocytes in the intercellular space, amino acids can move through diffusion, with diffusion coefficient D_1, as well as with overall movement of the skin towards the surface at velocity $v > 0$.

2. Diffusion in the SD is complex due to non-uniform removal of intercellular space which tape stripping does not take into consideration. Hence, diffusion in the stratum corneum is grouped with removal into a single, linear term.

The flux in the SC is due to diffusion, with diffusion coefficient D_1 and advection at velocity $v > 0$. Hence the governing equation for $C_4(x, t)$ is

$$\frac{\partial C_4}{\partial t}(x, t) - D_1 \frac{\partial^2 C_4}{\partial x^2}(x, t) - v \frac{\partial C_4}{\partial x}(x, t) = k_3, \quad x \in (d, L], \quad \forall t \geq 0, \tag{4.8}$$

and for $C_6(x, t)$ is given

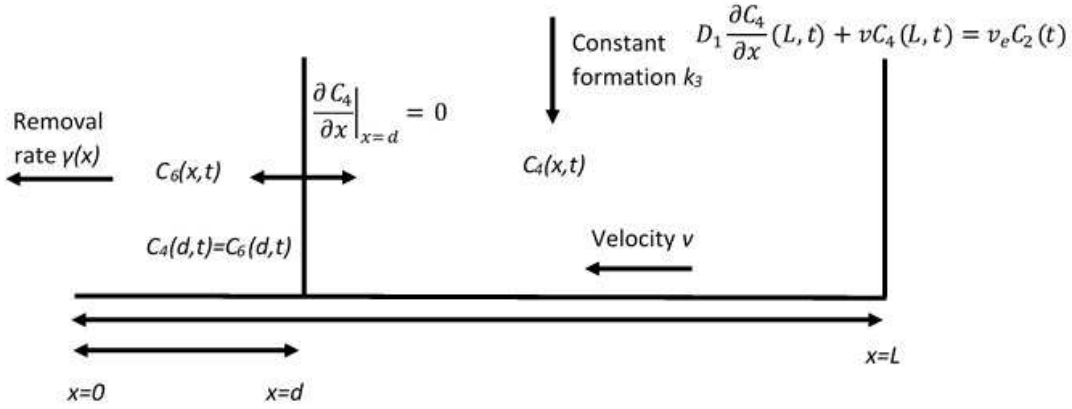

Figure 4-6: Graphical representation of the model for amino acid concentration in the intercellular space in skin. The SC and SD are considered to be linked spatially dependent compartments.

$$\frac{\partial C_6}{\partial t}(x,t) - v\frac{\partial C_6}{\partial x}(x,t) = -\gamma(x)C_6(x,t), \quad x \in [0,d], \quad \forall t \geq 0, \tag{4.9}$$

where $\gamma(x)$ is a spatially dependent removal rate from the stratum disjunctum. We consider $\gamma(x)$ to be spatially dependent as layers of the SD closer to the surface are removed with greater frequency than the deeper layers. For simplicity, we consider a linear function

$$\gamma(x) = \sigma(d-x), \quad x \in [0,d],$$

where $\sigma > 0$.

Providing conservation over the SC-viable epidermis boundary at $x = L$ gives the boundary condition

$$D_1\frac{\partial C_4}{\partial x}(L,t) + vC_4(L,t) = v_eC_2(t), \quad \forall t \geq 0,$$

hence, using equation (4.7):

$$\frac{\partial C_4}{\partial x}(L,t) = \frac{v}{D_1}\left(\frac{V_2}{V_3+V_4}C_2(t) - C_4(L,t)\right) = \beta(\alpha C_2(t) - C_4(L,t)),$$

$$\beta = \frac{v}{D_1}. \tag{4.10}$$

As we consider the structure of the skin to remain unchanged over the SC-SD boundary, the concentration of amino acid on this boundary is considered to be equal in the SC and SD:

$$C_4(d,t) = C_6(d,t), \quad \forall t \geq 0. \tag{4.11}$$

In order to conserve the amount of amino acid in the system, the flux must be equal from both sides of the boundary between the SC and SD giving the final boundary condition:

$$\frac{\partial C_4}{\partial x}(d,t) = 0, \quad \forall t \geq 0. \tag{4.12}$$

We consider an arbitrary constant initial condition in the SC

$$C_4(x,0) = C_{4s}, \quad x \in (d,L] \quad \forall t \geq 0, \tag{4.13}$$

and a decaying initial condition based on γ in the SD:

$$C_6(x,0) = C_{6s} e^{-\int_x^d \frac{\gamma}{v} \mathrm{d}x} = C_{6s} e^{\frac{1}{2v}(x^2 - 2dx + d^2)}, \quad x \in [0,d], \quad \forall t \geq 0. \tag{4.14}$$

In order to fulfil the boundary condition in equation (4.11) $C_{6s} = C_{4s}$.

4.4.4 Total Concentration Model

In vivo [2] and *in vitro* [1] experiments give the concentration of amino acid through a tape stripped layer of the skin at n discrete intervals x_i, $i \in [1,n]$, from the surface of the skin to 75% of the way through the stratum corneum, hence $0 < x_i \leq 0.75L$. The point at which 75% of the outer layer of the skin had been extracted was determined by TEWL measurements [10].

To compare the model results at steady state to *in vivo* and *in vitro* data, we first changed the experimental results to show average concentration in each layer, rather than amount through the layer, by dividing the amount obtained per unit area by the thickness of the layer and considering these discrete points to occur in the middle of the layer considered. The model results were compared to this using a continuous concentration curve, $T(x, \mathbf{\Omega})$, which incorporates both corneocytes and the intercellular space based on the unknown parameter set $\mathbf{\Omega} = (k_2, k_3, \sigma)$. We initially assume $k_2 = k_3$ to reduce the number of unknown parameters.

Under these assumptions

$$T(x, \mathbf{\Omega}) = \begin{cases} pC_5^*(x, \mathbf{\Omega}) + (1-p)C_6^*(x, \mathbf{\Omega}), & x \in [0, d], \\ pC_3^*(x, \mathbf{\Omega}) + (1-p)C_4^*(x, \mathbf{\Omega}), & x \in (d, L], \end{cases} \tag{4.15}$$

where p is the packing fraction of the stratum corneum.

The Gauss-Newton algorithm for minimising the least squares approximation [48], detailed in section 2.2, was employed to obtain estimates for unknown parameters in $\mathbf{\Omega}$ based on results obtained *in vivo* for phenylalanine [2].

4.5 Model analysis - Time Dependent and Steady State Solutions

4.5.1 Corneocyte Model

Time Dependent

Taking the Laplace transform, discussed in section 2.7, of equation (4.3)

$$s\hat{C}_3 - C_{3s} - v\frac{\mathrm{d}\hat{C}_3}{\mathrm{d}x} = \frac{k_2}{s},$$

where:

$$\hat{C}_3(x,s) = \int_0^\infty C_3(x,t)\exp(-st)\mathrm{d}t. \tag{4.16}$$

This has solution

$$\hat{C}_3 = \frac{C_{3s}}{s} + \frac{k_2}{s^2} - \frac{\hat{c}_a}{v}e^{\frac{s(L-x)}{v}},$$

where

$$\hat{c}_a = -\alpha\hat{C}_2 + \frac{\hat{C}_{3s}}{s} + \frac{k_2}{s^2},$$

is found by consideration of the boundary condition in equation (4.6). Inverse transforming using standard transforms yields the solution

$$C_3(x,t) = \begin{cases} C_{3s} + k_2 t, & \text{if} \quad t < \dfrac{L-x}{v}, \\ \dfrac{k_2(L-x)}{v} + \alpha C_2\left(t - \dfrac{L-x}{v}\right), & \text{if} \quad t \geq \dfrac{L-x}{v}, \end{cases} \qquad x \in (d, L]. \tag{4.17}$$

For $x \in [0, d]$, we consider the solution to equation (4.5):

$$C_5(t) = \begin{cases} (1-e^{-\lambda t})(C_{3s} - \lambda k_2) + k_2 t + C_{5s}e^{-\lambda t} & \text{if} \quad t < \dfrac{L-d}{v} \\ \left(C_{3s} - \dfrac{k_2 d}{v}\right)(e^{-\lambda(t-\frac{L-d}{v})} - e^{-\lambda t}) + \dfrac{k_2(L-d)}{v} + y(t) & \text{if} \quad t \geq \dfrac{L-d}{v}, \end{cases}, \tag{4.18}$$

$$y(t) = C_{5s}e^{-\lambda t} + \lambda\alpha e^{-\lambda t}\int_{\frac{L-d}{v}}^{t} C_2\left(t - \frac{(L-d)}{v}\right)e^{\lambda t}\mathrm{d}t.$$

As $C_2(t)$ is not yet defined, solutions presented in equations (4.17) and (4.18) are presented graphically in section 4.9 when considering variable concentrations in the viable epidermis.

Steady State

As replenishment of the outer layers of the skin occur continuously from birth, it's important to explore steady state solutions at a constant concentration in the viable epidermis, C_2^*:

$$C_3^*(x) = \alpha C_2^* + \frac{k_2(L-x)}{v}, \quad x \in (d, L]. \tag{4.19}$$

$$C_5^* = \alpha C_2^* + \frac{k_2(L-d)}{v}, \tag{4.20}$$

A typical steady state profile is shown in Figure 4-7 and shows that there is a linear increase in concentration through the stratum corneum with the stratum disjunctum levelling off at a constant concentration. Equations (4.19) and (4.20) demonstrate that the steady state is linearly dependent on the selection of k_2 with $k_2 = 0$ giving a constant profile based on viable epidermis concentration.

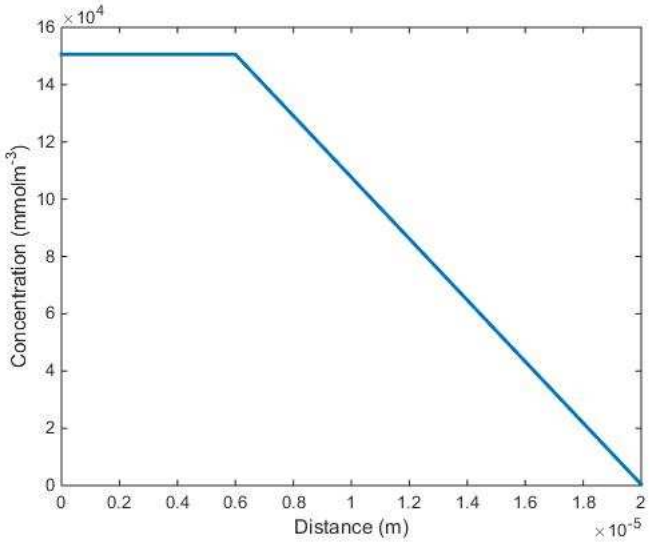

Figure 4-7: Demonstration of the steady state behaviour of concentration of phenylalanine in corneocytes using $k_2 = 0.14\text{mmolm}^{-3}\text{s}^{-1}$ as a trial value with all other parameters given in table 4.1.

As all parameters must be greater than or equal to 0, considering equations (4.17) and (4.19) parameters shifts change where the viable epidermis concentration starts to influence the SC and the position of the steady state but not the general behaviour of the model.

4.5.2 Intercellular Space Model

Time Dependent

This is determined using the GITT method, detailed in section 2.6.1, by making the substitution

$$M(x,t) = C_4(x,t) + f(x), \tag{4.21}$$

into equation (4.8) where:

$$f(x) = \frac{k_3(L-x)}{v} + \frac{k_3 D}{v^2}\left(1 - e^{\frac{-v(x-d)}{D_1}}\right) + \alpha C_2(t).$$

Equation (4.8) becomes

$$\frac{\partial M}{\partial t}(x,t) - D_1\frac{\partial^2 M}{\partial x^2}(x,t) - v\frac{\partial M}{\partial x}(x,t) = -\psi\frac{\partial C_2}{\partial t}(t),$$

with homogeneous boundary conditions formed from equations (4.11) and (4.12)

$$\frac{\partial M}{\partial x}(L,t) + \beta M(L,t) = \frac{\partial M}{\partial t}(d,t) = 0,$$

and initial condition from equation (4.13):

$$M(x,0) = \alpha C_2(0) - f(x).$$

Using the substitution

$$M(x,t) = \theta(x,t)\exp(px+qt),$$

with $p = \frac{-v}{2D_1}$ and $q = \frac{-v^2}{4D_1}$, we obtain the diffusion equation

$$\frac{\partial \theta}{\partial t} - D_1 \frac{\partial^2 \theta}{\partial x^2} = \frac{-\alpha}{\exp(px - qt)} \frac{\partial C_2}{\partial t}, \quad \forall t \geq 0, \quad x \in (d, L],$$

with homogeneous boundary conditions

$$\frac{\partial \theta}{\partial x}(L, t) + \left(\beta - \frac{v}{2D_1}\right) \theta(L, t) = \frac{\partial \theta}{\partial x}(d, t) - \frac{v}{2D_1} \theta(d, t) = 0, \quad \forall t \geq 0,$$

and initial condition:

$$\theta(x, 0) = \frac{\alpha C_2(0) - f(x, 0)}{\exp(px + qt)}, \quad x \in (d, L].$$

To solve the diffusion equation, we apply the GITT by considering an eigenvalue problem with the same kind of boundary conditions specified for $\theta(x, t)$

$$\frac{\mathrm{d}^2 \phi}{\mathrm{d}x^2}(x) + \mu^2 \phi(x) = 0,$$

$$\frac{\mathrm{d}\phi}{\mathrm{d}x}(L) + \left(\beta - \frac{v}{2D_1}\right) \phi(L) = \frac{\mathrm{d}\phi}{\mathrm{d}x}(d) - \frac{v}{2D_1} \phi(d) = 0,$$

which only has non-trivial solutions for certain values of $\mu = \mu_i$, $i \in [1, \infty]$, eigenvalues, with the corresponding solutions, $\phi_i(x)$, being eigenfunctions with the orthogonality property

$$\int_d^L \phi_i(x) \phi_j(x) \mathrm{d}x = N_i \delta_{ij},$$

where N_i is the normalisation integral and δ_{ij} is the Kronecker delta function. Solving the diffusion equation results in

$$\phi_i(x) = A_i \sin(\mu_i x) + B_i \cos(\mu_i x),$$

where A_i and B_i are determined by the boundary conditions. For ease, μ_i is set to ${}^{\pi i}/_{d}$, $i \in [1, \infty)$. This results in the normalised eigenfunctions, $\tilde{\phi}_i$

$$\tilde{\phi}_i(x) = \frac{A_i \sin(\mu_i x) + B_i \cos(\mu_i x)}{\sqrt{N_i}}, \quad \mu_i = \frac{\pi i}{d},$$

$$\begin{aligned} A_i &= \frac{-v}{2D_1 s_i} - \frac{\beta v}{2D_1 s_i \mu_i} - \frac{v^2}{4D_1^2 s_i \mu_i}, \\ B_i &= \frac{-v}{2D_1 s_i}, \\ s_i &= \left(\mu_i + \beta - \frac{v}{2D_1}\right) \cos(\mu_i L) - \mu_i \sin(\mu_i L), \end{aligned}$$

with normalisation constant:

$$N_i = \frac{A_i^2}{2}\left((L-d) - \frac{\sin(\mu_i L)\cos(\mu_i L)}{\mu_i}\right) + \frac{AB}{\mu_i}\sin^2(\mu_i L) + \frac{B_i^2}{2}\left((L-d) + \frac{\sin(\mu_i L)\cos(\mu_i L)}{\mu_i}\right).$$

Using the orthogonality property of eigenfunctions, the integral transform pair is derived as

$$\bar{\theta}_i(t) = \int_d^L \tilde{\phi}_i(x)\theta(x,t)\mathrm{d}x, \quad \text{(Transform)}$$

$$\theta(x,t) = \sum_{i=1}^{\infty} \tilde{\phi}_i(x)\bar{\theta}_i(t), \quad \text{(Inverse)}$$

and applying this to the governing equation for θ yields a infinite system of decoupled ordinary differential equations

$$\frac{\mathrm{d}\bar{\theta}_i(t)}{\mathrm{d}t} + \mu_i^2 \theta_i(t) = \bar{G}_i(t), \quad i \in [1, \infty),$$

where

$$\bar{G}_i(t) = \int_d^L \tilde{\phi}(x) \frac{-\alpha}{\exp(px+qt)} \frac{\partial C_2}{\partial t} \mathrm{d}x,$$

with initial conditions

$$\bar{\theta}_i(t=0) = \bar{f}_i = \int_d^L \tilde{\phi}_i(x) \frac{-\frac{k_3(L-x)}{v} - \frac{k_3 D_1}{v^2}(1 - e^{\frac{-v(x-d)}{D_1}})}{\exp(\frac{-vx}{2D_1} - \frac{v^2 t}{4D_1})} \mathrm{d}x,$$

and hence solution:

$$\bar{\theta}_i(t) = \exp(-\mu_i^2 t) \left[\bar{f}_i + \int_0^t \bar{G}_i(\tau) \exp(\mu_i^2 \tau) \mathrm{d}\tau \right].$$

We now have an expression for $\theta(x,t)$

$$\theta(x,t) = \sum_{i=1}^{\infty} \tilde{\phi}_i(x) \exp(-\mu_i^2 t) \left[\bar{f}_i(x) + \int_0^t \bar{G}_i(\tau) \exp(-\mu_i^2 \tau) \mathrm{d}\tau \right],$$

which can be used to find $C_4(x,t)$ exactly:

$$\begin{aligned} C_4(x,t) = \theta(x,t) \exp\left(\frac{-vx}{2D_1} - \frac{v^2 t}{4D_1}\right) + \frac{k_3(L-x)}{v} \\ + \frac{k_3 D_1}{v^2}\left(1 - e^{\frac{-v(x-d)}{D_1}}\right) + \alpha C_2(t), \quad x \in (d, L], \quad \forall t \geq 0. \end{aligned} \tag{4.22}$$

In order to obtain an exact solution to the concentration of amino acids in the SD intercellular space, $C_6(x,t)$, we first consider the substitution $Q(x,t) = C_6(x,t) e^{\int_x^d \frac{\gamma}{v} \mathrm{d}x}$ which reduces the governing equation, given in (4.9), to

$$Q_t - vQ_x = 0,$$

with initial condition

$$Q(x,0) = C_{6s}, \quad x \in [0,d],$$

and boundary condition:

$$Q(d,t) = C_6(d,t) = C_4(d,t).$$

We consider the Laplace transform of this equation where $\mathcal{L}\{Q(x,t)\}(s)$ is given by $\hat{Q}(x,s)$

$$\frac{\mathrm{d}\hat{Q}}{\mathrm{d}x} - \frac{s\hat{Q}}{v} = \frac{-C_{6s}}{v},$$

and solve using the integrating factor $e^{\frac{-sx}{v}}$

$$\hat{Q} = \frac{C_{6s}}{s} + \hat{c}_b e^{\frac{s(x-d)}{v}},$$

where:

$$\hat{c}_b = \mathcal{L}\{C_4(d,t)\}(s) - \frac{C_{6s}}{s}. \tag{4.23}$$

Hence applying the inverse Laplace transform where $H(t)$ is the unit step function

$$Q(x,t) = C_{6s}H(t) + C_4\left(d, t - \frac{d-x}{v}\right) H\left(t + \frac{x}{v}\right) - C_{6s}H\left(t - \frac{d-x}{v}\right),$$

we obtain

$$\begin{aligned} C_6(x,t) = \Bigg(C_{6s}H(t) + C_4\left(d, t - \frac{d-x}{v}\right) H\left(t + \frac{x}{v}\right) \\ -C_{6s}H\left(t - \frac{d-x}{v}\right)\Bigg) e^{-\int_x^d \frac{\gamma}{v}\mathrm{d}x}, \quad x \in [0,d], \quad \forall t \geq 0, \end{aligned} \tag{4.24}$$

which is based on the solution to the SC intercellular space, $C_4(x,t)$. Again due to $C_2(t)$ not being defined yet, equations (4.22) and (4.24) are demonstrated graphically in section 4.9 when dealing with variable concentrations in the viable epidermis.

Steady State

At a constant concentration in the viable epidermis, C_2^*, the steady state levels are

$$C_4^*(x) = \frac{k_3(L-x)}{v} + \frac{k_3 D}{v^2}(1 - e^{\frac{-v(x-d)}{D}}) + \psi C_2^*, \quad x \in (d, L], \tag{4.25}$$

and:

$$C_6^*(x) = C_4^*(d) e^{\frac{1}{2v}(x^2 - 2dx + d^2)}, \quad x \in [0, d). \tag{4.26}$$

A typical profile is shown in Figure 4-8. This shows that, similarly to the corneocyte model, the stratum corneum concentration is linear with respect to production through the skin with $k_2 = 0$ giving a constant profile. The concentration decays non-linearly in the stratum disjunctum and is equal to the concentration in the stratum corneum on the boundary between the two layers, $x = d$. It noticeable that the decay never results in zero concentration at the skin surface.

4.6 Model Analysis - Parameter estimation

Having obtained exact solutions for each compartment, we now look to establish unknown parameters from *in vivo* data in human skin [2]. Many parameters in the model can be derived from published literature sources as shown in table 4.1. The unknown parameters are the production rate of phenylalanine in the stratum corneum cells, k_2, intercellular space, k_3, and the removal rate in the stratum disjunctum, σ. The goodness of fit of the predicted results is then assessed using standard error of the estimate, S, detailed in section 2.2.1

It is currently unknown if tape stripping analyses the contents of the intercellular space or the whole outer layer of the skin. We propose that if cells in the stratum corneum are almost impermeable to amino acids [73], then tape stripping only samples the intercellular

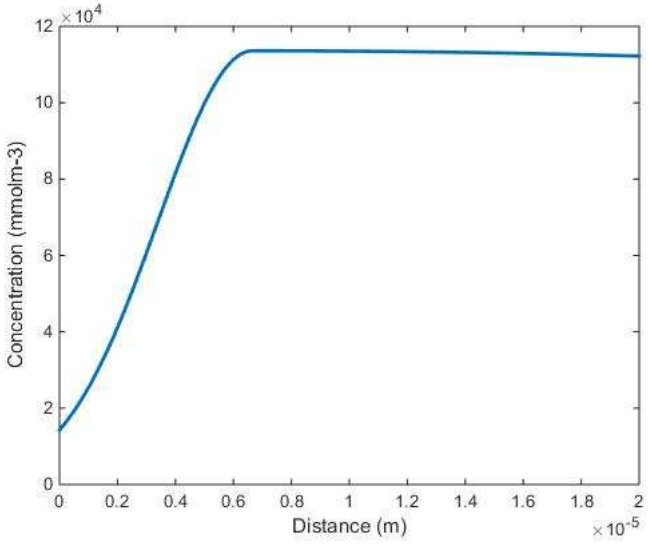

Figure 4-8: Demonstration of the steady state behaviour of concentration of phenylalanine in the intercellular space using $k_3 = 0.14\text{mmolm}^{-3}\text{s}^{-1}$ and $\sigma = 1.54\text{m}^{-1}\text{s}^{-1}$ as trial values with all other parameters given in table 4.1.

space. Experimental work sampling amino acid concentrations through the skin works by weighing the amount of skin stripped and then converting this into a depth through the skin by considering the skin to be at a constant density of 1gcm^{-3} and comparing this to the surface area sampled [1, 2]. This method ignores such effects as partially desquamated layers of skin which can lead to thinner depths measured than have actually been extracted.

As cells take up 90% of the skin, the majority of the sample obtained from the tape strip will consist of cells which, if impermeable, should have a consistent behaviour from the start of the stratum corneum, at $x = L$, to the surface of the skin, at $x = 0$. For example, if an amino acid is produced by breakdown of proteins inside a cell and not broken down further within the cell each individual cell would be expected to have more of that particular amino acid inside it at the surface of the skin than at the boundary between the stratum corneum and viable epidermis. Due to depth calculated being linearly dependent on weight extracted, this increase would be expected to be reflected in the tape stripping results with minor variation due to 10% of the layer being occupied by intercellular space.

A least square regression analysis, more specifically using the Gauss-Newton method detailed in section 2.2, was used to approximate the unknown parameters based on *in vivo* data [2] and the steady state equations given in equations (4.19), (4.20), (4.25) and (4.26). We consider tape stripping results from 8 patients from the top 75% of the stratum corneum/stratum disjunctum. Due to the limited data available for each patient, k_2 and k_3 were initially considered to be equal, reducing the number of parameters that required estimation. The results

Table 4.2: Parameters used with equal production in corneocytes and the intercellular space, $k_2 = k_3 = k$.

Patient	**L**(μm)	**d**(μm)	**k**(mmolm^{-3}s^{-1})	$\boldsymbol{\sigma}$(m^{-1}s^{-1})	**v**(x10^{-11}ms^{-1})	**S**(x10^{3}mmolm^{-3})
1	9.3	4.0	0.018	2.21x10^{18}	0.77	5.96
2	11.0	2.5	0.010	1.93x10^{20}	0.91	4.05
3	11.3	3.5	0.010	6.95x10^{18}	0.93	3.89
4	10.0	3.5	0.009	132.61	0.83	3.08
5	10.0	3.2	0.014	507.53	0.83	5.41
6	10.0	5.0	0.023	23.28	0.83	6.34
7	14.7	4.5	0.017	556.22	1.22	6.11
8	16.0	7.0	0.022	28.68	1.32	6.38

of the regression analysis are shown in Figure 4-9 with the specific parameters calculated for each patient given in table 4.2. It is noticeable that the range of values predicted for σ is quite large as is the standard error of the estimate.

Considering Figure 4-3, which shows the results of *in vivo* experiments in human skin, there is a clear increase in all the amino acids from the viable epidermis, reaching a peak and then decay towards zero at the surface of the skin [2] which is also reflected in *in vitro* experiments [1]. Considering Figure 4-9, it is clear that this peak is not reflected when considering significant production in the corneocytes. Significant production in corneocytes results in a very small concentration drop towards the surface of the skin. The behaviour observed in Figure 4-9 closely resembles that observed for the steady state for cells in Figure 4-7 which is expected as corneocytes comprise over 90% of the stratum corneum.

Production in cells causing unrealistic behaviour near the surface of the skin suggests that either:

1. The production of amino acids in cells is eclipsed by production in the intercellular space.

2. Concentration of amino acids is not assessed in cells during tape stripping.

We consider both approaches in the following two subsections. In both cases, due to the parameters being patient specific, each patient was considered separately and the resulting estimates used to establish a range.

The thickness of the stratum corneum, L, and stratum disjunctum, d, varied between patients. L was calculated using that the deepest point considered in each patient was 75% of the way through the SC [2] and d was approximated by considering the location of the 'peak' result

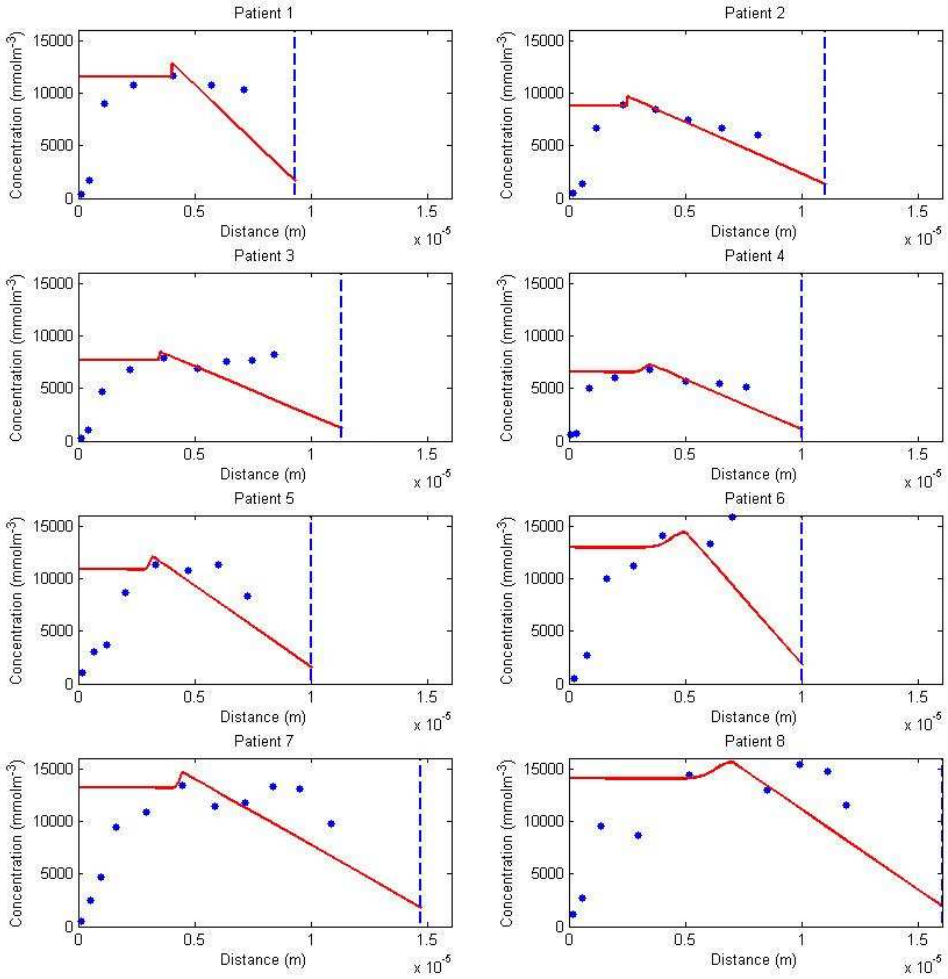

Figure 4-9: The results of regression analysed σ, k_2 and k_3 with $k_2 = k_3$ for each patient entered into the phenylalanine concentration model, red line, compared to *in vivo* data, blue dots. The dotted line represents the estimated final depth through the skin, L, for each patient. Based on *in vivo* results, shown in Figure 4-3, concentration should decrease significantly through the stratum disjunctum. The parameters used to generate this figure are given in table 4.1.

Table 4.3: Parameters used with zero production in corneocytes.

Patient	**L**(μm)	**d**(μm)	$\mathbf{k_3}$(mmolm^{-3}s^{-1})	$\boldsymbol{\sigma}$(m^{-1}s^{-1})	**v**(x10^{-11}ms^{-1})	**S** (x10^{3}mmolm^{-3})
1	9.3	4.0	0.166	0.631	0.77	3.08
2	11.0	2.5	0.076	3.621	0.91	1.68
3	11.3	3.5	0.087	1.781	0.93	1.33
4	10.0	3.5	0.071	0.588	0.83	1.97
5	10.0	3.2	0.125	3.402	0.83	1.19
6	10.0	5.0	0.244	0.962	0.83	1.99
7	14.7	4.5	0.139	1.238	1.22	2.08
8	16.0	7.0	0.221	0.766	1.32	2.34

in each case.

4.6.1 Zero Cell Production

If we consider production in corneocytes, k_2, to be equal to zero and production in the intercellular space, k_3, to be variable then performing regression analysis results in the plots given in Figure 4-10 and the k_3 values given in table 4.3.

At zero production, the corneocytes have a very limited effect on the model - this does open the possibility for very limited production in cells which could be approximated from the concentration gradient in *in vivo* data. In some cases, such as patient 1 and 4, the decline in amino acid concentration observed experimentally is greater than predicted close to the boundary of the skin, $x = 0$.

Comparing the standard error of the estimate given in tables 4.2 and 4.3, it is clear that regression analysis using a model with zero production in cells better fits the observed data than using equal production in cells and the intercellular space for all 8 patients considered.

4.6.2 Tape Stripping only Assesses the Intercellular Space

The parameters found for each patient using the intercellular space only are given in table 4.4 with the resulting distributions given in Figure 4-11. Additionally, comparing the k_3 values in table 4.3 and table 4.4 the difference between the values obtained is negligible. Indeed, figures 4-10 and 4-11 are also very similar. Comparing the standard error of the estimate between the two models, it is clear that not including cells results in a model that fits the experimental results slightly better. Hence, we do not consider cells to contribute to tape

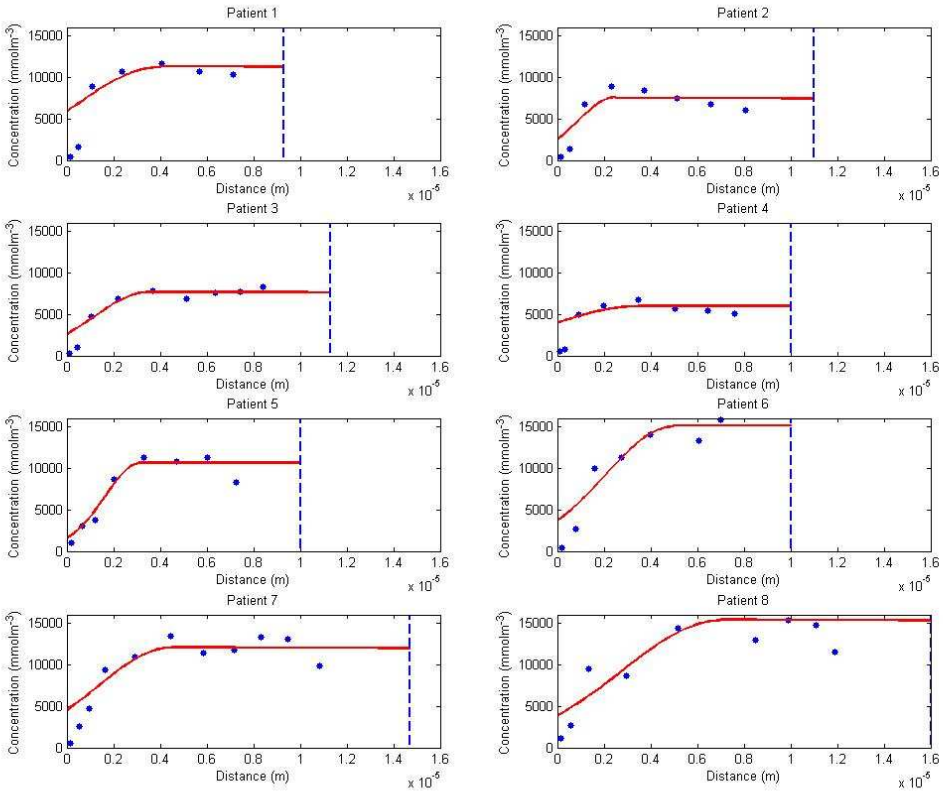

Figure 4-10: The results of regression analysed k_3 and σ for each patient entered into the phenylalanine concentration model, red line, compared to *in vivo* data, blue dots. The dotted line represents the estimated final depth through the skin, L, for each patient.

Table 4.4: Table of parameters for individual patients considering intercellular space only.

Patient	**L**(μm)	**d**(μm)	$\mathbf{k_3}$(mmolm^{-3}s^{-1})	$\boldsymbol{\sigma}$(m^{-1}s^{-1})	**v**(x10^{-11}ms^{-1})	**S**(x10^{3}mmolm^{-3})
1	9.3	4.0	0.163	0.633	0.77	2.95
2	11.0	2.5	0.080	3.289	0.91	1.51
3	11.3	3.5	0.091	1.688	0.93	1.15
4	10.0	3.5	0.076	0.578	0.83	1.79
5	10.0	3.2	0.129	3.246	0.83	1.04
6	10.0	5.0	0.249	0.954	0.83	1.91
7	14.7	4.5	0.143	1.197	1.22	1.94
8	16.0	7.0	0.225	0.756	1.32	2.28

stripping results for the remainder of this chapter.

The standard error of the estimate in table 4.4 is of a similar magnitude for each patient and represents some scatter around the model prediction and those observed experimentally.

Using this data, we obtain a value of -0.43 for the Pearson coefficient between k and σ, which suggests low negative correlation [84] between the two parameters with the exact distribution shown in Figure 4-12. Production and decay in the stratum corneum should be completely independent. However, it is difficult to draw any firm conclusions on correlation from a dataset of 8 patients, so more experimental data would be useful to draw a full conclusion from.

The depth of the stratum disjunctum is affected by the amount/thoroughness of washing the skin. It is also likely that the decay rate, σ, is based on the amount of washing of the skin, hence we consider the correlation between σ and $^{d}/_{L}$ for each patient. Figure 4-13 and the Pearson coefficient of -0.694 suggests that there is a moderate to strong negative correlation between σ and $^{d}/_{L}$. This supports the implication that more skin washing, and hence a smaller stratum disjunctum, leads to a lower decay rate.

4.7 Comparison without the Stratum Disjunctum

Motivation for the inclusion of the stratum disjunctum came from consideration of experimental data [1, 2]. To determine the effect of this additional compartment, we now consider a model system where this compartment is not included. For the intercellular space the governing equation is

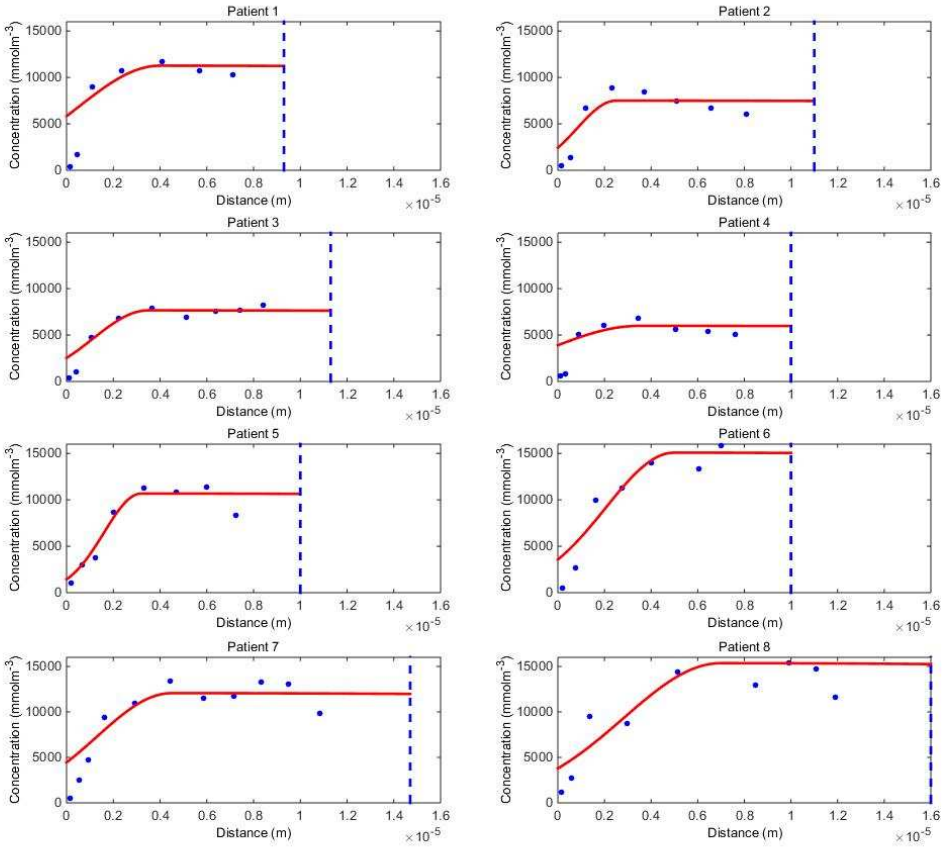

Figure 4-11: The results of regression analysed k_3 and σ for each patient entered into the phenylalanine concentration model, red line, compared to *in vivo* data, blue dots. The dotted line represents the estimated final depth through the skin, L, for each patient.

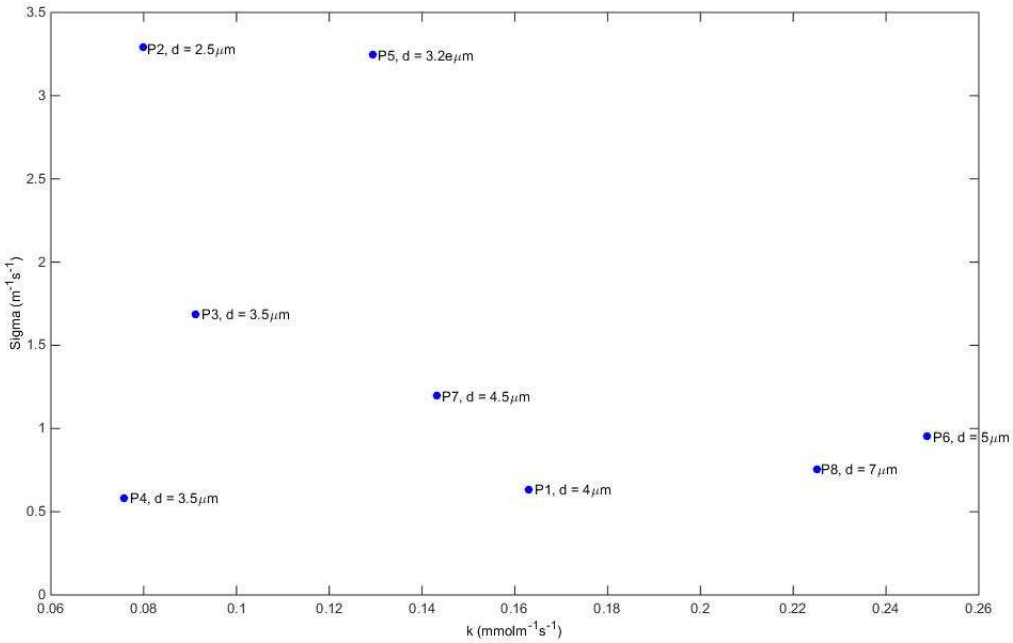

Figure 4-12: Plot of production rate against decay rate for each patient with corresponding SD depth labelled on each point.

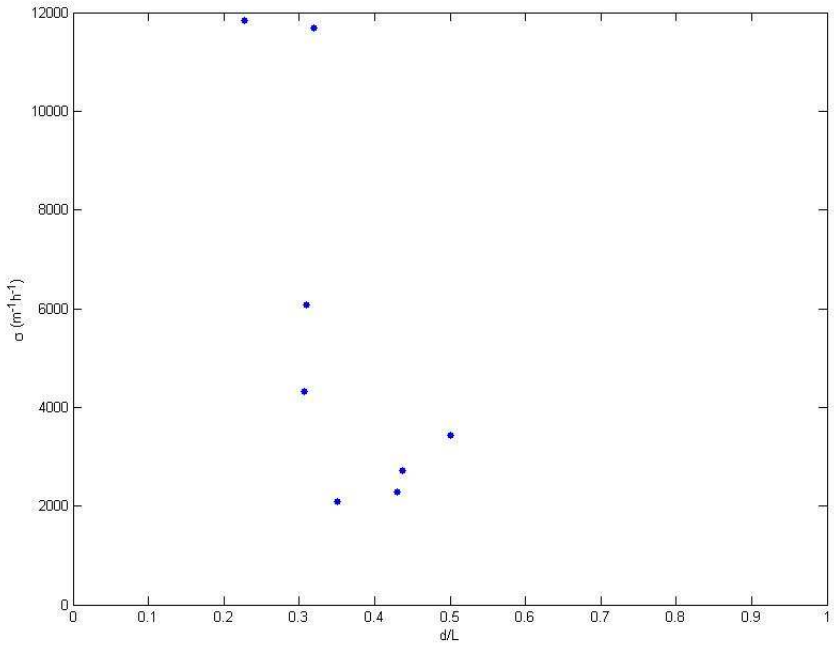

Figure 4-13: Plot of the correlation between $^{d}/_{L}$ and σ.

$$\frac{\partial C_4}{\partial t}(x,t) - D_1 \frac{\partial^2 C_4}{\partial x^2}(x,t) - v\frac{\partial C_4}{\partial x}(x,t) = k_2, \quad x \in [0,L], \quad \forall t \geq 0.$$

with initial condition:

$$C_4(x,0) = C_{4s}(x).$$

The boundary condition at the stratum corneum, viable epidermis boundary, $x = L$, remains as a flux conservation condition

$$\frac{\partial C_4}{\partial x}(L,t) = \beta(\alpha C_2(t) - C_4(L,t)), \quad \forall t \geq 0,$$

and we consider the boundary condition on the surface of the skin, $x = 0$, to be a sink:

$$C_4(0,t) = 0, \quad \forall t \geq 0. \tag{4.27}$$

The corresponding steady state

$$C_4^*(x) = c_1 \left(1 - \exp\left(\frac{-vx}{D}\right)\right) - \frac{k_2 x}{v}, \quad x \in [0,L], \tag{4.28}$$

where c_1 is a positive constant:

$$c_1 = \psi C_2^* + \frac{k_2 D}{v^2} + \frac{k_2 L}{v}.$$

Equation (4.28) has a stationary point, x_s, at

$$x_s = \frac{D}{v} \ln\left(\frac{c_1 v^2}{k_2 D}\right) = \frac{D}{v} \ln\left[\frac{\psi C_2^* v^2}{k_2 D} + 1 + \frac{Lv}{D}\right],$$

hence as k_2 increases, the position of the stationary point decreases. As $k_2 \to \infty$

$$x_s \to \frac{D}{v} \ln\left[1 + \frac{Lv}{D}\right], \tag{4.29}$$

which, using parameters given in table 4.1, results in $x_s \approx L$ as demonstrated in Figure 4-14. Clearly not including removal effects in stratum disjunctum does not reflect the behaviour observed *in vivo* as shown by Figure 4-3 as, using physiological parameters, the peak occurs close to the viable epidermis boundary.

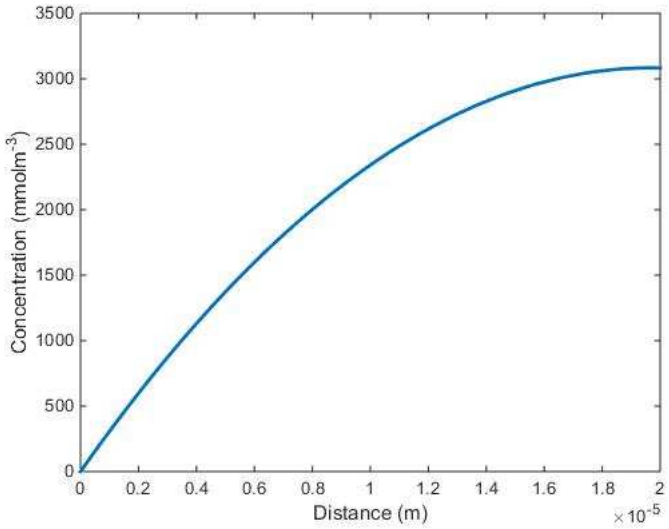

Figure 4-14: Demonstration of the concentration profile through the stratum corneum with a zero concentration initial condition on the surface of the skin.

4.8 Comparison with Tyrosine

If we expect our model to describe amino acid distribution in the skin in general terms, then we might expect $\gamma(x)$ to be independent of a particular amino acid. To explore this, we consider *in vivo* data for tyrosine [2] from the same patients using the same model for the SC and SD and a constant concentration $C_2 = 0.075\text{mmoldm}^{-3}$ in the viable epidermis compartment. We fix σ, v d and L to the parameters given in table 4.4 for each patient and the diffusion coefficient for tyrosine, D_2, is set to $3.71\text{x}10^{-13}\text{m}^2\text{s}^{-1}$ using the Potts and Guy correlation [34], described in section 4.3.4. All other parameters are independent of molecule and hence given in table 4.1 with regression analysis performed to find the production rate of tyrosine in the intercellular space, k_4.

Figure 4-15 shows the resulting total plots for tyrosine with the corresponding production

Table 4.5: Production rate in stratum corneum intercellular space for tyrosine.

Patient	$\mathbf{k_4}$(mmolm^{-3}s^{-1})	**S**(x10^{3}mmolm^{-3})
1	0.395	6.81
2	0.262	4.87
3	0.293	3.83
4	0.243	5.67
5	0.294	1.12
6	0.596	5.48
7	0.281	3.40
8	0.454	4.05

Table 4.6: List of ranges and trial parameters.

Parameter	**Set value**	**Variable range**
L	20μm	[10,40]μm
d	6μm	[0,20]μm
k_2	0mmolm^{-3}h^{-1}	[0,900]mmolm^{-3}h^{-1}
k_3	504mmolm^{-3}h^{-1}	[0,900]mmolm^{-3}h^{-1}
σ	5544m^{-1}h^{-1}	[2088,11700]$^{-1}$h^{-1}

rates given in table 4.5. These plots match the experimental data well, suggesting that the model formation is valid for a variety of amino acids.

4.9 Effect of Parameter Variation on Total Amount in the Skin

For most of the previous sections, we have used trial parameters based on ranges found in the literature. Here we investigate the effect of varying some key parameters on the total amount of phenylalanine in the stratum corneum in a fasting state. We consider the depth of the stratum corneum, L, the depth of the stratum disjunctum, d, the production of phenylalanine in cells, k_2, in the intercellular space, k_3 and the decay rate in the stratum disjunctum, σ. To do this, we fix all other variables to the values given in table 4.6 and alter the parameter considered over the range given in table 4.6.

Total amount in the skin is found by considering the integral of equation (4.15) with respect to x at steady state given in equations (4.19), (4.20), (4.25) and (4.26). Due to the $\exp(x^2)$ term in equation (4.26), the integral is found numerically.

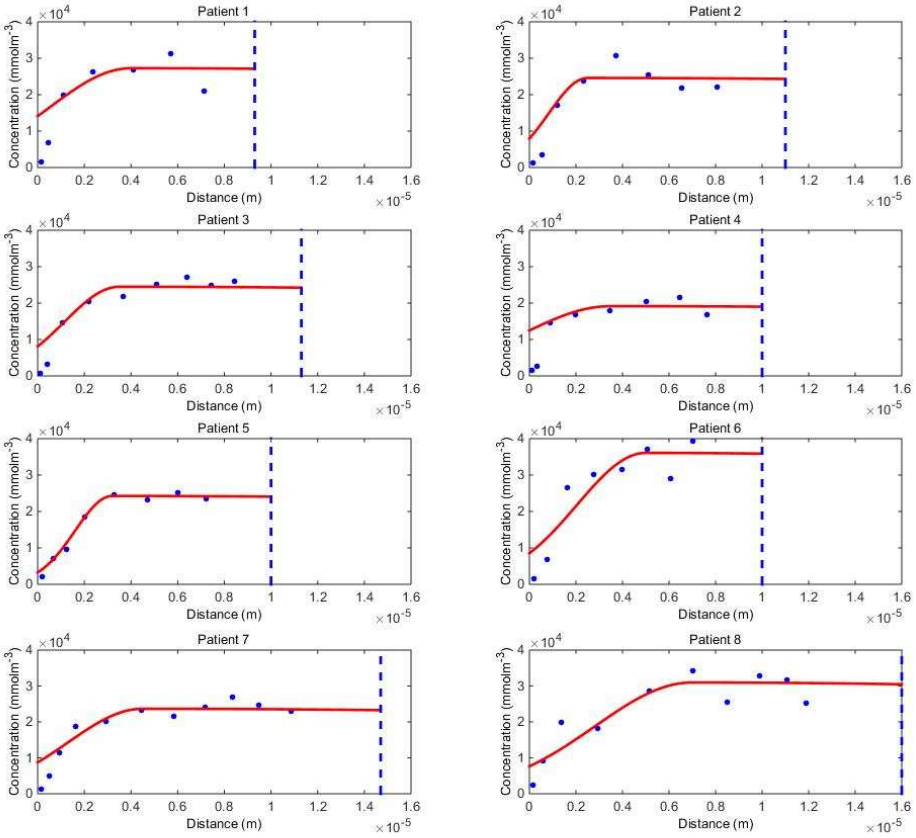

Figure 4-15: The results of regression analysed k for each patient inputted into the tyrosine concentration model, red line, with fixed σ based on the phenylalanine regression analysis compared to *in vivo* data, blue dots. The dotted line represents the estimated final depth through the skin, L, for each patient.

4.9.1 Varying Stratum Corneum Depth

Figure 4-16 indicates that the relationship between L and the total amount in the stratum corneum is approximately linear. This is to be expected as increasing the depth of the stratum corneum effectively increases the depth which phenylalanine is sampled over.

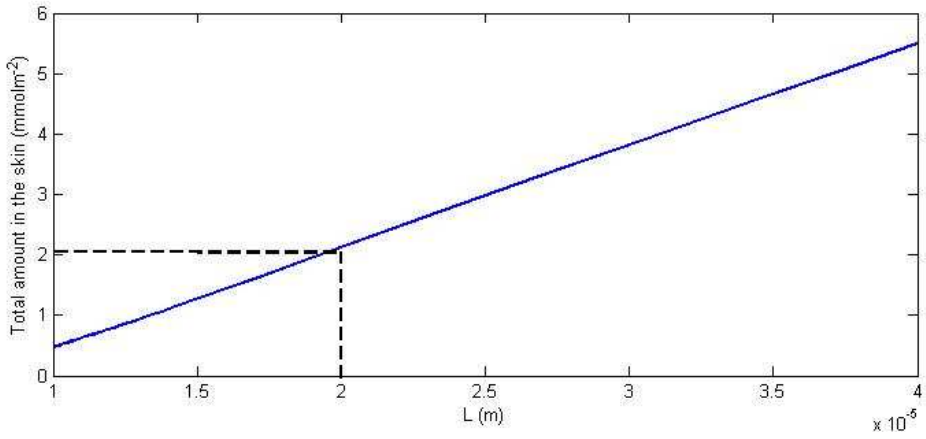

Figure 4-16: Effect of varying stratum corneum depth, L, on the total amount of phenylalanine in the stratum corneum per unit area.

4.9.2 Varying Stratum Disjunctum Depth

Varying stratum disjunctum depth has a non-linear effect on total amount of amino acid in the stratum corneum. As demonstrated by Figure 4-17, the thinner the stratum disjunctum, the more amino acid is in the stratum corneum. This is because removal effects are considered to not start until the stratum disjunctum has been reached.

4.9.3 Varying Production in Corneocytes and the Intercellular Space

Figures 4-18 and 4-19 demonstrate, respectively, that production in cells and intercellular space has a linear effect on amount of phenylalanine in the stratum corneum. As cells occupy 90% of the stratum corneum - it is unsurprising that changes in k_2 have a much larger effect than changing k_3.

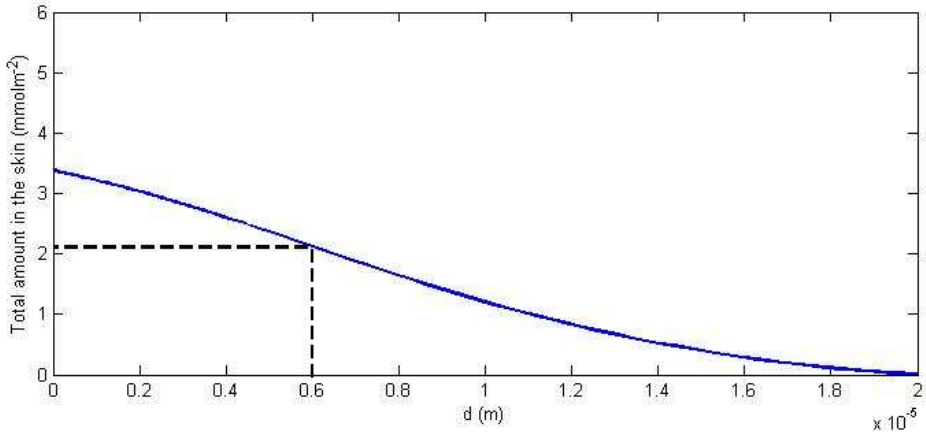

Figure 4-17: Effect of varying the stratum disjunctum depth, d, on the total amount of phenylalanine in the stratum corneum per unit area. L is fixed at 20μm. The dotted line indicates the value of d given in table 4.6.

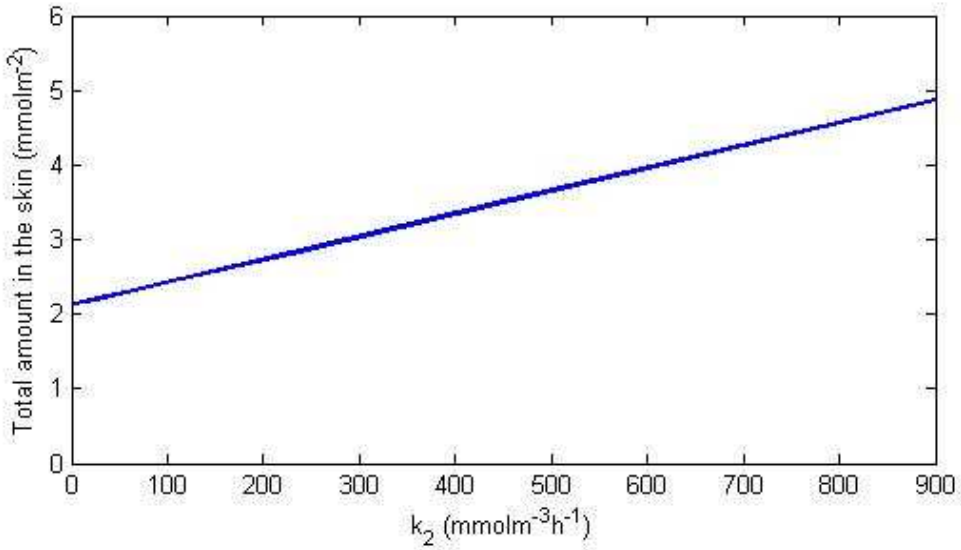

Figure 4-18: Effect of varying production of phenylalanine in stratum corneum cells, k_2, on the total amount of phenylalanine in the stratum corneum per unit area. $k_2 = 0$ in table 4.6.

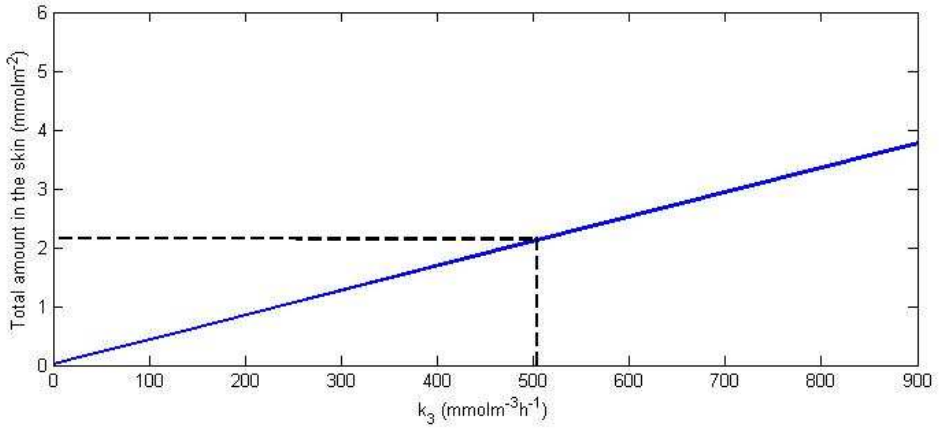

Figure 4-19: Effect of varying production of phenylalanine in stratum corneum intercellular space, k_3, on the total amount of phenylalanine in the stratum corneum per unit area. The dotted line indicates the value of d given in table 4.6.

4.9.4 Varying Stratum Disjunctum Decay Rate in the Intercellular Space

Figure 4-20 demonstrates that varying the decay rate of phenylalanine in the stratum disjunctum intercellular space has a non-linear effect on the amount of phenylalanine in the stratum corneum. Increasing decay rates causes a smaller total amount in the stratum corneum with changes having less effect at high rates than low rates. The change to total concentration is relatively small as the decay rate only affects the concentration in the stratum disjunctum intercellular space.

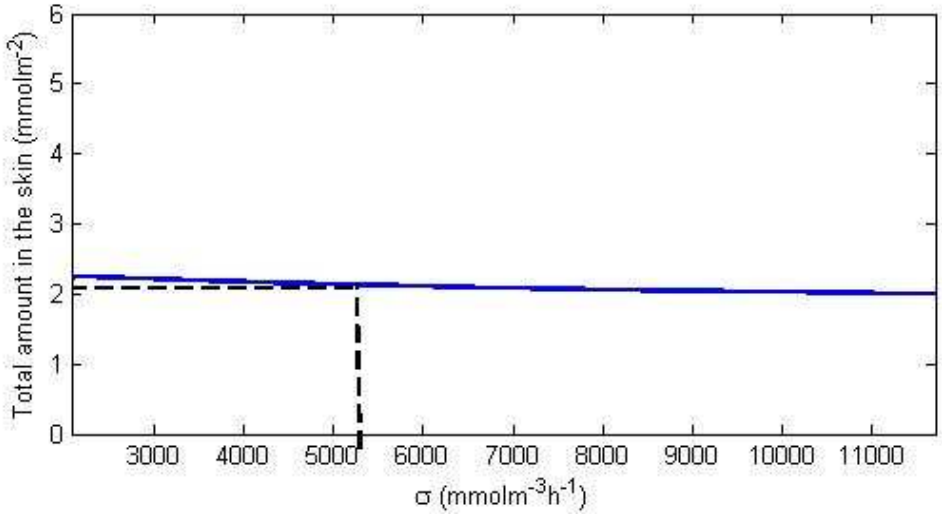

Figure 4-20: Effect of varying decay rate of phenylalanine in stratum disjunctum intercellular space, k_3, on the total amount of phenylalanine in the stratum corneum per unit area. The dotted line indicates the value of d given in table 4.6.

4.10 Model analysis - Non-fasting state

Having obtained estimates for the unknown parameters in human skin, the concentration of phenylalanine through corneocytes and intercellular space was considered in a non-fasting state. Using the trial parameters listed in table 4.1, the plot given in Figure 4-21 was produced for phenylalanine concentration within stratum corneum corneocytes with $k_2 = 0$. This plot is very similar to that produced in the systemic compartment in a non-fasting state as shown in chapter 3 when scaled by the volume ratio α.

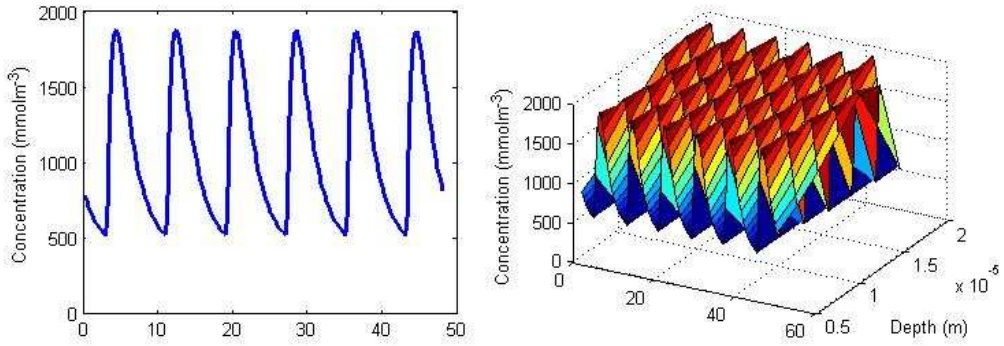

Figure 4-21: Amino acid concentration profiles in SD (left) and SC (right) corneocytes under a variable viable epidermis concentration.

Figure 4-22 shows the non-fasting state behaviour for the intercellular space over a period of one month, 672 hours, as this is double the time taken to fully replenish the stratum corneum [69]. Variation in the viable epidermis concentration has an unnoticeable effect on skin concentrations. Hence, we conclude that production dominates the amount of phenylalanine in the SC and SD intercellular space. Comparing Figures 4-21 and 4-22, and remembering that cells occupy nine times more volume than the intercellular space, it is clear that there is significantly more phenylalanine in the intercellular space than in corneocytes. This also suggests that phenylalanine concentration in the stratum corneum and stratum disjunctum is dominated by production.

As the impact of systemic concentration of phenylalanine is almost unnoticeable under realistic concentration ranges, this also means that changes in systemic concentration due to phenylketonuria are unlikely to have a large impact on the skin reservoir.

It is also noticeable that the concentration profile is almost flat through the stratum corneum intercellular space. This is not due to the movement of amino acids from the viable epidermis, but is instead due to phenylalanine being allowed to spread through the compartment via diffusion. Additionally, by construction of removal in the stratum disjunctum, the concentration will never hit zero at $x = 0$.

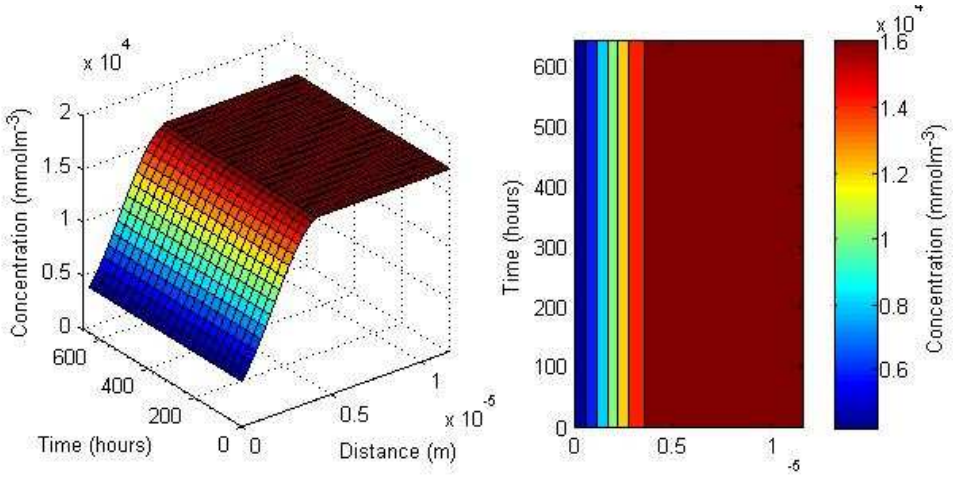

Figure 4-22: Amino acid concentration through the intercellular space in a non-fasting state. The effect of varying viable epidermis concentration on the concentration of amino acids in the intercellular space is unnoticeable.

Table 4.7: Parameters used when performing regression analysis on porcine skin.

Parameter	**Definition**	**Range**	**Value used**
L	Depth of the stratum corneum	[21, 26]μm	24μm
d	Depth of the stratum disjunctum	[3, 6.25]μm	-
v	Velocity of advection	[1.74, 2.15]x10^{-11}ms^{-1}	1.98x10^{-11} ms^{-1}
C_2^*	Steady state plasma concentration	[0.066, 0.074]mM	0.070mM

4.11 Model Analysis - *In Vitro* Porcine Skin

Having considered *in vivo* data for human skin, we consider *in vitro* data for pig skin. Pig skin is different from human skin and will, hence, have different parameters, such as the depth of the stratum corneum. We consider the structure of the stratum corneum to remain the same with the new model parameters given in table 4.7.

Performing least squares regression analysis on the 6 sets of pig data results in the plots given in Figure 4-23 with corresponding k_2 and σ for each pig given in table 4.8. Pigs do not wash as much as humans, which results in much less removal of amino acids from the outer layer of the skin. The model seems to predict *in vitro* data well with some scatter, which is measured using standard error of the estimate, S, in table 4.8, in all but pig 2 where there is a significant drop in amino acids concentration deep within the stratum corneum.

Table 4.8: Parameters obtained from regression analysis for each pig.

Patient	$\mathbf{k}_3$ ($mmolm^{-3}s^{-1}$)	$\boldsymbol{\sigma}$ ($m^{-1}s^{-1}$)	$\mathbf{S}$($mmolm^{-3}$)
1	0.027	2.78	616
2	0.024	6.71	817
3	0.050	3.79	325
4	0.024	1.76	400
5	0.027	0.36	606
6	0.021	0.65	319

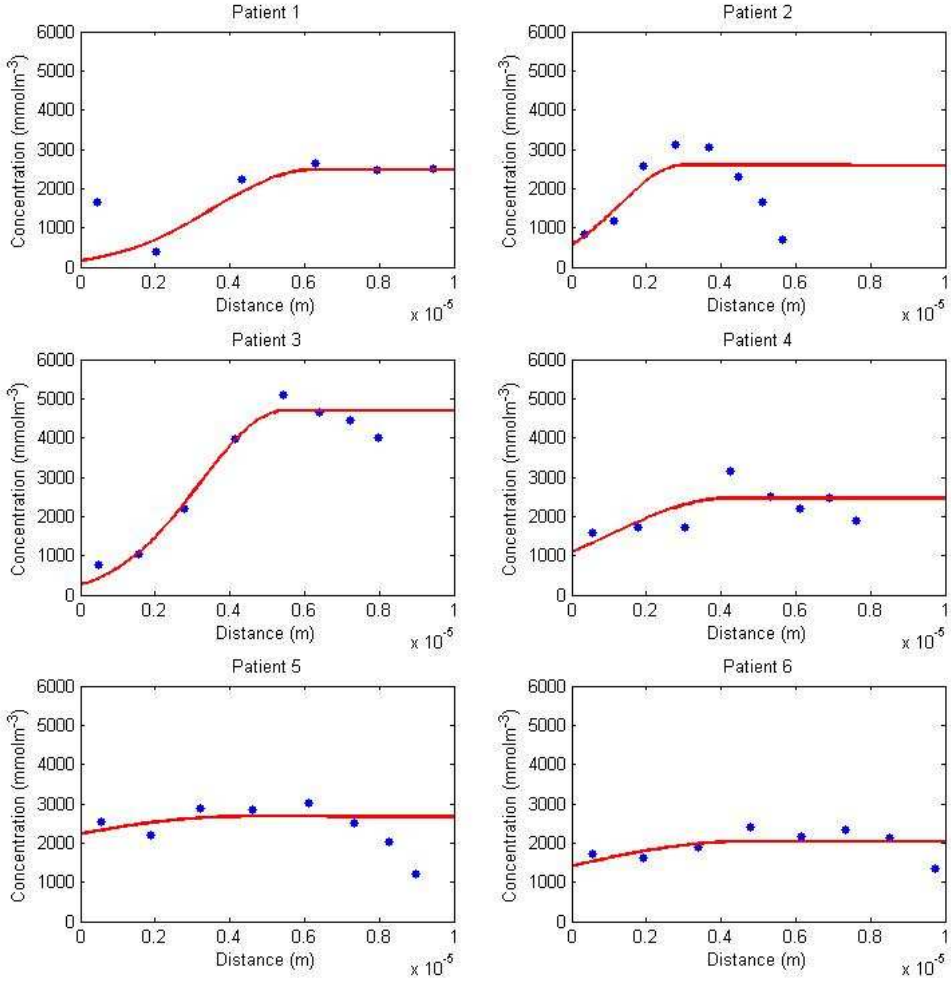

Figure 4-23: Individual regression analysis on each pig.

4.12 Chapter Summary

A simple, generic model for amino acid concentration through the SC and SD has been developed. This model builds on prior *in vitro* and *in vivo* [1, 2] experimental work into the formation of reservoirs of amino acids in the skin. The model results are directly compared to *in vivo* [1] and *in vitro* [2] work and matches well for intercellular space amounts of the amino acids phenylalanine and tyrosine. The model suggests that the production of phenylalanine in the stratum corneum is in the range $[0.08,0.25]\text{mmolm}^{-3}\text{s}^{-1}$ for humans and that the decay in the stratum disjunctum can be modelled using a linear profile with decay constant in the range $[0.58,3.25]\text{m}^{-1}\text{s}^{-1}$. The ranges on these parameters are large and an improvement to the results would involve considering a larger sample size in order to get an accurate mean and standard deviation for these parameters.

The results of the model were also strengthened by considering *in vivo* tyrosine data from the same patients as the phenylalanine data was obtained from [1]. Regression analysis on tyrosine produced similar decay rates.

The model presented suggests that analysis of historic systemic concentrations of amino acids via consideration of the skin reservoir alone is not possible as production of amino acids in the skin significantly eclipses movement from deeper in the body. However, it may be possible to find systemic concentrations by considering extraction of the stratum corneum reservoir and the viable epidermis simultaneously. This is investigated in later chapters.

In order to check the validity of this model for specific amino acids, parameters such as production rate in the skin and the decay constant need to be verified experimentally. The same decay rate seems to produce reasonable results for both phenylalanine and tyrosine decay in the stratum disjunctum, which makes the parameter selection more valid. However, there is significant variation between patients which is likely due to some patients experiencing a much more rapid drop on the surface of the skin than others.

Varying the removal rate of the amino acid from the stratum disjunctum intercellular space, σ, is a possible way of modelling different levels of washing with larger removal rates representing more washing. Indeed pigs, who wash less than humans, experience a less steep decay rate through the stratum corneum and a definitive non-zero concentration on the surface of the skin. Unfortunately, due to the large range and small number of patients and pigs observed it is not possible to draw any firm conclusions from these results.

Considering the steady state concentrations and exact solution for the stratum corneum intercellular space, equations (4.22) and (4.25), a reduced amount of diffusion in the stratum

corneum intercellular space would significantly increase the spatial variation of amino acid in the stratum corneum. By extension this would also increase the spatial variation in the stratum disjunctum and increase the time taken to reach the steady state. This is important as it suggests that viable epidermis variations will be more obvious when considering compounds with limited diffusion in the stratum corneum.

Opinions vary on whether cells in the stratum corneum are permeable or impermeable [73]. In this chapter we assumed that the cells were completely impermeable. Prior work into drug diffusivity into SC corneocytes has suggested that this movement, if it exists, is very small, even for lipophilic compounds [73]. Hence having impermeable cells is a reasonable assumption, especially as considering permeable cells would introduce more unknown parameters into the system which would need to be estimated experimentally.

Prior work [73] has suggested that the diffusion coefficient may vary through the skin, however incorporating this increases the complexity of the model. It is reasonable to assume the rate as a constant initially, especially as the solution profiles seem to match those obtained experimentally.

Chapter 5

Electro-osmotic Flow Dynamics

5.1 Chapter Objective

In this chapter, we consider the movement of uncharged compounds through channels under an applied electric field. As the compounds considered, like phenylalanine, are uncharged [70], the primary mechanisms of transport are passive diffusion and electro-osmotic flow. The objective of this chapter is to combine prior work into surface chemistry and electro-osmosis in order to fully describe solvent flows through a channel in the skin.

This chapter uses known theory from micro-fluids to find electro-osmotic velocity in terms of known constants, properties of the fluid, applied field and zeta potential on the channel walls. We then use surface chemistry in order to express the zeta potential in terms of the surface charge density and compare several approaches for finding the surface charge density including consideration of the ionic charge density in the fluid through the channel and using streaming potential.

The novelty of this chapter is combining theory from different disciplines, namely classical Navier-Stokes from fluid dynamics, electric potential theory and surface chemistry theory, to obtain the electro-osmotic flow velocity through skin in terms of measurable quantities. We present the general theory and apply it to different geometries. Following unrealistically high predicted velocities, the theory is then further modified using surface chemistry.

5.2 Parameters

This section lists the parameters used in this chapter for reference. As this chapter mostly develops theory into electro-osmotic flow, most of the parameters are either unspecified or are dependent upon values such as the bulk concentration of the ionic salt, c_0, which varies between cases. For these parameters, values are dealt with in the text.

Additionally, most known parameters are universal constants and are hence known to a high degree of accuracy.

Table 5.1: Table of parameters for this chapter. Where explicit values are not given, units are listed if appropriate.

Parameter	**Definition**	**Range**	**Value used**	**Sources**
J_v	Volume flow rate	-	m^3s^{-1}	-
L_{ij}	Onsager Coefficients, $i, j \in [1, 4]$	-	-	-
F	Faraday constant	-	$9.65x10^4 Cmol^{-1}$	[85]
ΔP	Applied pressure gradient	-	Pa	-
$\Delta\phi$	Applied potential difference	-	V	-
$\lambda = \kappa^{-1}$	Debye Length	-	m	-
ϵ_0	Permittivity of free space	-	$8.854x10^{-12}m^{-3}kg^{-1}s^4A^2$	[85]
ϵ_w	Relative permittivity of the fluid at T	-	74	[86]
k_B	Boltzmann constant	-	$1.381x10^{-23}$ JK^{-1}	[85]
T	Temperature	[308.65,310.65]K	310K	[59]
N_a	Avogadro's constant	-	$6.022x10^{23}mol^{-1}$	[85]
e	Elementary charge	-	$1.60x10^{-19}C$	[85]
c_0	Bulk ionic salt concentration	-	mM	-
ρ_m	Mass density	-	kgm^{-3}	-
$v(r)$ or $v(y)$	Velocity of electro-osmotic flow	-	ms^{-1}	-
$\mathbf{x}$	Position in the tube	-	-	-
t	Time	-	s	-
$P(\mathbf{x}, t)$	Pressure	-	Pa	-
η	Dynamic viscosity (of water at 310K)	-	$0.7x10^{-3}Nsm^{-2}$	[85]
$f(\mathbf{x}, t)$	Applied body force	-	$kgms^{-2}$	-
ζ	Zeta potential	-	V	-
ρ_e	Net charge density	-	Cm^{-3}	-

σ	Surface charge density	-	Cm^{-2}	-
c_i	Concentration of ionic species i	-	mM	-
z_i	Valence of ionic species i	-	-	-
$W_i(\mathbf{x})$	Work required to move ions i to $\mathbf{x}$ from an infinitely far distance	-	J	-
ΔU	Streaming Potential	-	V	-
ν	Ratio of streaming potential to pressure gradient	-	nV/Pa	-
δ	Ion radius	-	m	-
r_0	Radius of the tube/channel	-	m	-
D_+	Aqueous diffusion coefficient of the positive ion (Potassium)	-	$1.957x10^{-9}m^2s^{-1}$	[85]
D_+	Aqueous diffusion coefficient of the positive ion (Sodium)	-	$1.344x10^{-9}m^2s^{-1}$	[85]
D_-	Aqueous diffusion coefficient of the negative ion (Chlorine)	-	$2.032x10^{-9}m^2s^{-1}$	[85]
κ_e	Pore conductivity	-	Sm^{-1}	-
κ_b	Bulk conductivity	-	Sm^{-1}	-
r	Distance from the center of the tube	-	-	-
$\psi(\mathbf{x})$	Electric potential	-	V	-
y	Distance from the channel surface	-	-	-
$\mathbf{E}(\mathbf{x})$	Electric field strength	-	Vm^{-1}	-
E_x	x component of electric field strength	-	-	-
A	Surface area of the tube/channel	-	m^2	-
V	Volume of the tube/channel	-	m^3	-
μ_{eo}	Ion mobility	-	$kgAs^{-2}$	-
L	Channel Length	-	m	-
t_+^M	Transport number of Na^+ through skin	-	0.62	[87]
t_+^w	Transport number of Na^+ in water	-	0.5	[87]
δ_c	Average charge concentration in the fluid	-	mM	-

θ	Parameter linking c_0 and δ_c	-	0.26	[87]
δ_{max}	Maximum fluid charge concentration	-	2.8mM	[87]
b	Adsorption constant for fluid charge concentration	-	0.17mM^{-1}	[87]
σ_{max}	Maximum surface charge density	-	Cm^{-2}	-
b_σ	Adsorption coefficient for surface charge density	-	-	-
n	Freundlich Isotherm constant	-	-	-

5.3 Introduction to Electro-Osmotic Flow

Electro-osmotic flow is an electrokinetic phenomenon where an externally applied electric field interacts with an electric double layer to cause bulk flow of a liquid [88]. Electro-osmotic flow was first observed by Reuss in 1809 who observed water migration through porous clay under an externally applied field [89]. Since this time, electro-osmotic flow has become a critical technology in a variety of fields ranging from transdermal delivery [21, 33, 87] to integrated micro- and nanofluidic systems [88, 89, 90].

An electric double layer is a layer of non-zero net charge that forms near the interface between two mediums [88] - for cases of interest in this thesis, this is a solid-liquid interface. In this case, the electric double layer is formed by the adsorption or desorption of ions by the surface which causes ions in the fluid to re-arrange to compensate for the charge imbalance and maintain overall electro-neutrality [88]. The effect caused by the double layer exhibits approximately exponentially decay in potential with distance from the interface.

When an electric field, with electric potential ϕ, is applied parallel to the surface, the surplus of positive or negative charges in the fluid, depending on the charge on the surface, results in a net body force on the fluid towards the oppositely charged diode [89]. For example, Figure 5-1 represents an excess of negative charges in the fluid moving towards the positively charged cathode. The electro-osmotic flow velocity generated is directly proportional to the electric field applied [33] based on some mobility constant μ_{eo} that can be found experimentally or derived from theory. The mobility constant is a property of the system considered and is based on the electric potential generated by the charge on the surface, ψ. Here we focus on direct current (DC) electro-osmotic flow.

Far away from the double layer, the velocity of electro-osmotic flow is considered to be constant and is largely independent of channel size [88]. This behaviour, combined with the ease of application and the ability to perform precise, nano-scale fluid handling via manipulation of external voltages, has made electro-osmotic flow key in micro-fluid and nano-fluid systems [88, 89].

Transdermal iontophoresis and reverse iontophoresis utilises electro-osmotic effects in order to enhance extraction of compounds through the skin. There has been significant research into this field using *in vitro* experiments [1], *in vivo* experiments [2] as well as mathematical modelling [21, 33]. Approaches to transdermal iontophoresis are very varied and, when considering the flow of charged species, electro-osmotic effects are frequently ignored [36, 91]. The amino acid phenylalanine is uncharged, hence the primary movement mechanism through the skin under reverse iontophoresis is electro-osmotic flow.

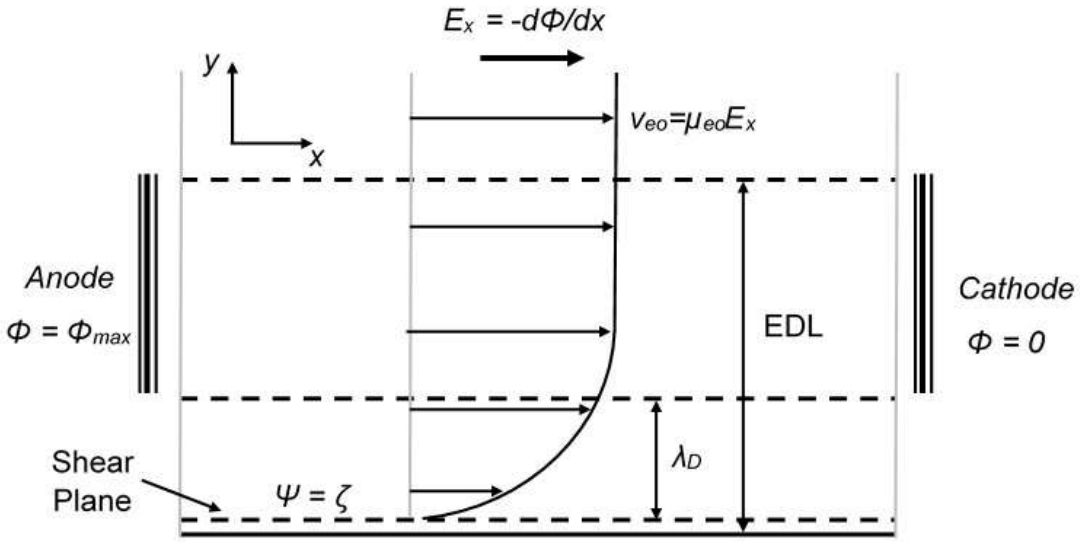

Figure 5-1: Depiction of the electric double layer created by a single surface. In this E_x represents the electric field applied between the anode and cathode, v_{eo} the electro-osmotic velocity with mobility μ_{eo}. The thickness of the electric double layer (EDL) is quantified using the Debye length, λ_D. The shear plane measures the point where charged particles can start to move with the potential, ψ, at this point defined as the zeta potential, ζ. The potential on the shear plane, psi, is different to the potential applied across the membrane, ϕ.

When considering electro-osmotic flow through skin, consistent with fluid dynamics, flux is considered to be proportional to the electric field applied [33, 87] with the proportionality constant determined experimentally. In pharmacy, a common approach is to consider that all flows are linear combinations of all the forces involved in the system [33]. That is that the volume flux, J_v, and current density, i, in a system under an applied potential, $\nabla\phi$, and pressure, ∇P, gradient are

$$J_v = L_{11}\nabla P + L_{12}(-\nabla\phi),$$

$$i = L_{21}\nabla P + L_{22}(-\nabla\phi),$$

where L_{ij} are properties of the system considered called Onsager coefficients. The Onsager coefficient associated with electro-osmotic flow is L_{12} with the electro-osmotic flow velocity determined by $J_v|_{\nabla P=0}$. L_{12} is determined either experimentally or by using mathematical models.

One example of mathematical modelling is called the limiting law theory. This theory considers the force balance between viscous fluid forces and the electrical volume force [33] in the case of a thin double layer. This results in a constant velocity and corresponding Onsager coefficient

$$L_{12} = 10^4 \frac{F r_0^2 (-z_m) C_m}{4\eta L} \left(\frac{\kappa r_0}{2}\right)^{-1},$$

where F is the Faraday constant, r_0 the pore radius, z_m is the sign of the charge on the pore, C_m is the concentration of the compound of interest, η is the dynamic viscosity of the solvent, L is the membrane thickness and $\lambda_D = \kappa^{-1}$ is the Debye length. As the Debye length is inversely proportional to the root of the ionic salt concentration, the limiting law suggests that electro-osmotic flow velocity will decrease with a greater concentration of ionic salt, which is not observed experimentally [33].

There have been several expansions to limiting law theory which produce more realistic results such as the Manning 'lattice' model. In this model, the pore is considered to be a single channel between two rectangular planes which are separated by r_0 [92]. These rectangles are lattices containing evenly distributed fixed point charges which are considered not to have electrostatic interactions with mobile ions flowing through the pore. This leads to the

alternative statement of the Onsager coefficient [93]

$$L_{12} = 10^4 \frac{Fr_0^2(-z_m)C_m}{4\eta L} G(y), \quad \text{with} \quad y = \frac{\kappa r_0}{2},$$

$$G(y) = \frac{1}{y}\left(\coth(y) - \frac{1}{y}\right),$$

$$\kappa = A\sqrt{\frac{C_m}{2} + \underline{C}},$$

where A is an experimentally derived constant and $\underline{C}$ is the concentration of co-ions in the membrane. Other, more complex expansions, such as the Hildreth 'plate' model [94], exist but are not considered in this chapter. None of these approaches consider fluid dynamics concepts, such as the Navier-Stokes equations, and make large assumptions about the system, although the proposed end result can give good approximations when based on experimentally derived constants [33].

In this chapter, we attempt to model electro-osmotic flow from base micro-fluid, surface chemistry and electromagnetic concepts for use in a reverse iontophoresis model for amino acids in the next chapter. We begin by introducing key background concepts, such as the Navier-Stokes equations and the Poisson-Boltzmann equation, before developing electro-osmotic flow models.

5.4 Navier-Stoke Equations

The Navier-Stoke equations describe the motion of a viscous fluid based on pressure, density and temperature [95]. The full Navier-Stokes equation is, as yet, unsolved analytically and is an area of significant interest in fluid dynamics [95]. Generally, several assumptions are applied to the Navier-Stokes equation to make the system analytically solvable, or numerical methods are used. In this chapter, we consider fluid in the skin to be at a constant viscosity, η and mass density, ρ_m. Hence the fluid flow obeys the incompressible Navier-Stokes equation [95]

$$\rho_m(\frac{\partial \mathbf{v}}{\partial t}(\mathbf{x},t) + \mathbf{v}(\mathbf{x},t).\nabla \mathbf{v}(\mathbf{x},t)) = -\nabla P(\mathbf{x},t) + \eta \nabla^2 \mathbf{v}(\mathbf{x},t) + \mathbf{f}(\mathbf{x},t),$$

where $\mathbf{v}$ is the fluid velocity, $P(\mathbf{x}, t)$ is the pressure and $\mathbf{f}(\mathbf{x}, t)$ represents an applied body force to the fluid at spatial location $\mathbf{x}$ and time t. For electro-osmotic flow the applied body force is created by the applied electric field.

In order to find the electro-osmotic flow velocity, we reduce the full Navier-Stokes equation into a more manageable form by assuming that:

1. The solvent is incompressible.

2. The fluid has a low Reynolds number [96] - hence inertia forces are negligible compared to viscous forces.

3. The fluid velocity reaches steady state quickly.

4. In line with prior work, we consider the induced electro-osmotic pressure to be negligible [97].

5. There is no pressure gradient in the system.

Under these assumptions, and noting that the body force under an applied electric field is equal to the local electric charge density, $\rho_e(\mathbf{x})$ multiplied by the applied field, $\mathbf{E}(\mathbf{x})$, the Navier-Stokes equation reduces to:

$$\eta \nabla^2 \mathbf{v}(\mathbf{x}) + \rho_e(\mathbf{x}) \mathbf{E}(\mathbf{x}) = 0. \tag{5.1}$$

5.5 Poisson-Boltzmann Equation

The Poisson-Boltzmann equation is a mean field theory that aims to describe the distribution of electrochemical potential, the total chemical and electrical potential, in a solution next to a charged surface under the assumptions [88, 98]:

1. Ions are point charges, hence ion size effects are ignored. Although valid far away from the surface, this theory breaks down close to the surface.

2. The surface is uniformly charged.

3. Non-Coulombic interactions, being any interaction not between static electric charges such as the interaction between hydrogen shells in water, are ignored.

4. Each ion only interacts with the average electrostatic field of all its neighbours rather than its individual neighbours. This is called a mean field approximation.

5. The ions in solution are considered as a continuous charge distribution which ignores the discrete nature of ions.

6. The permittivity of the medium, $\epsilon = \epsilon_w \epsilon_0$, is constant.

Under these assumptions, the electric potential distribution, $\psi(\mathbf{x})$ can be described using the Poisson equation [98]

$$\nabla^2 \psi(\mathbf{x}) = -\frac{\rho_e(\mathbf{x})}{\epsilon_w \epsilon_0} \tag{5.2}$$

based on the local electric charge density, $\rho_e(\mathbf{x})$, the permittivity of free space, ϵ_0, and the relative permittivity of the fluid, ϵ_w. The local electric charge density is found by considering the sum of charges at each point - which is found by summing the concentration, c_i, of each individual ion species, $i = 1, ..., N$, multiplied by the charge on that ion

$$\rho_e(\mathbf{x}) = N_a e \sum_{i=1}^{N} (-1)^n z_i c_i(\mathbf{x}), \tag{5.3}$$

where z_i is the corresponding valence of ionic species i and n is 1 for negatively charged species and 2 for positively charged species. The Boltzmann equation can be used to calculate the local ion concentration [88]

$$c_i(\mathbf{x}) = c_i^0 \exp\left(\frac{-W_i(\mathbf{x})}{k_B T}\right), \tag{5.4}$$

based on the temperature, T, the Boltzmann constant, k_B, and the work required to move an ion closer to the surface from an infinitely far distance, $W_i(\mathbf{x})$. It is assumed that the only forces acting are electrical in nature, hence [88]:

$$W_i(\mathbf{x}) = (-1)^n z_i e \psi(\mathbf{x}). \tag{5.5}$$

Combining equations (5.2)-(5.5) with the specific surface geometry and ionic species present in the fluid gives the Poisson-Boltzmann equation. Despite the large number of assumptions associated with Poisson-Boltzmann theory, the behaviour of the electric double layer is described well [88]. For aqueous solutions, predictions are good for monovalent salt concentrations below 0.2M and potentials below 50-80mV [88] where monovalent salts are salts consisting of ions with a valency of 1 such as NaCl.

5.6 Boundary Behaviour

Key to understanding electro-osmotic flow is the boundary effects caused on the interface between the fluid flowing through a channel and the channel walls. This section details key concepts in defining the behaviour at this interface.

5.6.1 Zeta Potential

When considering fluid flow along charged surfaces, ions binding to the surface can cause the shear plane, where ions begin to move in the fluid - shown in Figure 5-1, to be away from the interface between the surface and the fluid. The potential exerted by the surface at a distance from the surface interface where ions start to move is called the zeta potential, ζ [88]. The zeta potential plays a very important role in electro-kinetic phenomena such as electro-osmotic flow.

5.6.2 Surface Charge Density

Surface charge density, σ, measures the electric charge per unit area on a surface. Gauss' law states that net electric flux through a closed surface is equal to the net electric charge within that surface multiplied by $^1/_\epsilon$ [98]. Hence, if there is a overall charge on a surface, an electric field will be generated away from that surface. This electric field drives electro-osmotic flow.

If the system is electro-neutral, the charge density on the surface will be mirrored by a net charge density in the fluid. The region away from the charged surface in which a charge

imbalance, and hence an electric field, exists is called the electric double layer with the properties of this double layer affecting the velocity of electro-osmotic flow.

5.6.3 Debye Length

The Debye length is the characteristic length of the electric double layer [33, 88, 89] . The Debye length measures how far an electrostatic effect persists into a solution with the electric potential decreasing by a factor of $1/\exp(1)$ every Debye length. Generally, it is assumed that if the channel in question is much wider than the Debye length, then effects that take place in the double layer can be considered to be negligible. The Debye length, λ is given by

$$\lambda = \kappa^{-1} = \sqrt{\frac{\epsilon_w \epsilon_0 k_B T}{2 N_a e^2 c_0}},$$

with why this expression comes about derived through section 5.7.

5.6.4 Streaming Potential

A common method in characterising zeta potential in a system with a well defined geometry involves measuring the streaming potential. When a pressure difference, ∇P, is applied to fluid flowing through a channel, the liquid drags some of the charge attached to the double layer with it. This process causes accumulation of ions at the ends of the channel - resulting in a potential difference called the streaming potential, ∇U [88].

Streaming potential has been previously considered when dealing with microfluids and porous membranes [88, 87, 99] and resulted in the relation

$$\nu = \frac{\nabla U}{\nabla P} = \frac{-\sigma \lambda}{\eta \kappa_e} \frac{I_2(\kappa r_0)}{I_1(\kappa r_0)}$$

where $I_n(\kappa r_0)$ are modified Bessel functions of order n, described in section 2.8, and κ_e is the pore conductivity. In a binary 1-1 electrolyte, one ion to one cation in the salt such as NaCl, the pore conductivity is given by [90]

$$\kappa_e = \kappa_b \left[1 - \frac{D_+ - D_-}{D_+ + D_-} \frac{2F\sigma}{\epsilon_0 \epsilon_w N_a k_B T} \frac{\lambda^2}{r_0}\right] + \frac{\sigma^2}{\eta} \left[1 + \frac{I_0(\kappa r_0)}{I_1(\kappa r_0)} \left(\frac{2\lambda}{r_0} - \frac{I_0(\kappa r_0)}{I_1(\kappa r_0)}\right)\right],$$

where the bulk conductivity, κ_b, is

$$\kappa_b = \frac{\epsilon_0 \epsilon_w (D_+ - D_-)}{2\lambda^2}, \tag{5.6}$$

D_+ and D_- are, respectively, the ionic diffusion coefficients for the cation and anion, R is the ideal gas constant, T is temperature and r_0 is the channel radius. If the channel radius, r_0, is much greater than the Debye length, then $\kappa_e \to \kappa_b$ [90]. Additionally, considering section 2.8, $I_2(\kappa r_0) \approx I_1(\kappa r_0)$, hence the streaming potential can be expressed as:

$$\nu = \frac{\nabla U}{\nabla P} = \frac{-\sigma\lambda}{\eta\kappa_b}. \tag{5.7}$$

5.6.5 Stern Theory

As shown in section 5.5, Poisson-Boltzmann theory has several strong assumptions which can introduce inaccuracies when describing the electric double layer. However, the inaccuracies introduced tend to cancel each other out, for example including non-Coloumbic forces leads to an increased ionic concentration at the surface and a corresponding decrease in surface potential whereas taking the finite ion size into account reduces the ionic concentration and the surface and causes an increased surface potential [88].

One extension to Poisson-Boltzmann theory is called Stern theory. In this theory, the electric double layer is divided into two parts, the Stern layer, close to the surface, and an outer part where Poisson-Boltzmann theory holds [88]. The Stern layer is considered to end when the potential is equal to the zeta potential.

The simplest way to consider the Stern Layer involves considering ions to have a finite size with the layer of ions closest to the surface being fixed. The distance between the surface and the center of the ion, δ, marks the boundary between the Stern Layer and the outer layer, called the outer Helmholtz plane. By definition, at δ the potential is equal to the zeta potential and is demonstrated graphically in figure 5-2. More complex versions of the Stern Layer exist [88], but we do not consider them as it is currently not possible to get a greater level of detail in the skin.

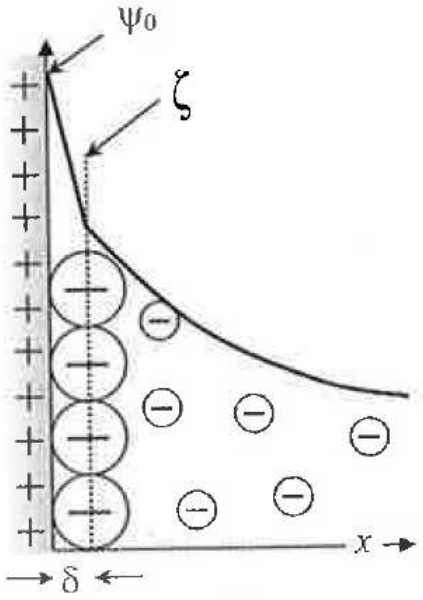

Figure 5-2: Demonstration of the Stern Layer on a positively charged surface. Modified from [88].

5.7 Application

Having established the base theory behind electro-osmotic flow, we now apply this theory to different channel geometries to calculate the electro-osmotic flow velocity. We consider the electro-osmotic flow velocity in both the parallel plate (one-dimensional) and cylindrical (two-dimensional) case. The goal in both cases is to express the electro-osmotic flow velocity in terms of known properties of the system and the surface charge density which can then be calculated using experimental work into streaming potential. The theory for streaming potential is detailed in section 5.6.4 and it's application to find electro-osmotic flow velocity in shown in section 5.8.

In both the parallel plate and cylindrical geometries, the derivation of the velocity in terms of surface charge density is split into three distinct stages, namely:

1. Starting from the incompressible Navier-Stokes equations, detailed in section 5.4, express electro-osmotic flow velocity in terms of double layer potential.

2. Express the double layer potential, and hence velocity, in terms of the zeta potential.

3. Express the zeta potential in terms of surface charge density, leading to an expression for velocity in terms of surface charge density and known parameters for the system.

How these steps were achieved for the parallel plate and cylindrical cases under the assumptions given in section 5.7.1 are expanded on in sections 5.7.2 and 5.7.3 respectively.

5.7.1 Assumptions

In both the parallel plate and cylindrical case, there are consistent assumptions. In the channel, we assume that:

1. Channel walls are identical with constant surface charge density at all points.

2. Charge density and channel dimensions are constant along the channel, the x direction.

3. There are either no or negligible effects created at each end of the channel.

In order to calculate the velocity of electro-osmotic flow, we first consider the Navier-Stokes equation for fluid flow in an electric field, given in equation (5.1), and the Poisson equation, given in equation 5.8, under the additional assumptions:

1. The electric field applied is constant.

2. The concentration of ions with respect to time is constant throughout the system and uniformly distributed in x.

3. The channel walls have a no-slip boundary condition.

4. The electric current is primarily carried by the salt NaCl - the most prevalent electrolyte in skin as demonstrated by the composition of PBS buffer solutions [18].

5. Ions are point charges, hence we consider the Stern layer to have zero size and the surface potential on the channel walls to be equal to the zeta potential.

Under these assumptions, the velocity can be expressed as a function of the potential created in the double layer. We then express the potential created in the double layer in terms of the zeta potential under the assumptions:

1. The system is electro-neutral - this makes the overall system stable and means we don't have a net overall charge created. This is in line with prior research [33].

2. The potential created by the electric double layer, ψ, is small ($\leq$ 25mV).

This results in an expression for electro-osmotic velocity where the only unknown is the zeta potential. We then move on to express the zeta potential in terms of the surface charge density. There are several approaches for modelling surface charge density based on streaming potential which we address later in the chapter.

Additional assumptions in each case are given in the appropriate section.

5.7.2 Parallel Plate Approach

The parallel plate approach considers two parallel plates separated by distance $2r_0$ as demonstrated in Figure 5-3. In order to model electro-osmosis in this case, we consider the effect of one plate in $y \in [0, r_0]$, i.e. between the surface and the center of the channel, and assume the behaviour is mirrored by the second plate.

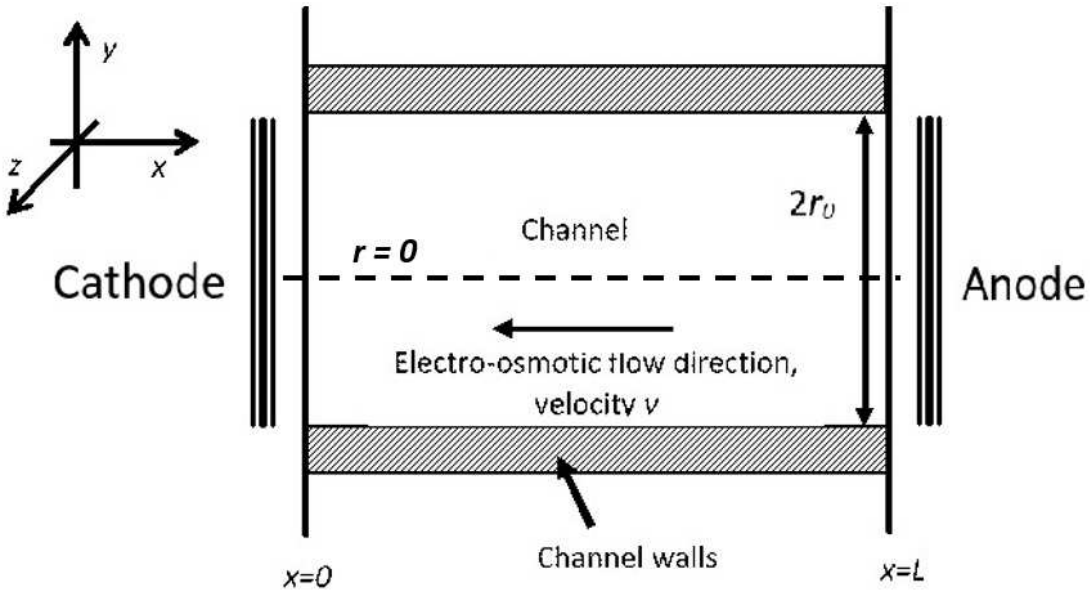

Figure 5-3: Graphical representation of electro-osmotic flow between two parallel plates. Like skin at physiological pH, the channel walls are considered to be negatively charged. In order to maintain electro-neutrality, this is reflected by more positively charged ions in the channel, hence the predominant flow direction is towards the cathode. If the membrane was positively charged the flow direction would be reversed. L represents the length of the channel.

For the parallel plate case, the steps given in section 5.7 are achieved as follows:

1. Express electro-osmotic flow velocity in terms of double layer potential:

(a) This section was started by considering the incompressible Navier-Stokes equations with body force due to an applied electric field, as detailed in section 5.4.

(b) Using the Poisson equation, detailed in section 5.5, charge density was then linked to double layer potential.

(c) The expression for charge density in terms of double layer potential was then substituted into the body force term in the incompressible Navier-Stokes equation. Solving the resulting ODE gave an expression for electro-osmotic flow velocity in terms of double layer potential.

2. Express the double layer potential in terms of zeta potential:

(a) Using the Poisson-Boltzmann equation, detailed in section 5.5, an ODE for double layer potential was found.

(b) Solving the ODE for double layer potential using boundary conditions on the parallel plate case, an expression for double layer potential in terms of zeta potential was found.

(c) Combining the expression obtained for double layer potential in terms of zeta potential with the results from step 1 expressed the electro-osmotic flow velocity in terms of zeta potential.

3. Express the zeta potential in terms of surface charge density:

(a) Assuming that the system was electro-neutral, it was possible to link the charge density in the fluid to the surface charge density.

(b) Using the Poisson equation, detailed in section 5.5, an expression was found for surface charge density in terms of the double layer potential which, using the results of step 2, could be expressed in terms of zeta potential.

(c) It was then possible to combine the relation between surface charge density and zeta potential with the result of step 2 in order to express the electro-osmotic flow velocity in terms of known properties of the system and the surface charge density.

We now move on to expand these steps in the following sections.

Expressing velocity in terms of the double layer potential

In order to find the velocity of electro-osmotic flow in terms of double layer potential, we consider the fluid flow through the channel given in figure 5-3 using the incompressible Navier-Stokes equations [96] discussed in section 5.4:

$$\eta \nabla^2 \mathbf{v}(\mathbf{x}) + \rho_e(\mathbf{x})\mathbf{E}(\mathbf{x}) = 0.$$

As discussed in section 5.5, the Poisson [96] equation links the net charge density to the dielectric permittivity of the fluid, $\epsilon = \epsilon_w \epsilon_0$, and the double layer potential, $\psi(\mathbf{x})$, which, under the constant charge density on the surface assumption, only varies in the y direction:

$$\rho_e(y) = -\epsilon_w \epsilon_0 \frac{\mathrm{d}^2\psi}{\mathrm{d}y^2}(y). \tag{5.8}$$

As the only non-zero component of velocity occurs in the x-direction and only varies in the y direction, $v_x(y)$, the applied field is considered to be constant and to only act in the x direction, E_x, hence fluid velocity is governed by

$$\eta \frac{\mathrm{d}^2 v_x}{\mathrm{d}y^2}(y) - \epsilon_w \epsilon_0 \frac{\mathrm{d}^2\psi}{\mathrm{d}y^2}(y) E_x = 0, \tag{5.9}$$

which is an ODE with boundary conditions given by:

1. The no slip assumption on the channel wall (shear plane) means that $v_x(0) = 0$ and, as we consider ions to be point charges, potential on the shear boundary, $\psi(0)$, is equal to the zeta potential, ζ.

2. As demonstrated by figure 5-3, the velocity in the middle of the channel is maximal, hence ${}^{\mathrm{d}v_x}/_{\mathrm{d}y}(r_0) = 0$. The potential is also at a minimum in the center of the channel, hence ${}^{\mathrm{d}\psi}/_{\mathrm{d}y}(r_0) = 0$.

Integrating equation (5.9) twice with respect to y and applying these boundary conditions gives

$$v_x(y) = \frac{\epsilon_w \epsilon_0 E_x}{\eta}(\psi(y) - \zeta), \tag{5.10}$$

which is the electro-osmotic flow velocity in terms of the zeta potential and electric potential caused by the double layer.

Expressing the double layer potential in terms of the zeta potential

The next stage in expressing the electro-osmotic velocity in terms of known constants is to express $\psi(y)$ in terms of ζ. This was done by constructing an ordinary differential equation for $\psi(y)$ using the Poisson equation, given in equation (5.8) and explained in section 5.5. To express $\rho_e(y)$ in terms of $\psi(y)$, we use the Boltzmann equation given in equation (5.4) in section 5.5 [88]. Using the Boltzmann equation, the local ion concentration for ionic species i, c_i, in one spatial dimension y is given by

$$c_i(y) = c_i^0 \exp\left(\frac{-W_i(y)}{k_B T}\right), \tag{5.11}$$

where c_i^0 is the bulk concentration of ion i in the solvent, i.e. where the work done by the field is equal to zero, k_B is the Boltzmann constant, T is temperature and $W_i(y)$ is the work exerted by the field on ion i at distance y.

As we have assumed that the predominant ions are sodium, $i = 1$ charge $+e$, and chlorine, $i = 2$ charge -e, the work exerted by the field on these ions is $W_i(y) = \mp e\psi(y)$ where e is the elementary charge. In order to calculate charge density at a point, we take the sum of the charge on each ionic species at that point, hence in this system:

$$\rho_e(y) = N_a e(c_2(y) - c_1(y)). \tag{5.12}$$

It is assumed that concentration of ions is measured in moles, hence to obtain charge we multiply concentration by the number of ions in 1 mol, Avogadro's number, N_a, and the charge on each ion, e. Combining equations (5.11) and (5.12) results in

$$\rho_e(y) = N_a e\left(c_2^0 \exp\left(\frac{e\psi(y)}{k_B T}\right) - c_1^0 \exp\left(\frac{-e\psi(y)}{k_B T}\right)\right),$$

and, as the bulk concentration of ions is equal to the bulk concentration of the salt due to NaCl being monovalent, $c_1^0 = c_2^0 = c_0$:

$$\rho_e(y) = N_a e c_0 \left(\exp\left(\frac{e\psi(y)}{k_B T} \right) - \exp\left(\frac{-e\psi(y)}{k_B T} \right) \right) = -2N_a e c_0 \sinh\left(\frac{e\psi(y)}{k_B T} \right). \tag{5.13}$$

Substituting into (5.8) gives the Poisson-Boltzmann equation for this geometry:

$$\epsilon_w \epsilon_0 \frac{\mathrm{d}^2\psi}{\mathrm{d}y^2}(y) = 2N_a e c_0 \sinh\left(\frac{e\psi(y)}{k_B T} \right).$$

Assuming that the potential created by the electric double layer is small, the $\sinh(\frac{e\psi(y)}{k_B T})$ term can be considered to be approximately equal to $\frac{e\psi(y)}{k_B T}$ we obtain the ODE

$$\frac{\mathrm{d}^2\psi}{\mathrm{d}y^2}(y) = \kappa^2 \psi(y), \tag{5.14}$$

where

$$\kappa = \sqrt{\frac{2N_a c_0 e^2}{\epsilon_w \epsilon_0 k_B T}}, \tag{5.15}$$

and $\kappa^{-1} = \lambda_D$ is the Debye length described in section 5.6.3 [88]. Solving equation (5.14) results in the expression for the potential through the double layer

$$\psi(y) = \alpha \exp(-\kappa y) + \beta \exp(\kappa y), \tag{5.16}$$

where α and β are constants determined by the boundary conditions. Using that $\psi(0) = \zeta$ and that solution is bounded as $y \to \infty$, we get that $\alpha = \zeta$ and $\beta = 0$ and therefore can replace $\psi(y)$ in equation (5.10) to express velocity as

$$v_x(y) = -\frac{\epsilon_w \epsilon_0 \zeta E_x}{\eta}(1 - \exp(-\kappa y)),$$

and results in the velocity profile given in figure 5-4 which shows that far away from the electric double layer, the velocity generated by a single plate tends towards a constant

$$v_x = -\frac{\epsilon_w \epsilon_0 \zeta E_x}{\eta}, \tag{5.17}$$

which is in-line with prior theory [96]. Permittivity of free space, ϵ_0, is a known constant, the relative permittivity ϵ_w, and dynamic viscosity, η, are based on the fluid considered, which can be found in the literature for many types of fluids and the electric field, E_x, is a property of the field applied to the skin. The zeta potential, ζ, is unknown, but can be found in terms of known parameters using results from surface chemistry [88] and the electro-neutrality assumption, which is addressed in the next section.

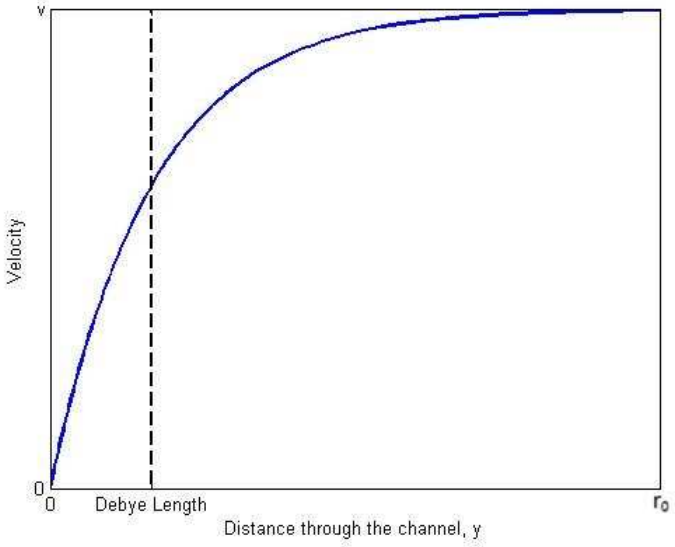

Figure 5-4: Demonstration velocity profile formed in the electric double layer in the one dimensional case.

Finding the zeta potential

Equation (5.17) gives the velocity due to electro-osmosis based on known constants, the permittivity of free space, ϵ_0, properties of the solvent, ϵ_w and η, properties of the field applied across the membrane, E_x, and the zeta potential, ζ, on the channel walls. This section considers how to find the zeta potential in terms of surface charge which is then investigated later in the chapter.

As the system is assumed to be electro-neutral and the charge considered to be split evenly between the two plates, the surface charge density on the channel walls, σ, can be related to the net charge density in the solvent [88]:

$$\sigma = -\int_0^{r_0} \rho_e(y) \mathrm{d}y.$$

Using the Poisson equation in equation (5.8), this can be expressed as

$$\sigma = \epsilon_w \epsilon_0 \int_0^{r_0} \frac{\mathrm{d}^2\psi}{\mathrm{d}y^2} \mathrm{d}y,$$

which, by integrating, becomes:

$$\sigma = \epsilon_w \epsilon_0 \left(\left.\frac{\mathrm{d}\psi}{\mathrm{d}y}\right|_{y=r_0} - \left.\frac{\mathrm{d}\psi}{\mathrm{d}y}\right|_{y=0} \right).$$

As we have assumed that the velocity in the center of the channel, $y = r_0$, is maximised and that the channel is symmetric around the center, the electric potential of the double layer will tend towards a minima at this point

$$\left.\frac{\mathrm{d}\psi}{\mathrm{d}y}\right|_{y=r_0} = 0,$$

hence:

$$\sigma = -\epsilon_w \epsilon_0 \left.\frac{\mathrm{d}\psi}{\mathrm{d}y}\right|_{y=0}. \tag{5.18}$$

Under the low potential assumption $\psi(y)$ is given in equation (5.16). Differentiation of equation (5.16) combined with equation (5.18) results in

$$\sigma = \epsilon_w \epsilon_0 \zeta \kappa = \frac{\epsilon_w \epsilon_0 \zeta}{\lambda_D},$$

since $\kappa^{-1} = \lambda_D$ which matches prior theory into surface chemistry [88]. So, we have shown that the zeta potential can be linked to the surface charge density in this case. Hence, we obtain the velocity equation

$$v(y) = \frac{-\sigma E_x}{\kappa\eta}(1 - \exp(-\kappa y)), \tag{5.19}$$

which in a thin double layer becomes

$$v = \frac{-\sigma E_x}{\kappa\eta},$$

where κ is given in equation (5.15). Equation 5.19 gives the electro-osmotic flow velocity through the channel in terms of properties of the solvent, universal constants, properties of the applied field and the surface charge density. The only current unknown is the surface charge density. We discuss methods of finding surface charge density later in this chapter.

5.7.3 Cylindrical Approach

In the previous section, we calculated the velocity of electro-osmosis by considering the channel through the skin as being sandwiched between two parallel plates. This had several issues when calculating $\psi(y)$ and neglects the effects of curved walls. A more accurate scenario is to consider channels through the skin as being cylindrical, as depicted in figure 5-5. In this case, in addition to the assumptions listed in section 5.7.1, we also assume that the system is radially and axially symmetric.

For the cylindrical case, the steps given in section 5.7 are achieved as follows:

1. Express electro-osmotic flow velocity in terms of double layer potential:

   (a) This section was started by considering the incompressible Navier-Stokes equations with body force due to an applied electric field, as detailed in section 5.4.

   (b) The Poisson-Boltzmann equation, detailed in section 5.5, was used to find an expression for the net charge density in terms of the double layer potential.

   (c) The expression for net charge density in terms of double layer potential was com-

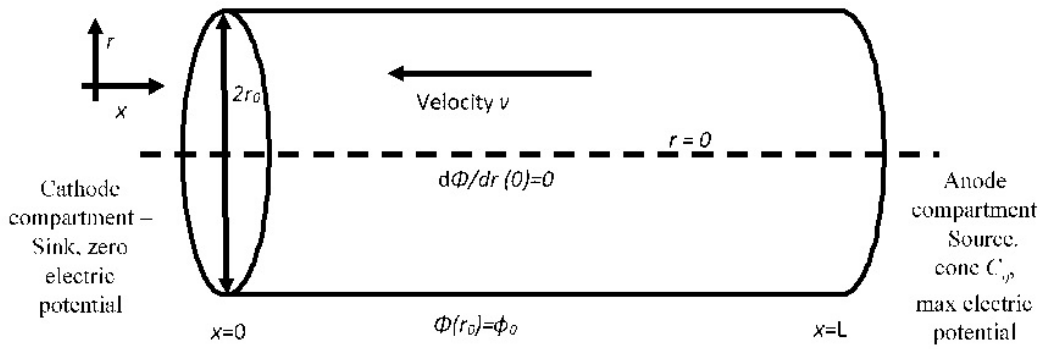

Figure 5-5: Graphical representation of the cylindrical reverse iontophoresis model. This model is considered to be radially symmetric and uniform in x. The length of the tube is L.

bined with the incompressible Navier-Stokes equation to form a differential equation for velocity of electro-osmotic flow in terms of the double layer potential. As the double layer potential was an unknown function at this point it was not possible to solve the differential equation formed at this stage.

2. Express the double layer potential in terms of zeta potential:

   (a) Using the Poisson-Boltzmann equation, an ODE for the double layer potential was found and solved using boundary conditions on the system to give an expression for double layer potential in terms of zeta potential.

   (b) The expression for the double layer potential in terms of zeta potential was combined with the results of step 1 in order to obtain a differential equation for electro-osmotic flow velocity in terms of zeta potential.

   (c) The resulting differential equation for the electro-osmotic flow velocity was solved in order to give the electro-osmotic flow velocity in terms of the zeta potential.

3. Express the zeta potential in terms of surface charge density:

   (a) Assuming that the system was electro-neutral, it was possible to link the charge density in the fluid to the surface charge density.

   (b) Using the Poisson equation, detailed in section 5.5, an expression was found for surface charge density in terms of the double layer potential which, using the results of step 2, could be expressed in terms of zeta potential.

(c) It was then possible to combine the relation between surface charge density and zeta potential with the result of step 2 in order to express the electro-osmotic flow velocity in terms of known properties of the system and the surface charge density.

We now move on to expand these steps in the following sections.

Expressing velocity in terms of the double layer potential

Electro-osmotic flow velocity is governed by the Navier-Stokes equation for an incompressible flow under the assumptions of constant pressure, low Reynolds number and steady state

$$\eta\nabla^2\mathbf{v}(\mathbf{x}) + \rho_e(\mathbf{x})\mathbf{E}(\mathbf{x}) = 0,$$

which, in a radially symmetric system which is uniform in x, becomes:

$$\eta\frac{1}{r}\frac{\mathrm{d}}{\mathrm{d}r}\left(r\frac{\mathrm{d}v}{\mathrm{d}r}(r)\right) = -\rho_e(r)E_x. \tag{5.20}$$

In order to express, $\rho_e(r)$ in terms of ζ, we first need to express $\rho_e(r)$ in terms of $\psi(r)$. Using the Poisson equation, given in equation (5.2), in a radially symmetric system, results in:

$$\frac{1}{r}\frac{\mathrm{d}}{\mathrm{d}r}\left(r\frac{\mathrm{d}\psi}{\mathrm{d}r}(r)\right) = \frac{-\rho_e(r)}{\epsilon_w\epsilon_0}. \tag{5.21}$$

If we now consider the definition of net charge density based on the ion concentration and Boltzmann equation, as discussed in section 5.5, the resulting Poisson-Boltzman equation that links net charge density to the electric potential is

$$\rho_e(r) = -2N_a e c_0 \sinh\left(\frac{e\psi(r)}{k_B T}\right),$$

which, under the low potential assumption, becomes:

$$\rho_e(r) = \frac{-2N_a e^2 c_0 \psi(r)}{k_B T}. \tag{5.22}$$

Combining equations (5.20) and (5.22) gives an ODE for electro-osmotic velocity based on $\psi(r)$:

$$\eta \frac{1}{r}\frac{\mathrm{d}}{\mathrm{d}r}\left(r\frac{\mathrm{d}v}{\mathrm{d}r}(r)\right) = \frac{2N_a e^2 c_0 E_x \psi(r)}{k_B T}. \tag{5.23}$$

Expressing double layer potential in terms of the zeta potential

We now look to express $\psi(r)$ in terms of ζ potential for substitution into equation (5.23). Solving the resulting ODE will then give an expression of velocity in terms of zeta potential. Combing equations (5.21) and (5.22) gives the ODE:

$$\frac{1}{r}\frac{\mathrm{d}}{\mathrm{d}r}\left(r\frac{\mathrm{d}\psi}{\mathrm{d}r}\right) = \kappa^2 \psi(r). \tag{5.24}$$

Using the substitution $\alpha = \kappa r$, we can rewrite equation (5.24) in the form

$$\alpha^2 \frac{\mathrm{d}^2\psi}{\mathrm{d}\alpha^2}(\alpha) + \alpha\frac{\mathrm{d}\psi}{\mathrm{d}\alpha}(\alpha) - \alpha^2\psi(\alpha) = 0,$$

which is a zero order Bessel equation and hence, as there is no singularity in $\psi(r)$ at $r = 0$, the solution is given as a constant, β, multiplied by a zero order modified Bessel function of the first kind, $I_0(\kappa r)$. Bessel functions are detailed further in section 2.8. Using this definition, the potential in the electric double layer is:

$$\psi(r) = \beta I_0(\kappa r).$$

Using the boundary condition displayed in figure 5-5 at the edge of the cylinder, $\psi(r_0) = \zeta$, it is possible to calculate β which gives the distribution of electric potential in a cylinder based on the zeta potential

$$\psi(r) = \zeta \frac{I_0(\kappa r)}{I_0(\kappa r_0)}, \tag{5.25}$$

which matches prior work [96]. Using the Navier-Stokes equation given in equation (5.20) with velocity only acting in the x direction and only varying in the r direction, ρ_e in equation (5.22) and the electric potential given in equation (5.25), we now find the ODE for velocity based on the zeta potential

$$\eta \frac{1}{r} \frac{\mathrm{d}}{\mathrm{d}r} \left(r \frac{\mathrm{d}v}{\mathrm{d}r}(r) \right) = -\epsilon_w \epsilon_0 \kappa^2 \zeta \frac{I_0(\kappa r)}{I_0(\kappa r_0)} E_x,$$

with corresponding boundary conditions based the no-slip condition on the channel walls and that velocity is maximised in the center of the tube:

$$v(r_0) = \left. \frac{\mathrm{d}v}{\mathrm{d}r} \right|_{r=0} = 0.$$

Using standard identities for integrating Bessel functions [100], namely

$$\int u I_0(u) \mathrm{d}u = u I_1(u), \tag{5.26}$$

and

$$\int I_1(u) \mathrm{d}u = -I_0(u), \tag{5.27}$$

the velocity is found to be

$$v = -\frac{\epsilon_w \epsilon_0 \zeta E_x}{\eta} \left(1 - \frac{I_0(\kappa r)}{I_0(\kappa r_0)} \right), \tag{5.28}$$

which not only matches prior theory [96] but, in the case of a thin electric double layer, the velocity reduces to be exactly the same as that found in the 1D case, in equation (5.17). In the non-thin case, the velocity profile is shown in figure 5-6.

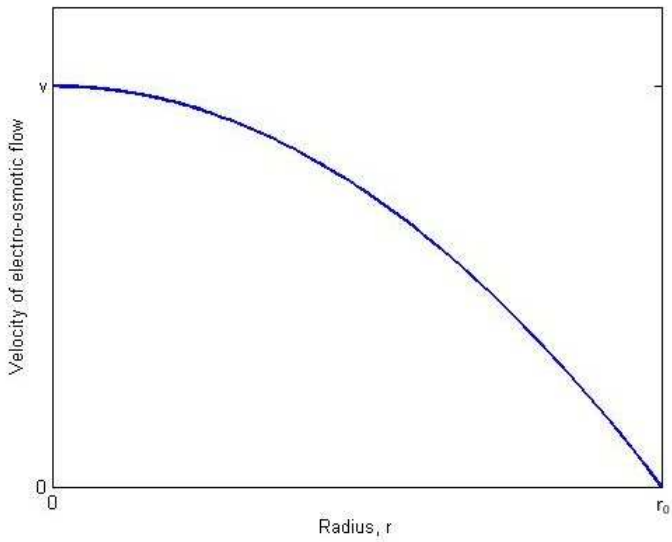

Figure 5-6: Plot of how velocity varies with distance in a radial direction from the center of the cylinder in the non-thin double layer case. Velocity reaches a maxima in the middle of the channel.

Finding the zeta potential

Having found the velocity profile based on the zeta potential, we now attempt to find the zeta potential based on the surface charge density. This starts in much the same way as in the one dimensional case, where we use the electro-neutrality assumption to say that the surface charge density on the channel walls is matched by the net charge density in the fluid

$$\int_A \sigma \mathrm{d}A = -\int_V \rho_e \mathrm{d}V,$$

where A is the surface area and V the volume. Under the assumption that the charge is distributed evenly across the channel walls and the channel is uniform with respect to x

$$\pi h L \sigma = -2\pi L \int_0^{r_0} \rho_e(r) \mathrm{d}r,$$

and using the definition of $\rho_e(r)$ under a low potential in equation (5.22)

$$\sigma = \frac{1}{r_0}\int_0^{r_0} 2rN_a e c_0 \frac{e\psi}{k_B T}\mathrm{d}r = \frac{2N_a e^2 c_0}{k_B T r_0}\int_0^{r_0} r\psi \mathrm{d}r,$$

which can be combined with equation (5.25), which gives the electric potential in terms of a Bessel function, to give the integral:

$$\sigma = \frac{2N_a e^2 c_0 \zeta}{k_B T r_0 I_0(\kappa r_0)}\int_0^{r_0} r I_0(\kappa r)\mathrm{d}r. \tag{5.29}$$

Using the identities for the integrals of Bessel functions given in equations (5.26) and (5.27) [100] and the substitution $\alpha = \kappa r$, we can solve (5.29) to give:

$$\sigma = \frac{\epsilon_w \epsilon_0 \zeta \kappa I_1(\kappa r_0)}{I_0(\kappa r_0)}.$$

Hence, the electro-osmotic velocity in the cylindrical case is:

$$v(r) = \frac{-\sigma E_x I_0(\kappa r_0)}{\eta \kappa I_1(\kappa r_0)}\left(1 - \frac{I_0(\kappa r)}{I_0(\kappa r_0)}\right). \tag{5.30}$$

As demonstrated in section 2.8, modified Bessel functions of the first kind are monotonically increasing with the ratio between two modified Bessel functions of the first kind tending to one as $\kappa r_0 \to \infty$. Hence, considering a thin double layer, in which $r_0 >> \kappa^{-1}$, and the velocity away from the double layer, $r \approx r_0$, results in

$$v = \frac{-\sigma E_x}{\eta \kappa} \tag{5.31}$$

which is the same as the one-dimensional case. Hence, calculating electro-osmotic flow in a cylinder and as a one dimensional channel only has a significant difference when considering effects close to the double layer or in the case where the tube radius is close to the size of the double layer. This is demonstrated in figure 5-7 for variation through the tube. Figure 5-8 shows the difference in velocity in the center of the tube as r_0 increases and demonstrates that the difference between the approaches tends to zero as the channel becomes much larger

than the Debye length.

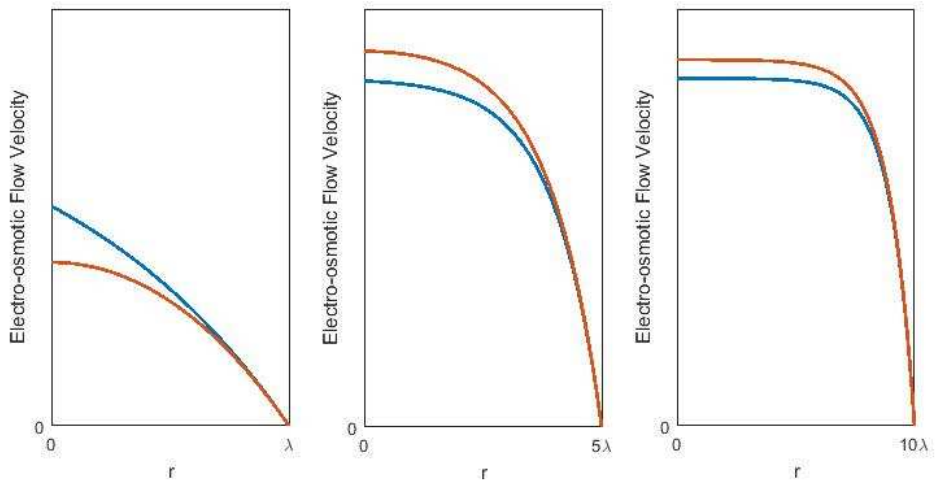

Figure 5-7: Comparison of the electro-osmotic velocity predicted in the 1D system (blue) and cylindrical system (red) for a variety of tube sizes.

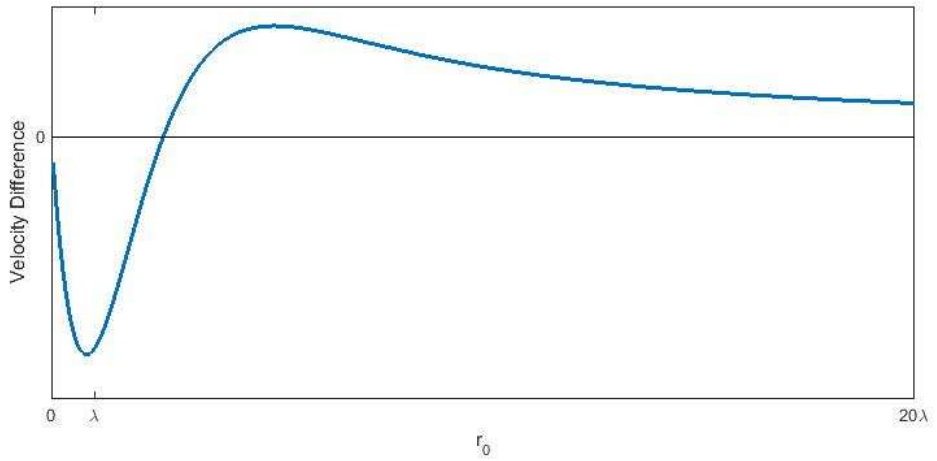

Figure 5-8: This figure demonstrates the difference between the cylindrical velocity and the 1D velocity in the center of a channel of radius r_0. As is observed in figure 5-7, the 1D velocity is greater than the cylindrical velocity when r_0 is comparable to λ with this reversing as the channel gets larger.

5.8 Surface Charge Density Calculation

Having established the electro-osmotic flow velocity in terms of known parameters and the surface charge density for both the parallel plate and cylindrical channel geometries, we now consider methods for finding the surface charge density.

5.8.1 Average Charge Concentration in the Fluid

Surface charge in the channel is caused by a surface absorbing unequal charges of positive and negative ions from the surrounding fluid. In order to maintain an electro-neutral system, this surface charge must be exactly matched by an opposite charge within the fluid, the net charge density. Hence we have that the sum of charge through the fluid volume, V, is equal to the sum of charge over the channel surface, S:

$$\int_V \rho_e \mathrm{d}V = -\int_S \sigma \mathrm{d}S.$$

Prior work has investigated finding the average charge concentration in the fluid, δ_c, in the channel based on the bulk concentration of the ionic solvent and experimentally derived parameters [87]. By definition

$$\delta_c = \frac{1}{N_a e V} \int_V \rho_e \mathrm{d}V,$$

hence by the electro-neutrality assumption:

$$\delta_c = \frac{-1}{N_a e V} \int_S \sigma \mathrm{d}S.$$

It is assumed that the surface charge density is uniform at the channel and tube walls, hence

$$\sigma = -N_a e r_0 \delta_c,$$

for the parallel plate case and

$$\sigma = -\frac{N_a e r_0 \delta_c}{2},$$

for the cylindrical case. Using equations (5.19) and (5.30) we obtain the velocities of electro-osmotic flow for the non-thin parallel plate and cylinder case respectively

$$v = \frac{N_a e r_0 \delta_c E_x}{\kappa \eta}(1 - \exp(-\kappa y)),$$

$$v(r) = \frac{N_a e r_0 \delta_c E_x I_0(\kappa r_0)}{2\eta\kappa I_1(\kappa r_0)} \left(1 - \frac{I_0(\kappa r)}{I_0(\kappa r_0)}\right). \tag{5.32}$$

Having established expressions for velocity in terms of channel dimensions and ionic charge concentration in the solvent for both the parallel plate and cylindrical channel cases, we now consider how to calculate ionic concentration based on the bulk electrolyte concentration. There are two approaches for this, the first, named the Donnan approach [87], considers a low bulk electrolyte concentration and hence ignores saturation effects. The second, the adsorption isotherm approach, considers the ionic concentration when saturation effects begin to become significant.

Donnan Approach

The Donnan approach links the average charge concentration in the fluid to the bulk electrolyte concentration [87] using the Nernst-Planck equation in a strong, 1-1 electrolyte solution where electro-migration dominates the flow of ions. The result of this was that

$$\delta_c = c_0 \frac{\theta}{\sqrt{1-\theta}}, \tag{5.33}$$

where c_0 is the bulk concentration of the salt and

$$\theta = -\frac{D_+}{D_-}\left(\frac{1}{t_+^M} - \frac{1}{t_+^w}\right),$$

where D_+ and D_- are the aqueous diffusion coefficient of the cation and anions respectively, in this case Na^+ and Cl^-, and t_+^M and t_+^w are the transport numbers of the cation in the membrane and water. All of these parameters can be found in the literature and are given in tables 5.1 and 5.2.

Hence, δ_c at a bulk electrolyte concentration of 133mM is 39mM which corresponds to a surface charge density of 18.78 mCm^{-3} at a channel radius of 20nm.

Table 5.2: Table of parameters for calculating the ionic charge concentration using the Donan approach.

Parameter	Value	Definition	Reference
D_+	1.344x10^{-5}cm^{2}s^{-1}	Aqueous diffusion coefficient of Na^+	[85]
D_-	2.032x10^{-5}cm^{2}s^{-1}	Aqueous diffusion coefficient of Cl^-	[85]
t_+^M	0.62	Transport number of Na^+ in the membrane	[87]
t_+^w	0.50	Transport number of Na^+ in water	[87]

The calculated value for δ_c is 10 times larger than would be expected for a corresponding KCl solution [87]. This is likely due to saturation of ions in the channel walls, especially for a 133mM solution as saturation is achieved far before this in a corresponding KCl solution [87], hence we consider the adsorption isotherm approach.

Adsorption Isotherm Approach

The Donnan approach is valid when saturation of ionic charge in the channel walls is not a limiting factor. When this saturation does become a factor, the adsorption isotherm approach is used [87] which gives

$$\delta_c = \delta_{max} \frac{bc_0}{1 + bc_0}, \tag{5.34}$$

based on the maximum charge concentration, δ_{max}, and an adsorption constant, b. For the salt KCl, δ_{max} is predicted to be 2.8mM and b to be 0.17mM^{-1} by using electromotive force measurements [87]. As this adsorption is based on the ability of the channel walls to absorb Cl^-, NaCl is likely to give a similar result. At low concentrations, equations (5.33) and (5.34) should be equivalent. For low c_0, $1 + bc_0 \to 1$, hence comparing equations (5.33) and (5.34) results in

$$\delta_{max} b \approx \frac{\theta}{\sqrt{1-\theta}}, \tag{5.35}$$

which suggests that $\delta_{max} b = 0.294$ for sodium chloride. Without specific experiments into streaming potential through human skin with sodium chloride, as has been performed for potassium chloride, it is not possible to separate δ_{max} and b without experimental data.

Analysis

If we consider the electro-osmotic velocity given in equation (5.32) with δ_c given by the adsorption isotherm approach in equation (5.34) then the complete expression for electro-osmotic flow velocity is given by

$$v(r) = \frac{N_a e \delta_{max} r_0 E_x}{2\eta\kappa} . \frac{I_0(\frac{\kappa h}{2})}{I_1(\frac{\kappa h}{2})} . \frac{bc_0}{1+bc_0} \left(1 - \frac{I_0(\kappa r)}{I_0(\kappa r_0)}\right), \tag{5.36}$$

where:

$$\kappa = \sqrt{\frac{2N_a c_0 e^2}{\epsilon_w \epsilon_0 k_B T}}.$$

Estimates for intercellular pore radius in the literature vary from 0.5nm [101] to 20nm [87] with hair follicles having a pore radii varying between 50μm and 200μm depending on body location and inter-person variability [102]. Using parameters from the literature given in table 5.1, the Debye length at human body temperature is approximately 0.8nm. Hence for all but the smallest pore radii

$$v(r) \rightarrow \frac{N_a e \delta_{max} r_0 E_x}{2\eta\kappa}, \quad r_0 >> \kappa^{-1}, \tag{5.37}$$

which is proportional to pore radii, r_0, as demonstrated in figure 5-9, and is contrary to prior work into electro-osmotic flow effects in nano- and micro- fluid systems [88]. The difference in pore diameter will result in a minimum velocity difference of order 10^3 between hair follicles and intercellular space. Considering an applied field of 1V through a hair follicle results in an electro-osmotic flow velocity of order 10^{-2}ms^{-1} - which, considering L is approximately 20μm [18], would mean that compounds would travel completely through hair follicles in the stratum corneum in a fraction of a second.

Additionally, the zeta potential predicted in hair follicles becomes of the order of 5V which is much greater than the 25mV and hence violates the small potential assumption on the electric double layer.

This suggests that using δ_c to find surface charge density, and hence electro-osmotic flow

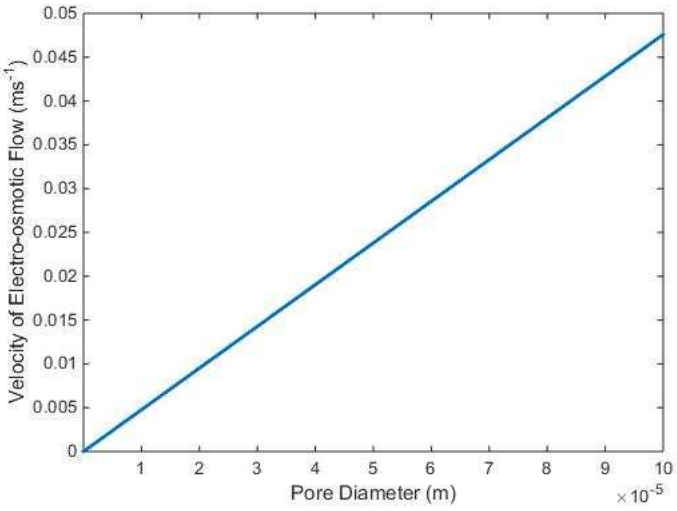

Figure 5-9: Demonstrating the dependence of electro-osmotic flow velocity on pore diameter.

velocity, is unsuitable when moving from nano-scale pore radii to micro-scale pore radii as the resulting velocity scales linearly with pore size. Due to this, we propose that the limiting law on ionic concentration in the solvent should instead be a limiting law on the surface charge density as the limit is due to saturation of charge within the pore walls.

5.8.2 Modifications to Surface Charge Modelling

As identified in the previous section, the velocity of electro-osmotic flow through hair follicles is very large due to an extremely large surface charge resulting in a zeta potential of approximately 5V, far above the limit of 25mV previously suggested in theory. We showed that, in this case, v was dependant on pore size, contradicting prior nano- and micro-fluid work [88]. This is unrealistic suggesting that the theory needs to be modified when considering micro-channels.

We consider three different approaches to calculating surface charge density that will stop the velocity scaling linearly with pore radius. We begin by considering the simplest case by having surface charge density linearly dependent on the bulk concentration of the fluid

$$\sigma = Ac_0, \tag{5.38}$$

where A is a constant based on the system considered. The second approach, in line with

other micro-fluid theory [90], extends this relation to impose a limit on charge absorbed by the tube surfaces. This is reflected by limiting the surface charge density using the adsorption isotherm approach

$$\sigma = \sigma_{max} \frac{b_\sigma c_0}{1 + b_\sigma c_0}, \tag{5.39}$$

where σ_{max} is the maximum possible surface charge and b_σ is the adsorption constant. Previous research into streaming potential in the skin has been used to identify ionic charge concentration in the fluid under the assumption that this is limited rather than the surface charge density [90] and additionally suggested that a more accurate approach would be to use a Freundlich isotherm of the form

$$\sigma = \sigma_{max} \frac{b_\sigma c_0^n}{1 + b_\sigma c_0^n}, \tag{5.40}$$

in order to account for chloride ions adsorption into the pore wall with a quasi-normal distribution of binding energies [90]. For the purpose of estimating parameters, we consider the double layer to be thin.

Putting the velocity given in equation (5.30) in terms of the surface charge in the linear approach gives

$$v = \frac{A c_0 E_x}{\kappa \eta} . \frac{I_0(\kappa r_0)}{I_1(\kappa r_0)}, \tag{5.41}$$

the adsorption isotherm approach gives

$$v = \frac{E_x I_0(\kappa r_0)}{\kappa \eta I_1(\kappa r_0)} . \frac{\sigma_{max} b_\sigma c_0}{1 + b_\sigma c_0}, \tag{5.42}$$

and in the Freundlich isotherm case gives

$$v = \frac{E_x I_0(\kappa r_0)}{\kappa \eta I_1(\kappa r_0)} . \frac{\sigma_{max} b_\sigma c_0^n}{1 + b_\sigma c_0^n}, \tag{5.43}$$

Table 5.3: Table summarising streaming potential results from prior work [87]. We also consider Debye length based on the bulk concentration c_0.

$\mathbf{c_0(mM)}$	$\boldsymbol{\nu}$**(nV/Pa)**	$\boldsymbol{\lambda}$**(nm)**
1	-85.9	9.54
5	-36.1	4.27
10	-20.5	3.02
50	-3.48	1.35
100	-2.26	0.95

all of which, for $r_0 >> \lambda$, are independent of pore size as would be expected.

Parameter Estimation

In order to estimate A, σ_{max}, b_σ and n for our three approaches, prior work into streaming potential through human skin was considered [87]. Details of streaming potential are given in section 5.6.4 and the experimental results summarised in table 5.3.

As a first approximation, we consider the pore size to be much larger than the Debye length and use the expression for streaming potential and conductivity in equations (5.7) and (5.6) respectively to give

$$\nu = \frac{2Ac_0\lambda^3}{\eta\epsilon_0\epsilon_w(D^+ - D^-)}, \tag{5.44}$$

in the linear case, detailed in equation (5.38),

$$\nu = \frac{2\sigma_{max}\lambda^3}{\eta\epsilon_0\epsilon_w(D^+ - D^-)}.\frac{b_\sigma c_0}{1 + b_\sigma c_0}, \tag{5.45}$$

for the adsorption isotherm case, detailed in equation (5.39), and

$$\nu = \frac{2\sigma_{max}\lambda^3}{\eta\epsilon_0\epsilon_w(D^+ - D^-)}.\frac{b_\sigma c_0^n}{1 + b_\sigma c_0^n}, \tag{5.46}$$

in the Freundlich isotherm case, detailed in equation (5.40).

We use equations (5.44), (5.45) and (5.46) in combination with the results in table 5.3 to obtain estimates for A, b_σ, σ_{max} and n focusing around the results obtained at higher c_0 values due to the Debye length being smaller and compare the results. Figure 5-10 plots the predicted streaming potential using $A = 4.16\text{x}10^{-8}\text{m}^3\text{mol}^{-1}$ for the linear case, $\sigma = 2.97\text{mCm}^{-2}$ and $b = 0.0016\text{molm}^{-3}$ for the adsorption isotherm approach and $\sigma_{max} = 14.2\text{mCm}^{-2}$, $b = 0.0066\text{molm}^{-3}$ and $n = 0.167$ for the Freundlich isotherm.

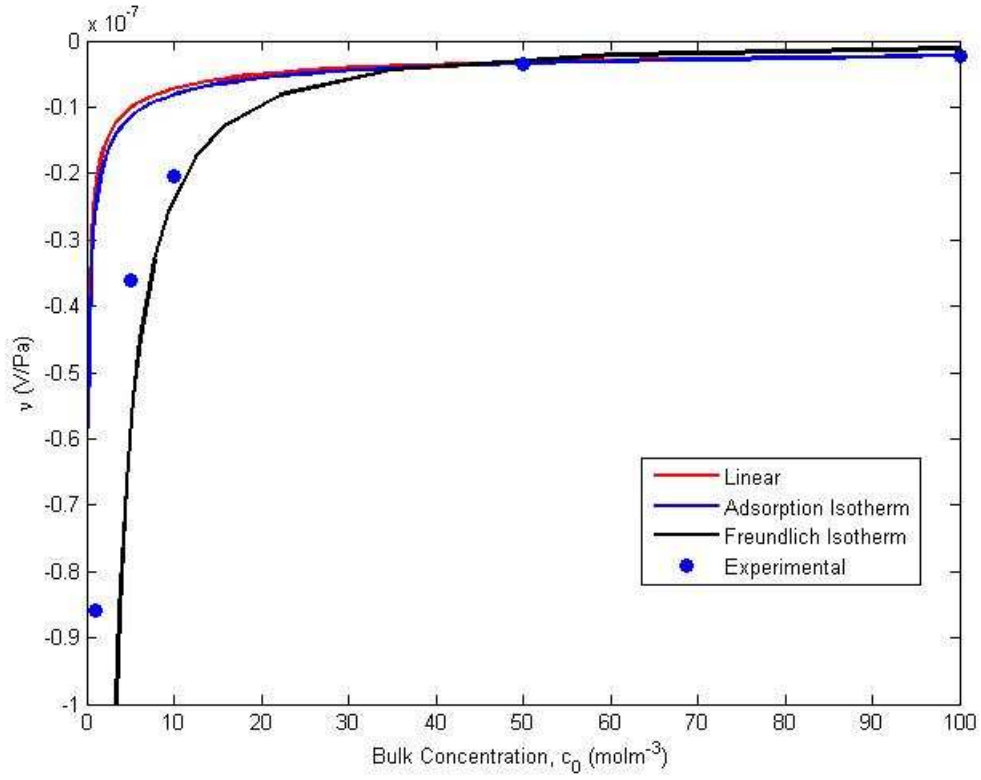

Figure 5-10: Comparison of the three different approaches to modelling surface charge density compared to experimental data. Due to the limited number of points and potentially high variability it is difficult to say which approach is most suitable.

All three approaches predict similar surface charge densities at high concentrations, but differ significantly at low concentrations with the Freundlich approach seeming to mirror the data closest. It is worth noting that at low concentrations, the Debye length increases which could make the thin double layer assumption invalid and the small sample size makes it difficult to identify experimental error. To validate these predicted parameters, more experimental work is required.

As the bulk salt concentration of the PBS buffer used in iontophoresis experiments for phenylalanine is 133mM [1, 2], issues at low concentrations are not key to this research. At 133mM, the streaming potentials, and corresponding surface charge predicted for each of

Table 5.4: Comparison of the streaming potential and surface charge density predicted by each of the three approaches at 133mM.

Approach	**Streaming Potential (nV/Pa)**	$\boldsymbol{\sigma}$ **(μCm^{-2})**
Linear	-1.98	553
Adsorption Isotherm	-1.87	521
Freundlich Isotherm	-0.76	208

the three approaches are given in table 5.4.

The sample size used to predict these measurements is very small, hence doing a full statistical analysis is not appropriate. We instead consider the surface charge density at bulk NaCl concentration of 133mM to be in the range [208,521]μCm^{-2} with a mean of 427μCm^{-2}.

5.9 Chapter Summary

In this chapter we have presented methods of predicting the electro-osmotic flow velocity in both a 1D and cylindrical channel using a combination of surface chemistry, electromagnetism and fluid dynamics in a thin and non-thin double layer. As the amino acids we are considering are uncharged, we do not consider electro-migration. The overall objective of the chapter was to present the electro-osmotic velocity in terms of parameters that could be found or derived from the literature.

In both the 1D and cylindrical cases, the derivation of flow velocity started by considering the incompressible Navier-Stokes equations under an applied body determined by the external electric field. Doing this allows the velocity of electro-osmosis to be calculated in terms of the double layer potential.

Considering the potential using a mean field approximation, the Poisson-Boltzmann equation then links the double layer potential to the zeta potential which allows the electro-osmotic flow velocity to be expressed in terms of the zeta potential and position in the tube.

Having obtained this, we then moved on to consider finding the zeta potential in terms of surface charge by using the Poisson-Boltzmann equation and considering the system to be electro-neutral. This led to respective velocity equations for the 1D and cylindrical system of

$$v(y) = \frac{-\sigma E_x}{\kappa\eta}(1 - \exp(-\kappa y)), \tag{5.47}$$

$$v(r) = \frac{-\sigma E_x I_0(\kappa r_0)}{\eta \kappa I_1(\kappa r_0)} \left(1 - \frac{I_0(\kappa r)}{I_0(\kappa r_0)}\right), \tag{5.48}$$

which were compared in figure 5-7. Comparison suggests that velocity increases away from the channel walls, reaching a maxima in the center of the channel and that the difference between the two approaches decreases as the pore size becomes much greater than the Debye length. Indeed, in the case of a thin double layer, both models result in

$$v = \frac{-\sigma E_x}{\kappa \eta}, \tag{5.49}$$

which is the Helmholtz result [90]. Considering the case of a thin electric double layer, it is possible to find all parameters except surface charge directly from the literature and consideration of the field applied to the channel. In order to approximate surface charge density, we considered several approaches starting with calculating the average charge concentration in the fluid and using the electro-neutrality assumption, as has been considered in previous work [87]. Average charge concentration in the fluid was considered to be based on the bulk concentration of the ionic salt which saturates as bulk concentration tends to infinity. We showed that this approach results in an electro-osmotic velocity that is directly proportional to the pore radius, violating prior work into nano- and micro-fluids [88]. Hence this approach is not appropriate for considering both nano-channels through the intercellular space and micro-channels through the hair follicles.

It was then proposed, again in line with prior surface chemistry work [90], that this limiting effect was instead on the surface charge density directly. This meant that velocity did not scale directly with pore radius making this approach appropriate for both nano- and micro-fluid systems. We considered three different approaches to the behaviour of surface charge based on the bulk concentration of the ionic salt namely linear, adsorption isotherm and Freundlich isotherm and compared these approaches to experimental results for streaming potential in the case of a thin double layer [87]. Due to the limited data available, it was not possible to say which was the best approach out of these three, although prior literature favours the Freundlich approach [90]. At 133mM this lead to a range of [208,521]μCm^{-2} for surface charge density. More experimental work into streaming potential through human skin would help verify which of these approaches was most suitable and provide more data points for better estimation of parameters, especially for the Freundlich isotherm approach which attempts to estimate 3 unknown parameters from 5 data points.

Overall we have combined information from several fields in order to find a working theory

and parameters for electro-osmotic flow velocity through human skin based on the applied field and known properties of fluid. More experimental work would be required to validate some of these parameters, especially those associated with surface charge density over a range of ionic salts and concentrations.

In the next chapter, we will use the theories on electro-osmotic velocity to model and test fluid flows through the skin under an electric current.

Chapter 6

Reverse Iontophoresis

6.1 Chapter Objective

In the previous chapters we have established models for blood serum concentration and skin distribution of amino acids, specifically phenylalanine. We have also presented electro-osmotic flow in terms of known or derived parameters.

The objective of this chapter is to combine all of this work into an extraction model for phenylalanine under both passive extraction and extraction via reverse iontophoresis. An initial model is formed and compared to *in vitro* and *in vivo* prior work [1, 2, 42]. We also consider *in vivo* extraction of phenylalanine from patients with phenylketonuria (PKU) to assess the possibility of identifying higher systemic levels of phenylalanine via transdermal extraction [103].

This chapter then considers extensions to the initial model and proposes future avenues of theoretical and supporting experimental development.

6.2 Parameters

Table 6.1 lists the key parameters for extraction through the skin as a reference for this chapter. As hair follicles have been previously identified as a potential extraction route, table 6.2 details the density, shaft diameter and orifice diameter of hair follicles at various body sites.

Table 6.1: Table of parameters and variables. Values of known parameters are given ± one standard deviation. $i = 1$ represents the stratum corneum intercellular space, $i = 2$ the viable epidermis intercellular space and $i = 3$ the hair follicle. Stratum corneum is denoted SC and viable epidermis VE. Refences are not listed for surface charge density in pores and the Debye length as these are the combination of several parameters and theories detailed in work into electro-osmotic flow in chapter 5. Other unreferenced parameters are usually a combination of other parameters listed in the table. Where explicit values are not given, units are listed if appropriate.

Description	**Symbol**	**Value**	**Reference**
Aqueous diffusion coefficient	D	$9.11\pm0.5\text{x}10^{-10}\text{m}^2\text{s}^{-1}$ (PHE) $10.8\pm0.5\text{x}10^{-10}\text{m}^2\text{s}^{-1}$ (MAN)	[85]
Diffusion coefficient in stratum corneum (PHE)	D_{SC}	$8.91\pm4.5\text{x}10^{-15}\text{m}^2\text{s}^{-1}$	[70, 34]
Length of stratum corneum intercellular pathway	L_1	$6.96\pm2.34\text{x}10^{-4}\text{m}$	[71, 104]
Total length of intercellular pathway	L_2	$7.85\pm2.34\text{x}10^{-4}\text{m}$	[42, 71, 72]
Total length of hair follicle pathway	L_3	10^{-4}m	[42]
Stratum corneum - water partition coefficient	k	0.25 (PHE) 0.4±0.2 (MAN)	[105, 70]
Source/subdermal concentration	C_s	See specific case	-
Depth of the viable epidermis	L_{VE}	$85.2\pm4.8\text{x}10^{-6}\text{m}$	[2, 104]
Depth of stratum corneum	L_{SC}	$14.8\pm4.8\text{x}10^{-6}\text{m}$	[104]
Depth of stratum disjunctum	d	$4.15\pm1.39\text{x}10^{-6}\text{m}$	[2]
Velocity of cells in the stratum corneum	v_c	$1.65\pm0.58\text{x}10^{-11}\text{ms}^{-1}$	[69]
Unit cell volume ratio between SC and VE	ψ	8.19	[71, 72]
Potential difference applied across the skin	$\Delta\phi$	See specific case (V)	-

Current across the skin	I	See specific case (mA)	-
Skin resistivity	ρ	$8x10^4 Sm^{-1}$	[106]
Velocity of electro-osmotic flow in i	v_i	ms^{-1}	-
Area fraction occupied by SC intercellular route	A_1	-	-
Area fraction occupied by VE intercellular route	A_2	-	-
Area fraction occupied by hair follicles	A_3	See table 6.2	[102]
Maximum surface charge density in pores	σ_{max}	$2.97x10^{-3}$ Cm^{-2}	-
Surface charge adsorption coefficient	b_σ	0.0016 m^3mol^{-1}	-
Dynamic viscosity of PBS buffer	η	$7x10^{-4}$ Nsm^{-2}	[85]
Debye length	$\lambda_D = {}^1/_\kappa$	0.83 nm	-
Faraday constant	F	$9.65x10^4 Cmol^{-1}$	[85]
Tortuosity constant in SC intercellular space	τ_1	0.021±0.007	-
Tortuosity constant in viable epidermis intercellular space	τ_2	0.957	-
Production rate of phenylalanine in human SC	k_p	$[0.08,0.25]mmolm^{-3}s^{-1}$	-
Removal constant in the stratum disjunctum	γ	$[0.58,3.25]m^{-1}s^{-1}$	-

Table 6.2: Hair follicle properties in different skin areas [102].

Location	**Density (m^{-2})**	**Orifice diameter (m)**	**Shaft diameter (m)**	**Area fraction**
Forehead	$29.2±4.4x10^5$	$66±52x10^{-6}$	$16±8x10^{-6}$	$94.0x10^{-4}$
Back	$2.9±0.5x10^5$	$105±60x10^{-6}$	$18±7x10^{-6}$	$24.0x10^{-4}$
Thorax	$2.2±0.5x10^5$	$100±40x10^{-6}$	$17±6x10^{-6}$	$17.0x10^{-4}$
Upper arm	$3.2±0.7x10^5$	$85±35x10^{-6}$	$17±6x10^{-6}$	$17.0x10^{-4}$
Forearm	$1.8±0.4x10^5$	$78±30x10^{-6}$	$18±6x10^{-6}$	$8.1x10^{-4}$
Thigh	$1.7±0.2x10^5$	$125±45x10^{-6}$	$29±12x10^{-6}$	$20.0x10^{-4}$

Calf	$1.4\pm0.4x10^{5}$	$170\pm40x10^{-6}$	$42\pm11x10^{-6}$	$30.0x10^{-4}$
Abdomen	$0.6x10^{5}$	$70x10^{-6}$	$17\pm6x10^{-6}$	$2.2x10^{-4}$

6.3 Background Information

6.3.1 Reverse Iontophoresis

Iontophoresis is the enhanced delivery of compounds through the skin via the application of a small electric current. This technique has been used since the early 20th century to treat various disorders, as detailed in chapter 1 [36]. Reverse iontophoresis is iontophoresis applied in reverse so instead of delivering compounds through the skin, the focus is extraction of compounds already in the skin [21].

As we have detailed basic reverse iontophoresis principles and its application potential in chapter 1, this section focusses on prior mathematical modelling techniques for reverse iontophoresis. As the focus of this thesis is large, uncharged compounds, we tend to focus around papers that consider electro-osmotic flow.

Prior work suggests that for small ions, electro-migration dominates flux through the skin [33]. Hence, when modelling extraction of small ions through the skin, electro-osmotic flow effects are frequently considered negligible [21, 36, 38, 107]. Interestingly, work into electro-migration suggests that the electro-migration flux is proportional to the electric field applied [36, 91]. As shown in chapter 5, electro-osmotic velocity is also proportional to the electric field applied. By definition, electric field strength is equal to the potential gradient in the system so fixing the voltage would make the system easier to model, especially considering previous work has shown that skin resistance changes over time based on voltage applied [91, 105]. However, due to the dangers of high currents to living creatures, current is fixed in many *in vivo* and *in vitro* reverse iontophoresis experiments [1, 2]. Noticeably, it is rare that voltage is measured in these experiments, which could contribute significantly to the error observed in these experiments and the time taken to achieve steady state.

Considering electro-osmotic transport through skin, the most prevalent approaches appear to be either experimentally considering permeability of individual compounds through the stratum corneum [42] where permeability, P, is defined as:

$$P = -\frac{J^*(0)A_s}{C_s}, \tag{6.1}$$

where $J(x)$ is the flux at spatial co-ordinate x, where $x = 0$ represents the skin surface, A_s is the surface area of skin considered and C_s is the source concentration. $J^*(x)$ represents the steady state flux hence $J^*(0)$ is the steady state flux at the skin surface. Another approach

is to consider the Nernst-Planck flux

$$N_i = -\frac{D_i z_i F}{RT} c_i \nabla \phi - D_i \nabla c_i + v c_i,$$

where N_i is the flux density, D_i the diffusion coefficient, z_i the valence of species i, F is the Faraday constant, R is the gas constant, T is the temperature and v is the electro-osmotic flow velocity. The electro-osmotic flow velocity is then calculated using Onsager coefficients, as discussed in chapter 5.

The permeability approach is an empirically calculated value, whereas the Nernst-Plank equation is based on theoretical work. There are advantages and disadvantages to both approaches. The theoretical approach is based on validated theories and hence can model real life with significant confidence, but generally requires a deep understanding of the mechanisms driving the system which can be very complex or not fully known. An empirical approach is must faster and allows complicated models to be simulated via a more simple mechanism which can be especially useful if the simplified results are then used in another model.

6.3.2 Hair Follicles

One of the routes of extraction through skin samples is considered to be through appendages, such as hair follicles, through the skin. Although appendage routes only cover approximately 0.1% of the skin surface it has been suggested that they play a critical role in extraction [32, 102].

Figure 6-1 demonstrates a hair follicle penetrating through the epidermis and bypassing the tortuous lipid matrix that is the stratum corneum. The body of the hair follicle in this case is called the shaft and the pore containing it the orifice. The shaft and orifice have different diameters in different sites as demonstrated in table 6.2 and it is considered that transport through the hair follicle route will occur in the orifice space not occupied by the hair shaft.

Noticeably, in the pharmaceutical case, there is not much consideration of area fraction of the skin utilised in transport or the split between intercellular, intracellular and hair follicle extraction. Indeed, for the most part hair follicles seem to be ignored in theoretical treatment of the skin with flow considered to occur through pores with sizes estimated between 0.675nm and 20nm, which ignores micro-fluid flows that would occur through hair follicles through the stratum corneum [33, 87, 91].

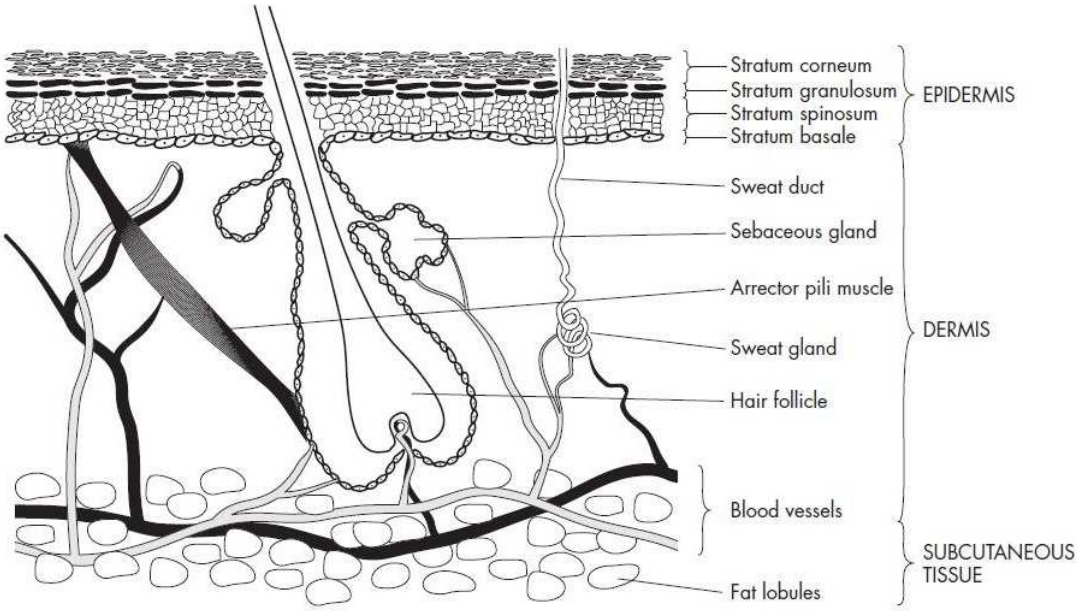

Figure 6-1: Cross section of human skin showing a hair follicle through the stratum corneum. As an initial approximation, the hair follicle is considered to be uniform through the epidermis. Taken from [19].

Prior experimental work using scanning electrochemical microscopy (SCEM) has identified that there is significant flux of large, uncharged compounds - specifically acetaminophen - through hair follicles through the stratum corneum with almost no transport observed through the intercellular space over the time period considered [32]. As hair follicles occupy a very small fraction of the skin surface area and are a much less tortuous pathway than the intercellular route, it is important to consider this extraction route separately. Even though the experiment considering acetaminophen extraction showed no flux through the intercellular space, it is important to note that acetaminophen does not occur naturally in the skin, steady state was considered to be reached after 30 minutes of extraction and identified some penetration into the intercellular space [32]. This might mean that the time considered was not sufficient for the acetaminophen to fully penetrate the intercellular space route.

6.3.3 Hindrance Modelling

Hindered transport models have been previously utilised to characterise flows through capillaries in channels through porous membranes [35]. Hindered transport theory includes inter-particle and particle-wall interactions. These interactions become of concern in transport systems where the channel is comparable to the size of the particle. Curvature effects

are also considered which are of concern in both small and large channels. The general form for flux in this case is analogous to the Nernst-Planck expression

$$N_i = \tau \left[-HD_i \left(\frac{z_i F c_i}{RT} \nabla \phi + \nabla c_i \right) + W v c_i \right],$$

where τ is the tortuosity of the system, H and W represent the hindrance factors for diffusion and advection respectively and are based on the radius of the channel. Tortuosity characterises the curvature and interconnectedness of the pore space and is used to relate transport properties of the porous structure to its microscopic structure [108]. Tortuosity is often empirically measured and is commonly estimated to be the length of the curve divided by the the distance between the ends of it [109]. Prior work has derived expressions for H and W empirically [110]

$$H(\lambda_*) = (1-\lambda_*)^2(1 - 2.144\lambda_* + 2.089\lambda_*^3 - 0.0948\lambda_*^5),$$

$$W(\lambda_*) = (1-\lambda_*)^2(2 - (1-\lambda_*)^2)(1 - \frac{2}{3}\lambda_*^2 - 0.163\lambda_*^3),$$

$$\lambda_* = \frac{r_{pa}}{r_p},$$

where r_p is the radius of the pore and r_{pa} is the radius of the particle of interest. Clearly if $r_p >> r_{pa}$ then $\lambda_* \to 0$ causing H and W to tend to 1. In the case of an uncharged compound, like phenylalanine, in one spatial dimension the hindered transport flux would be of the form

$$N_i = \tau \left[-HD_i \frac{\partial c_i}{\partial x} + W v c_i \right],$$

which further reduces to

$$N_i = \tau \left[-D_i \frac{\partial c_i}{\partial x} + v c_i \right],$$

when the pore size is much larger than the particle size. Along its largest axis, a molecule of phenylalanine has length of order 10^{-10}m hence can be considered small compared to the pore size for all but the smallest estimates of pore size through the intercellular space.

6.4 Initial Model

In order to construct an initial model for reverse iontophoresis through the skin we consider flow through both the interceullar space and hair follicles as demonstrated graphically in Figure 6-2. In order to model the flow, we make several assumptions, namely:

1. All channels are perfectly cylindrical.

2. The electric field applied is constant and uniform in x.

3. The intercellular and hair follicle routes are completely separate.

4. In line with prior theory, we consider cells as highly impermeable at the voltages used in reverse iontophoresis [73]. If the voltage were significantly higher, cells would begin to become permeable due to electroporation.

5. The system is initially considered to only vary in one spatial dimension and time. To do this, the intercellular space route is considered in one spatial dimension, x, with path length equal to the path length of the torturous route through the skin. Although this will not affect the initial concentrations, it will change the surface area considered by the ratio of the path length to the actual distance travelled through the skin.

6. Tortuous path effects are initially considered to be negligible.

7. The electric double layer described in chapter 5 is considered to be thin.

8. We initially consider the skin to follow the circuit diagram given in figure 6-3 where R_1, R_2 and R_3 are constant. It has been previously shown that skin resistance changes with time and voltage applied [105], but not the effect under constant current.

9. Electro-osmotic velocity and diffusion coefficients are constant through the skin.

10. Hair follicles are considered to be unchanged from the viable epidermis to the stratum

corneum.

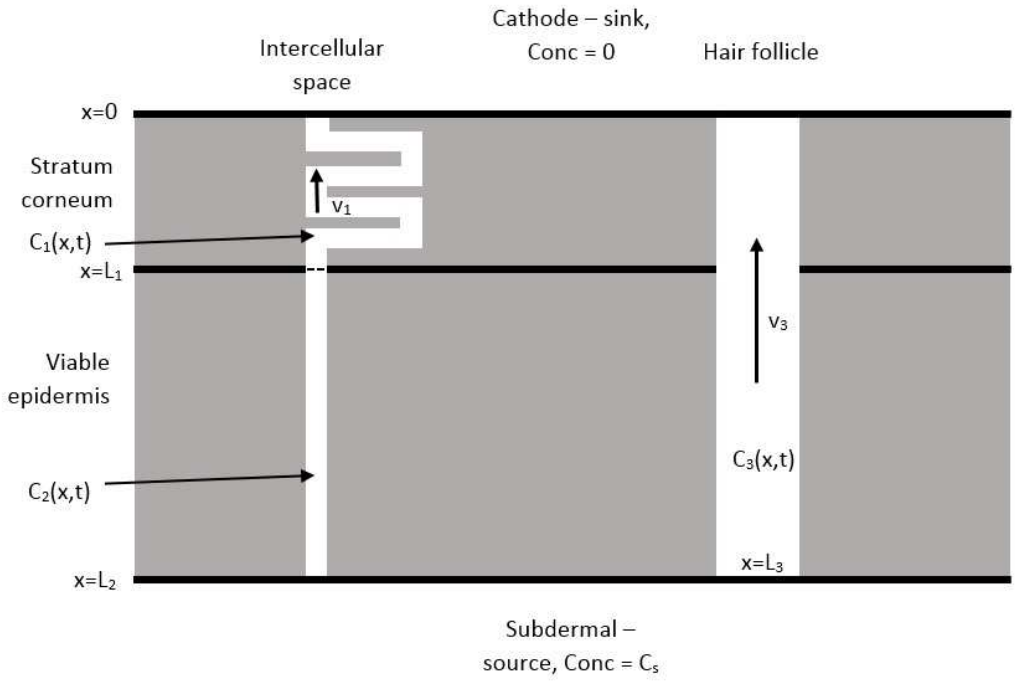

Figure 6-2: Schematic diagram of the initial model. $C_i(x,t)$, $i \in [1,3]$ represents concentration in each compartment with $x = 0$ representing the surface of the skin with depth through the skin increasing with x. The hair follicle is considered to be unchanged through the stratum corneum and viable epidermis whereas the intercellular route is split with boundary conditions at $x = L_1$ given later. Later in the chapter L_1 is extended to the path length of the intercellular route, hence $L_2 \neq L_3$.

Figure 6-2 does not give a velocity of electro-osmotic flow through the intercellular viable epidermis because the skin is initially modelled according to the circuit diagram given in Figure 6-3. As the resistance through the stratum corneum, R_1 is much larger than through the intercellular space, R_2, for low frequency AC or DC currents [106], the potential drop over the viable epidermis will be negligible compared to that over the stratum corneum. Hence, as velocity of electro-osmotic flow is proportional to the potential gradient, the velocity of electro-osmosis in the viable epidermis intercellular pathway is considered to be negligible.

The resistivity of the stratum corneum has been previously found to be $8\text{x}10^4\text{Sm}^{-1}$. This value, in combination with L_1 and Ohm's law [98], will be used to calculate the voltage across the stratum corneum in the case of constant current density.

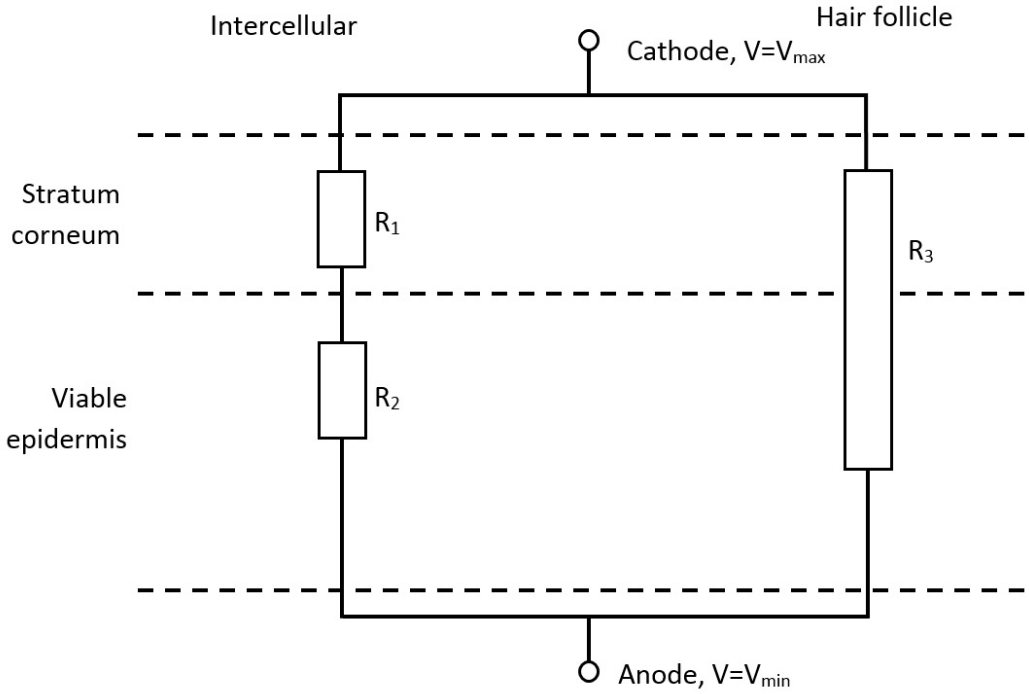

Figure 6-3: Initial circuit diagram through the skin. Although there are much more complex effects through the skin, this is sufficient to demonstrate why electro-osmotic flow does not occur through the intercellular space in the viable epidermis. Resistance of each layer is found by considering the resistivity of the layer multiplied by it's length. As this is a parallel circuit, the potential difference across each route will be the same.

6.4.1 Model Formation

The model schematic shown in figure 6-2 results in the following system of governing equations where v_1 and v_3 are non-zero in the case with iontophoresis and zero in the passive case

$$\frac{\partial C_1}{\partial t}(x,t) - D\frac{\partial^2 C_1}{\partial x^2}(x,t) - v_1\frac{\partial C_1}{\partial x}(x,t) = 0, \quad x \in [0, L_1], \quad \forall t \geq 0, \tag{6.2}$$

$$\frac{\partial C_2}{\partial t}(x,t) - D\frac{\partial^2 C_2}{\partial x^2}(x,t) = 0, \quad x \in (L_1, L_2], \quad \forall t \geq 0, \tag{6.3}$$

$$\frac{\partial C_3}{\partial t}(x,t) - D\frac{\partial^2 C_3}{\partial x^2}(x,t) - v_3\frac{\partial C_3}{\partial x}(x,t) = 0, \quad x \in [0, L_3], \quad \forall t \geq 0, \tag{6.4}$$

with corresponding cross sectional surface areas A_1, A_2 and A_3 respectively. We consider the intercellular pathway through the stratum corneum and viable epidermis to occupy the same physical surface area, A, but are required to scale this due to the change in porosity between the two compartments. Porosity measures the fraction of space not occupied by objects in a material and can be calculated by multiplying the surface area occupied by pores by the tortuosity of the path

$$A_1 = \tau_1 A, \tag{6.5}$$

$$A_2 = \tau_2 A, \tag{6.6}$$

where τ_1 and τ_2 are the tortuosity factors of the stratum corneum and viable epidermis respectively:

$$\tau_1 = \frac{L_{SC}}{L_1},$$

$$\tau_2 = \frac{L_{VE}}{L_2 - L_1}.$$

The boundary conditions are based on the cathode compartment on the skin surface, $x = 0$, being a sink

$$C_1(0,t) = C_3(0,t) = 0, \quad \forall t \geq 0, \tag{6.7}$$

on the amount on the stratum corneum/viable epidermis boundary, $x = L_1$, being equal when scaled by partition coefficient, k, to represent the material changes between the stratum corneum and viable epidermis

$$C_1(L_1,t) = kC_2(L_1,t) \tag{6.8}$$

and flux conservation over the stratum corneum/viable epidermis boundary, $x = L_1$:

$$A_1\left(D\frac{\partial C_1}{\partial x}(L_1,t) + vC_1(L_1,t)\right) = A_2\left(D\frac{\partial C_2}{\partial x}(L_1,t)\right), \quad \forall t \geq 0.$$

Hence, using equations (6.5) and (6.6), we obtain:

$$\tau_1\left(D\frac{\partial C_1}{\partial x}(L_1,t) + vC_1(L_1,t)\right) = \tau_2\left(D\frac{\partial C_2}{\partial x}(L_1,t)\right), \quad \forall t \geq 0. \tag{6.9}$$

The final boundary condition is found by considering the donor (anode) compartment as a source, $x = L_2$ or L_3 for the intercellular and hair follicle routes respectively:

$$C_2(L_2,t) = C_3(L_3,t) = C_s, \quad \forall t \geq 0. \tag{6.10}$$

We also consider initial conditions based on previously calculated steady state profiles, given in chapter 3 in the stratum corneum and viable epidermis:

$$C_1(x,0) = \begin{cases} g\left(d\dfrac{L_1}{L_{SC}}\right)\exp\left(\dfrac{-\gamma}{2v_c}(y(x)^2 - 2dy(x) + d^2)\right), & x \in \left[0, d\dfrac{L_1}{L_{SC}}\right], \\ g(y(x)) + \dfrac{k_p D_{SC}}{v_c^2}\left(1 - \exp\left(\dfrac{-v_c(y(x)-d)}{D_{SC}}\right)\right), & x \in \left(d\dfrac{L_1}{L_{SC}}, L_1\right], \end{cases} \tag{6.11}$$

$$g(x) = \frac{k_p(L_{SC} - y(x))}{v_c} + \psi C_s,$$

$$C_2(x, 0) = C_s, \quad x \in (L_1, L_2], \tag{6.12}$$

$$C_3(x,0) = \begin{cases} \left(\dfrac{k(L_{SC}-d)}{v_c} + \psi C_s\right) \exp\left(\dfrac{-\gamma}{2v_c}(x^2 - 2dx + d^2)\right), & x \in [0, d], \\ \dfrac{k(L_{SC}-x)}{v_c} + \dfrac{kD_{SC}}{v_c^2}\left(1 - \exp\left(\dfrac{-v(y(x)-d)}{D_{SC}}\right)\right) + \psi C_s, & x \in (d, L_{SC}], \\ C_s, \quad x \in (L_{SC}, L_3], \end{cases} \tag{6.13}$$

where

$$y(x) = \frac{L_{SC}}{L_1}x,$$

is a correction based on the path length as the initial conditions calculated previously are based on the physical depth of the stratum corneum, L_{SC}, and not adjusted for the length of the intercellular pathway. k_p is the production rate of amino acid in the stratum corneum, d is the depth of the stratum disjunctum, v_c is the velocity of cells towards the surface of the skin, D_{SC} is the diffusion coefficient in the stratum corneum using the Potts and Guy model [34], ψ is the volume ratio between the stratum corneum and viable epidermis and γ is a removal constant for amino acid in the stratum disjunctum. The values for these parameters are given in table 6.1 and discussed in more detail in chapter 3.

From our previous work into electro-osmosis theory, given in chapter 5, we know that the velocity of electro-osmosis, v_i, $i \in [1, 3]$, is based on the Debye length, $\lambda = \kappa^{-1}$, dynamic viscosity of the fluid, η, and the electric field in the x direction through route i, E_{xi},

$$v_i = \pm\frac{\sigma E_{xi}}{\eta\kappa}, \tag{6.14}$$

where the $\pm$ depends upon the definition of the flow direction. The electric field, E_{xi}, is considered uniform and constant during the course of the experiment

$$E_{xi} = \frac{\Delta\phi}{L_i}, \tag{6.15}$$

where $\Delta\phi$ is the potential difference applied and σ is considered to follow the adsorption isotherm approach detailed in section 5.8.2

$$\sigma = \sigma_{max}\frac{bc_0}{1+bc_0},$$

where σ_{max} is the maximum surface charge density and b is the absorption coefficient.

6.4.2 Model Analysis

In order to analyse steady state behaviour, we consider the steady state solutions, $C_i(x,t) = C^*_{ip}(x)$, $i \in [1,2,3]$, of equations (6.2), (6.3) and (6.4) under the corresponding boundary conditions in the passive case where $v_1 = v_3 = 0$

$$C^*_{1p}(x) = C_s\frac{kx}{L_1 + k\delta(L_2 - L_1)}, \quad x \in [0, L_1], \tag{6.16}$$

$$C^*_{2p}(x) = C_s\frac{k\delta(x - L_1) + L_1}{L_1 + k\delta(L_2 - L_1)}, \quad x \in (L_1, L_2], \tag{6.17}$$

$$C^*_{3p}(x) = C_s\frac{x}{L_3}, \quad x \in [0, L_3], \tag{6.18}$$

where:

$$\delta = \frac{\tau_1}{\tau_2}.$$

In the reverse iontophoresis case at steady state, $C_i(x,t) = C^*_{ir}(x)$, $i \in [1,2,3]$, where $v_1 \neq 0$ and $v_3 \neq 0$:

$$C^*_{1r}(x) = C_s \frac{kD}{D(1-\exp(\frac{-v_1 L_1}{D})) + kv_1\delta(L_2 - L_1)} \left(1 - \exp\left(\frac{-v_1 x}{D}\right)\right), \quad x \in [0, L_1], \quad (6.19)$$

$$C^*_{2r}(x) = C_s \frac{k\delta v_1(x - L_1) + D(1-\exp(\frac{-v_1 L_1}{D}))}{D(1-\exp(\frac{-v_1 L_1}{D})) + k\delta v_1(L_2 - L_1)}, \quad x \in (L_1, L_2], \quad (6.20)$$

$$C^*_{3r}(x) = C_s \frac{1-\exp(\frac{-v_3 x}{D})}{1-\exp(\frac{-v_3 L_3}{D})}, \quad x \in [0, L_3]. \quad (6.21)$$

Consideration of equations (6.17) and (6.20) show that the profiles for $C^*_{2p}(x)$ and $C^*_{2r}(x)$ are both linear with respect to x. At steady state, $C_1(x,t)$ and $C_3(x,t)$ are both linear in the passive case and based on a constant multiplied by $1 - \exp({}^{-v_i x}/_D)$ in the reverse iontophoresis case. This behaviour is demonstrated for the passive case and varying values of v_i in Figure 6-4.

When measuring experimental results of extraction through the stratum corneum, the measured quantity is usually based on flux at the skin surface, $x = 0$. In the passive case, the flux is described by

$$J_{ip}(x,t) = -D\frac{\partial C_{ip}(x,t)}{\partial x}, \quad i \in [1,2,3],$$

hence using equations (6.16) and (6.18) we obtain the passive flux at steady state at the skin surface for the intercellular stratum corneum

$$J^*_{1p}(0) = -\frac{DkC_s}{L_1 + k\delta(L_2 - L_1)}, \quad (6.22)$$

and hair follicle routes:

$$J^*_{3p}(0) = -\frac{DC_s}{L_3}. \quad (6.23)$$

For iontophoretic extraction, the flux is described by

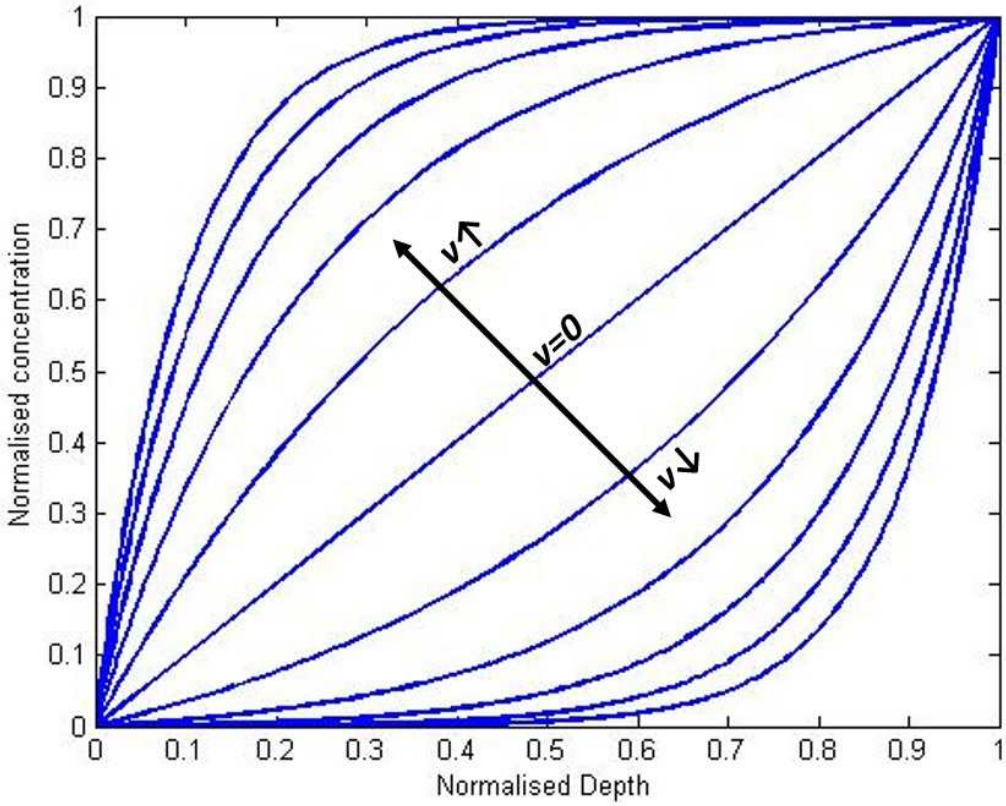

Figure 6-4: Demonstration of the profile obtained for $C_1(x,t)$ and $C_3(x,t)$ at steady state with no electro-osmosis and varying velocities. As velocity increases out of the skin, the gradient at $x = 0$ increases which will increase flux out the skin.

$$J_{ir}(x,t) = -D\frac{\partial C_{ir}(x,t)}{\partial x} - v_i C_{ir}, \quad i \in [1,2,3],$$

which, combined with equations (6.19) and (6.21), leads to the reverse iontophoretic flux at steady state

$$J^*_{1r}(0) = -\frac{kDv_1C_s}{D(1-\exp(\frac{-v_1L_1}{D})) + kv_1\delta(L_2-L_1)}, \tag{6.24}$$

$$J^*_{3r}(0) = -\frac{C_s v_3}{1-\exp(\frac{-v_3L_3}{D})}, \tag{6.25}$$

for the intercellular route and hair follicle route respectively at the skin surface.

In the time dependent case, numerical solutions, specifically the method of lines described in section 2.6.2, are utilised as they offer greater insight into the extraction profile than the analytical solution.

6.4.3 Application to Experimental Work

In order to analyse the results of this model, we compare the model predictions with real data in the following scenarios:

- *In vitro* passive mannitol permeability at steady state in abdominal skin [111].
- *In vitro* iontophoretic mannitol permeability at steady state in mixed skin samples [42].
- *In vivo* passive and iontophoretic phenylalanine flux at steady state [2].
- *In vivo* passive and iontophoretic phenylalanine flux at non-steady state [2].
- *In vivo* iontophoretic extraction of phenylalanine in patients with PKU [103].

Passive mannitol permeability in abdominal skin

The aim of this section is to consider *in vitro* passive diffusion of mannitol through abdominal skin [43] which considers extraction for hair and intercellular extraction separately. Hence, we use these results to check our predictions for hair follicle extraction predictions and obtain estimates for intercellular surface area.

Using the definition of permeability in equation (6.1) in combination with equations (6.22) and (6.23), the permeability for the intercellular space, P_{1p}, and hair follicle route, P_{3p}, are found to be:

$$P_{1p} = \frac{D\tau_1 kA}{L_2 k + L_1\delta(1-k)}, \tag{6.26}$$

$$P_{3p} = \frac{DA_3}{L_3}. \tag{6.27}$$

A is currently unknown whereas A_3 is known based on body site considered [102] as shown in table 6.2.

In vitro [43] results for abdominal skin attempt to split the permeability of mannitol through the hair follicle and intercellular route by considering extraction through two stacked skin samples. Using the results for intercellular permeability in the passive case combined with equation (6.26), we attempt to predict the area fraction, A, of the skin sample utilised by the intercellular route. The *in vitro* results for hair follicles are then compared to the predictions obtained using equation (6.27). The parameters values used are listed in table 6.1 with the skin site considered being abdominal skin for hair follicle density in 6.2.

The results for area fraction occupied by the intercellular space in abdominal skin and the comparison of predicted and *in vitro* hair follicle permeability are summarised in table 6.3. These results initially suggests that the predicted permeability due to the hair follicles is far higher than the permeability measured experimentally. It also suggests that the area fraction used by the intercellular route is very small compared to the surface area of the skin exposed.

Comparing the permeability measured in this experiment with other *in vitro* data [42], the permeability found in abdominal skin in this experiment is of order 10^2-10^4 lower compared to other *in vitro* sources [42]. This may be due to the diffusion area considered being 0.126cm^2 [43] and the hair follicle density in abdominal skin being 6cm^{-2} [102]. Hence it is entirely

Table 6.3: Result summary for initial model applied to *in vitro* mannitol permeability through abdominal skin [43]. Area fraction quoted is with respect to the whole skin surface.

	In vitro	**Prediction**	**Equation**
Intercellular space permeability (ms^{-1})	$3.13\pm1.76x10^{-11}$	-	-
Area fraction used with IC route	-	$5.95\pm4.56x10^{-4}$	(6.26)
Hair follicle permeability (ms^{-1})	$2.73\pm0.94x10^{-11}$	$2.35\pm2.14x10^{-9}$	(6.27)

possible that hair follicles were not present in the 3 samples considered for this part of the experiment and did not contribute to transport.

Due to this result, we consider the case where all of the extraction in this experiment occurred through the intercellular space. Considering this case, the predicted area fraction occupied by the intercellular pathway is $11.1\pm8.53x10^{-4}$, which is again very small compared to the surface area of skin considered.

In vitro mannitol permeability under iontophoresis

There has been some work into mannitol extraction from the skin under a variety of constant potential differences [42]. Here we compare the predicted extraction results with those obtained experimentally. Similar to the previous section, extraction results are recorded by considering permeability which is linked to flux in the passive case for intercellular space and hair follicles via equations (6.26) and (6.27) respectively. When an electric field is applied, the permeability of the intercellular space, P_{1r}, and hair follicle, P_{3r}, routes are determined using flux through the skin under an applied field. At steady state at the skin surface, these fluxes are given by equations (6.24) and (6.25) which, in combination with the definition of permeability in equation (6.1), gives:

$$P_{1r} = \frac{kDv_1A_3}{D(1-\exp(\frac{-v_1L_1}{D})) + kv_1\delta(L_2-L_1)}, \tag{6.28}$$

$$P_{3r} = \frac{v_3A_3}{1-\exp(\frac{-v_3L_3}{D})}. \tag{6.29}$$

The location for the skin is obtained from is not stated for *in vitro* mannitol extraction, with the acceptable range of starting permeabilities being between $3x10^{-9}ms^{-1}$ and $3x10^{-7}ms^{-1}$. Hence, we consider the mean area fraction occupied by hair follicles for this experiment to be the mean of all sites considered by prior work given in table 6.2 [102] which corresponds

Table 6.4: Result summary for initial model applied to *in vitro* mannitol permeability under iontophoresis[42]. Corresponding equations to calculate predicted values are also given in the table.

Permeability	***In vitro***	**Samples**	**Prediction**	**Equation**
Passive (ms^{-1})	$1.07\pm1.79x10^{-9}$	12	$2.87\pm3.09x10^{-8}$	(6.26)(6.27)
125mV (ms^{-1})	$2.55\pm4.32x10^{-9}$	4	$2.97\pm3.09x10^{-8}$	(6.28)(6.29)
250mV (ms^{-1})	$1.69\pm2.18x10^{-9}$	3	$3.09\pm3.32x10^{-8}$	(6.28)(6.29)
1000mV (ms^{-1})	$7.54\pm6.19x10^{-9}$	5	$3.76\pm4.06x10^{-8}$	(6.28)(6.29)

to a skin surface area fraction of $2.7x10^{-3}$. Using this skin surface area in combination with equation (6.27) and the parameters given in table 6.1 results in a passive permeability of $2.87\pm3.09x10^{-8}ms^{-1}$.

Electro-osmotic flow velocity is calculated using equation (6.14) based on the potential difference across the skin.

The predicted results using the parameters given in table 6.1 are compared to *in vitro* mannitol extraction results under passive and iontophoretic extraction [42] in table 6.4. It is clear that, similar to the passive case, the hair follicle route dominates the extraction profile with the predicted results being 10 times higher than those predicted experimentally. This is again likely due to the variability in hair follicle size between different sites. We also notice a drop in average permeability between 125mV and 250mV which is likely an error due to different pieces of skin and a low sample size.

Steady state phenylalanine extraction *in vivo*

Having established a prediction for the fraction of the skin surface utilised by the intercellular route and having identified the need for skin site considered to be known to reduce hair follicle variability, we now consider the extraction profile obtained for phenylalanine at steady state and compare it to *in vivo* data [2]. Samples are taken from 4 subjects ventral forearm skin for both passive extraction and under a constant applied current density of $0.3mAcm^{-2}$. Unlike the previous cases, the area from which the skin is taken is known so the area utilised by the hair follicle pathway can be estimated with a higher degree of accuracy from table 6.2.

Instead of considering permeability, these *in vivo* results directly consider flux at the surface of the skin. Hence, equations (6.22) and (6.23) are used for the passive case and equations (6.24) and (6.25) are used for the iontophoretic case. As the area the flux is considered over in the experiment is the surface area of the skin exposed, it is necessary to multiply all fluxes by the area fraction that route occupies.

Table 6.5: Result summary for initial model applied to *in vivo* phenylalanine flux at steady state [2].

Flux	***In vitro***	**Prediction**
Passive total ($molm^{-2}s^{-1}$)	$8.3x10^{-10}$	$5.93\pm5.40x10^{-10}$
Passive through hair ($molm^{-2}s^{-1}$)	-	$5.92\pm5.40x10^{-10}$
Passive through intercellular space ($molm^{-2}s^{-1}$)	-	$1.79\pm1.42x10^{-12}$
Reverse iontophoresis total ($molm^{-2}s^{-1}$)	$2x10^{-9}$	$1.58\pm1.71x10^{-9}$
Reverse iontophoresis hair ($molm^{-2}s^{-1}$)	-	$1.58\pm1.71x10^{-9}$
Reverse iontophoresis intercellular space ($molm^{-2}s^{-1}$)	-	$2.52\pm2.70x10^{-12}$

Electro-osmotic flow velocity is directly proportional to electric field strength which is, in turn, directly proportional to the potential difference across the membrane. Considering the resistance of the skin to remain constant throughout the experiment and using Ohm's law [98], $V = IR$, we obtain estimates for the voltage applied based on the parameters given in table 6.1. Hence, using equation (6.14) we obtain predictions for the electro-osmotic flow velocity, $v_1 = 3.18 \pm 1.06x10^{-6}ms^{-1}$ and $v_3 = 3.10 \pm 1.03x10^{-5}ms^{-1}$.

The results for the steady state are given in table 6.5. These results show that both passive and iontophoretic phenylalanine extraction fluxes are comparable between the predicted and experimentally obtained results. Additionally, transport in both cases is again dominated by the hair follicle pathway.

Time dependent phenylalanine extraction *in vivo*

For non-steady state flux measurements, we use numerical solutions to the model system presented in section 6.4.1. Figure 6-5 compares the experimentally obtained flux of phenylalanine *in vivo* [2] with that predicted by the model in 30 minute intervals under both passive and iontophoretic extraction. The parameters used are those presented in table 6.1 with a fixed current of $0.3mA/cm^2$. In both cases, the model results show the steady state is being achieved far faster than is observed experimentally. The steady state displayed in Figure 6-5 is the same as predicted in table 6.5 with units changed to match *in vivo* extraction results [2].

By contrast, Figure 6-6 considers having a zero initial condition in the stratum corneum hair follicles

$$C_3(x,0) = \begin{cases} 0, & x \in [0, L_{SC}], \\ C_s, & x \in (L_{SC}, L_3], \end{cases} \tag{6.30}$$

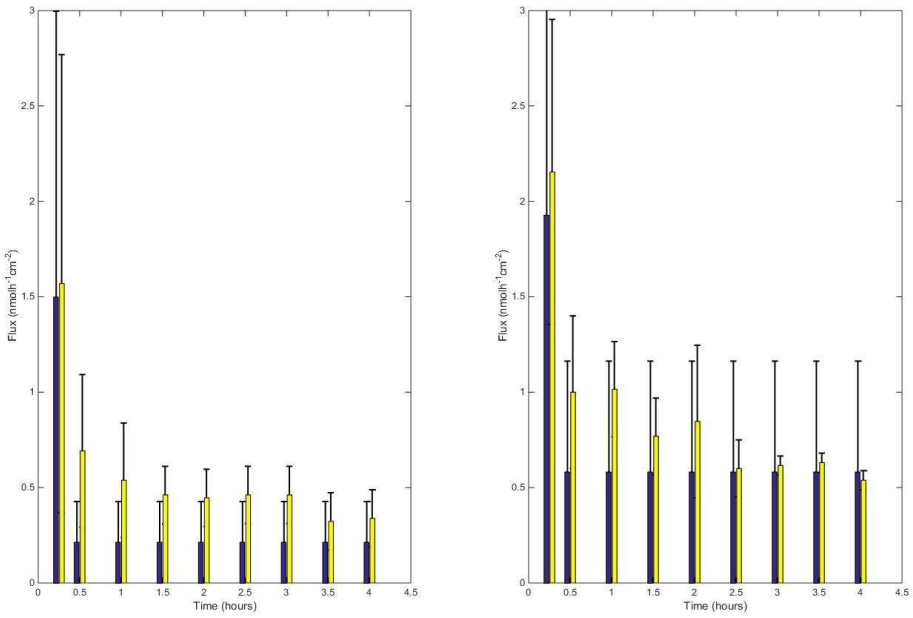

Figure 6-5: Comparison between *in vivo* (yellow) and predicted (blue) extraction profiles in the passive (left) and iontophoretic (right) case.

as the rapid transport through this route could mean that no phenylalanine is stored here naturally. This again demonstrates a rapidly obtained steady state and suggests little interference from the intercellular route.

Phenylketonuria

Prior experimental work into phenylalanine extraction through human skin has suggested that there is a measurable difference in observed extraction fluxes of phenylalanine with higher systemic concentrations causing higher extraction fluxes as demonstrated in Figure 6-7 [103]. These fluxes were obtained through ventral forearm skin.

Considering the flux expressions in equations (6.22), (6.23), (6.24) and (6.25) the model predicts the steady state extraction flux to be linear with respect to systemic concentration. Figure 6-8 considers the extraction flux through forearm skin with systemic concentrations corresponding to a non-PKU suffering patient, with $C_s = 0.057$mM, and a PKU suffering patient, with $C_s = 0.6$mM. The parameters used are given in table 6.1 under an applied current of 0.3mA/cm^2 which is converted into a electro-osmotic velocity using Ohm's law and equation (6.14).

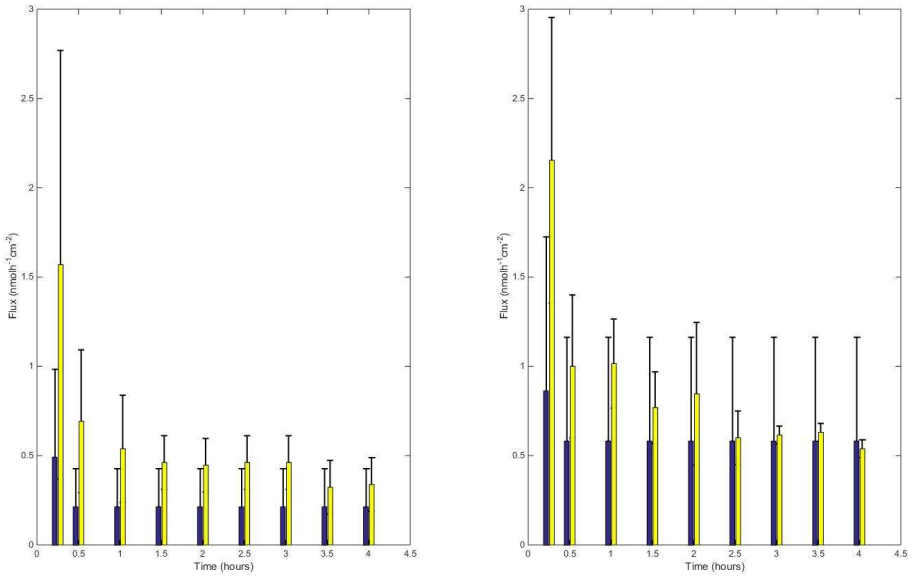

Figure 6-6: Comparison between *in vivo* (yellow) and predicted (blue) extraction profiles in the passive (left) and iontophoretic (right) case with a zero initial condition in the hair follicles.

Comparing Figures 6-5 and 6-8 demonstrates that the initial model predicts a significant difference in extracted phenylalanine concentrations between patients with and without PKU. However, comparing Figures 6-7 and 6-8 it is suggested that the predicted flux reaches a steady state faster than expected and that the steady state reached is higher than would be expected.

6.4.4 Summary of Initial Model Findings

The initial model suggests that the hair follicle route is vitally important in determining the permeability of skin, as has been demonstrated in prior experimental work [32]. Due to the importance of hair follicle routes, and the variability in hair follicle density and size over the body, we have demonstrated that predicting results from passive or iontophoretic extraction without knowledge of the exact body site considered is very difficult. In the case of phenylalanine extraction from ventral forearm skin, both the passive and iontophoretic extraction cases are predicted well by the model at steady state, but appear to reach the steady state faster than expected, as demonstrated by Figure 6-5. As a very small proportion of the intercellular space it utilised in transport, this also means that only a fraction of the skin reservoir is extracted.

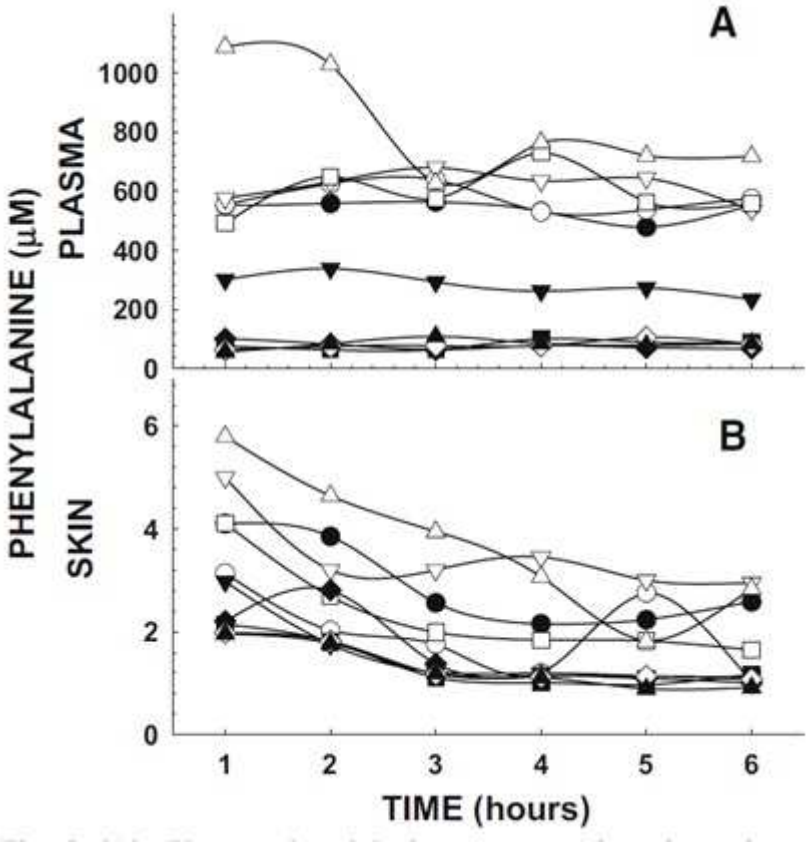

Figure 6-7: **(A)** - Plasma phenylalanine concentrations in the PKU suffering patients and control patients over the 6 hour extraction period. **(B)** - Phenylalanine concentration obtained in the extracted solution. As the extraction area was $1cm^2$, the units are equivalent to $nmolcm^{-2}h^{-1}$. Taken from [103]. In both **A** and **B**, different symbols represent different patients with PKU systemic concentrations ranging from 200-1000μM and the patients below this representing the control group.

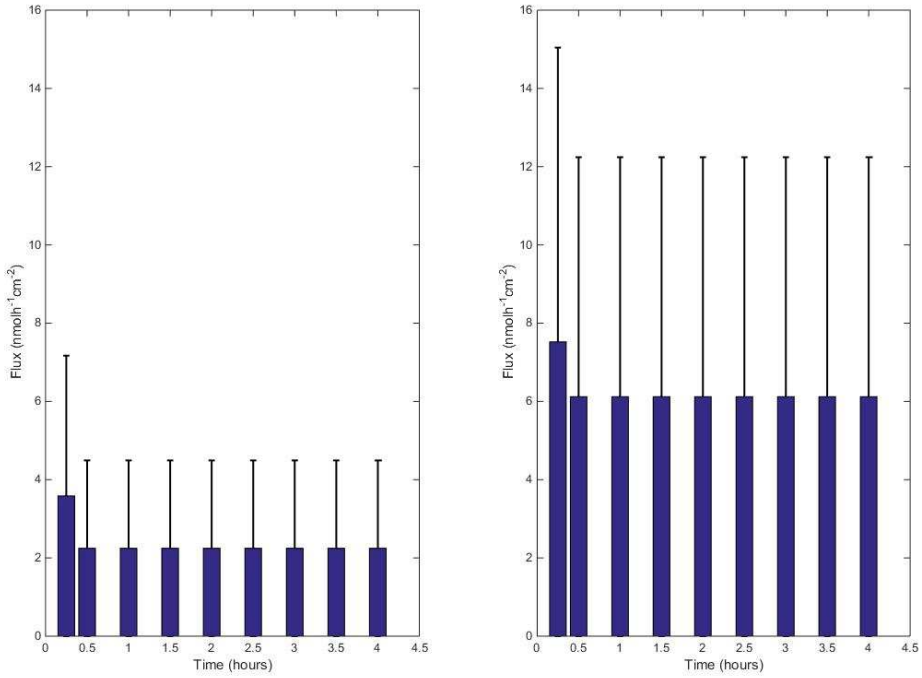

Figure 6-8: Passive (left) and iontophoretic (right) extraction profiles of phenylalanine in patients with phenylketonuria with a non-zero initial condition, given in equation (6.13) in the hair follicle stratum corneum.

Considering the initial model system, it should also be possible to tell significant differences between systemic concentrations of phenylalanine after a relatively short period of time. This is especially relevant when considering that prior work has shown that, at steady state, a patient suffering from PKU will have 10 times the systemic concentration of phenylalanine than a patient not suffering from PKU. Considering equations (6.22)-(6.25), the model predicts that the flux extracted at steady state is directly proportional to C_s, hence the 10-fold increase in C_s in patients suffering from PKU is reflected by a 10-fold increase in extraction profile.

For iontophoresis, prior *in vitro* work into extraction with zero concentration of phenylalanine in the subdermal compartment suggests that porcine stratum corneum is fully analysed within the first two hours of extraction [1]. If this behaviour holds true for human skin, then we would expect the model to predict a greater amount of the skin reservoir to be extracted at a slower rate than it suggests.

In order to tackle this discrepancy, hindered transport theory, explained in section 6.3.3, is considered for flux through the porous intercellular space.

6.5 Model Adaptation Including Hindrance Effects

The previous section, and prior work into acetaminophen extraction [32], has suggested that the majority of transdermal extraction occurs through hair follicles. However, the extraction of the skin reservoir still proves complex with the initial model predicting the skin reservoir emptying far faster than would be expected.

This section applies hindrance modelling techniques that have been used previously in capillary flow through porous membranes to model flow through the stratum corneum intercellular space as described in section 6.3.3 [110, 112].

6.5.1 Model Alterations

As the hair follicle route is considered to be directly through the skin, we do not consider hindrance modelling for flows through this route. The stratum corneum and the viable epidermis however, as demonstrated in chapter 4, have torturous pathways. Hindered transport has been described in section 6.3.3 and, under the assumption that the radius of the phenylalanine molecule is not comparable to the pore size which, considering the size of phenylalanine is of

the order of 10^{-10}m [5], holds for all but the smallest estimates of pore size, results in scaling the flux by the tortuosity of the pathway. Applying this to the governing equations for the intercellular space, presented in equations (6.2) and (6.3) for the initial model, results in the new governing equations:

$$\frac{\partial C_1}{\partial t} + \tau_1 \left(-D \frac{\partial^2 C_1}{\partial x^2} - v_1 \frac{\partial C_1}{\partial x} \right) = 0, \quad x \in [0, L_1], \quad \forall t \geq 0,$$

$$\frac{\partial C_2}{\partial t} + \tau_2 \left(-D \frac{\partial^2 C_2}{\partial x^2} \right) = 0, \quad x \in (L_1, L_2], \quad \forall t \geq 0.$$

The sink, source and concentration boundary conditions, given in equations (6.7), (6.10) and (6.8) respectively, for the initial model still hold for the hindered model. However, due to the tortuous modification, the flux condition given in equation (6.9) at $x = L_1$ becomes:

$$\tau_1^2 \left(D \frac{\partial C_1}{\partial x}(L_1, t) + v C_1(L_1, t) \right) = \tau_2^2 D \frac{\partial C_2}{\partial x}(L_1, t), \quad \forall t \geq 0.$$

with the initial conditions for the intercellular space remaining unchanged from the initial model system, given in equations (6.11) and (6.12). For the hair follicles, we consider both the zero initial condition, given in equation (6.30), and a non-zero initial condition, given in equation (6.13).

6.5.2 Steady State Solution

The steady state for the hair follicle route remains unchanged in both the passive and iontophoretic case, given in equations (6.18) and (6.21) respectively. For the intercellular space route however

$$C_{1p}^*(x) = \frac{kC_s}{L_1 + k\delta^2(L_2 - L_1)} x, \quad x \in [0, L_1],$$

$$C_{2p}^*(x) = C_s \frac{\delta^2 k(x - L_1) + L_1}{L_1 + k\delta^2(L_2 - L_1)}, \quad x \in (L_1, L_2],$$

are the passive steady state concentrations with corresponding steady state flux

$$J_{1p}^{*}(0) = -\frac{kD\tau_1 C_s}{L_1 + k\delta^2(L_2 - L_1)},$$

at the surface of the skin. In the iontophoretic case

$$C_{1r}^{*}(x) = \frac{C_s kD}{D(1-\exp(\frac{-v_1 L_1}{D})) + kv_1\delta^2(L_2 - L_1)}\left(1 - \exp\left(\frac{-v_1 x}{D}\right)\right), \quad x \in [0, L_1],$$

$$C_{2r}^{*}(x) = C_s\frac{k\delta^2 v_1(x - L_1) + D(1-\exp(\frac{-v_1 L_1}{D}))}{D(1-\exp(\frac{-v_1 L_1}{D})) + k\delta^2 v_1(L_2 - L_1)}, \quad x \in (L_1, L_2],$$

with corresponding steady state flux

$$J_{1r}^{*}(0) = -\frac{C_s kD\tau_1 v_1}{D(1-\exp(\frac{-v_1 L_1}{D})) + kv_1\delta^2(L_2 - L_1)},$$

at the surface of the skin.

6.5.3 *In Vivo* time dependent

The initial model, and prior experimental work into acetaminophen extraction through human skin [32], suggest that the majority of extraction, especially at steady state, is through hair follicles. Thus we focus on the non-steady state *in vivo* case [2] as the skin site used in this experiment is known and the modifications will not affect the steady state position of hair follicle extraction. In the same manner as the initial model, we consider numerical solutions for non-steady state behaviour using the method of lines detailed in section 2.6.2.

Figures 6-9, 6-10, 6-11 and 6-12 consider the extraction profiles generated when using the initial condition for hair given in equation (6.13) over a range of fractions of the intercellular space utilised. The range considered is between 0 and the volume fraction of the skin occupied by the intercellular space, $p = 0.084$. From these results, it is clear that the model predicts that a very small fraction of the intercellular space is utilised in extraction - approximately 10% of the intercellular area available which translates to 0.84% of the total skin surface area.

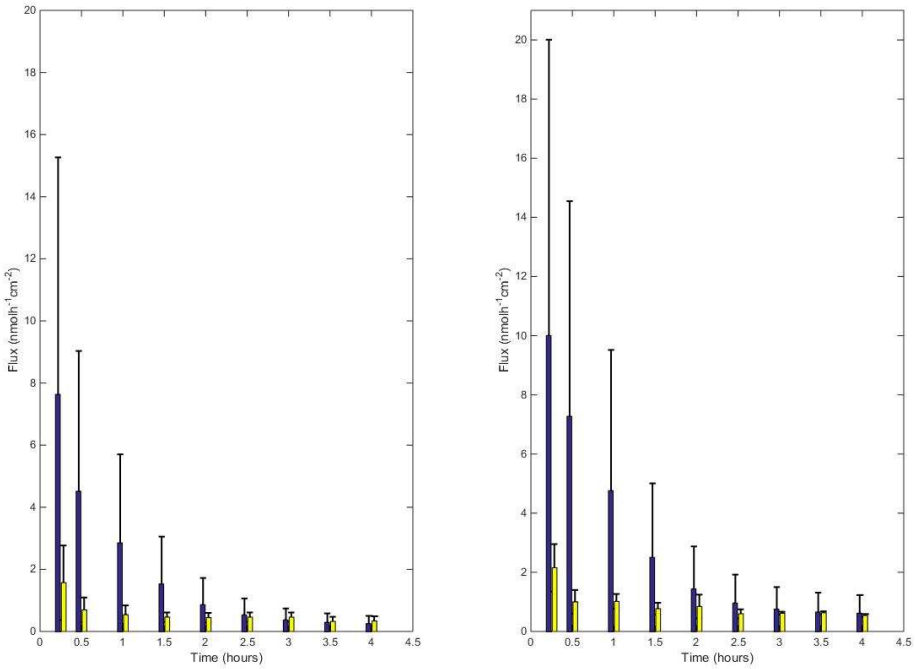

Figure 6-9: Hindrance model with the whole of the intercellular space fraction utilised in transport. These show both model (blue) and *in vivo* experimental data [2] (yellow) in the passive (left) and iontophoretic (right) case. The hair follicle is considered to have the same initial concentration as the stratum corneum intercellular space given in equation (6.13). Parameters are calculated using table 6.1.

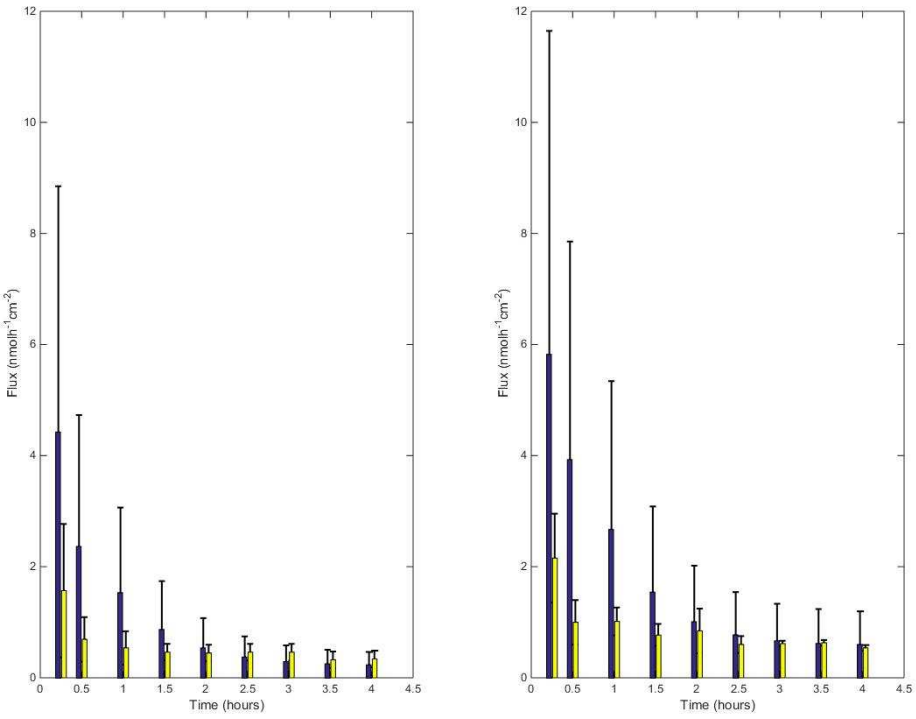

Figure 6-10: Hindrance model with 50% of the intercellular space fraction utilised in transport. These show both model (blue) and *in vivo* experimental data [2] (yellow) in the passive (left) and iontophoretic (right) case. The hair follicle is considered to have the same initial concentration as the stratum corneum intercellular space given in equation (6.13). Parameters are calculated using table 6.1.

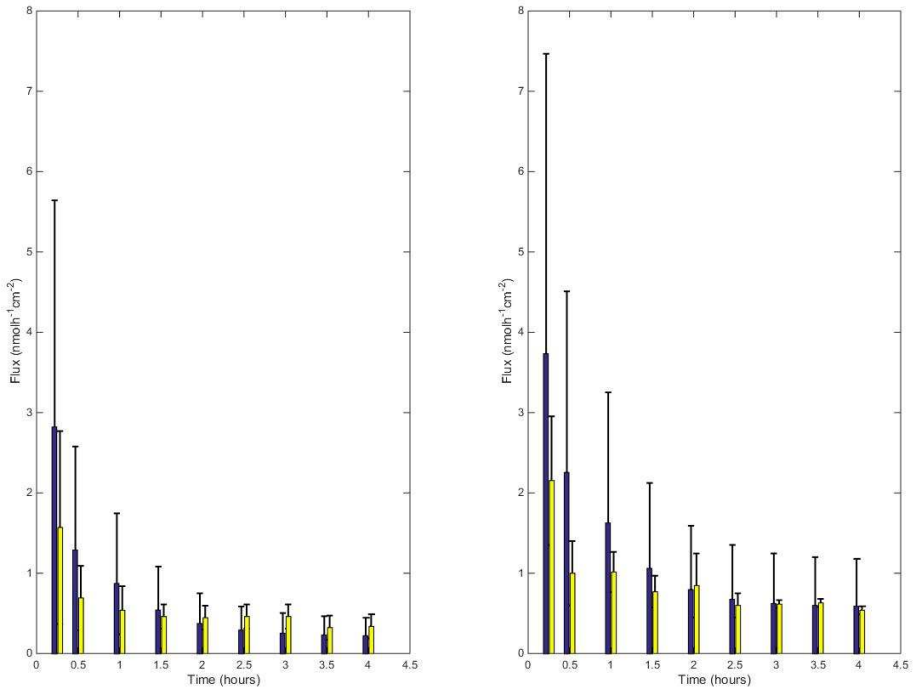

Figure 6-11: Hindrance model with 25% of the intercellular space fraction utilised in transport. These show both model (blue) and *in vivo* experimental data [2] (yellow) in the passive (left) and iontophoretic (right) case. The hair follicle is considered to have the same initial concentration as the stratum corneum intercellular space given in equation (6.13). Parameters are calculated using table 6.1.

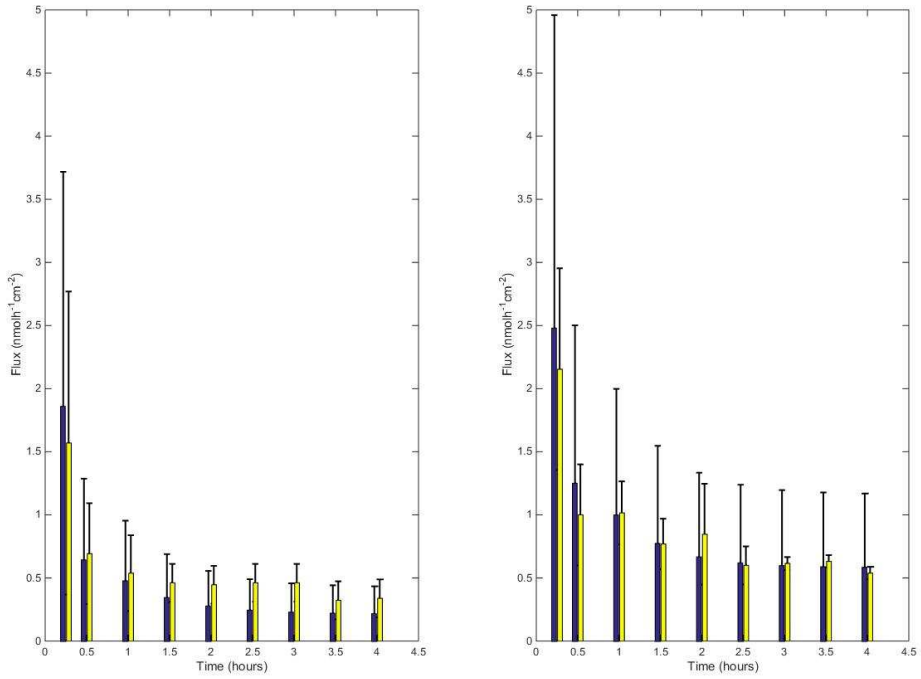

Figure 6-12: Hindrance model with 10% of the intercellular space fraction utilised in transport. These show both model (blue) and *in vivo* experimental data [2] (yellow) in the passive (left) and iontophoretic (right) case. The hair follicle is considered to have the same initial concentration as the stratum corneum intercellular space given in equation (6.13). Parameters are calculated using table 6.1.

Figures 6-13, 6-14, 6-15 and 6-16 consider the extraction profile generated when using a zero initial condition in hair follicles, as given in equation (6.30). Both passive and iontophoretic extraction are considered for a range of intercellular space utilised. Similarly to using a non-zero initial condition in the hair follicle, the model predicts a small fraction of the intercellular space is used in extraction - approximately 10-25% of the area available.

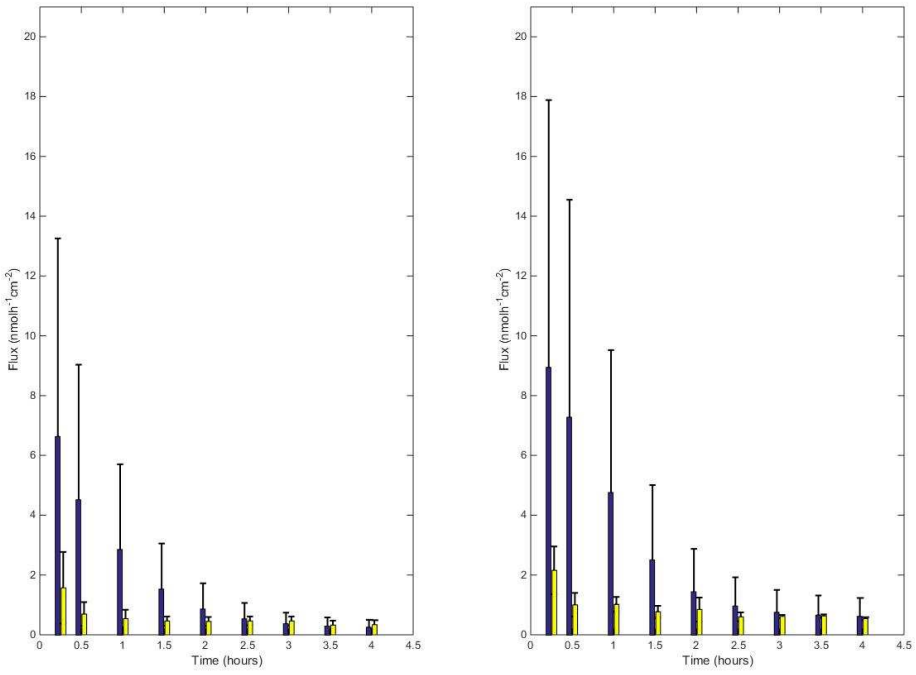

Figure 6-13: Hindrance model with the whole of the intercellular space fraction utilised in transport. These show both model (blue) and *in vivo* experimental data [2] (yellow) in the passive (left) and iontophoretic (right) case. The hair follicleis considered to initially have no phenylalanine in the stratum corneum part, given in equation (6.30). Parameters are calculated using table 6.1.

Considering the PKU case for the non-zero initial condition in hair follicles, demonstrated in Figure 6-17 for a utilised volume fraction of $0.1p$ of the SC, and zero initial condition for hair follicles, demonstrated in Figure 6-18 for a utilised surface area of $0.25p$, it is clear that higher concentrations of systemic phenylalanine cause an observable difference in extraction profiles. Similarly to the initial model, however, the steady state predicted is still higher than expected from Figure 6-7 [103].

As shown in chapter 3, the skin reservoir is not noticeably affected by PKU. Hence the change in amount extracted from the reservoir is small compared to the change in amount extracted from deeper levels of the skin.

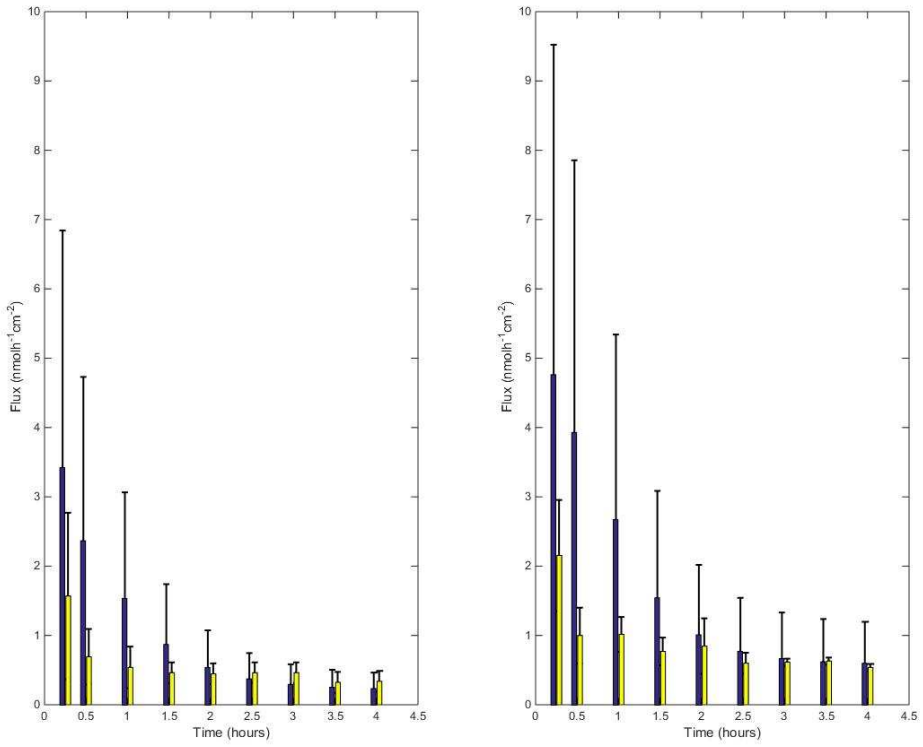

Figure 6-14: Hindrance model with 50% of the intercellular space fraction utilised in transport. These show both model (blue) and *in vivo* experimental data [2] (yellow) in the passive (left) and iontophoretic (right) case. The hair follicle is considered to initially have no phenylalanine in the stratum corneum part, given in equation (6.30). Parameters are calculated using table 6.1.

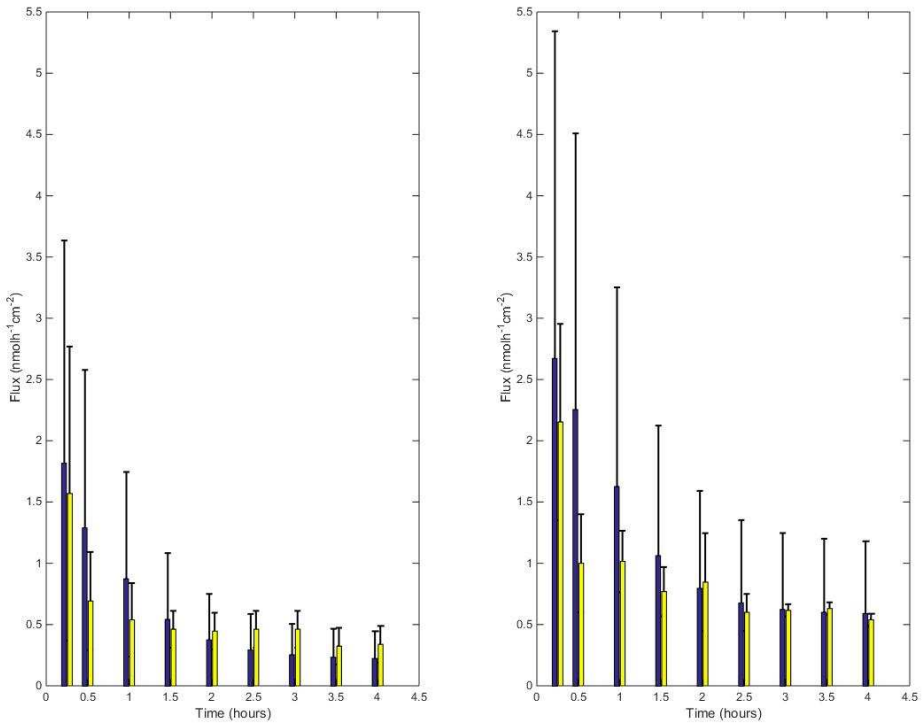

Figure 6-15: Hindrance model with 25% of the intercellular space fraction utilised in transport. These show both model (blue) and *in vivo* experimental data [2] (yellow) in the passive (left) and iontophoretic (right) case. The hair follicle is considered to initially have no phenylalanine in the stratum corneum part, given in equation (6.30). Parameters are calculated using table 6.1.

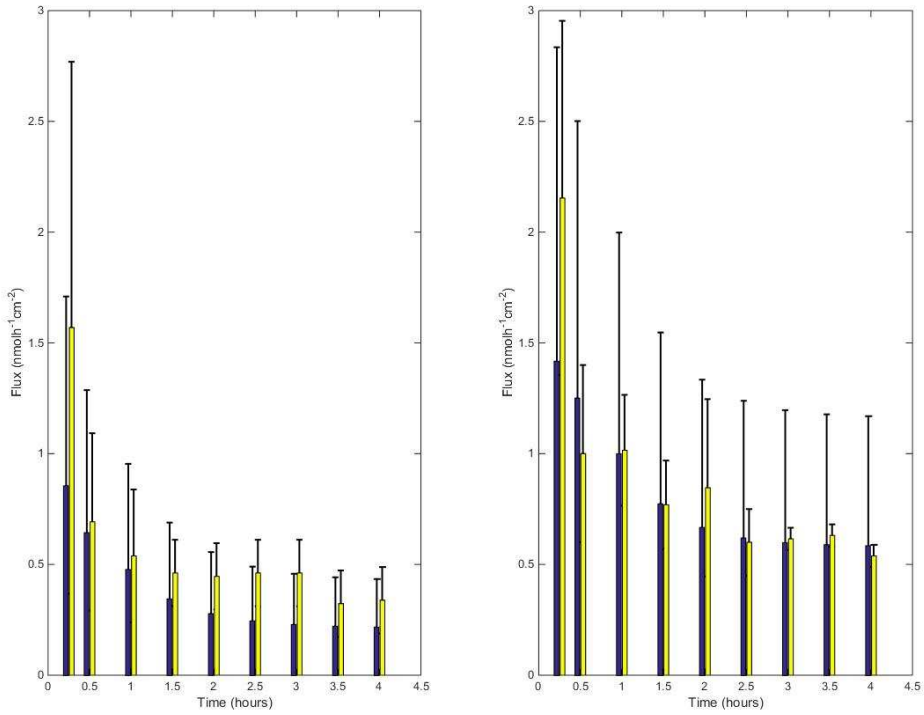

Figure 6-16: Hindrance model with 10% of the intercellular space fraction utilised in transport. These show both model (blue) and *in vivo* experimental data [2] (yellow) in the passive (left) and iontophoretic (right) case. The hair follicle is considered to initially have no phenylalanine in the stratum corneum part, given in equation (6.30). Parameters are calculated using table 6.1.

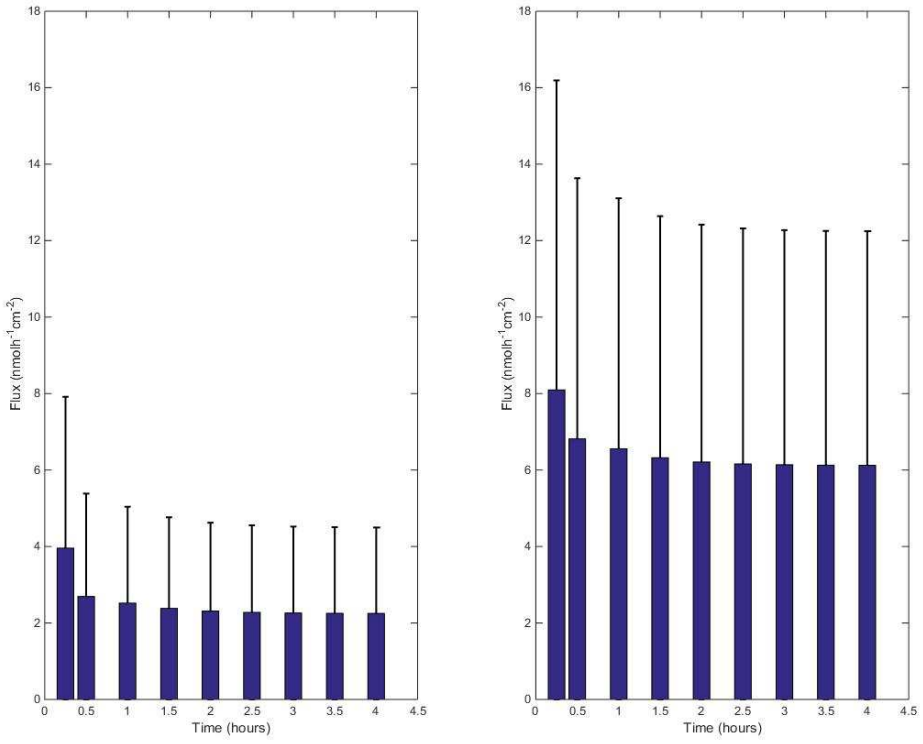

Figure 6-17: Hindrance model with 10% of the intercellular space fraction utilised in transport. The hair follicle is considered to have the same initial concentration as the stratum corneum intercellular space given in equation (6.13). Parameters are calculated using table 6.1. The concentration of systemic phenylalanine corresponds to a patient with PKU at $C_s = 0.6$mM. Both passive, left, and iontophoretic, right, cases are considered.

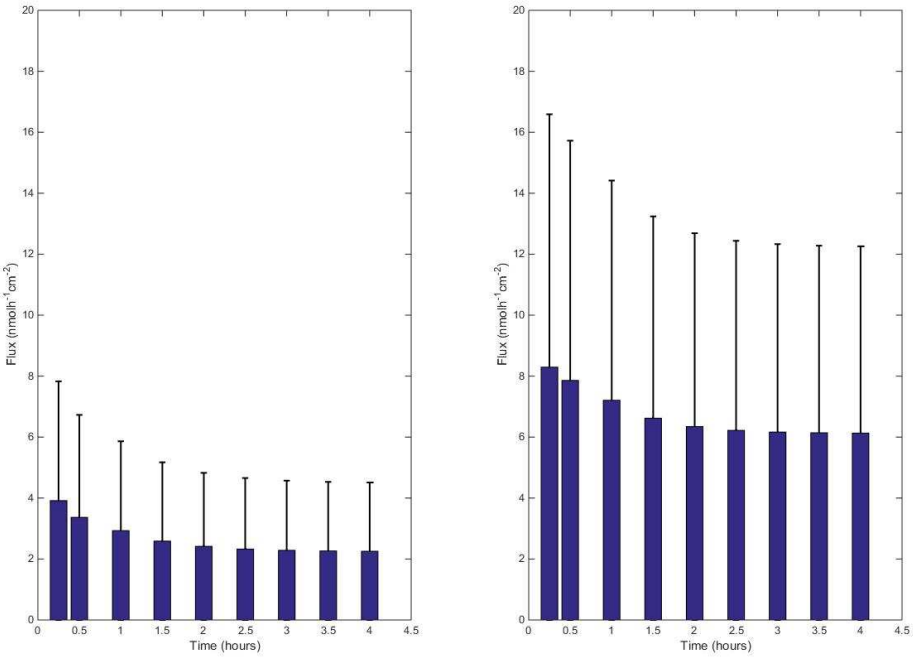

Figure 6-18: Hindrance model with 25% the intercellular space fraction utilised in transport. The hair follicle is considered to initially have no phenylalanine in the stratum corneum part, given in equation (6.30). Parameters are calculated using table 6.1. The concentration of systemic phenylalanine corresponds to a patient with PKU at $C_s = 0.6$mM. Both passive, left, and iontophoretic, right, cases are considered.

6.5.4 Summary for Hindrance Model

Similarly to the initial model system, the hindered transport approach again suggests that the majority of steady state extraction occurs through the appendageal route. The incorporation of hindrance transport methods to the intercellular route increases the time taken for the initial amount in the stratum corneum to be extracted in both the iontophoretic and passive case and agrees well with previous experimental results when the fraction of the intercellular space utilised is considered to be 10-25% of the total volume occupied by the intercellular space.

Additionally, utilising the hindered transport does not significantly affect the steady state profile obtained for PKU patients in the initial model. As suggested by chapter 4, PKU does not significantly affect the skin reservoir of amino acid. Hence, it should still be possible to get indicators of PKU from a short sample time.

There are still several issues with the model however. Firstly, due to the formation of the model, it is never possible to fully assess the skin reservoir of amino acid unless the whole volume fraction is considered to contribute towards extraction which, in turn, results in an extremely high initial profile. Secondly, as the hair follicle route dominates transport at steady state and similarly to the initial model, the steady state flux for PKU patients is higher than that observed experimentally - albeit in a very small sample size. Finally, and perhaps most critically, the error bars associated with the model are very large - especially in iontophoresis due to the variability in skin resistance and hence voltage applied.

As mentioned previously, the reverse iontophoresis experiments considered are at a constant current of 0.3mAcm^{-2} [1, 2, 103] which, combined with skin resistivity [106], results in an applied potential of 3.54 ± 1.14V. The resistivity of skin has been shown to change under applied fields of greater than 250mV with the amount of change dependent upon the voltage applied [105]. This voltage drop would affect the electro-osmotic velocity and could explain the differences observed in iontophoretic extraction profiles.

Due to the large error bars and the absence of data as to how the resistance of the skin behaves under a constant current, it is impractical to attempt to further extend the model before more experiments that measure key parameters, such as voltage during reverse iontophoresis, have been performed.

6.6 Chapter Summary

In this chapter, we started by constructing an initial model for the extraction of large, uncharged compounds via passive diffusion and reverse iontophoresis. In the initial model, the intercellular and hair follicle pathways are split and modelled separately using partial differential equations. Initial conditions are based on the profiles obtained in chapter 4 and the electro-osmotic velocity on the results of chapter 5. Comparing the predictions of the model to prior *in vitro* [43, 42] and *in vivo* [1] experimental data for mannitol and phenylalanine suggests that the hair follicle route dominates transport of large, uncharged compounds through the skin. Considering the difference in hair follicle density in different sites in the body [102], this makes it critically important to record the area of skin considered in extraction experiments.

Hair follicles in prior work have been considered to negligibly contribute to flux through the stratum corneum [33, 87, 91]. Hence the suggestion, using the mathematical model presented here and prior work into identifying pathways through the skin under an applied electric field using scanning electrochemical microscopy [32], is a key result. As the hair follicle pathway rapidly obtains steady state, this result suggests that it is possible to detect systemic concentrations of large, uncharged compounds, like phenylalanine, directly via reverse iontophoresis.

When considering extraction in the non-steady state case, Figures 6-5 and 6-6 demonstrate that the initial model predicts the steady state flux to be achieved quicker than has been observed experimentally and, due to the very small fraction of the intercellular route utilised, not assess much of the reservoir in the skin.

Having identified this issue, we move on to modify the initial model by considering hindered transport methods through the stratum corneum. As the hair follicle pathway is considered to have a radius that is large in comparison to the phenylalanine molecule and is straight through the stratum corneum, hindrance modelling has no effect on this pathway. The intercellular route, however, is tortuous and hence affected by hindrance effects.

Applying hindrance effects to the model significantly slows down the transport of compounds through the intercellular pathway and, considering Figures 6-9 to 6-16 which compare model predictions to *in vivo* data [2], suggests that 10-25% of the intercellular route is utilised during extraction. This results in more of the skin reservoir being extracted and a greater time to achieve steady state.

In both the initial model and the hindered model, the effect of increased systemic concentrations of phenylalanine, corresponding to a patient with PKU, is investigated. Figures 6-8,

6-17 and 6-18 show that both models predict a noticeably increased flux of phenylalanine from patients with higher systemic concentrations of phenylalanine. This result has also been suggested in prior *in vivo* work [103]. However the predicted flux at steady state in the case of a patient with phenylketonuria is higher than has been observed experimentally in the reverse iontophoresis case. There currently does not exist any data on passive phenylalanine extraction in PKU patients.

Although the hindered model approach gives a good prediction for passive and iontophoretic extraction there are still several issues with this approach. Firstly, we assume that the pore radius of the intercellular space route is large compared to both the Debye length and the radius of the phenylalanine molecule. This assumption is not valid for the smallest pore radius predicted by prior work, being 0.5nm [101] compared to a Debye length of 0.83nm and a molecule radius of order 10^{-1}nm. Additionally, prior work into skin resistance under a constant voltage has suggested that skin resistance changes over time when a voltage of over 250mV is applied [105]. Due to the dangers of high current in the body, reverse iontophoresis experiments tend to fix current rather than voltage with the current selected resulting in an initial voltage of over 250mV. To date, there has not been any experimental work into skin resistance changes under a constant current.

6.6.1 Variable Resistance

Prior *in vitro* work has identified that skin resistance decreases when exposed to a constant voltage of over 250mV [105]. This work has also suggested that the change in skin resistance is based on voltage applied with greater voltages causing a lower final resistance. Ohm's law means that a drop in resistance at fixed voltage results in a proportional increase in current. Equations (6.14) and (6.15) show that electro-osmotic flow velocity is directly proportional to the potential difference over the membrane, hence at a fixed voltage changes in skin resistance should have no effect on electro-osmotic flow velocity.

In the case of *in vivo* phenylalanine extraction under reverse iontophoresis, the current density applied across the skin is constant at 0.3mAcm^{-2} rather than the voltage [2]. Using the resistivity given in table 6.1 the resistance of the stratum corneum is calculated to be 11.8$\pm$3.8kΩcm^2 which corresponds to a starting voltage of 3.54$\pm$1.14V. This means that the voltage applied across the stratum corneum is greater than 250mV hence prior work has suggested that there will be a change in skin resistance over the course of experiments using this constant current density [105]. As the current density is fixed, a drop in resistance will cause a corresponding drop in voltage, leading to a decrease in electro-osmotic flow velocity.

Currently, there are no experiments that have looked at skin resistance changes under a constant current. Producing a circuit diagram to model the decreasing resistance under a constant current is very complex and requires the introduction of many unknown variables.

Considering a constant voltage, as has been done in prior *in vitro* work into resistance changes through the skin [103], we propose that resistance, R, decays exponentially at rate, τ_0 from it's start point, R_0, and finishes at a non-zero fraction, p_f, of this initial value:

$$R(t) = p_f R_0 + (1 - p_f) R_0 \exp(-\tau_0 t). \tag{6.31}$$

Figure 6-19 takes the results from prior *in vivo* resistance work under a constant voltage [103] and compares them to the results of equation (6.31) with τ_0 considering to correspond to a half life of 10 minutes hence $\tau_0 = {}^1/_{10\text{x}60} = 6.67\text{x}10^{-3}\text{s}^{-1}$. This seems to be a good fit for resistance behaviour under a constant voltage.

More experimental work would be required to ascertain if this relation holds for a constant current and to find estimates for corresponding decay rates and end resistance. Alternatively recording voltage during iontophoretic experiments would be very useful.

Due to the large error bars present in the hindered model and the uncertainty surrounding both pore size in the intercellular space and resistance changes in the skin under a constant current, further changes are not made to the hindered model at this stage. However, this section and chapter 5 set up theory that can be used in the case of a pore radius comparable to the molecule size and Debye length respectively. The model proposed for resistance changes in the skin under a constant voltage using prior *in vitro* work [105] might be used as a basis when considering skin resistance changes under a constant applied current.

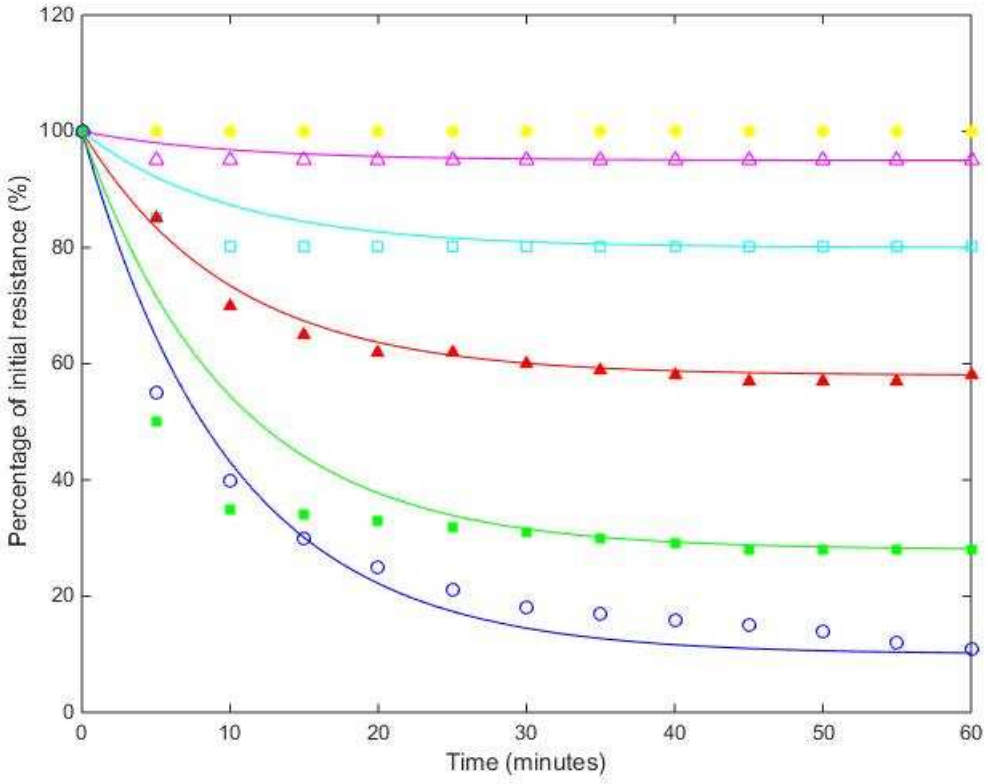

Figure 6-19: Comparing the resistance changes predicted by equation (6.31) with *in vivo* data [105]. Filled in, yellow circles represent an applied constant voltage of 250mV, clear, pink triangles 500mV, clear, blue squares 750mV, filled, red triangles 1000mV, filled, green squares 1500mV and clear, purple circles 2000mV.

Chapter 7

Summary and Future Work

The aim of this thesis was to investigate the formation and extraction of reservoirs of amino acids in the stratum corneum, using phenylalanine as a case study, to assess the potential for non-invasive monitoring of amino acid concentrations in blood serum. The clinical application of this would be to allow monitoring of amino acid disorders, such as phenylketonuria, via non-invasive methods. Non-invasive methods are preferred to invasive methods as they avoid several issues such as risk of infection and the need for trained personnel to administer [18]. The non-invasive method focussed on was transdermal extraction which utilises passive diffusion through the skin and can be enhanced by the application of an electric field, called reverse iontophoresis. Extraction of amino acids via this method has been considered experimentally both *in vitro* [1] and *in vivo* [2]. We use this data to test the mathematical models proposed and predict unknown parameters.

In order to investigate this topic, the thesis addresses 3 distinct components namely:

1. Blood serum concentrations of amino acids, specially phenylalanine, under food intake.

2. Skin reservoir formation based on blood serum concentrations.

3. Extraction of phenylalanine via reverse iontophoresis.

Having addressed background biological theory and mathematical techniques required to pursue these goals in chapters 1 and 2, chapter 3 addresses blood serum concentrations. The aim of chapter 3 was to extend previous fasting state models of phenylalanine concentration in blood serum to include the effect of metabolism only occurring in the liver and adding food intake effects. This chapter suggested that there were only minor differences between

including liver only metabolism and having metabolism occur throughout the body. One of the differences highlighted was that the resilience of a two-compartment system was much less than the single-compartment system meaning that the single-compartment system would return to a steady state faster after a perturbation. However, this did seem to have a significant effect when considering perturbations due to food intake. Clinically, this means that, although including a second compartment is more physiologically realistic, it does not change the dynamics of the system enough to warrant the additional model complexity and error that this introduces.

Considering food intake into the system was done via a Bateman function. This suggested that fluctuations due to food intake into the body caused visible changes in both PKU suffering and non-PKU suffering patients. As would be expected from discrete doses, food intake causes periodic oscillations in blood serum concentration. These fluctuations reinforce the need for phenylalanine tolerance tests via blood sample to be performed in a fasting state. If systemic concentrations have a noticeable impact on the skin reservoir, these fluctuations should also have a noticeable effect on the reservoir.

Having established a baseline model for blood serum concentrations of phenylalanine, chapter 4 moved on to consider the skin reservoir of amino acids based on the blood serum concentration profile established in chapter 3. To date, mathematical models have not considered the formation of reservoirs of amino acids in the skin, primarily focussing on extraction methods. Considering prior work has suggested that corneocytes are impermeable [73], we proposed a model for the stratum corneum that splits corneocytes and the intercellular space into two compartments, further stratified into the stratum corneum and stratum disjunctum.

Modelling the skin reservoir highlighted several interesting results. Firstly, when tape stripping, the depth each strip is considered to analyse is based on the mass of skin removed [1, 2]. Hence, a similar number of corneocytes should be present for the same depth assessed through the stratum corneum. If corneocytes are impermeable and contribute significantly to amino acid levels in the stratum corneum, then the decrease observed *in vitro* [1] and *in vivo* [2] in amino acid concentration near the surface of the skin, namely the stratum disjunctum, should not occur. Based on this, our model suggests that most of the amino acid found in the stratum corneum is in the intercellular space.

We also suggest that modelling removal of compounds from the stratum disjunctum intercellular space can be modelled using a linear removal term and verify this approach by considering *in vivo* phenylalanine and tyrosine data [2]. However, chapter 4 also suggests that the systemic concentration has an unnoticeable effect on phenylalanine and tyrosine concentrations in the stratum corneum, with production eclipsing movement from the blood serum.

Production in the stratum corneum dominating the formation of the skin reservoir suggests that assessing historic phenylalanine concentrations via direct consideration of the skin reservoir is not possible. However, recent *in vivo* work suggests that variations in serum phenylalanine levels are detectable via reverse iontophoresis [103]. Combined with the results of chapter 4, this suggests that there is significant flux of phenylalanine from the systemic compartment through the stratum corneum during reverse iontophoresis. Chapter 5 and 6 investigate this experimental result mathematically by considering electro-osmotic flow through the stratum corneum.

As phenylalanine is an uncharged compound, flux through the stratum corneum under an applied field is governed by electro-osmotic flow and passive diffusion. The main objective of chapter 5 was to combine previous work into fluid dynamics, surface chemistry and electromagnetism to form an expression for electro-osmotic flow velocity in terms of known parameters in different system geometries. Although the theories proposed in the chapter are not new, they have not been previously utilised in skin models and are combined in a novel way to determine electro-osmotic flow velocity in the skin. Using streaming potential data [87] we obtain predictions for surface charge density based on the concentration of ionic solvent in the fluid, allowing us to predict electro-osmotic flow velocity based on known properties of the skin, applied field and fluid.

Chapter 6 then aimed to use the results of chapter 5 to form a model for extraction of uncharged compounds through reverse iontophoresis. The initial reservoir in the skin was based on the model results from chapter 4. Prior modelling work through the stratum corneum tends to ignore the effect of appendageal transport [33, 87, 91]. However, experimental work using scanning electrochemical microscopy has suggested that appendageal transport is the primary extraction route for compounds through the skin [32]. This was investigated by considering intercellular and hair follicle routes separately.

The main result of chapter 6 is to suggest, using mathematical models, that hair follicles are indeed critical to extraction of compounds through the skin with this route becoming fully established very quickly. It is further suggested that the contribution to flux through the stratum corneum from the intercellular space at steady state is completely eclipsed by hair follicles. However, consideration of the intercellular route is still important when looking at reservoir extraction.

The results presented by chapters 5 and 6 develop the field of transdermal monitoring significantly. The formulation of electro-osmotic flow velocity from fundamental principles of electromagnetism, fluid dynamics and surface chemistry predicts that hair follicles are the primary extraction route through the skin. This explains the large variation observed in

experiments where the origin of skin samples is often not stated. Clinically, this result also suggests that direct monitoring of amino acid disorders via transdermal extraction is possible, particularly in areas of the skin where there are lots of hair follicles.

7.1 Future Work

One of the biggest limitations encountered in this thesis was the amount of experimental data available. Small sample sizes and human variability lead to large standard deviations, making it difficult to draw solid conclusions from the model results. The first instance of this occurs in chapter 3 where it is not possible to compare non-fasting state model results to real data. Experiments measuring these properties would validate model predictions.

The quantity of experimental data becomes a more pressing issue when considering extraction through the skin. In this case, the small data set and the variability in parameters such as voltage causes the standard deviation to be comparable to the size of the result measured.

Although human variability is always going to be an issue, there are several experiments that can be done to decrease the error measured. Firstly, it has been established by this thesis, and prior work in both reverse iontophoresis [33] and micro-fluids [89], that electro-osmotic flow velocity is directly proportional to the electric field applied. By definition, in a uniform electric field the field strength is equal to the voltage applied across the membrane divided by the path length and voltage is equal to current multiplied by resistance, Ohm's law [98]. Due to the harmful effect of high currents on the human body most experimental work into reverse iontophoresis uses a constant current of 0.3mA/cm^2 [1, 2, 103]. Skin resistance is highly variable which means that this constant current can result in an applied voltage of anywhere between 2-5V, resulting in a large range of electro-osmotic flow velocities. Measuring voltage throughout the experiment would allow a better prediction of electro-osmotic flow velocity and significantly reduce modelling error.

On this note, prior research has also shown that voltages of over 250mV cause changes in skin resistance with the change observed based on voltage applied [105]. To date, this phenomenon has not been investigated under a constant current. Doing so would allow models to be developed of this voltage change to be applied to electro-osmotic flow rates and could contribute to the decrease in flux over time.

Recording the site from which skin is taken would also help to reduce error as hair follicle density varies between different locations in the body [102]. Chapter 6 and [32] also suggest

that hair follicles are the primary extraction route through the skin making this differentiation critical.

Having performed these experiments and compared the results to the model structure presented in this thesis, there are several modifications that could potentially improve the model presented. Firstly, having a time varying velocity based on the time varying voltage would result in a reduction in flux over time. This could be similar to the structure presented in section 6.6.1 or different depending on the experimental results.

One of the other limitations is that the pores through the stratum corneum are considered to be large, with respect to both the Debye length and molecule size, resulting in a constant electro-osmotic flow velocity. For the 133mM NaCl solution used in the extraction experiments considered, the Debye length is 0.83nm. Hence, this assumption is valid for hair follicles which are micro-channels, but predictions for pore sizes in the intercellular space vary between 0.5nm [101] and 20nm [87]. Hence this assumption will not be valid if pore sizes are on the lower end of this spectrum. We have presented theory for modifying the electro-osmotic flow velocity accordingly in chapter 5 and empirical relations for hindrance based on a pore size comparable to molecule size in chapter 6. These modifications will slow down flow through the intercellular space and, thus, also slow reservoir extraction.

Applying these modifications may also mean that more of the skin reservoir is predicted to be extracted during reverse iontophoresis. In the current model proposal, the whole reservoir is not analysed as the results predicted using the full reservoir have a far too high initial extraction flux. The other potential reason for this could also be due to some of the compound being trapped in the skin.

Overall, the models proposed by this thesis identify significant changes to the field of mathematically modelling transdermal extraction which reflect recent experimental developments [32, 103]. Clinically, this also identifies the potential for non-invasive monitoring of amino acids, specifically phenylalanine, via reverse iontophoresis. The next stage in this research is to perform experiments to validate predicted parameters and reduce the error associated with several parameters, such as voltage, by direct measurement.

Bibliography

[1] C.C. Bouissou, J.P. Sylvestre, RH Guy, and MB Delgado-Charro. Reverse iontophoresis of amino acids: Identification and seperation of stratum corneum and subdermal sources in vitro. *Pharmaceutical Research*, 26:2630–2638, 2009.

[2] J.P. Sylvestre, C.C. Bouissou, R.H. Guy, and M.B. Delgado-Charro. Extraction and quantification of amino acids in human stratum corneum in vivo. *British Journal of Dermatology*, 163:458–465, 2010.

[3] T. McKee and J.R. McKee. *Biochemistry: The Molecular Basis of Life*. McGraw-Hill, 3 edition, 2003.

[4] R.A. Freitas Jr. *Nanomedicine, Volume 1: Basic Capabilities*. Landes Bioscience, 1999.

[5] B.G. Carvalho, L.J. Raniero, A.A. Martin, and P.P. Favero. Phenylalanine ab initio models for the simulation of skin natural moisturizing factor. *Spectrochimica Acta Part A: Molecular and Biomolecular Spectroscopy*, 106:73–79, 2013.

[6] R.R. Lenke amd H.L. Levy. Maternal phenylketonuria and hyperphenylalaninemia. An international survey on the outcome of treated and untreated pregnancies. *The New England Journal of Medicine*, 303:1202–1208, 1980.

[7] NEUROtiker. Image of phenylalanine molecule. Available online from http://commons.wikimedia.org/wiki/File:L-Phenylalanine_DJR.png, Accessed 2014.

[8] R.A. Williams, C.D.S. Mamotte, and J.R. Burnett. Phenylketonuria: An inborn error of phenylalanine metabolism. *Clinical Biochemistry Reviews*, 29:31–41, 2008.

[9] M. Bik-Multanowski and J.J Pietrzyk. Blood phenylalanine clearance and BH_4-responsiveness in classic phenylketonuria. *Molecular Genetics and Metabolism*, 103:399–

400, 2011.

[10] S. Kaufman. A model of human phenylalanine metabolism in normal subjects and in phenylketonuric patients. *Proceedings of the National Academy of Sciences USA*, 96:3160–3164, 1999.

[11] U. Langenbeck, J. Zschocke, U. Wendel, and V. Hönig. Modelling the phenylalanine blood level response during treatment of phenylketonuria. *Journal of Inherited Metabolic Disorders*, 24:805–814, 2001.

[12] J.M. Berg, J.L. Tymoczko, and L. Stryer. *Biochemistry.* W H Freeman, 5 edition, 2002.

[13] W.E. Nelson, V.C. Vaughan, and R.J. McKay. *Textbook of Pediatrics.* W.B. Saunders Company, 9 edition, 1969.

[14] J.F. Guest, J.J. Bai, R.R. Taylor, E. Sladkevicius, P.J. Lee, and R.H. Lachmann. Costs and outcomes over 36 years of patients with phenylketonuria who do and do not remain on a phenylalanine restricted diet. *Journal of Intellectual Disability Research*, 57:567–579, 2013.

[15] M.J. de Groot, M. Hoeksma, D.J. Reijngoud, H.W. de Valk, A.M.J. Paans, P.J.J. Sauer, and F.J. van Spronsen. Phenylketonuria: reduced tyrosine brain influx relates to reduced cerebral protein synthesis. *Journal of Rare Diseases*, 8:1–9, 2013.

[16] N. Blau, J.B. Hennermann, U. Langenbeck, and U. Lichter-Konecki. Diagnosis, classification, and genetics of phenylketonuria and tetrahydrobiopterin (BH_4) deficiencies. *Molecular Genetics and Metabolism*, 104:S2–S9, 2011.

[17] E.L. MacLeod, S.T. Gleason, S.C. van Calcar, and D.M. Ney. Reassessment of phenylalanine tolerance in adults with phenylketonuria is needed as body mass changes. *Molecular Genetics and Metabolism*, 23:331–337, 2009.

[18] A. Djabri. *Iontophoresis in paediatric medicine: Non-invasive drug delivery and monitoring applications.* PhD thesis, University of Bath, 2009.

[19] A. Williams. *Transdermal and Topical Drug Delivery.* Pharmaceutical Press, 2003.

[20] S.I. Yum and J. Roe. Capillarly blood sampling for self-monitoring of blood glucose. *Diabetes Technology and Therapeutics*, 1:29–37, 1999.

[21] B. Leboulanger, M. Fathi, R.H. Guy, and M.B. Delgado-Charro. Reverse iontophoresis as a noninvasive tool for lithium monitoring and pharmacokinetic profiling. *Pharmaceutical Research*, 21:1214–1222, 2004.

[22] L. Eckhart, S. Lippens, E. Tschachler, and W. Declercq. Cell death by cornification. *Biochimca et biophysica acta*, 12:3471–80, 2013.

[23] K.J. Green and J.C.R. Jones. Desmosomes and hemidesmosomes: Structure and function of molecular components. *The FASEB journal : Official publication of the Federation of American Societies for Experimental Biology*, 10:871–881, 1996.

[24] L. Norlén and A. Al-Amoudi. Stratum corneum keratin structure, function, and formation: The cubic rod-packing and membrance templating model. *The Journal of Investigative Dermatology*, 123:715–732, 2004.

[25] N. Dragicevic and H.I. Maibach. *Modification of the stratum corneum.* Springer Berlin, 2015.

[26] T.N. Tozer and M. Rowland. *Introduction to Pharmacokinetics and Pharmacodynamics: The Quantitative Basis of Drug Therapy.* Lippincott Williams & Wilkins, 1st edition, 2006.

[27] W.J. Jusko and S.J. Szefler. Pharmacokinetic design of digoxin dosage regimens in relation to renal function. *The Journal of Clinical Pharmacology*, 14:525–535, 1974.

[28] J. Hadgraft. Skin, the final frontier. *International Journal of Pharmaceutics*, 224:1–18, 2001.

[29] K.W. Ng and W.M. Lau. Skin deep: The basics of human skin structure and drug penetration. In D.N. Maibach, editor, *Percutaneous Penetration Enhancers Chemical Methods in Penetration EnhacementL Drug Manipulation Strategies and Vehicle Effects*, pages 3–11. Springer, 2015.

[30] H. Schaefer and T.E. Redelmeier. *Skin Barrier: Principles of Percutaneous Absorption.* Karger, 1996.

[31] J.C. Keister and G.B. Kasting. The use of transient diffusion to investigate transport pathways through the skin. *Journal of Controlled Release*, 4:111–117, 1986.

[32] O.D. Uitto and H.S. White. Electroosmotic pore transport in human skin. *Pharmaceutical Research*, 20:646–652, 2003.

[33] M.J. Pikal. The role of electroosmotic flow in transdermal iontophoresis. *Advanced Drug Delivery Reviews*, 9:201–237, 1992.

[34] A. Bunge and R. Cleek. A new method for estimating dermal absorption from chemical exposure: 2. Effect of molecular weight and octanol-water partitioning. *Pharmaceutical Research*, 12:88–95, 1995.

[35] M.A. Membrino. *Transdermal delivery of therapetuic compounds by iontophoresis*. PhD thesis, University of Florida, 2002.

[36] J.C. Keister. Ionic mass transport through a homogeneous membrane in the presence of a uniform electric field. *Journal of Membrane Science*, 29:155–167, 1986.

[37] S. Duke-Elder. Iontophoresis in the foundation of ophthalmology. *CV Mosby*, 7:507–514, 1960.

[38] J.M. Hill, L.P. Gangarosa, and N.H. Park. Iontophoretic application of antiviral chemotherapeutic agents. *Annals New York Academy of Sciences*, 284:604–612, 2006.

[39] R.H. Guy. Current status and future prospects of transdermal drug delivery. *Pharmaceutical Research*, 13:1765–1769, 1996.

[40] S. Garg, R. Potts, N. Ackerman, S. Fermi, J. Tamada, and H. Chase. Correlation of finger stick blood glucose measurements with GlucoWatch biographer glucose results in young subjects with type 1 diabetes. *Diabetes Care*, 22:1708–1714, 1999.

[41] A. Kim, P.G. Green, G. Rao, and R.H. Guy. Convective solvent flow across the skin during iontophoresis. *Pharmaceutical Research*, 10:1315–1320, 1993.

[42] S.M. Sims, W.I. Higuchi, and V. Srinivasan. Skin alteration and convective solvent flow effects during iontophoresis: I. Neutral solute transport across human skin. *International Journal of Pharmaceutics*, 69:109–121, 1991.

[43] E.A. Essa, M.C. Bonner, and B.W. Barry. Human skin sandwich for assessing shunt route penetration during passive and iontophoretic drug and liposome delivery. *Journal of Pharmacy and Pharmacology*, 54:1481–1490, 2002.

[44] M.G. Neubert and H. Caswell. Alternatives to resilience for measuring the responses of ecological systems to perturbations. *Ecology*, 78:653–665, 1997.

[45] B.C. Patten and M. Witkamp. Systems anaylsis of 134-cesium kinetics in terrestrial microsystems. *Ecology*, 48:813–824, 1967.

[46] D.L. DeAngelis. Energy flow, nutrient cycling, and ecosystem resilience. *Ecology*, 61:764–771, 1980.

[47] R.A. Horn and C.R. Johnson. *Matrix Analysis*. Cambridge University Press, 1985.

[48] A. Björck. *Numerical methods for least squares problems*. SIAM, 1996.

[49] A.N. Spiess and N. Neumeyer. An evaluation of r^2 as an inadequate measure for nonlinear models in pharmacological and biochemical research: A monte carlo approach. *BMC Pharmacology*, 10:1–11, 2010.

[50] R.E. McAuliffe. *Standard Error of Estimate*, volume 8:1 of *Wiley Encyclopedia of Management*. Wiley, 2015.

[51] H.H. Ku. Notes on the use of propagation of error formulas. *Journal of Research of the National Burea of Standards*, 70C:263–273, 1966.

[52] A. Couto, R. Fernandes, M. Natália, S.Cordeiro, S.S Reis, R.T. Ribeiro, and A.M. Pessoa. Dermic diffusion and stratum corneum: A state of the art review of mathematical models. *Journal of Controlled Release*, 2013.

[53] J. Perez Guerroero, L Pimentel, T. Skaggs, and M. van Genuchten. Analytical solution of the advection-diffusion transport equation using a change-of-variable and integral transform technique. *International Jounral of Heat and Mass Transfer*, 52:3297–3304, 2009.

[54] W.E. Schiesser and G.W. Griffiths. *A Compendium of Partial Differential Equation Models: Method of Lines Analysis with Matlab*. Cambridge University Press, 2009.

[55] L.C. Evans. *Partial Differential Equations*. American Mathematical Society, 2 edition, 2010.

[56] G. Arfken. *Mathematical Techniques for Physicists*. Academic Press, 3 edition, 1985.

[57] D. Kowlessur, B.A. Citron, and S. Kaufman. Recombinant human phenylalanine hydroxylase: Novel regulatory and structural properties. *Archives of Biochemistry and Biophysics*, 333:85–95, 1996.

[58] Important basics food charts. Available online from apjcn.nhri.org.tw/server/info/books-phds/books/foodfacts/html/data/data2e.html. Accessed: 2014-06-25.

[59] J.E. Hall and A.C. Guyton. *Guyton and Hall Textbook of Medical Physiology*. Saunders/Elsevier, 2011.

[60] I. Arias, A. Wolkoff, J. Boyer, D. Shafritz, N. Fausto, H. Alter, and D. Cohen. *The Liver:Biology and Pathobiology*. Wiley-Blackwell, 5 edition, 2009.

[61] A. Moody. Chapter 10: Adult anthropometric measures, overweight and obesity. In R. Craig and J. Mindell, editors, *Health Survey for England - 2012*. Health and Social Care Information Centre, 2012.

[62] M.P. Pai and F.P. Paloucek. The origin of the 'ideal' body weight equations. *The Annals of Pharmacotherapy*, 34:1066–1069, 2000.

[63] E.L. Dobson, G.F. Warner, C.R. Finney, and M.E. Johnston. The measurement of liver circulation by means of the colloid disappearance rate: I. Liver blood flow in normal young men. *Circulation*, 7:690–695, 1953.

[64] I.H. Segel. *Enzyme Kinetics*. Wiley-interscience, 1975.

[65] J.L. Launer and T. Harris. Weight, height and body mass index distributions in geographically and ethnically diverse samples of older persons. *Age and Ageing*, 25:300–306, 1996.

[66] M.H. Vendelbo, A.B. Møller, B. Christensen, B. Nellemann, B.F.F. Clasen, K.S. Nair, J.O.L. Jørgensen, N. Jessen, and N. Møller. Fasting increases human skeletal muscle net phenylalanine release and this is associated with decreased mtor signaling. *PLoS One*, 9:1–8, 2014.

[67] U. Lichter-Konecki, C.M. Hipke, and D.S. Konecki. Human phenylalanine hydroxylase gene expression in kidney and other non-hepatic tissues. *Molecular Genetics and Metabolism*, 67:308–316, 1999.

[68] S.D. Ehrlich. Phenylalanine. Available online from http://umm.edu/Health/Medical/AltMed/Supplement/Phenylalanine, 2015.

[69] Y. Paulley, B. Delgado-Charro, and J. White. Modelling formation of a drug reservoir in the stratum corneum and its impact on drug monitoring using reverse iontophoresis. *Computational and Mathematical Methods in Medicine*, 11:353–368, 2010.

[70] E. Bolton, Y. Wang, P.A. Thiessen, and S.H. Bryant. *PubChem: Integrated Platform of Small Molecules and Biological Activities. Chapter 12 IN Annual Reports in Computational Chemistry*, volume 4. American Chemical Society, Washington, DC, 2008.

[71] G. Charambopoulou, P. Karamertzanis, E. Kikkinides, A. Stubos, N. Kanellopoulos, and A. Papaioannou. A study on structural and diffsuion properties of porcine stratum corneum based on very small angle neutron scattering data. *Pharmaceutical Research*, 17:1085–91, 2000.

[72] J. Nitsche and G. Kasting. A microscopic multiphase diffusion model of viable epidermis permeability. *Biophysical Journal*, 104:2307–2320, 2013.

[73] M. Heisig, R. Lieckfeldt, G. Wittum, G. Mazurkevich, and G. Lee. Non steady-state descriptions of drug permeation through stratum corneum. I. The biphasic brick-and-mortar model. *Pharmaceutical Research*, 13:421–426, 1996.

[74] S.M. Jackson, M.L. Williams, and K.R. Feingold. Pathobiology of stratum corneum. *The Western Journal of Medicine*, 158:279–285, 1993.

[75] M. Fartasch, J. Teal, and G.K. Menon. Mode of action of glycolic acid on human stratum corneum: ultrastructural and functional evaluation of the epidermal barrier. *Archives of Dermatological Research*, 289:404–409, 1997.

[76] R. Potts and R. Guy. Predicting skin permeability. *Pharmaceutical Research*, 9:663–669, 1992.

[77] P. Green, R. Hinz, A. Kim, C. Cullander, G. Yamane, F. Szoka, and R. Guy. Transdermal iontophoresis of amino acids and peptides in vitro. *Journal of Controlled Release*, 21:187–190, 1992.

[78] M. Robinson, M. Visscher, A. LaRuffa, and R. Wickett. Natural moisturizing factors (NMF) in the stratum corneum (SC). I. Effects of lipid extraction and soaking. *Journal*

of Cosmetic Science, 61:13–22, 2010.

[79] M. Ochalek, H. Podhaisky, H.H. Ruettinger, J. Wohlrab, and R.H.H. Neubert. SC lipid model membranes designed for studying impact of ceramide species on drug diffusion and permeation - Part II: Diffusion and permeation of model drugs. *European Journal of Pharmacuetics and Biopharmaceutics*, 82:360–366, 2012.

[80] M. Ochalek, R.H.H. Neubert, and J. Wohlrab. SC lipid model membranes designed for studying impact of ceramide species on drug diffusion and permeation - Part III: Influence of penetration enhancer on diffusion and permeation of model drugs. *Internation Journal of Pharmaceutics*, 436:206–213, 2012.

[81] P. Schumm. A network model of successive partitioning-limited solute diffusion through the stratum corneum. *Journal of Theoretical Biology*, 262:471–477, 2010.

[82] T.F. Wang, G.B. Kasting, and J.M. Nitsche. A multiphase microscopic diffusion model for stratum corneum permeability. i. formulation, solution and illustrative results for representative compounds. *Journal of Pharmaceutical Sciences*, 95:620–648, 2006.

[83] N.A. Monteiro-Riviere, A.O. Inman, and J.E. Riviere. Identification of the pathway of iontophoretic drug delivery: Light and ultrastructural studies using mercuric chloride in pigs. *Pharmaceutical Research*, 11:251–256, 1994.

[84] M.M. Mukaka. Statistics corner: A guide to appropriate use of correlation coefficient in medical research. *Malawi Medical Journal*, 24:69–71, 2012.

[85] W.M. Haynes. *Handbook of chemistry and physics*. CRC Press, 93 edition, 2013.

[86] C. Malmberg and A. Maryott. Dielectric constant of water from 0^0 to 100^0c. *Journal of Research of the National Bureau of Standards*, 56:2641–2648, 1956.

[87] V. Aguilella, K. Kontturi, L. Murtomaki, and P. Ramirez. Estimation of the pore size and charge density in human cadaver skin. *Journal of Controlled Release*, 32:249–257, 1994.

[88] H. Butt, K. Graf, and M. Kappl. *Physics and Chemistry of Interfaces*. Wiley-VCH, 2 edition, 2008.

[89] G. Karniadakis, A. Beskok, and N. Aluru. *Microflows and Nanoflows*. Springer, 1

edition, 2005.

[90] J.A Manzanares and P. Ramirez et al. Pore conductivity and streaming potential in charged capillary tubes with concentration dependent pore wall charge. *Journal of non-equilibrium thermodynamics*, 16:255–265, 1991.

[91] T. Gratieri and Y.N. Kalia. Mathematical models to describe iontophoretic transport *in vitro* and *in vivo* and the effect of current application on the skin barrier. *Advanced Drug Delivery Reviews*, 65:315–329, 2013.

[92] M.J. Pikal. Transport mechanisms in iontophoresis. I. A theoretical model for the effect of electroosmotic flow on flux enhancement in transdermal iontophoresis. *Pharmaceutical Research*, 7:118–126, 1990.

[93] G.S. Manning. Model for electroosmosis in fixed charge systems. *Journal of Physical Chemistry*, 46:4976–4980, 1967.

[94] D. Hildreth. Electrokinetic flow in fine capillary channels. *Journal of Physical Chemistry*, 74:2006–2015, 1970.

[95] G.K. Batchelor. *An Introduction to Fluid Dynamics*. Cambridge University Press, 1 edition, 2000.

[96] S. Ghosal. Fluid mechanics of electroosmotic flow and its effect on band broadening in capillary electrophoresis. *Electrophoresis*, 25:214–228, 2004.

[97] M. Pikal. Transport mechanisms in iontophoresis. I. A theoretical model for the effect of electroosmotic flow on flux enhancement in transdermal iontophoresis. *Pharmaceutical Research*, 7:118–126, 1990.

[98] P.A. Tipler and G. Mosca. *Physics for scientists and engineers*. Freeman, 6 edition, 2008.

[99] K. Kontturi, A. Savonen, and M. Vuoristo. Study of adsorption and ion-exchange properties of some porous membranes. *Acta Chemica Scandinavica*, 48:1–11, 1994.

[100] A.D. Poularikas. *The Handbook of Formulas and Tables for Signal Processing*. CRC Press, 1999.

[101] Y. Itoh, A. Shimazu, Y.Sadzuka, T. Sonobe, and S. Itai. Novel method for stratum corneum pore size determination using positron annihilation lifetime spectroscopy. *International Journal of Pharmaceutics*, 358:91–95, 2008.

[102] U. Blume-Peytavi et al. Variations of hair follicle size and distribution in different body sites. *Journal of Investigative Dermatology*, 122:14–19, 2004.

[103] N. Longo, S.K. Li, G. Yan, R.P. Kochambilli, K. Papangkorn, D. Berglund, A.H. Ghanem, C.L. Ashurst, S.L. Ernst, M. Pasquali, and W.I. Higuchi. Noninvasive measurement of phenylalanine by iontophoretic extraction in patients with phenylketonuria. *Journal of Inherited Metabolic Disorders*, 30:910–915, 2007.

[104] J.S. Sandby-Moller, T. Poulsen, and H.C. Wulf. Epidermal thickness at different body sites: Relationship to age, gender, pigmentation, blood content, skin type and smoking habits. *Acta Dermato Venereologica*, 83:410–413, 2003.

[105] H. Inada, A.H. Ghanem, and W.I. Higuchi. Studies on the effects of applied voltage and duration on human epidermal membrane alteration/recovery and the resultant effects upon iontophoresis. *Pharmaceutical Research*, 11:687–697, 1993.

[106] T. Yamamoto and Y. Yamamoto. Dielectric constant and resistivity of epidermal stratum corneum. *Medical and Biological Engineering*, 14:494–500, 1976.

[107] G. Kasting and J. Keister. Application of electrodiffusion theory for a homogeneous membrane to iontophoretic transport through skin. *Journal of Controlled Release*, 8:195–210, 1988.

[108] M.J. Keohler, T. Vogel, P. Elsner, K. König, R. Bückle, and M. Kaatz. In vivo measurement of the human epidermal thickness in different localizations by multiphoton laser tomography. *Skin Research and Technology*, 16:259–264, 2010.

[109] N. Epstein. On tortuosity and the tortuosity factor in flow and diffusion through porous media. *Chemical Engineering Science*, 44:777–779, 1989.

[110] J.L. Anderson and J.A. Quinn. Restricted transport in small pores: A model for steric exclusion and hindered particle motion. *Biophysics Journal*, 14:130–150, 1974.

[111] B.W. Barry and S.L. Bennett. Effect of penetration enhancers on the permeation of mannitol, hydrocortisone and progesterone through human skin. *Journal of Pharmacy*

and Pharmacology, 39:535–546, 1986.

[112] C.J. Gommes, A.J. Bons, S. Blacher, J.H. Dunsmuir, and A.H. Tsou. Practical methods for measuring the tortuosity of porous materials from binary or gray-tone tomographic reconstructions. *American Institute of Chemical Engineers Journal*, 55:2000–2012, 2009.